Transactions of the ASME

Journal of Fluids Engineering

Published Quarterly by The American Society of Mechanical Engineers

VOLUME 107 • NUMBER 4 • DECEMBER 1985

The Journal of Fluids Engineering (ISSN 0098-2202) is published quarterly for $100 per year by The American Society of Mechanical Engineers, 345 East 47th Street, New York, NY 10017. Second class postage paid at New York, NY and additional mailing offices. POSTMASTER: Send address changes to The Journal of Fluids Engineering, c/o THE AMERICAN SOCIETY OF MECHANICAL ENGINEERS, 22 Law Drive, Box 2300, Fairfield, NJ 07007-2300.
CHANGES OF ADDRESS must be received at Society headquarters seven weeks before they are to be effective. Please send old label and new address.
PRICES: To members, $24.00, annually: to nonmembers, $100. Add $6.00 for postage to countries outside the United States and Canada.
STATEMENT from By-Laws. The Society shall not be responsible for statements or opinions advanced in papers or . . . printed in its publications (B7.1, Par. 3).

INDEXED by Engineering Information

F. Gori
Fisica Tecnica,
Dipartimento di Energetica dell'Università,
50139 Firenze, Italy

Is Laminar Flow in a Cylindrical Container With a Rotating Cover a Batchelor or Stewartson-Type Solution?

Introduction

Bertelá and Gori (1982) have solved the flow of an incompressible viscous fluid inside a cylindrical container with a rotating cover. Some results are here reviewed in order to detect whether they exhibit any similarity to the so called Batchelor or Stewartson-type solutions for two infinite coaxial disks.

In connections with this geometry, Nguyen et al. (1975) numerically found that both types of solutions are possible but, using finite disks with low aspect ratio, they experimentally measured the unique Batchelor-type solution.

Hoodniok et al. (1977) have discovered the existence of multiple solutions for high enough Reynolds number when both disks are rotating.

Recently, Dijkstra and van Heijst (1983) and Szeri et al. (1983) have found experimentally a Batchelor-type solution for a disk rotating in an enclosed cylindrical system with very low aspect ratios and high Reynolds numbers.

Considerations

The dimensionless radial, tangential and axial components of the local velocity are, respectively, u, v, w with $u=u^*/\Omega^*R^*$, $v=v^*/\Omega^*R^*$, $w=w^*/\Omega^*R^*$. The variables with the star are the dimensional ones.

The chamber aspect ratio is $\lambda=d^*/R^*$, the rotational Reynolds number is $\mathrm{Re}=\Omega^*R^{*2}/\nu$, where d^* and R^* are the height and the radius of the container and Ω^* is the angular speed of the rotating cover.

Ekman number is given by $E_k=\nu/\Omega^*d^{*2}$ so that the following relation holds, $E_k^{-1}=\mathrm{Re}\cdot\lambda^2$. The dimensionless coordinates z and r are defined, respectively, as $z=z^*/d^*$ and $r=r^*/R^*$., where z^* and r^* are, respectively, the axial and radial distances from the middle of the rotating disk.

The numerical results of u/r, v/r in the closed container, Bertelà and Gori (1982), are reported for $r=0.475$ and $r=0.5$, respectively in Figs. 1-2 and 3-4. All the solutions are plotted for convenience versus the z coordinate.

The v/r profiles of Fig. 1 shows the tendency to assume a Stewartson structure with increasing λ. The tangential velocity on the bottom disk decreases for containers with higher λ and when $\lambda=2$ almost one fourth of the fluid is stagnant. A similar trend is evident from Fig. 2 where the solutions are relative to a higher Re number.

The velocity profiles of Fig. 1 are hence compared to those of Fig. 2 for the same λ. It is evident that an increase of Re modifies the solutions toward the Batchelor-type with the formation and intensification of the rotational boundary layer on the bottom disk. Externally to this, the angular speed is quasi constant.

To summarize what has been observed, the two figures seem to affirm that if in a closed container only Re is increased the solutions tend toward the Batchelor-type. Conversely if λ is increased the solutions tend to assume the Stewartson-type structure.

Figures 3-4 report the radial velocity profiles, u/r, for $\mathrm{Re}=100$ and 1000, respectively. The solutions of Fig. 3 show that, with increasing λ, the radial velocity on the bottom disk is decreasing and for $\lambda=2$ one fourth of the fluid is almost stagnant. A similar decrease is evident from Fig. 4 also if the radial velocity is not zero because of the higher Re.

The solutions for the vessel are now compared to those obtained between two infinite disks in order to point out the influence of the side wall.

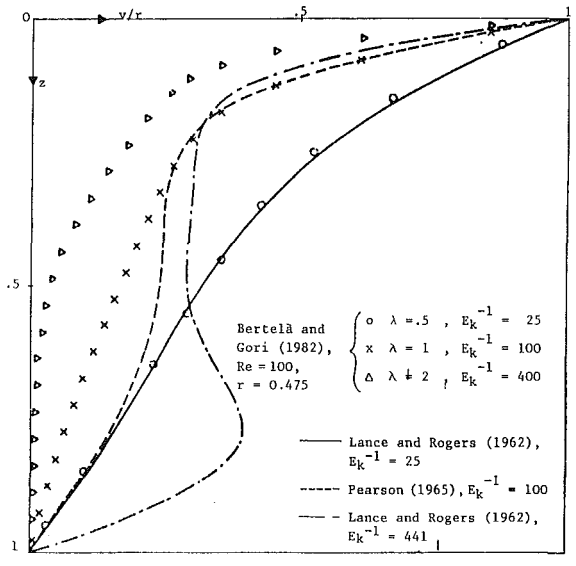

Fig. 1 Tangential velocities versus the z coordinate

Contributed by the Fluids Engineering Division for publication in the JOURNAL OF FLUIDS ENGINEERING. Manuscript received by the Fluids Engineering Division April 3, 1984.

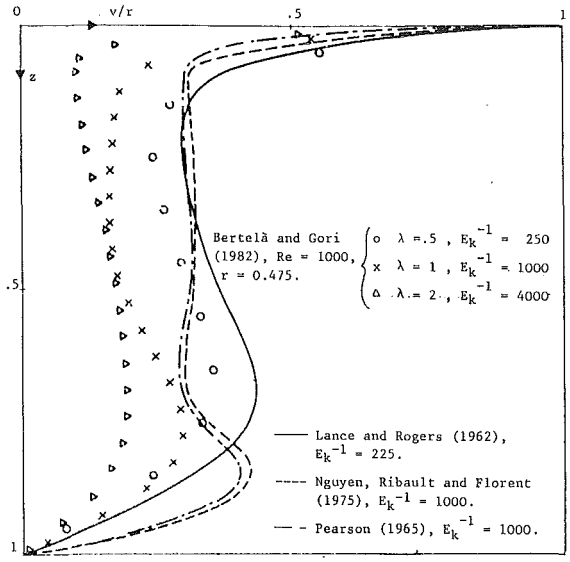

Fig. 2 Tangential velocities versus the *z* coordinate

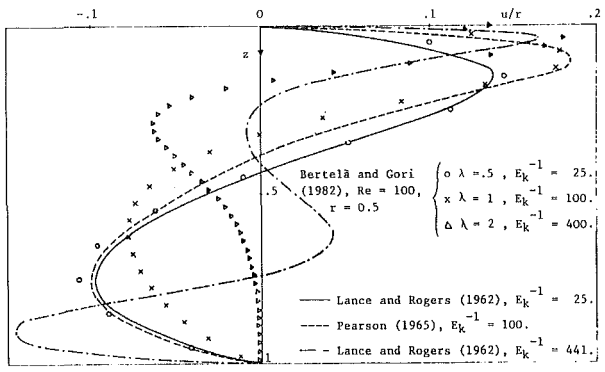

Fig. 3 Radial velocities versus the *z* coordinate

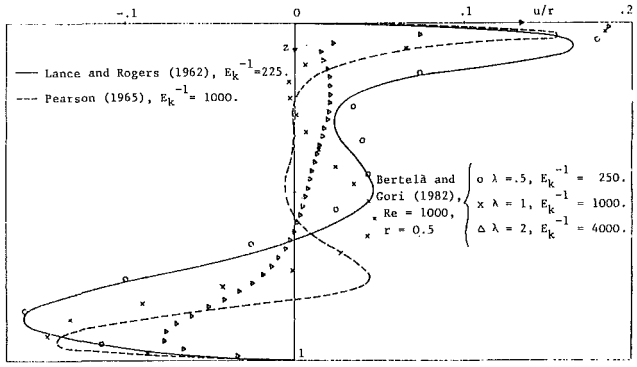

Fig. 4 Radial velocities versus the *z* coordinate

The velocity profiles between two infinite disks are considered corresponding to those in the vessel when they have the same E_k number. In some cases these equalities are only approximate; for instance, Lance and Rogers (1962) give solutions for $E_k^{-1} = 441$ and 225 while those of Bertelá and Gori (1982) are for $E_k^{-1} = 400$ and 250. These differences are not considered relevant to make the deductions questionable. The two-disk solutions for $E_k^{-1} = 4000$ are not available in the literature.

Figure 1 shows a very good agreement between the solutions for $E_k^{-1} = 25$. If E_k^{-1} is increased the disagreement becomes more apparent. The two-disk solutions for $E_k^{-1} = 441$ tend clearly toward the Batchelor-type configuration, differently from what happens in the container, whose profile has the Stewartson structure. Figure 2 presents a good agreement between the solutions for $E_k^{-1} = 225$. With increasing E_k^{-1}, again the disagreement is more evident. The solutions for two disks are stable, of the Batchelor-type for the increasing E_k^{-1} while for the closed container they tend to the Stewartson-type configuration for the higher λ.

No further comments are necessary to compare u/r graphs for two disks to the corresponding vessel solutions (Figs. 3–4).

The observation of the tangential velocity profiles for two disks (Figs. 1–2) is given according to the sequence: $E_k^{-1} = 25$; 100; 225; 441; 1000. It is clear the evolution toward the Batchelor-type configuration and it occurs whether the increase of E_k^{-1} is obtained from that of Ω or d.

In the case of the vessel solutions, the presence of the side wall, which introduces a new geometrical parameter, drastically modifies this conclusion. Either Batchelor or Stewartson-type profiles occur for a container with a given radius if either Ω or d are respectively increased.

Conclusion

The discussed numerical results seem to support the following statement: for a cylindrical container with a fixed radius the Batchelor-type solution occurs when the angular speed of the rotating disk is high enough; the Stewartson mode is found for a large enough distance between the top and bottom disks.

Comparisons between cylindrical vessel and two-infinite-disk solutions show that the increase of d accentuates their trends (toward Stewartson and Batchelor, respectively). Conversely, the increase of Ω determines that both the solutions evolve towards the Batchelor shape.

When Ω and d are small the two solutions are in very good agreement, particularly inside the central part of the fluid, and the role played by the shroud seems to be insignificant. For sufficiently high values of both Ω and d the side wall of the container becomes important and generates remarkable differences in the velocity distributions for the two systems.

References

Batchelor, G. K., (1951) Note on a Class of Solutions of the Navier-Stokes Equations representing steady rotationally-symmetric flow," *Quart. J. Mech. Appl. Math.*, Vol. 4, pp. 29–41.

Bertela, M., and Gori, F., (1982) Laminar Flow in a Cylindrical Container with a Rotating Cover, ASME JOURNAL OF FLUIDS ENGINEERING, Vol. 104, Mar. pp. 31–39.

Dijkstra, D., and van Heijst, G. J. F., (1983) "The Flow Between Two Finite Rotating Disks Enclosed by a Cylinder," *J. Fluid Mech.*, Vol. 128, pp. 123–154.

Holodniok, M., Kubicek, M., and Hlavacek, V., (1977) "Computation of the Flow Between Two Rotating Coaxial Disks," *J. Fluid Mech.*, Vol. 81, pp. 689–699.

Lance, G. N., and Rogers, M. H., (1962) "The Axially Symmetric Flow of a Viscous Fluid Between Two Infinite Rotating Disks," *Proc. Roy. Soc.*, A266, pp. 109–121.

Nguyen, N. D., Ribault, J. P., and Florent, P., (1975) "Multiple Solutions for Flow Between Coaxial Disks," *J. Fluid Mech.*, Vol. 68, pp. 369–388.

Pearson, C. E., (1965) "Numerical Solution for the Time Dependent Viscous Flow Between Rotating Coaxial Disks," *J. Fluid Mech.*, Vol. 21, p. 623.

Stewartson, K., (1953) "On the Flow Between Two Rotating Coaxial Disks," *Proc. Camb. Phil. Soc.*, Vol. 3, pp. 333–341.

Szeri, A. Z., Schneider, S. J., Labbe, F., and Kaufman, H. N., (1983) "Flow Between Rotating Disks. Part 1: Basic Flow," *J. Fluid Mech.*, Vol. 134, pp. 103–131.

Calculation of the Aerodynamic Forces on Automotive Lifting Surfaces

J. Katz*
Faculty of Mechanical Engineering,
Technion, I.I.T.,
Haifa, Israel

A numerical technique was developed to investigate the performance of automotive lifting surfaces in close proximity to ground. The model is based on the Vortex Lattice Method and includes freely-deforming wake elements. The ground effect was simulated by reflection and both steady and unsteady pressures and loads on various wing planforms were considered. Calculated results are presented for wings having both positive and negative incidences, with and without ground effect. Also the transient lift of a wing in a plunging motion was analyzed in ground proximity and at a negative angle of attack. Finally the periodic lift fluctuations on the front winglet of a racing car, due to its suspension oscillations, were calculated and found to exceed approximately twice the steady-state value.

Introduction

One of the major limitations on the performance of high-speed ground vehicles, such as racing cars, is the slip limit of their tires. Both the lateral and longitudinal traction of these tires is a direct function of the normal load applied on the axles of the vehicle. An increase in the normal downforce on these vehicles by aerodynamic means will directly improve their high-speed turning rates and acceleration [1, 2], without the penalty of excessive weight. An effective method for obtaining such aerodynamic forces is by integrating surfaces into the vehicle's body design (as shown by Fig. 1(*a*)). Analytical prediction of the aerodynamic forces on these lifting surfaces, however, differs slightly from the classical problem [3] of an aircraft wing flying near the ground. Consequently, not all the aspects of this aerodynamic phenomenon have been investigated. As an example, the winglets used on racing cars have a negative incidence, which under some conditions, increases the ground effect. They also oscillate in a heaving motion with the car, due to the relative motion of the suspension and due to the changing road conditions, and therefore the estimation of transient aerodynamic response is essential for the structural design.

In the current study, an unsteady lifting surface model is proposed for the investigation of the aerodynamic forces acting on a three dimensional thin wing moving in ground proximity. With this model the effects of the wing aspect ratio, ground clearance and transient response are investigated. Furthermore, the model does not require linearized boundary conditions. Also vortex wake deformations and arbitrary three-dimensional motions of the airfoil can be included.

The Mathematical Model

Consider the lifting surface of Fig. 1(*b*) moving through a continuous fluid with a velocity $U(t)$. The wing is represented by a three-dimensional surface and can have different geometries including camber, taper, forward or aft sweep and ground proximity. It is assumed that the fluid is incompressible, irrotational and homogeneous over the entire flow-field, excluding the wing and its wakes. Since the typical Reynolds Number of high-speed road vehicles is on the order of 10^6 the boundary layers are thin and the above assumptions are valid (excluding flow separations on the lifting surface). In-

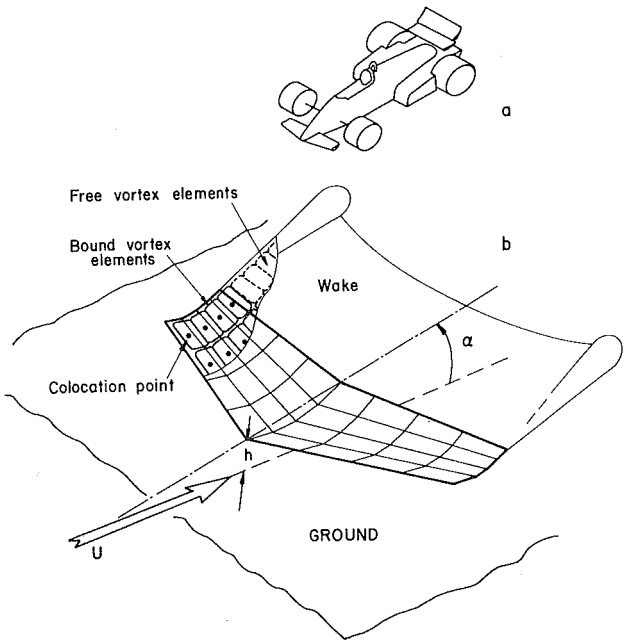

Fig. 1 *Typical racing car configuration with front and rear winglets (a), and the vortex lattice model for the front lifting surface (b)*

*Current address: NASA Ames 247-1, Moffett Field CA.

Contributed by the Fluids Engineering Division for publication in the JOURNAL OF FLUIDS ENGINEERING. Manuscript received by the Fluids Engineering Division, May 4, 1984.

teractions with the car body and wheels are not included in the current work. Future investigation of some of these problems, involving attached flow fields, is possible with the following model. Some of the more complex interactions, however, requires the modeling of separated flows (e.g., the wheel wake) and therefore can not be predicted by this method. Consequently, a simple geometry was used here to demonstrate the computational capability of the method. This capability is assumed to be sufficient to capture the potential ground effect, which is the dominant term in calculating the aerodynamic forces acting on the front winglet of current racing cars [4]. As a result of the above assumptions a velocity potential Φ can be defined and the following model [5] (equations (1) to (6)) is derived.

The continuity equation becomes:

$$\nabla^2\Phi = 0 \tag{1}$$

with the boundary condition (2) derived in a wing-fixed frame of reference, requiring zero normal velocity, relative to the wing's surface

$$\nabla\Phi \cdot n = V_f \cdot n \tag{2}$$

where n is a vector, normal to the wing surface and $V_f(t)$ is the time dependent local boundary surface velocity. This potential version of the continuity equation (1) does not have any derivative with respect to time, since the fluid is incompressible. The unsteady effects, therefore, will be introduced through the time dependent boundary condition (2). This unsteady formulation effectively transforms the elliptic problem of equation (1) into a parabolic one, requiring additional initial conditions. The major advantage of the solution derived hereafter is that this boundary condition (equation (2)) does not have to be linearized and consequently large amplitude and arbitrary nonsteady motions can be treated [6]. In addition, the wing-wake induced dusturbance should diminish far from the wing:

$$\lim \nabla\Phi_{r\to\infty} = 0 \tag{3}$$

The velocity at the trailing edge is limited by applying the Kutta condition:

$$\nabla\Phi < \infty \text{ (at the trailing edge)} \tag{4}$$

To calculate the instantaneous strength of the streamwise vortex sheet, shed at the trailing edge, Kelvin's theorem is applied. This theorem postulates that the circulation Γ around a closed circuit which moves with the fluid (including the wing and its wake) is constant. This integral derivation actually implies that any transient change in the wing's circulation is cancelled by the shedding of equal (but opposite in sign) wake elements.

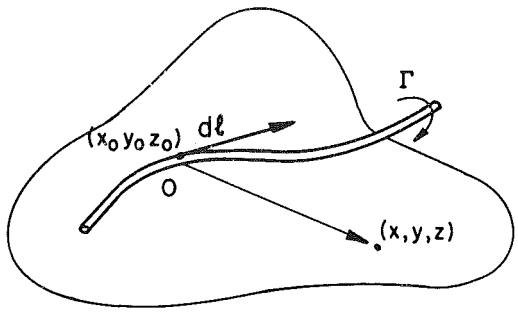

Fig. 2 The induced velocity at a point (x,y,z due to a vortex line segment *dl*)

$$\frac{d\Gamma}{dt} = \left(\frac{d\Gamma}{dt}\right)_{\text{wing}} + \left(\frac{d\Gamma}{dt}\right)_{\text{wake}} = 0 \text{ (for all time)} \tag{5}$$

The general solution of equations (1)–(5), at a point (x,y,z), can be obtained by Green's theorem as a sum of doublet and source distributions over the boundaries S including the wing surface and the wake.

$$\Phi(x,y,z,t) = \frac{-1}{2\pi}\int_{\text{wing+wake}} \left[\Phi\frac{\partial}{\partial n}\frac{1}{r} - \frac{1}{r}\frac{\partial\phi}{\partial n}\right] dS \tag{6}$$

$$r = r(x,y,z)$$

The first term, after an additional differentiation with respect to r, actually becomes a vortex element as shown in the diagram of Fig. 2 (this equivalence is shown in references [6] and [7]). Here the induced velocity ΔV due to a vortex line element dl (located at x_0, y_0, z_0) with the circulation Γ, at a point (x, y, z) is given by equation (7).

$$\Delta V(x,y,z) = \frac{-1}{4\pi}\Gamma(x_0,y_0,z_0)\frac{r\times dl}{|r|^3} \tag{7}$$

The source term in equation (6) represents the airfoil's thickness effect only and for studying the lifting problem (as it is used in this work), the solution based on the vortex distribution will be used.

The following unsteady Vortex Lattice Method is based on the vortex term of equation (6), and automatically fulfills equations (1) and (3). Therefore the wing surface and the wake is modeled by bounded and free vortex rings, respectively. The

Nomenclature

A_{ij} = influence coefficient (due to bound circulation)
B_{ij} = influence coefficient (due to trailing edge wake circulation)
AR = wing aspect ratio
b = wing span
c = wing chord
C_D = drag coefficient
C_l = spanwise, section lift coefficient
C_L = lift coefficient (steady state value)
$C_L(t)$ = time dependent lift coefficient
C_{L_g} = lift coefficient, near the ground
C_{L_α} = lift curve slope ($\partial C_L/\partial\alpha$)
C_{m_0} = pitching moment coefficient
dl = length of vortex segment
F = normal force
h = wing height above ground
n = vector, normal to wing surface
p = pressure
q = angular velocity about y axis
r = vector (x,y,z)
S = wing or panel reference area
t = time
U = wing forward velocity
u = induced velocity to the x direction
V = induced velocity
V_f = panel kinematic velocity
v = induced velocity to the y direction
w = induced velocity to the z direction
W = heaving velocity
x,y,z = wing coordinates
α = angle of attack
Γ = circulation
Γ_f = wing bound circulation
Γ_w = trailing edge wake circulation
Λ = wing sweep angle
ρ = density
σ = reduced frequency $\left(\frac{\omega\cdot c}{2U}\right)$
ϕ = velocity potential
ω = heaving frequency (rad/s)

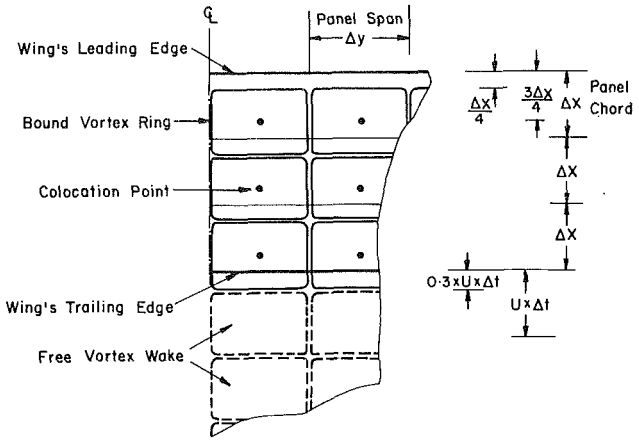

Fig. 3 The geometry of the vortex lattice

geometry of a vortex-ring panel element is shown by Fig. 3, where the bound vortex is placed at the panel quarter chord, and the colocation point (where boundary condition 2 is applied) is placed at the panel three quarter chord (at the center of the vortex ring). The vortex ring element also fulfills equation (5) and the Kutta condition (4) for the two dimensional case, which successfully was applied for three dimensional flows as well [6].

When rewriting boundary condition (2), with the use of the vortex elements, the momentary induced normal velocity $\partial\Phi/\partial z$ at any point on the wing will be a sum of all the velocities induced by the vortex elements:

$$\left.\frac{\partial\Phi}{\partial z}\right|_{\text{on wing}} = \frac{-1}{4\pi}\int_{\text{wing+wake}} \Gamma\frac{r\times dl}{|r|^3} \tag{8}$$

After discretizing the lifting surface into panel elements (Fig. 3); equation (8) is specified for each colocation point resulting in the following relation:

$$\begin{bmatrix} \partial\Phi/\partial z_1 \\ \vdots \\ \partial\Phi/\partial z_k \end{bmatrix} = [A_{ij}]\begin{bmatrix} \Gamma_{f1} \\ \vdots \\ \Gamma_{fk} \end{bmatrix} + [B_{ij}]\begin{bmatrix} \Gamma_{w1} \\ \vdots \\ \Gamma_{wm} \end{bmatrix} \tag{9}$$

Here Γ_{fi} are the bound vortex elements, Γ_{wi} are the free wake elements while (A_{ij}) and (B_{ij}) are the corresponding influence coefficients obtained by equation (8). The kinematic normal velocity w_{ij}, at each colocation point, due to the wing momentary forward velocity $U(t)$, plunging velocity $W(t)$, rotation q and local angle of attack α_i is:

$$w_{ij} = U(t)\sin\alpha_i + W(t) + qx_i \tag{10}$$

To fulfill equation (2) the sum of the velocities, relative to the panel, must be equal to zero:

$$w_{ij} + \left(\frac{\partial\Phi}{\partial z}\right)_{ij} = 0 \tag{11}$$

and by substituting (9) and (10) into (11) a set of k linear algebraic equations is obtained with k unknown bound vortices Γ_{fi}. The number m of wake elements in equation (9) is increasing with each time interval and the strength of the free vortices shed from the trailing edge Γ_{wi} are known from previous time steps. For a non-varying wing geometry with time, the matrix (A_{ij}) is calculated only once; matrix $(B)_{ij}$ on the other hand has to be determined at each time interval Δt.

The free vortex wake, that being shed at the wing's trailing edge, is simulated by releasing vortex-ring segments at each time interval Δt as shown by Fig. 1(*b*) and Fig. 3. The spanwise free-vortex segment is placed within (30 percent) of the path $(U^*\Delta t)$, covered by the trailing edge, during the momentary time interval Δt (Fig. 3). This vortex positioning was found to minimise numerical error, due to vortex sheet discretization, at the vicinity of curved streamlines (even for larger time steps, e.g., $\Delta t = c/(4^*U)$). More details about the technique which determines the motion of the vortex wake, can be found in references [6 and 9]. This scheme requires an in intial value type of solution, where at $t = -0$ the wing is at rest. Then at $t = +0$ the wing is suddenly set into motion and the vortex wake elements are shed in to the flow as shown in Fig. 1(*b*) and Fig. 3. Equation (11) is then solved providing the bound circulation distribution Γ_{fi} on the wing. As this calculation is completed the wake deformation is simulated by calculating the downwash $(u, v, w)_i$ at each free vortex tip and then moving this point by the displacement $(\Delta x, \Delta y, \Delta z)$:

$$\begin{bmatrix} \Delta x \\ \Delta y \\ \Delta z \end{bmatrix}_i = \begin{bmatrix} u \\ v \\ w \end{bmatrix}_i {}^*\Delta t \tag{12}$$

As the solution of the circulation distribution (equation (11)) is obtained, the pressure differenced Δp_i across each panel with the area S_i is determined by applying the unsteady Bernoulli equation:

$$\Delta p_i = \frac{2\rho}{S_i}\left[\left(U\int_{x_{i-1}}^{x_i}\frac{\partial\Phi}{\partial x}dx\right)\Delta y_i + \int_{x_{i-1}}^{x_i}\left(\frac{\partial}{\partial t}\int_0^{x_i}\frac{\partial\Phi}{\partial x}\,dx\right)dx\Delta y_i\right] \tag{13}$$

Equation (13) might be rewritten in terms of the panel chordwise bound circulation Γ_{ix}, as follows:

$$\Delta F_i = \Delta p_i \cdot S_i = \rho\left[U\Gamma_{ix}\cdot\Delta y_i + \frac{\partial}{\partial t}\left(\sum_{l=1}^{i-1}\Gamma_{l_x}\Delta x_l + \Gamma_{ix}\frac{\Delta x_i}{2}\right)\right] \tag{14}$$

The resulting lift, drag and pitching moment coefficients are obtained by integrating each panel normal force ΔF_i along the wing's surface:

$$C_L = \frac{\sum_{i=1}^{K}\Delta F_i\cos\alpha_i}{1/2\rho U^2 S} \tag{15}$$

$$C_0 = \frac{\sum_{i=1}^{K}\Delta F_i\sin\alpha_{ii}}{1/2\rho U^2 S} \tag{16}$$

$$C_{m_0} = \frac{\sum_{i=1}^{K}\Delta F_i x_i}{1/2\rho U^2 Sc} \tag{17}$$

For the induced drag computation the induced angle α_{ii} is used, rather than the geometric angle α_i. This angle is computed at each colocation point as the ratio between the total downwash induced by the spanwise vorticity of the wing and the wake, divided by the free stream velocity U.

Results

The computational capability of the present method will be demonstrated by solving three different physical situations. The first case being the steady state condition, with and without the effect of ground. In the second case the plunging motion of a rectangular wing planform is considered and the effect of ground proximity on the duration of the transient response is investigated. The third situation to be investigated

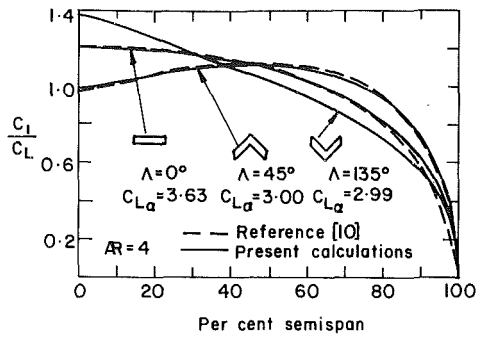

Fig. 4 Calculated spanwise loading of swept and unswept rectangular wings

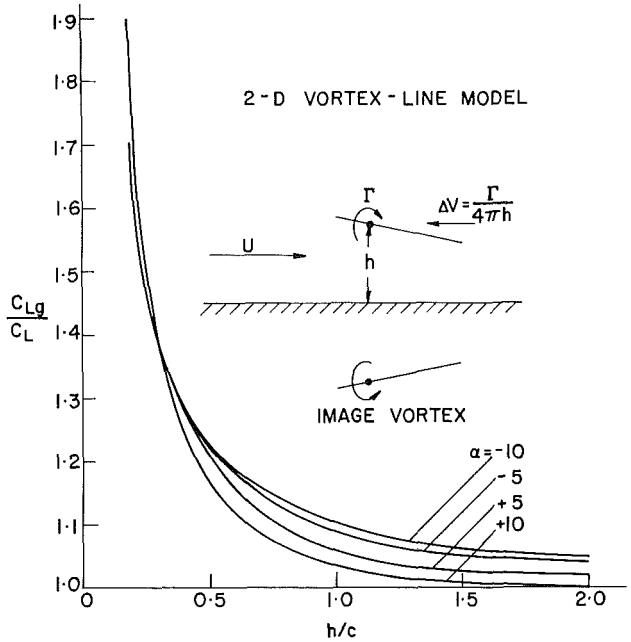

Fig. 5 Effect of angle of attack on the lift of a two dimensional thin wing near the ground

deals with the fluctuation of the negative lift forces on the front winglet of a racing car. This time dependent heaving motion is caused by the oscillations of the car's suspension.

The versatility in the geometry of the wing planforms that can be analyzed by the present model is shown by Fig. 4. Here the calculated spanwise loading C_l for three basic wing geometries is presented and compared with the results of reference [10]. The agreement between the two calculated diagrams, for unswept and aft swept wings, and the calculation of reference [10] is excellent. The deviation in the calculated lift coefficient slopes $C_{L\alpha}$ by the two potential methods is less than 1 percent. For completeness, the spanwise loading of a swept-forward wing is shown in Fig. 4; where the higher wing-root loading compared to the high tip-loading of the swept back wing is evident.

To calculate the wing lift, pressure distribution, spanwise loading etc., for a given steady state incidence as shown in Fig. 4 a vortex grid of 13 spanwise and 4 chordwise elements was used. Calculations that were carried out with larger number of vortex lattice elements showed a clear convergence to a value which differed by less than 1 percent (in C_L) from the results obtained with the 13 × 4 grid. In addition this particular discretization (13 × 4) allowed computational times to be less than 10 seconds, per case, on an IBM 3081D computer. Consequently, faster turn around times and higher computer job priorities were obtained.

The effect of ground proximity on the lift coefficient of a two-dimensional airfoil is shown by Fig. 5. This effect was ob-

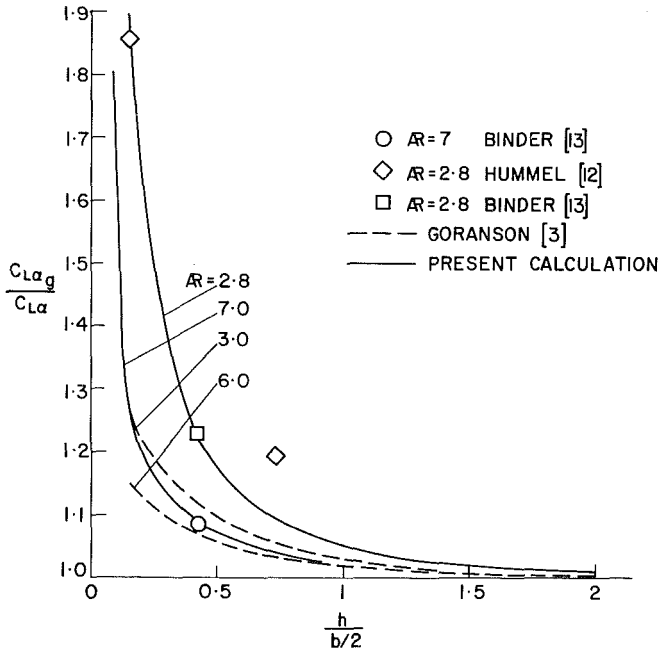

Fig. 6 Effect of ground proximity on the ratio of lift slopes $C_{L_{\alpha g}}/C_{L_\alpha}$ for rectangular wings

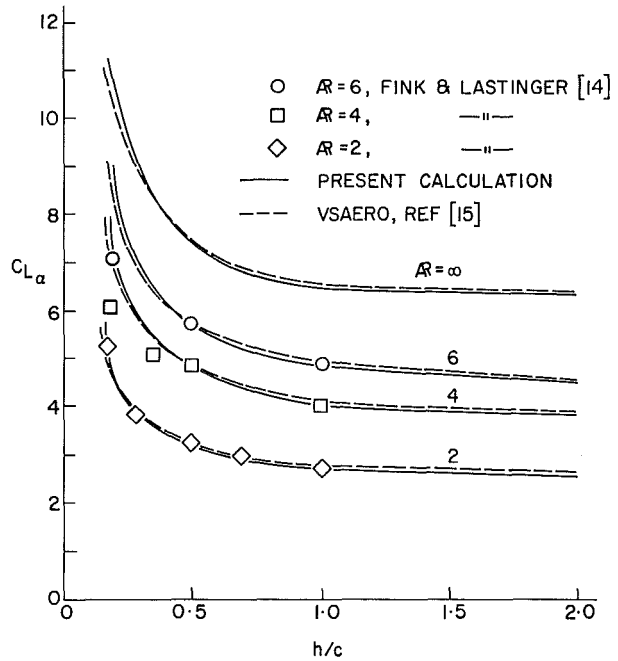

Fig. 7 Effect of ground proximity on the lift slope C_{L_α} of rectangular wings

tained by the mirror image technique, as indicated by the diagram inserted into Fig. 5. Thus, to simulate a ground clearance of h a symmetrical wing-planform is placed at a depth $-h$, resulting in a straight dividing stream line at $h=0$, which can be treated as a solid surface (ground). The interaction between the wing and the simulated ground is rather complex [11] and in general, this results in an increase of the lift for both positive and negative incidences. Two dimensional considerations, for explaining this phenomenon, can be divided into two separate categories. The first effect is due to the reduced mass flow under the wing in the presence of the ground, which tends to increase the pressure at the wing's lower surface (for positive α); resulting in an overall gain in the lift of the two dimensional wing section. The second effect, is due to the velocity induced by the reflected-wing (at $z=-h$) and can be explained by the lifting line model. The in-

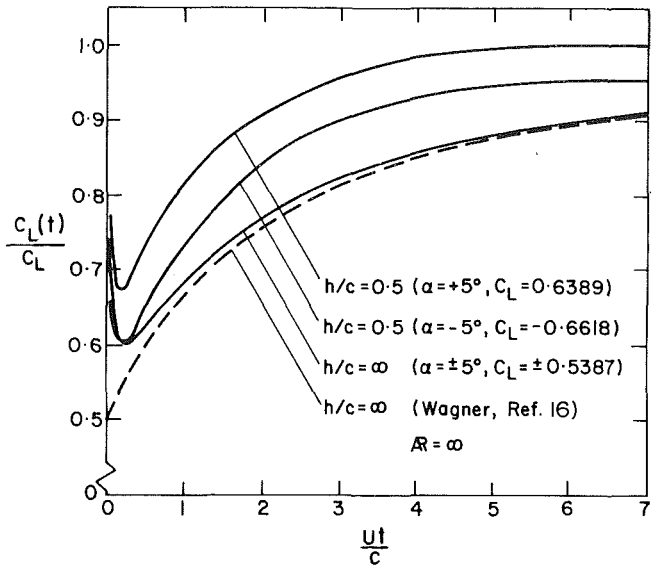

Fig. 8 Lift coefficient variation after a plunging motion for two dimensional airfoils, (with and without ground effect)

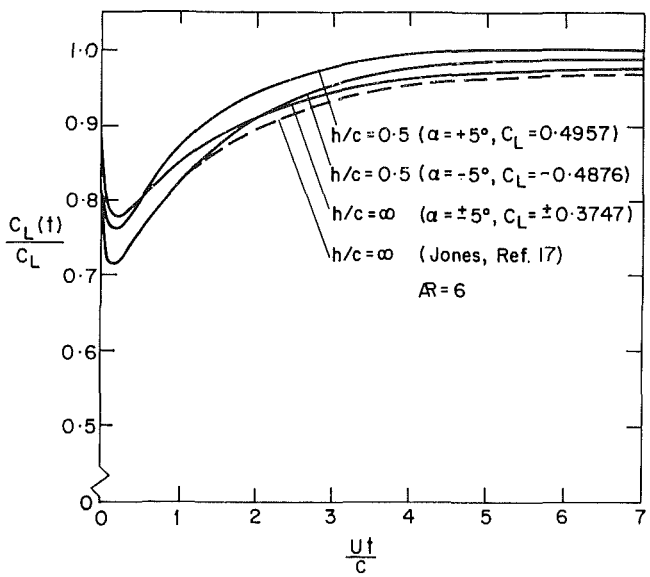

Fig. 9 Lift coefficient variation after a plunging motion for a rectangular finite wing (with and without ground effect)

sert in Fig. 5 clearly shows that in the case of positive α, the upper wing experiences an additional forward velocity ($\Delta V = \Gamma/4\pi h$) that reduces the free stream velocity and thereby decreasing the lift. This situation reverses itself for negative α resulting in an increase in the downforce. The increase in angle of attack enhances this effect which clearly can be observed in Fig. 5 (for the higher ground clearances ($h/c > 0.5$)). For the smaller values of ground clearance ($h/c < 0.5$) the above described first effect, which increases the lift coefficient (C_{Lg}) in the presence of the ground, takes over and a rapid increase in both positive and negative lift is observed.

The extension of the vortex line model, to explain the influence of the mirror image wing, on a three dimensional finite wing; leads to the conclusion that the wing tip vortices will always increase either the positive or negative lift of the wing. Consequently, for smaller aspect-ratio wings, the effect shown in Fig. 5 will decrease to an insignificant value. Because of this situation the results presented in Figs. 6 and 7, for finite wings does not distinguish between the cases of positive and negative α. Furthermore, when C_{Lg}/C_L versus h/c is plotted, the deviations among the wings having various aspect ratios becomes negligible. Therefore the classical results of Goranson's [3] calculations were plotted versus the parameter $h/(b/2)$ as it is in Fig. 6. The experimental data of Hummel [12] for $AR = 2.8$ and $h/c = 0.2$ and of Binder [13] for $h/c = 0.6$ agrees very well with the present calculation whereas the experimental point of Hummel for $h/c = 1$ ($AR = 2.8$) seems to be too high. Also the experimental point of Binder for the higher $AR = 7$ wing ($h/c = 1.5$) is in close agreement with the current calculations, whereas the relations derived by Goranson [3] are too low. Calculated curves, corresponding to the Goranson's data, were not added since they lay too close to the curves of $AR = 2.8$ ($AR = 3$) and to $AR = 7$ ($AR = 6$).

The parameter $h/(b/2)$ used in Fig. 6 does not allow the presentation of two dimensional data. On the other hand, when the parameter h/c is used in conjunction with the absolute $C_{L\alpha}$, a good resolution of the various AR curves in the diagram is obtained (as it is in Fig. 7). Additional experimental data is provided here which show good agreement with the calculated results over a wide spectrum of ground clearances and wing aspect ratios. These data of Fink and Lastinger, were obtained [14] by the image-wing method. Thus the ground effect was obtained by placing two airfoils that were separated by a distance of $2h$ and thereby eliminating the problem of the boundary layer thickness associated with the wing and ground board method. They used a Glenn Martin 21 percent thick nonsymmetric airfoil section and measured the ground clearance from the foil's lower surface. This thickness effect is probably why at $h/c < 0.3$ their data deviates from the current thin wing calculations. Further validation of the present method, relative to a widely used panel code [15], is presented in Fig. 7. For the VSAERO computations a 10×10 lattice and a 5 percent thick, symmetric airfoil section was used. This type of grid (which is larger than used in the vortex method) is coarse for the panel representation and therefore a small difference in the two computations is visible. This code, however, is still limited in predicting the flowfields associated with transient and large amplitude unsteady motions.

Figures 5, 6, and 7 show the large increase in the wing's lift due to ground proximity. This effect is well predicted by the potential flow method. In real flow situations, however, this large increase in the lift will be limited by viscous effects. On the ground of the above comparison with experimental results; it seems that these viscous effects will affect the predictions, based on this model, for ground clearance values under $h/c = 0.3$. It is evident, though, that more experimental data is needed to show the influence of airfoil thickness, camber, ground roughness and the relative motion of ground on this critical distance. From the engineering point of view, often the maximal lift coefficient has to be detemrined. Unfortunately, some of the aforementioned viscous effect will limit the maximal lift (to values not too far from its free stream value), which will be obtained now at lower angles of attack.

The transient response of a two-dimensional and a finite span ($AR = 6$) wings, after they were suddenly set into motion, is shown by Fig. 8 and Fig. 9, respectively. Here $C_L(t)$ is the momentary lift coefficient, C_L is the lift coefficient at $t = \infty$ (steady state value) and the nondimensional time ordinate tU/c actually measures the distance, travelled in wing chords. The limiting case of infinite acceleration as solved by Wagner [16] ($AR = \infty$), and Jones [17] ($AR = 6$) is shown by the dotted lines in Figs. 8 and 9. In the present calculation, however, the time steps were finite ($\Delta t = c/(16U)$); which actually represents a finite acceleration rate. The effect of this finite acceleration is to moderately increase the lift, as was shown in reference [18].

The effect of ground proximity on the lift growth of a suddenly accelerated lifting surface is to reduce the transient times, as can clearly be seen from Figs. 8 and 9. This effect can partially be explained by the presence of a second starting vortex (in the image plane) which induces an upwash (for positive α) thereby increasing the lift and reducing the

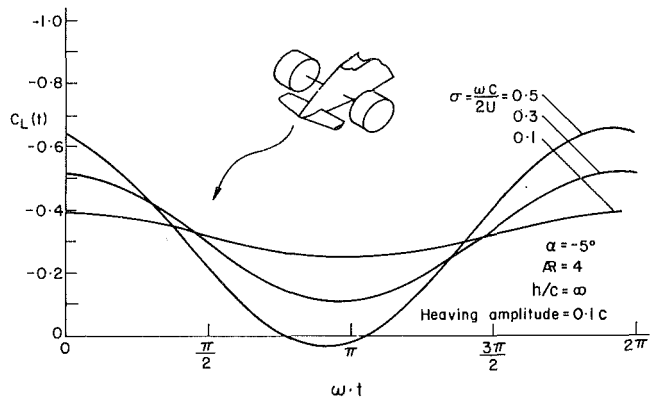

Fig. 10 Periodic lift variation during heaving oscillations of a finite wing

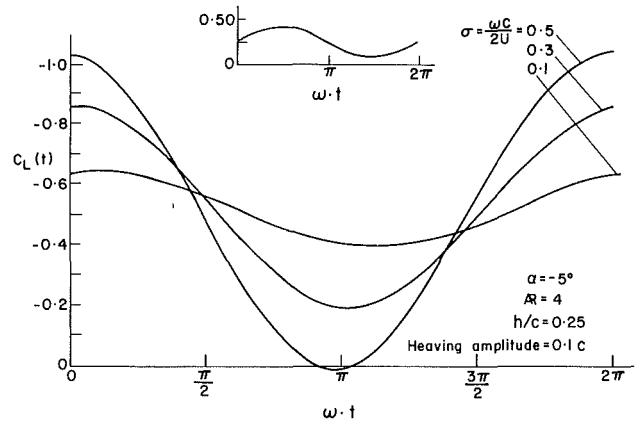

Fig. 11 Effect of ground on the lift of a finite wing undergoing oscillatory heaving motion

response times. Figures 8 and 9 also show that the steady state lift is obtained faster with positive angles of attack than with negative angles of attack, for both $AR = \infty$ and $AR = 6$. Similarly, smaller aspect ratio wings will have shorter response times, as is observed when comparing the results of Figs. 8 and 9.

The loads experienced by a lifting surface, moving in an unsteady motion in close proximity to the ground, can be considerably amplified by these two effects. In order to estimate the increase of these forces, relative to their steady state and out of ground effect values (on the front winglet of a typical racing car), the results shown by Figs. 10 and 11 for one cycle ($\omega t = 2\pi$) were calculated. The winglet to be considered is suspended above the ground at a height of $h = 0.25$c, and oscillates with the car (due to suspension travel) with an amplitude of 0.1c, as shown by the diagram in Fig. 11. As an example, the pure heaving oscillatory mode was considered here, therefore the wing's geometric angle of attack remained unchanged throughout the motion. The periodic variation of the negative lift on the winglet due to its oscillatory motion, in the absence of the ground is shown in Fig. 10, whereas with ground effect it is shown by Fig. 11. The additional up or downwash experienced by the wing, increases the momentary lift considerably above and below the steady state value ($C_L = -0.324$), as it can be observed in Fig. 10. When increasing the frequency (σ), the momentary lift is further amplified and a growing phase lag is observed.

The addition of ground effect to the oscillatory motion, described in Fig. 10, results in a further increase in the fluctuating value of the lift (see Fig. 11). Also the steady state value is increased ($C_L = -0.523$) and as in Fig. 10, momentary, positive lift values are experienced by the wing for the higher frequencies. The maximal loads are obtained near the middle of the upward stroke, where the upwash velocity is the highest. Since practical road conditions can introduce suspension oscillations within the range [19] of Fig. 10 and 11, the structural designer must take into account lift and wing-root bending moments, that exceed twice the steady-state load estimations.

Concluding Remarks

The lifting surface model that is presented in the current work was found to be capable of calculating the aerodynamic forces for various wing geometries with or without ground effect in steady or unsteady flow. Furthermore, the computational times required were minimal and for the simple test cases presented here, the length of the computer code was less than 1000 FORTRAN statements. Calculated results for conditions experienced by some high-speed ground vehicles (unsteady heaving oscillations and negative incidence) showed about 100 percent increase of the aerodynamic loads when compared with their steady state values.

References

1 Dominy, J. A., and Dominy, R. G., "Aerodynamic Influences on the Performance of the Grand Prix Racing Car," *Proceedings of the Institution of Mechanical Engineers*, Vol. 198 D, 1984, pp. 1-7.

2 Katz, J., Investigation of Negative Lifting Surfaces Attached to an Open-Wheel Racing Car Configuration," SAE Paper. No. 85-0283, Feb. 1985.

3 Goranson, R. F., "A Method for Predicting the Elevator Deflection Required to Land," NACA WR L-95, 1944.

4 Scibor-Rylski, A. J., "Road Vehicle Aerodynamics," Pentech Press Limited London, England, 1975, Chapter 4.

5 Newman, J. N., *Marine Hydrodynamics*, M.I.T. Press, Mass., 1980, Chapters 4 and 5.

6 Katz, J., "Lateral Aerodynamics of Delta Wings With Leading Edge Separation," *AIAA J.*, Vol. 22, No. 3, 1984, pp. 323-328.

7 Hess, J. L., "Calculation of Potential Flow About Arbitrary Three-Dimensional Lifting Bodies," Report No. MCD J5679-01, McDonell Douglas, Oct. 1972.

8 Bristow, D. R., and Grose, G. G., "Modification of the Douglas Neumann Program to Improve the Efficiency of Predicting Component Interference and High Lift Characteristics," NASA CR-3020, Aug. 1978.

9 Katz, J., "A Discrete Vortex Method for the Non-Steady Separated Flow Over an Airfoil," *J. of Fluid Mech.*, Vol. 102, Jan. 1981, pp. 315-328.

10 Donovan, A. F., and Lawrence, H. R., "Aerodynamic Components of Aircraft at High Speeds," Princeton Series Vol. VII, Princeton University Press, N. J., 1957.

11 Kuchemann, D., *The Aerodynamic Design of Aircraft*, Pergamon Press Ltd., Oxford, England 1978, pp. 298-299.

12 Hummel, D., "Nichtlineare Tragflugeltheorie in Bodennahe," *Z. Flugwissenschaften*, Vol. 21, No. 12, Dec. 1973, pp. 425-442.

13 Binder, G., "Nonlinear Lifting-Surface Theory for Yawed and Banked Wings in Ground Proximity," *Z. Flugwissenschaften und Weltraumforschung*, Vol. 1, No. 4, Aug. 1977, pp. 241-249.

14 Fink, P. M., and Lastinger, L. J., "Aerodynamic Characteristics of Low-Aspect-Ratio Wings in Close Proximity to the Ground," NASA TN D-926, July 1961.

15 Maskew, B., "Program VSAERO, A Computer Program for Calculating the Nonlinear Aerodynamic Characteristics of Arbitrary Configurations, NASA CR-166476, Nov. 1982.

16 Wagner, H., "Uber die Entstehung des Dynamischen Auftriebes von Tragflugeln," *Z.F.A.M.M.*, Vol. 5, No. 1, Feb. 1925, pp. 17-35.

17 Jones W. P., "Aerodynamic Forces on Wings in Non-Uniform Motion," R. & M. No. 2117, A.R.C. Aug. 1945.

18 Katz, J., and Weihs, D., "The Effect of Chordwise Flexibility on the Lift of a Rapidly Accelerated Airfoil," *Aeronautical Quarterly*, Feb. 1979, pp. 360-369.

19 Wright, P. G., "The Influence of Aerodynamics on the Design of Formula One Racing Cars," *Int. Journal of Vehicle Design*, Vol. 3, No. 4, 1982, pp. 383-397.

Application of a Reynolds Stress Model to Engine-Like Flow Calculations

Sherif El Tahry
Fluid Mechanics Department,
General Motors Research Laboratories,
Warren, Mich. 48090-9057

A version of a Reynolds stress turbulence model was adopted and applied for calculating turbulence in internal combustion engine flows. Simultaneously, to improve the numerical accuracy of the computations, a skew-upwind differencing scheme was introduced, thereby replacing the less accurate upwind differencing scheme originally present in the computations. With these modifications applied to an existing code, comparisons were made with measured mean and turbulent velocities of a flow field in an axisymmetric piston-cylinder assembly. The results of the computations were generally encouraging particularly for the mean flow. However, discrepancies were observed which are attributed to either (or both) unknown boundary conditions or shortcomings in the Reynolds stress model.

Introduction

Recently there has been a growing interest in applying multidimensional modeling to internal combustion engines (ICE's) [1]. In order that these models achieve their full potential and have an impact on the design and understanding of ICE's, it is necessary that physical submodels contained in these procedures be sufficiently versatile. That is, any submodel in these multidimensional procedures should cope with various operating conditions and design features without need for further empirical input. This, of course, demands both sufficient understanding of the different physical processes occurring in engines and their accurate representation.

One of the important mechanisms that control most processes in the combustion chambers of engines is turbulence. Its understanding and prediction, then, is paramount to the success of any prediction method. Except for the work of Ashurst [2], invariably all investigators have used a gradient diffusion hypothesis to account for turbulent transport in ICE's. With this approach, turbulent diffusion of any quantity is assumed proportional to the mean spatial gradient of that quantity. The coefficient of proportionality in this relationship is an appropriate "diffusivity." In general, two approaches have been used to estimate the diffusivity: the constant diffusivity model [3–5], and a two-equation turbulence model [6–7]. In the former the diffusivity is assumed constant in space and time, and its value is usually obtained by optimization such that the model yields the best agreement with some globally measured variable such as a cylinder-pressure trace. In the second approach the diffusivity is calculated from a two-equation turbulence model, typically the k-ϵ model (where k is the turbulent kinetic energy and ϵ is the dissipation rate of k).

While using the constant-diffusivity model is simple and occasionally may yield useful information [5], the model shares the drawbacks of all gradient diffusion approaches (mentioned below), and the assumption of a constant diffusivity is a gross simplification, particularly in the vicinity of solid boundaries. It should also be cautioned that procedures which resort to tuning parameters in a turbulence model to get agreement with some measured global quantity that depends on other submodels are liable to mask the effects of the submodels.

By calculating its own diffusivity, the k-ϵ model is an improvement over the constant-diffusivity type of model. It also has performed successfully in many two-dimensional applications. However, the model suffers from fundamental drawbacks that jeopardize its versatility. Among its drawbacks is that it is based on a gradient-diffusion type of assumption, implying that the turbulent stresses and the local mean rate of strain tensor share the same principal axis, which is normally not the case. Furthermore, the model uses an isotropic diffusion coefficient, which undermines its capabilities in three-dimensional flows.

Also, when employed to predict scalar diffusion, like of temperature, a parameter equivalent to a Prandtl number needs to be input to the model. This parameter is known to be a function of the flow, and its value generally is unknown. Whether these shortcomings or others in the model will serously affect the model's performance in ICE's applications has not yet been determined.

As an alternative to the models hitherto used for predicting turbulence in ICE's, a second-order closure model (see, for example, [8]) is proposed. In second-order closures, transport equations are developed and solved for all second-order moments (which are correlations between fluctuating quantities needed to close the mean equations) while higher-order moments are expressed in terms of lower-order moments. Hence any assumptions made will enter at the higher-order level and will presumably have a less significant effect on the model's accuracy. By solving directly for second-order moments, the fundamental shortcomings present in the k-ϵ model are eliminated. However second-order closures are more complex since to calculate the turbulence field alone re-

Contributed by the Fluids Engineering Division for publication in the JOURNAL OF FLUIDS ENGINEERING. Manuscript received by the Fluids Engineering Division, May 17, 1984.

quires seven differential equations, as opposed to only two with the k-ϵ model. At any rate, from the point of view of computational effort, this is not a severe problem since in unfired engine calculations the majority of the computational effort is spent in obtaining a solution to the momentum equations.

In the present study the second-order closure model suggested by Launder et al. [9] was adapted for use in an engine-like configuration and the model was incorporated in the computer code CONCHAS [10]. The code was then used to simulate the in-cylinder flow field measured by Morse et al. [11] for a cold flow in an axisymmetric noncompressing engine-like geometry.

The flow field under consideration is a complicated flow having several recirculating regions. In such flows it is inevitable that the flow direction becomes skewed relative to the computational mesh, with the consequence of introducing numerical diffusion into the solution [12]. In many instances the level of such diffusion is so high as to outweigh the effect of the physical diffusion represented by the turbulence model. To test the turbulence model it is therefore necessary to reduce numerical errors to a minimum.

Due to limitations of computer time, it was not possible with the differencing scheme present in CONCHAS to reduce numerical errors sufficiently by grid refinement. The alternative was to use a more complex (and hopefully more accurate) differencing scheme. The scheme chosen was the skew-upwind differencing scheme (SUDS) proposed by Raithby [13]. This scheme was tested in other flow situations by Leschziner [14], Leschziner and Rodi [15] and others, and their results show great improvement over the commonly used upwind differencing scheme (UDS).

Analysis

The equations that are solved are the conservation equations of mass, momentum and energy together with the equation of state. In addition, for closure of the mean momentum equation, the Reynolds stress (or second-order moments) equations and the dissipation-rate equation (which is required for the closure of the Reynolds stress equations) are solved. Because the internal energy of the flow considered is almost constant, solution of its equation could have been avoided. It is retained merely because it is an integral part of the solution procedure. However, this equation will not be discussed any further.

A cylindrical coordinate system is used in the CONCHAS code which leads to complex forms for the equations. Therefore, for brevity the equations in this report will be written in general curvilinear tensor notation. In what follows, superscript and subscript indices associated with tensor components will denote contravariant and covariant components, respectively. With this nomenclature and neglecting density variations, the continuity and the i-component momentum equations read, respectively,

$$\bar{U}^j{}_{,j} = 0 \tag{1}$$

$$\frac{\partial \bar{U}^i}{\partial t} + (\overline{U^i U^j})_{,j} = -\frac{1}{\rho} g^{ij} \bar{P}_{,j} + (\nu g^{jk} \bar{U}^i_{,k})_{,j} - (\overline{u^i u^j})_{,j} \tag{2}$$

where U^m and u^m are, respectively, the instantaneous and turbulent velocity components in the m-direction, P the pressure, ν the kinematic viscosity, ρ the density, g^{ij} the contravariant component of the unit tensor, and t is time. The '', j'' signifies convariant differentiation with respect to the j coordinate, and the overbars indicate ensemble averages. In equation (2) and in what follows, indices repreated diagonally (i.e., once as a superscript and once as a subscript) imply summation.

Turbulence Model. The transport equations for the Reynolds stresses are derived from the momentum equations (for details see, for example, [8]). By neglecting terms of the order of the reciprocal of the Reynolds number or smaller, in general curvilinear coordinates the transport equation of the ik component of the Reynolds stress reads:

$$\frac{\partial \rho \overline{u^i u^k}}{\partial t} + \overbrace{\bar{U}^j (\rho\, \overline{u^i u^k})_{,j}}^{\text{(Convection)}} = \overbrace{-\rho(\overline{u^k u^j}\ \bar{U}^i_{,j} + \overline{u^i u^j}\ \bar{U}^k_{,j})}^{\text{(Production)}}$$

$$\overbrace{-\rho(\overline{u^i u^k u^i})_{,j}}^{\text{Diffusion}} + \overbrace{(p g^{ij} u^k + p g^{kj} u^i)_{,j}}^{\text{Pressure diffusion}}$$

$$\overbrace{-p(g^{ij} u^k_{,j} + g^{kj} u^i_{,j})}^{\text{Pressure Rate of Strain}} \overbrace{-\rho \nu g^{jn} u^k_{,j} u^i_{,n}}^{\text{Dissipation}} \tag{3}$$

where p is the fluctuating pressure. The different terms in equation (3) have their physical significance appearing on top of each in the case when Cartesian coordinates are used. When curvilinear coordinates are used, the convection and diffusion terms may lead to extra source/sink terms akin to the centrifugal and Coriolis components appearing when the momentum equation is expressed in a general coordinate system.

The terms that are unknown and require modeling in equation (3) are the pressure-rate of strain, the diffusion, and the dissipation terms. The models employed for these terms are those suggested by Launder et al. [9]. They are as follows.

a − Pressure − Rate of Strain

$$\overline{p(g^{ij} u^k_{,j} + g^{kj} u^i_{,j})} = \rho(\Phi_1 + \Phi_2 + \Phi_w) \tag{4}$$

where

$$\Phi_1 = 1.6 \frac{\epsilon}{k} \left(\overline{u^i u^k} - \frac{2}{3} g^{ik} k\right)$$

$$\Phi_2 = 0.76[(\overline{u_k u_j}\ \bar{U}^i_{,j} + \overline{u^i u^j}\ \bar{U}^k_{,j}) - \frac{2}{3} g^{ij} g_{mn} \overline{u^m u^l}\ \bar{U}^n_{,l}] - 0.18k(g^{lk} \bar{U}^i_{,l} + g^{li} U^k_{,l}) - 0.11[(g_{jl} g^{km} \overline{u^i u^l}\ \overline{U^j_{,m}} + g_{jl} g^{im} \overline{u^k u^l}\ \overline{U^j_{,m}}) - \frac{2}{3} g^{ik} g_{mn} \overline{u^m u^l}\ \bar{U}^n_{,l}]$$

$$\Phi_w = \{0.125 \frac{\epsilon}{k} (\overline{u^i u^k} - \frac{2}{3} g^{ik} k) + 0.015[(\overline{u^k u^j}\ \bar{U}^i_{,j} + \overline{u^i u^j}\ \bar{U}^k_{,j}) - (g_{jl} g^{km} \overline{u^i u^l}\ \overline{U^j_{,m}} + g_{jl} g^{im} \overline{u^k u^l} U^j_{,m})]\} \frac{k^{3/2}}{\epsilon y}$$

Nomenclature

F = convection flux of Reynolds stress leaving a computational cell
g^{ij}, g_{ij} = contravariant and covariant components of the unit tensor
k = turbulence kinetic energy
l = length scale
$\bar{P}$ = mean pressure
p = turbulent pressure
t = time
$\bar{U}^i$ = contravariant mean velocity component in i-direction
u^i = contravariant turbulent velocity component in i-direction
y = normal distance to the wall
α = parameter used in equation (10)
γ = parameter used in equation (11)
ν = kinematic viscosity
ϵ = rate of dissipation of turbulence kinetic energy
ρ = density
Φ = pressure-rate of strain correlation

where y is the normal distance to the boundary

b – Diffusion

$$\rho(\overline{u^j u^k u^i})_{,j} + (\overline{pg^{ij}u^k} + \overline{pg^{kj}u^i})_{,j} = 0.11\rho \frac{k}{\epsilon}[\overline{u^i u^l}(\overline{u^j u^k})_{,l} + \overline{u^j u^l}(\overline{u^k u^i})_{,l} + \overline{u^k u^l}(\overline{u^i u^j})_{,l}]. \quad (5)$$

c – Dissipation

$$2\rho\nu g^{jn}\overline{u^k_{,j}u^i_{,n}} = \frac{2}{3} g^{ik}\rho\epsilon \quad (6)$$

Details on the derivation of these equations and the assumptions involved can be found in [9], [16], and [17].

The remaining equation required to have a closed set of equations is the ϵ equation. The modeled form used is that given by [9]. In curvilinear coordinates this equation becomes

$$\frac{\partial \epsilon}{\partial t} + \overline{U^j}\epsilon_{,j} = -1.44\frac{\epsilon}{k} g_{ij}\overline{u^j u^k} U^i_{,k} - 1.9\frac{\epsilon^2}{k} + 0.15\left(\frac{k}{\epsilon}\overline{u^j u^l}\epsilon_{,l}\right)_{,j} \quad (7)$$

The only differences between this equation and that used by Gosman et al. [7] and others in ICE's is that in equation (7), the diffusion coefficient of ϵ is not isotropic but is related to the Reynolds stresses. Also, in the production term the Reynolds stresses appear directly rather than being written in terms of the velocity gradient and the turbulent viscosity.

Numerical Aspects. The solution procedure used is based on the implicit-continuous fluid-Eulerian technique [18] with an arbitrary Lagrangian-Eulerian mesh [19]. These features were developed and implemented in the computer code CONCHAS by Butler et al. [10]. Apart from the turbulence model, two main changes were made to the code in the present work. The first change was in the manner by which the turbulent stresses were applied to the mean momentum equation. Since the Reynolds stresses are solved for, these are applied directly as the "diffusion term," which is in contrast to the gradient type of diffusion originally present. This new procedure was found to exacerbate oscillations present in the mean velocity field. These oscillations are not to be confused with those arising from unbounded differencing schemes. The oscillations that occur could be traced to the Lagrangian type of pressure iteration and the location of variables on the computational mesh coupled with certain boundary conditions. To dampen these oscillations, Butler et al. [10] use what is termed a "node coupler," which couples alternate mesh nodes with small, artificial restoring forces. Since in many cases the node coupler introduces artificial diffusion to the solution, it was decided to eliminate it. Due to the direct damping action of the turbulent diffusivity, this did not cause any serious problem when a gradient-diffusion type of model (specifically k-ϵ) was used. When the Reynolds stress model was used, however, the oscillations increased. To remedy the problem, the Reynolds stress acting at any numerical cell boundary was decomposed into two parts as follows:

$$\overline{u^i u^j} = \alpha(\overline{u^i u^j})_{\mathrm{RS}} + (1-\alpha)(\overline{u^i u^j})_{k\epsilon} \quad (8)$$

where the subscripts RS and $k\epsilon$ indicate that the values of $\overline{u^i u^j}$ are obtained from the Reynolds stress and the k-ϵ model, respectively. In equation (8) α is a constant set at about 0.95. This large value assigned to the calculation of $\overline{u^i u^j}$ by the Reynolds stress model ensured that the basic character of the model did not change, while the remaining 5 percent of the stress, calculated by the k-ϵ model, was found to be sufficient to reduce the oscillations to a tolerable level. Varying the value of α (from 0.99 to 0.9) was found to have a minor effect on the mean flow.

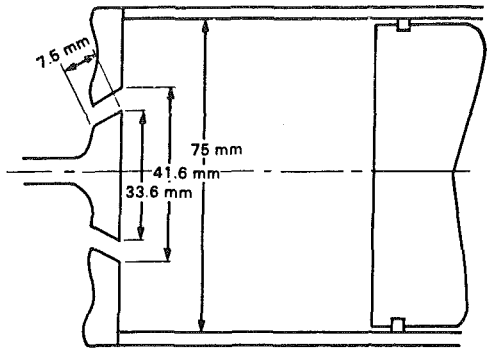

Fig. 1 Schematic of piston-cylinder assembly

The second main change made to CONCHAS was in the differencing scheme. The original scheme in the code (see [10]) was a mixture of upwind and central differencing in which the amount of each may be varied. For stability purposes, upwind differencing is usually prevalent; we will therefore refer, loosely, to the scheme as the upwind differencing scheme (UDS). Because of the problem of numerical diffusion posed by the standard UDS, the skew-upwind differencing scheme (SUDS) suggested by Raithby [13] was incorporated into CONCHAS. The scheme was applied to both the momentum equation and the Reynolds stress equations. No significant problems were encountered when SUDS was used only on the momentum equation. However, when the scheme was applied to the Reynolds stress equations, in some scattered regions where steep gradients of the stresses occurred, some of the normal stresses acquired negative values. The reason for that occurrence is that the scheme is not unconditionally bounded (in the sense given in [20]).

To alleviate this problem, convective fluxes of the Reynolds stresses (F) leaving a finite-difference cell are decomposed into two parts as follows:

$$F = \gamma F_b + (1-\gamma)F_u \quad (9)$$

where F_b is a convective flux of $\overline{u^i u^j}$ calculated from the bounded upwind-differencing scheme and F_u is the flux of $\overline{u^i u^j}$ calcualted from the more accurate but unbounded SUDS, and γ is a constant equal to 1.0 when $\overline{u^i u^j}$ at the cell in question falls below some preset fraction (β) of the arithmetic average values of neighboring $\overline{u^i u^j}$. Otherwise γ is 0.0. The value of β used was about 0.2. Using different values of β (varying from 0.1 to 0.4) did not produce any detected difference in the solution at the monitored locations. This insensitivity is apparently due to the fact that unbounded solutions occur only at a very few isolated (typically two or three) locations in the flow field. It should be mentioned that this procedure of using an accurate differencing scheme wherever the scheme is bounded while reverting to a bounded differencing scheme when the (accurate) scheme becomes unbounded has been used previously by Chapman [21]. Other procedures whereby the two schemes are blended were suggested by Book [22] and Gosman and Lai [23].

Operating, Initial and Boundary Conditions. The testing of the procedure was achieved by comparing the numerical results with the laser doppler anemometer measurements made by Morse et al. [11]. The measurements were carried out in the axisymmetric piston-cylinder assembly shown schematically in Fig. 1. The assembly consists of a flat-crowned piston, a transparent cylinder with 75 mm bore, a flat transparent cylinder head, and an axisymmetric intake/exhaust port. The annulus "valve seat" was inclined by 30 deg to the vertical direction. Further details of the geometry of the assembly are shown in Fig. 1. The piston was driven in simple harmonic motion at 200 r/min, and with a stroke of 600 mm, the

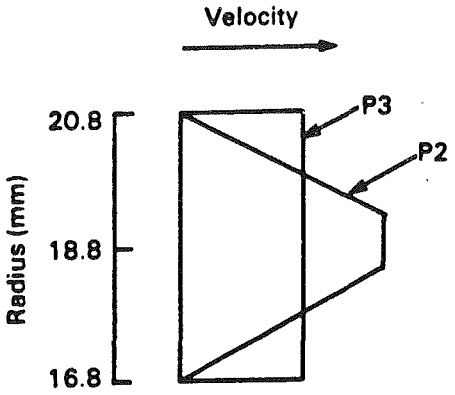

Fig. 2 Inlet velocity profiles

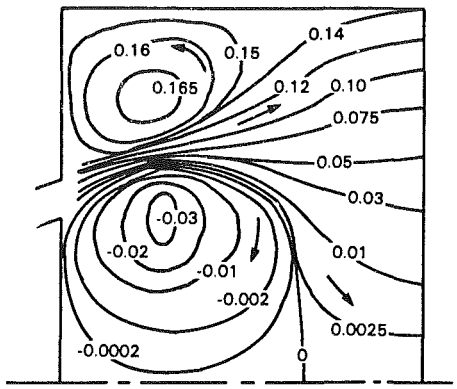

Fig. 3(a) Stream line contours given by [11] at 36° ATDC

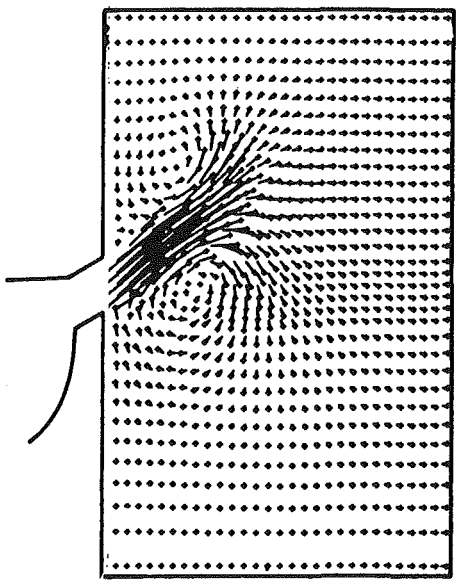

Fig. 3(b) Computed velocity vector plot at 36° ATDC

average piston speed (V_p) was 0.4 m/s. At this speed the flow was claimed to be fully turbulent.

Measurements were reported by Morse et al. [11] for a flow case with zero swirl (i.e., with zero azimuthal velocity) and for two other cases with different levels of swirl. For the zero-swirl case which was considered in the present comparisons, measurements were presented at crank angles of 36, 90, 144, and 270 degrees after top dead center (ATDC) for the mean and turbulent velocity components in the axial direction. At each crank angle, profiles of these velocities were presented at several axial locations.

The base calculations were carried out with 32×30 grid lines in the radial and axial directions, respectively. Computations with finer meshes were also attempted, and these will be discussed in the next section. In all cases the computations were initiated from top dead center, where the following conditions were assumed. The radial velocity and the axial velocity are equal to zero. The turbulence is assumed isotropic where each of the normal stresses was taken to be 0.0125 m^2/s^2. This number is approximately equal to the measured value of the normal axial stresses at 270 deg ATDC. The shear stresses were zero, and the dissipation rate was calculated from

$$\epsilon = 0.4 \frac{k^{3/2}}{l}$$

where l is the distance to the nearest solid boundary. We next discuss boundary conditions.

Solid Boundaries. The velocities at all solid boundaries are taken equal to the velocity of the boundaries, i.e., all velocities at solid boundaries are zero except at the piston, where the axial velocity is equal to the piston velocity. No logarithmic law of the wall was applied to the velocities tangent to the boundaries. The reason for not using the logarithmic law is that the stresses calculated from the model did not match the shear stresses calculated from the log law except in limited regions in the flow field. Hence when the logarithmic law was used, "kinks" appeared in the velocity profiles close to the boundary. Because of this reason and because in the flow field investigated the validity of the logarithmic law is questionable, it was decided not to use it. The boundary condition for the Reynolds stresses was a zero-flux condition, whereas the dissipation rate was calculatted near the boundary via

$$\epsilon = 0.4 \frac{k^{3/2}}{y},$$

y being the normal distance from the boundary to the center of the computational cell nearest to the boundary.

Axis of Symmetry. At the axis of symmetry the radial velocity component is set equal to zero and the fluxes of all other variables involved in transport equations are set to zero.

Intake Port. Unfortunately, no measurements were made at the intake port. This made it necessary to "guess" the flow conditions. Thus, the flow rate, the velocity profiles and the turbulence quantities had to be estimated.

On account of the low compressibility expected, the mass flow rate was assumed equal to the rate of change of volume displaced by the piston multiplied by the ambient density. Also, since the length of the annulus was roughly twice its width, the inlet flow was assumed to enter the cylinder parallel to the direction of the valve/seat annulus. Less guidance was available to estimate the remaining unknowns, and hence sensitivity calculations were made to assess their effect on the solution.

To test the sensitivity of the flow field to the inlet velocity profiles, two such profiles were tried. These are shown in Fig. 2. The first, referred to as $p2$, has a flat portion near the middle of the annulus and varies linearly near the annulus walls. The second is a much flatter profile and will be referred to as $p3$. Because of the unequal kinetic energies in the two profiles, the resultant flow fields were not identical. Profile $p2$ generally gave slightly better agreement with the measurements. However, because the majority of the data were obtained with profile $p3$, the results obtained with this profile are the ones reported here.

As for the turbulence quantities at the intake port, these were found to have no significant effect on the mean velocities but did influence the turbulence field. The value of k used in the results reported here was two percent of the kinetic energy based on mean inlet velocity. This value is somewhat higher than present in a fully developed pipe flow. The radial,

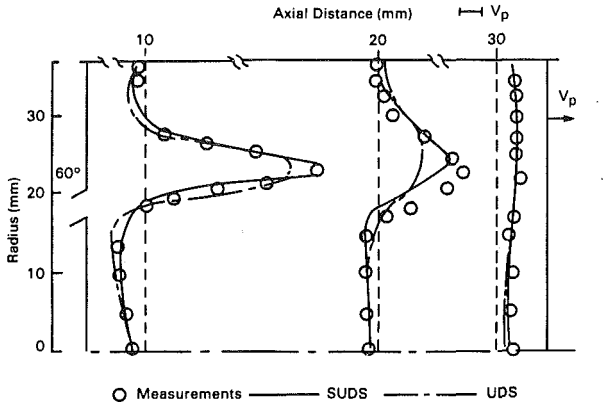

Fig. 4 Mean axial velocity profiles at 36° ATDC

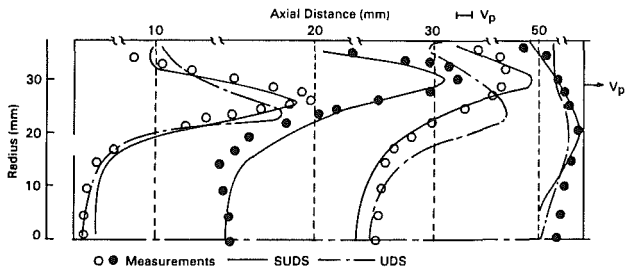

Fig. 5 Mean axial velocity profiles at 90° ATDC

azimuthal and axial normal stresses were taken as $0.5k$, $0.7k$, and $0.8k$, respectively, while the only nonzero shear stress was $0.2k$. The dissipation rate was set to $0.5k$/(annulus width). In review of the lack of data, uncertainties in the values of the turbulence quantities and mean velocity profiles at entry will be reflected in the results.

Results

To give an idea of the flow field generated, Figs. 3(*a*) and 3(*b*) show the experimental streamlines and computational velocity-vector plots respectively at 36 deg ATDC. It is apparent that close to the cylinder head the flow is dominated by a jet flow flanked by two vortices: a large clockwise rotating vortex residing in the vicinity of the centerline and a smaller counter-rotating vortex adjacent to the cylinder wall. Away from the cylinder head the flow emerging from the jet region spreads and enters normal to the piston. Except for a further vortex generated later in the induction stroke near the piston and cylinder wall and for some other minor changes, during the remaining part of the induction stroke the overall structure of the flow is quite similar to the flow structure at 36 deg ATDC (for details see [11]). In general, the calculations were found to reproduce the experimental flow field quite well at all crank angles.

In Figs. 4, 5, 6, and 7, measured and calculated mean velocity profiles at various locations in the flow field are shown, respectively, at crank angles of 36, 90, 144, and 270 deg. In these figures the velocities are normalized by the mean piston speed V_p (=0.4 m/s) and are plotted relative to datums[1] (vertical dashed lines) placed at various distances from the cylinder head. All data points lying to the right side of the datum indicate a flow moving towards the piston, while data points lying to the left side of the datum indicate flows moving towards the cylinder head. The base calculations shown in Figs. 4–7 were obtained with SUDS. However, to show the effect of the differencing scheme on the solutions at 36 and 90 deg ATDC (Figs. 4 and 5), some of the results obtained with UDS are also shown.

[1]The locations of the datum will be referred to as locations 1,2,3, etc., with 1 being closest to the cylinder head and 2 the second closest, etc.

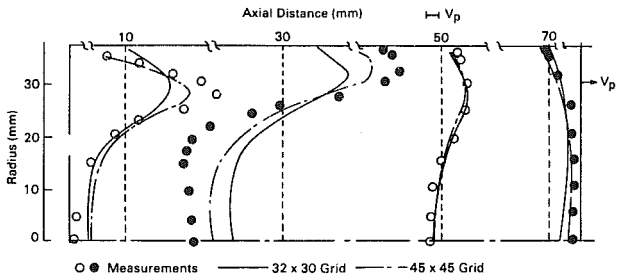

Fig. 6 Mean axial velocity profiles at 144° ATDC

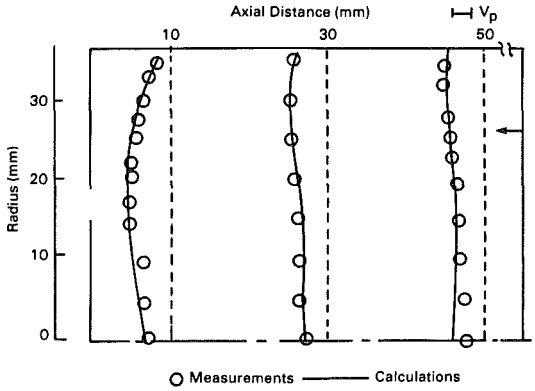

Fig. 7 Mean axial velocity profiles at 270° ATDC

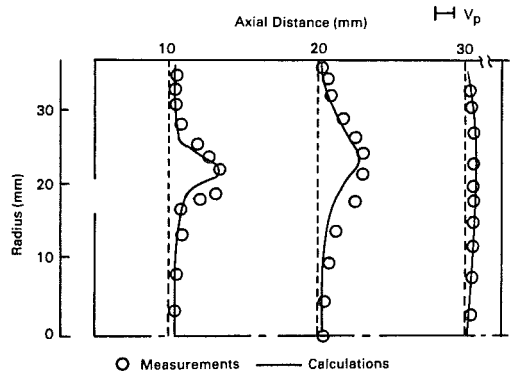

Fig. 8 Axial turbulent velocity profiles at 36° ATDC

At 36 deg ATDC (Fig. 4) the agreement between measurement and predictions is seen to be very good at locations 1 and 3. Although the calculated peak-velocity at location 2 is within 10 percent of the measured velocity, some discrepancies between measurements and predictions can be observed in the mid-radius region. With UDS we can see that the peak-velocity calculated at location 2 is only 50 percent of the measured peak velocity.

At 90 deg the calculations seem to simulate the flow field fairly well. Thus the location of the velocity peaks and flow reversals are well predicted. Quantitatively the peak-velocity discrepancies are somewhat larger than those observed at 36 deg. This is quite apparent at location 3, where the peak velocities of the flows in the forward (i.e., towards the piston) and backward directions are overestimated by about 30 percent. At all other locations, however, the peak velocities are within 20 percent of the experimentally observed values. Once again a difference between the results obtained with SUDS and UDS is evident, with SUDS generally yielding closer agreement with the measurements.

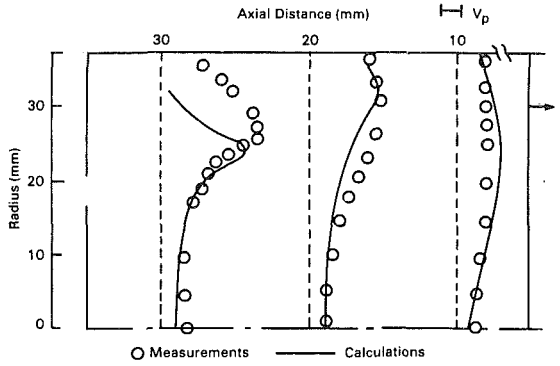

Fig. 9 Axial turbulent velocity profiles at 90° ATDC

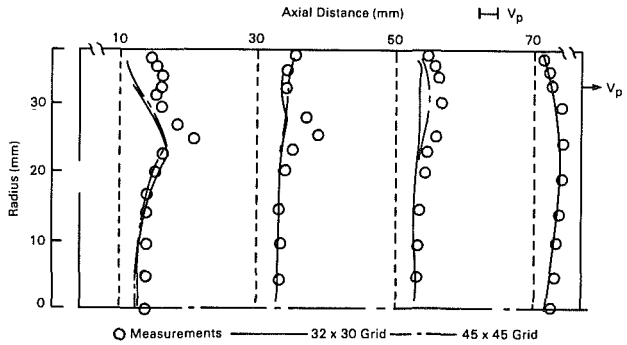

Fig. 10 Axial turbulent velocity profiles at 144° ATDC

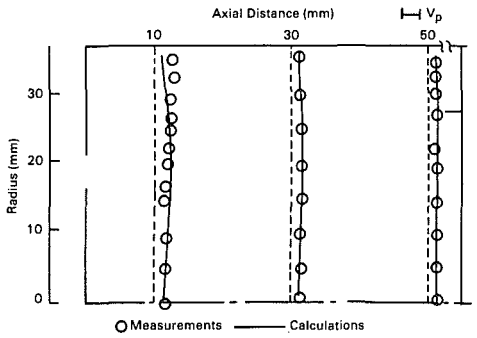

Fig. 11 Axial turbulent velocity profiles at 270° ATDC

The axial mean velocity profiles at 144 deg are shown in Fig. 6. It is seen that the calculation made with the 32×30 grid grossly underestimates the peak velocities at locations 1 and 2. Because of the relatively large axial grid spacing in the latter part of the induction stroke, numerical inaccuracies were thought to be causing the discrepancies. The flow was therefore recalculated using a 45×45 computational mesh. The results obtained with this mesh at 36 deg ATDC were found to be identical to those obtained with the coarser mesh. At 90 deg ATDC the discrepancies between the two solutions were less than 10 percent, which suggested that the solutions were sufficiently grid independent (i.e., solutions are insensitive to grid size) up to 90 deg ATDC. This was confirmed by a further calculation with a 60×60 mesh, which yielded results almost identical to those obtained with the 45×45 mesh at both 36 and 90 deg. The major difference, however, between the solutions obtained with the 32×30 and the 45×45 meshes was at 144 deg, as shown in Fig. 6. With the finer mesh we now observe much closer agreement with the experimental results. Due to the computational effort involved, the calculation made with the 60×60 mesh was not continued beyond 90 deg, so it is not possible to make any firm conclusions regarding the degree of grid independence of the computations made with the 45×45 mesh at 144 deg. At 270 deg ATDC, the velocity profiles shown in Fig. 7 indicates a significant reduction in the strength of the mean velocity field and, unlike the flow during the induction stroke, flow recirculations are absent; instead the flow becomes almost uniform. The agreement of measurements and predictions at this stage is quite good.

The turbulent velocities, normalized by V_p, are shown in Figs. 8, 9, and 10, respectively, at 36, 90, 144 and 270 deg ATDC. At 36 deg the agreement between measurements and predictions is quite encouraging. Thus, the trends and quantitative estimates of the peak velocities are in close agreement with the measurements. However in some regions, specifically those coinciding with the sides and edges of the jet, the predictions somewhat underestimate the turbulence levels. It should be remarked here that Morse et al. [11] have reported that their measurements could overestimate the turbulence levels, in the mentioned regions, by a factor of 15 percent; this observation might explain some, but not all of the discrepancies observed.

At mid-stroke (Fig. 9), the trends and peak velocities are also well predicted, but again an underestimation of the turbulence levels is observed in regions surrounding the jet. This underestimation is more pronounced at location 1 on the outer-radius side of the jet.

Later in the stroke, at 144 deg, it is seen from Fig. 10 that at locations 1 and 2, the measured turbulence velocity profiles exhibit double peaks, while the calculation shows only a single, somewhat weaker peak. At locations 3 and 4 the agreement between measurements and predictions improves.

Finally at 270 deg during the exhaust stroke, it is seen from Fig. 11 that the computed turbulence velocities agree well with the measurements.

Discussion

Although the comparisons made with the measurements showed that the calculations reproduced the observed qualitative trends fairly well, and in many instances good quantitative agreement was obtained, there still remain some discrepancies between measurements and predictions.

These discrepancies are more pronounced in the case of turbulence results. Due to the limitation in the available measurements, it is not possible to identify the causes of the discrepancies exactly, but several are possible. First, there is the unknown inlet conditions, which were found to influence the turbulence velocity profiles, particularly those adjacent to the inlet boundary; however, no attempt was made to alter these conditions in order to obtain better agreement. There is also the possibility of shortcomings in the turbulence model, but these cannot be uncovered until more measurements are available and the problem of the unspecified boundary conditions is resolved. Finally, there are numerical errors; these errors may cause some of the deviations at 144 deg, but are unlikely to be large at 36 deg and 90 deg ATDC since calculations made for the flow in this range of the induction stroke were made with quite a fine mesh.

Another significant question is, how do the present calculations compare with earlier calculations made with the k-ϵ model in the same flow situation? In answer to that, the results obtained from the present study were found to be in better agreement with the measurements than both the calculations of [7] and [24], both of which were made with the k-ϵ turbulence model. However the improvement in the calculated results cannot be attributed solely to the turbulence model since, as was observed, the skew-upwind differencing scheme used in the present work (and not used in the previous works) yielded better results than when the calculations were made with UDS (used in previous works). For an appropriate comparison between the two models, the same differencing schemes should be applied in the two calculations.

References

1 Mattavi, J. N., and Amann, C. A. (Eds.), *Combustion Modeling in Reciprocating Engines*, Plenum Press, New York, 1980.

2 Ashurst, W. T., "Vortex Dynamics Calculation of Fluid Motion in a Four Stroke Piston Cylinder – Planar and Axisymmetric Geometry," Sandia Laboratories Energy Report, SAND 78-8229, 1978.

3 Gupta, H. C., Steinberger, R. L., and Bracco, F. V., "Combustion in a Divided Chamber, Stratified Charge, Reciprocating Engine: Initial Comparison of Calculated and Measured Flame Propagation," *Combustion Science and Technology*, Vol. 22, 1980, p. 27.

4 Gupta, H. C., and Syed, S. A., "REC-P3, a Computer Program for Combustion in Reciprocating Engines," Princeton University Mech. and Aero. Engineering Dept., Report No. 1431, 1979.

5 Diwakar, R., "Multidimensional Modeling Applied to the Direct-Injection Stratified-Charge Engine – Calculation versus Experiments," SAE Paper 810225, 1981.

6 Ramos, J. I., and Sirignano, W. A., "Axisymmetric Flow Model with and without Swirl in a Piston-Cylinder Arrangement with Idealized Valve Operation," SAE Paper 800284, 1980.

7 Gosman, A. D., Johns, R. J. R., and Watkins, P. A., "Development of Prediction Methods for In-Cylinder Processes in Reciprocating Engines," *Combustion Modeling in Reciprocating Engines*, Mattavi, J. N., and Amann, C. A. (Eds.), Plenum Press, New York, 1980, p. 69.

8 Bradshaw, P. (Ed.), *Turbulence*, Springer-Verlag, Berlin, New York, 1978.

9 Launder, B. E., Reece, G. J., and Rodi, W., "Progress in the Development of a Reynolds-Stress Turbulence Closure," *J. Fluid Mech.*, Vol. 68, 1975, p. 537.

10 Butler, T. D., Cloutman, L. D., Dukowicz, J. K., and Ramshaw, J. D., "CONCHAS: An Arbitrary Lagrangian-Eulerian Computer Code for Multicomponent Chemically Reactive Fluid Flow at All Speeds," Los Alamos Scientific Laboratories Report LA-8129-MS, 1979.

11 Morse, A. P., Whitelaw, J. H., and Yianneskis, M., "Turbulent Flow Measurements by Laser-Doppler Anemometry in a Motored Reciprocating Engine," Imperial College Mech. Eng. Dept. Report FS/78/24, 1978.

12 Gosman, A. D., Pun, W. N., Runchal, A. K., Spalding, D. B., and Wolfstein, M., *Heat and Mass Transfer in Recirculating Flows*, Academic Press Inc., London and New York, 1969.

13 Raithby, G. D., "Skew Upstream Differencing Schemes for Problems Involving Fluid Flow," *Computer Methods in Applied Mechanics and Engineering*, Vol. 9, 1975, p. 153.

14 Leschziner, M. A., "Practical Evaluations of Three Finite Difference Schemes for the Computation of Steady-State Recirculating Flows," *Computer Methods in Applied Mechanics and Engineering*, Vol. 23, 1980, p. 293.

15 Leschziner, M. A., and Rodi, W., "Calculations of Annular and Twin Parallel Jets Using Various Discretization Schemes and Turbulence-Model Variations," ASME JOURNAL OF FLUIDS ENGINEERING, Vol. 103, 1981, p. 352.

16 Hanjalic, K., and Launder, B. E., "A Reynolds Stress Model of Turbulence and Its Application to Thin Shear Flows," *J. Fluid Mech.*, Vol. 52, 1973, p. 609.

17 El-Tahry, S., "Turbulent Plume Dispersal," PhD thesis, Imperial College, University of London, 1979.

18 Harlow, F. H., and Amsden, A., "A Numerical Fluid Dynamics Calculation Method for All Flow Speeds," *J. of Comp. Phys.*, Vol. 8, 1971, p. 197.

19 Hirt, C. W., Amsden, A. A., and Cook, J. L., "An Arbitrary Lagrangian-Eulerian Computing Method for All Speeds," *J. of Comp. Phys.*, Vol. 14, 1974, p. 227.

20 Roache, P. J., *Computational Fluid Dynamics*, Hermosa Publishers, Albuquerque, 1972.

21 Chapman, M., "FRAM, – Nonlinear Damping Algorithm for the Continuity Equation," *J. Comp. Phys.*, Vol. 44, 1981, p. 84.

22 Book, D. L. (Ed.), "Flux-Corrected Transport," *Finite-Difference Techniques for Vectorized Fluid Dynamics Calculations*, Springer-Verlag, 1981.

23 Gosman, A. D., and Lai, K. Y. M., "Finite-Difference and Other Approximations for the Transport and Navier-Stokes Equations," Imperial College Mech. Eng. Dept. Report, 1982.

24 Diwakar, R., and El-Tahry, S., "Comparison of Computed Flow-Field and Wall Heat Fluxes with Measurements from Motored Reciprocating Engine-Like Geometries," presented at ASME Third Int. Compt. Eng. Conference, Aug. 1983.

Instability of a Moving Cylindrical Liquid Sheet

G. Biswas

S. K. Som

Department of Mechanical Engineering,
Indian Institute of Technology,
Kharagpur 721302, India

A. S. Gupta

Department of Mathematics,
Indian Institute of Technology,
Kharagpur 721302, India

The instability of a cylindrical liquid sheet of finite thickness moving with a uniform velocity in still air is studied theoretically with the aim of throwing light on the break-up of films during atomization. It is shown that instability occurs for an axisymmetric disturbance when its wavelength exceeds the outer circumference of the sheet. For small values of the Weber number $W(=T/\rho_a U^2 r_a)$ a sheet of given thickness tends to become unstable for disturbances of large wavelengths although it is completely stabilized when $W < 2.5$ (approx.). The maximum growth rate for instability increases with W for fixed value of the sheet thickness. For fixed W, it is found that $\bar{\lambda}_m$ (the wavelength corresponding to maximum growth rate) increases rather slowly with increase in the sheet thickness. The value of $\bar{\lambda}_m$ decays rapidly from a high value as Weber number increases for a fixed sheet thickness. Further as $W \to \infty$, $\bar{\lambda}_m$ approaches asymptotically the value 10 (approx.) which agrees with the corresponding value due to Rayleigh in his study of the capillary instability of a jet.

Introduction

It is found that when a thin liquid sheet is injected into the atmosphere, unstable waves are formed and the sheet eventually breaks down into drops. The instability of such a sheet or film due to its interaction with the surrounding air is of special interest in studying atomization of liquids. Moving films also occur on seaplane hulls as the blister which is flung forward and sideways and which gives rise to spray. There is evidence [1, 2] to show that instability in film arises through the formation of transverse waves (lines of crest normal to the direction of motion) which grow until a break in the film occurs. The principal cause of instability is due to interaction of the sheet with the surrounding atmosphere such that rapidly growing waves are imposed on the sheet. Disintegration occurs when the disturbance amplitude reaches a critical value and fragments of sheet are torn off. As pointed out by Dombrowski and Johns [3], these fragments rapidly contract into instable ligaments under the action of surface tension and drops are produced as these ligaments subsequently break down. Squire [4] and York, Stubbs, and Tek [5] studied the disintegration of a plane sheet of inviscid liquid moving with a uniform velocity relative to the surrounding atmosphere. Hagerty and Shea [6] explained the occurrence of sinuous waves on a thin plane liquid sheet on the grounds that the wavelength is large compared to the sheet thickness and the growth rates of these waves are consequently greater than those of the alternative dilational forms. The linearized stability analysis in [4] and [6] cannot, however, throw any light as to why a sheet breaks down since they show that the air-liquid interfaces remain a constant distance apart during the growth of the disturbance. Clark and Dombrowski [7] carried out a second-order analysis of the aerodynamic growth of sinuous waves on a plane inviscid liquid sheet and this analysis gives some insight into the mechanism of sheet disintegration. The results are then used to derive a relation for the break-up lengths of sheets produced by fan and swirl spray nozzles. Fraser, Eisenklam, Dombrowski and Hasson [8] extended the previous analyses on the aerodynamic instability [3–6] of liquid sheets of uniform thickness to the flow of attenuating liquid sheets as observed in the flow in a fan spray sheet by Dombrowski, Hasson and Ward [9]. The results in [8] were also extended to provide a theoretical basis for predicting the effects of several factors (e.g., the development of turbulence in the liquid sheet or the effects of dissolved and entrained gases etc.) on the drop size and the predictions were compared with experimental data.

In most of the above investigations, however, the sheet is treated as plane (two-dimensional) and of constant thickness. But a conical sheet issuing from a swirl nozzle differs from a two-dimensional parallel-sided sheet both with respect to curvature and sheet thickness. It is therefore felt that for studying the mechanism of instability in a conical sheet and for predicting the drop size when such a sheet disintegrates, it would be desireable to take account of curvature as well as the attenuation of the sheet thickness. But, as Squire pointed that, it would be quite difficult to investigate the stability of a conical film of variable thickness. On the other hand it is an established fact that for a high flow velocity, the conical sheet from a swirl nozzle breaks up very close to the nozzle orifice such that the small segment of the sheet near the orifice can be well approximated by a cylindrical sheet. This provides the motivation for the present investigation where we make a theoretical analysis of the instability of a cylindrical sheet of constant thickness moving with a uniform velocity relative to the surrounding atmosphere. We believe such an analysis, albeit an approximate one, will form a basic step in understanding the mechanism of instability in a curved liquid sheet.

Further it may be pointed out that when a fluid possesses a

Contributed by the Fluids Engineering Division for publication in the JOURNAL OF FLUIDS ENGINEERING. Manuscript received by the Fluids Engineering Division, July 6, 1984.

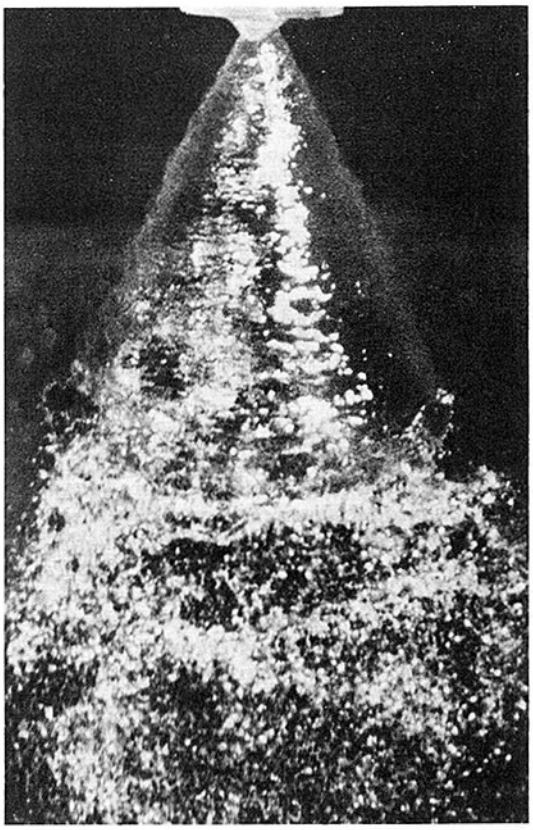

Fig. 1 Waves on a hollow cylindrical liquid sheet

rotary motion, it undergoes a centrifugal acceleration. This means that a net centrifugal force is present to maintain the rotation. As long as the fluid is confined within an enclosure the centrifugal force is supplied by a radial pressure exerted by the wall of the enclosure on the fluid. As the fluid emerges out from the enclosure there is no wall to give it a centrifugal force. Hence the rotation cannot be maintained and the fluid flies off tangentially. Since the fluid is moving axially as well, the resultant motion causes a cone to be formed and in this conical region there is no centrifugal force.

Mathematical Formulation and Stability Analysis

The system considered consists of a cylindrical liquid sheet of thickness $2h$ and central radius r_a. The sheet is moving with a uniform velocity U in stagnant air (Fig. 1). For investigating instability, the disturbances on the outer surface of the sheet only are considered. Following Squire, we assume that the displacements of corresponding points on the inner and outer free surfaces of the sheet are equal in magnitude and in the same direction.

Let η be the displacement of a point on the outer surface of the sheet given by

$$\eta = Ae^{i(kz-\sigma t)} \tag{1}$$

where the constant A represents the amplitude of oscillation.

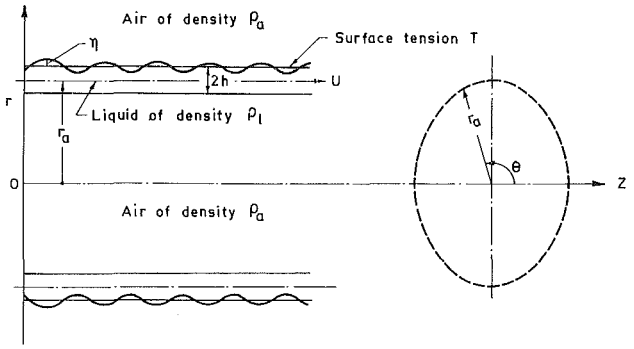

Fig. 2 Disintegration of water sheet from a swirl nozzle

Here a cylindrical polar coordinate system is used with z representing the distance along the axis of the cylindrical sheet. Further k is related to the wavelength λ of the oscillation by $k = 2\pi/\lambda$ and σ represents the wave velocity and damping (or growth) of the waves. We have assumed the disturbance represented by (1) on the outer surface as axisymmetric and this is consistent with Fig. 2 where the lines of crest of the waves are circular on the sheet.

We assume that the liquid in the sheet and the surrounding medium (say, air) are frictionless and are both incompressible. Further the motions in these two media are taken to be irrotational. Let ϕ_1 $(= -Uz + \phi_f)$ be the velocity potential of motion in the liquid sheet and ϕ_a be the corresponding potential for the motion of air.

The kinematic conditions are

$$\frac{\partial \eta}{\partial t} + U\frac{\partial \eta}{\partial z} = -\frac{\partial \phi_1}{\partial r}, \quad \frac{\partial \eta}{\partial t} = -\frac{\partial \phi_a}{\partial r} \tag{2}$$

which are to be satisfied, to a good degree of approximation, at the undisturbed surface $r = r_a + h$.

Using (1), it can be readily shown that ϕ_1 and ϕ_a both of which satisfy Laplace's equation and the kinematic conditions (2) are given by

$$\phi_1 = A\left(\frac{\sigma}{k} - U\right)\frac{J_0(ikr)}{J_0'[ik(r_a+h)]}\exp\left[i(kz-\sigma t)\right] - Uz \tag{3}$$

$$\phi_a = \frac{A\sigma}{k}\frac{J_0(ikr)}{J_0'[ik(r_a+h)]}\exp\left[i(kz-\sigma t)\right] \tag{4}$$

where, J_0 is the Bessel function of zeroth order.

The pressures p_1 and p_a in the liquid film and in the air, respectively, are given by Bernoulli's equations as

$$p_1 = \rho_1\left[\frac{\partial \phi_1}{\partial t} - \frac{1}{2}\left(U - \frac{\partial \phi_f}{\partial z}\right)^2 - \frac{1}{2}\left(\frac{\partial \phi_f}{\partial r}\right)^2 + C_1\right] \tag{5}$$

$$p_a = \rho_a\left[\frac{\partial \phi_a}{\partial t} - \frac{1}{2}\left(\frac{\partial \phi_a}{\partial r}\right)^2 - \frac{1}{2}\left(\frac{\partial \phi_a}{\partial z}\right)^2 + C_a\right] \tag{6}$$

where C_1 and C_a are constants.

The instantaneous force balance across the air liquid interface involving the pressures of the liquid and air at the interface and the pressure resulting from the surface tension and the principal curvature leads to

Nomenclature

$2h$ = thickness of the liquid sheet
k = wave number along the sheet
p_a = pressure of air
p_1 = pressure of liquid
r = radial distance
t = time variable
T = surface tension
U = velocity of the liquid sheet
W = Weber number defined by equation (13)
z = distance along the axis of the sheet
η = displacement on the surface of the sheet
ϕ = velocity potential function
σ_r/k = phase velocity of a disturbance
σ_i = growth rate of disturbance
ρ_1 = density of liquid
ρ_a = density of air
λ = wavelength of disturbance along z-direction

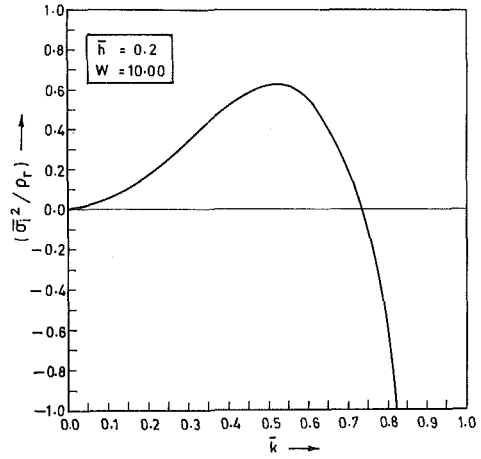

Fig. 3 Variation of $(\bar{\sigma}_i^2/\rho_r)$ with $\bar{k}$

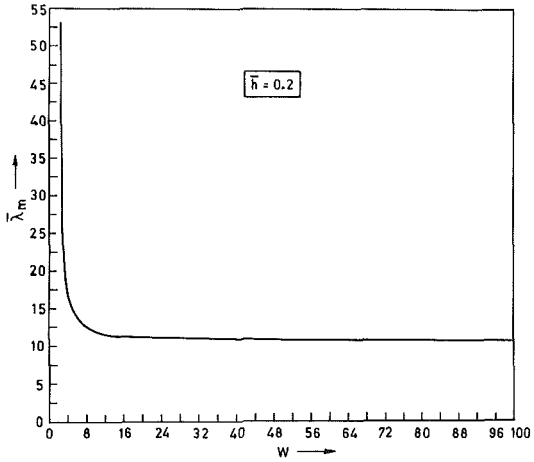

Fig. 4 Variation of $\bar{\lambda}_m$ with W

$$p_1 - p_a = \frac{T}{(r_a+h)} - \frac{T}{(r_a+h)^2}\left[\eta + (r_a+h)^2\frac{\partial^2\eta}{\partial z^2}\right] \tag{7}$$

where the surface tension T is assumed constant. Since we are making a linear stability analysis, equation (7) may be assumed to hold on the undisturbed interface $r = r_a + h$, to a sufficient degree of accuracy. Substituting (1), (3), (4), (5), and (6) in (7) and retaining only first order terms in the disturbance quantities (within the framework of a linear stability theory), we obtain

$$-\left(\frac{\sigma^2}{k} - \sigma U\right)M + (\sigma U = kU^2)M + \rho_r\frac{\sigma^2}{k}M$$

$$= \frac{i\,T}{(r_a+h)^2\rho_1}[1-(r_a+h)^2k^2] \tag{8}$$

where

$$\rho_r = \frac{\rho_a}{\rho_1},\quad M = \frac{J_0[ik(r_a+h)]}{J_0'[ik(r_a+h)]} \tag{9}$$

It may be noted that in deriving (8) from (7), the terms involving C_1, C_a, and U disappear due to the force balance on the undisturbed sheet as

$$\rho_1 C_1 - \rho_a C_a = \frac{T}{(r_a+h)} + \frac{1}{2}U^2 \tag{8a}$$

The solution of (8) is

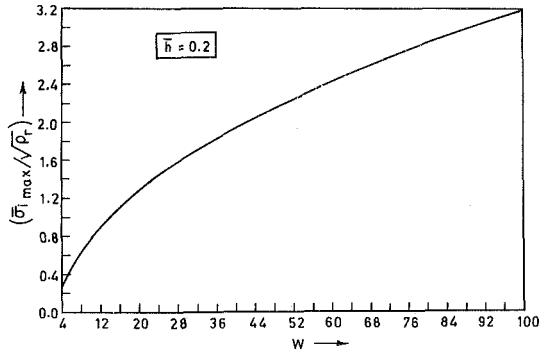

Fig. 5 Variation of $[\bar{\sigma}_{i_{max}}/(\rho_r)^{1/2}]$ with W

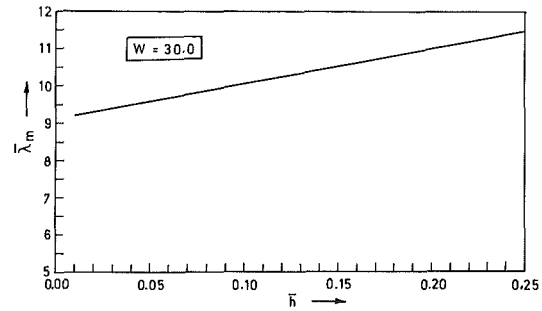

Fig. 6 Variaiton of $\bar{\lambda}_m$ with h

$$\frac{\sigma}{k\,U} = \frac{1}{1-\rho_r} \pm \frac{(\rho_r)^{1/2}}{(1-\rho_r)}\left[1 - \frac{(1-\rho_r)\,T[1-(r_a+h)^2k^2]P}{\rho_a U^2 k(r_a+h)^2}\right]^{1/2} \tag{10}$$

where $$P = \frac{I_0'[k(r_a+h)]}{I_0[k(r_a+h)]} \tag{11}$$

I_0 being the modified Bessel function of zeroth order.

Unstable waves will arise if the expression inside the large square brackets on the right-hand side of (10) is negative so that σ will be complex. If $\sigma = \sigma_r + i\sigma_i$, where σ_i is the growth rate of unstable waves, equation (10) gives

$$\frac{\sigma_i}{kU} = (\rho_r)^{1/2}\left[\frac{T[1-(r_a+h)^2k^2](1-\rho_r)P}{\rho_a U^2 k(r_a+h)^2} - 1\right]^{1/2} \tag{12}$$

where the factor $1-\rho_r$ is the denominator is replaced by 1 since $\rho_r = 0(10^{-3})$ for air-water density ratio.

Introducing the Weber number W (representing the ratio of surface tension and inertia force) as

$$\mathrm{W} = \frac{T}{\rho_a U^2 r_a} \tag{13}$$

equation (12) can be rewritten in a dimensionless form as

$$\bar{\sigma}_i = (\rho_r)^{1/2}\left[\mathrm{W}[1-\bar{k}^2(1+\bar{h})^2](1-\rho_r)\bar{k}\,P - \bar{k}^2(1+\bar{h})^2\right]^{1/2} \tag{14}$$

where $\bar{\sigma}_i = \dfrac{\sigma_i(r_a+h)}{U}$, $\bar{k} = k\,r_a$, $\bar{h} = \dfrac{h}{r_a}$

and $$P = \frac{I_0'[\bar{k}(1+\bar{h})]}{I_0[\bar{k}(1+\bar{h})]} \tag{15}$$

For instability σ_i is real and this demands from (14)

$$\bar{k}(1+\bar{h}) < 1 \tag{16}$$

and

$$\mathrm{W}[1-\bar{k}^2(1+\bar{h})^2](1-\rho_r)\bar{k}\,P - \bar{k}^2(1+\bar{h})^2 > 0 \tag{17}$$

The inequality (16) implies that for instability, the wavelength of the axisymmetric disturbance must exceed the outer circumference of the liquid sheet. This criterion is similar to that of the capillary instability of a cylindrical liquid jet, where the surface tension is the primary cause of instability (see Rayleigh [10]). It may be noted in this connection that Taylor [11] also studied waves on a fluid sheet of uniform thickness where effects of surface tension are important, while those due to aerodynamic forces and gravity are neglected. He showed that these capillary waves are of two kinds, symmetrical waves in which the displacements of opposite surfaces are in opposite directions and the antisymmetrical waves which are nondispersive and in which the displacements at corresponding points of the opposite surfaces are in the same direction. However it should be emphasized that in our present analysis, the aerodynamic forces are the principal cause of instability. For $\bar{\sigma}_i$ to be maximum, we must have

$$\frac{\partial}{\partial \bar{k}}\left[\mathrm{W}[1-\bar{k}^2(1+\bar{h}^2)](1-\rho_r)\bar{k}\,p-\bar{k}^2(1+\bar{h})^2\right]=0. \tag{18}$$

Equation (18) is solved numerically for several values of W and $\bar{h}$ and from this, $\bar{k}_m$, the value of $\bar{k}$ corresponding to maximum growth rate is determined. The corresponding wavelength $\bar{\lambda}_m$ is then given by

$$\bar{\lambda}_m=\frac{2\pi}{\bar{k}_m} \tag{19}$$

Thus from (14) and (18), the maximum growth rate $(\bar{\sigma}_{i_{\max}}$ is given by

$$\frac{(\bar{\sigma}_i)_{\max}}{(\rho_r)^{1/2}}=\left[\frac{\mathrm{W}[1-\bar{k}_m^2(1+\bar{h})^2]\bar{k}_m(1-\rho_r)I_0'[k_m(1+\bar{h})]}{I_0[\bar{k}_m(1+\bar{h})]}-\bar{k}_m^2(1+\bar{h})^2\right]^{1/2} \tag{20}$$

Results and Discussions

A photograph of disintegration of water sheet from a swirl nozzle is shown in Fig. 2. It may be seen from (18) that the wavelength corresponding to the mode of maximum instability depends on the Weber number W. Further it it clear from (14)–(17) that the nondimensional wave number $\bar{k}$ for which instability occurs, is always less than unity. Figure 3 shows that for W = 10.00 and $\bar{h}$ = 0.2, the value of $\bar{k}_m$ corresponding to maximum growth rate is 0.52 (approx.). Figure 4 shows the variation of $\bar{\lambda}_m$ (the wavelength corresponding to the maximum growth rate) with W for h = 0.2. It may be seen that the sheet becomes unstable with respect to long wavelength disturbances when W is small i.e., when the inertia forces dominate over the surface tension. It may also be seen from Fig. 4 that as W increases, $\bar{\lambda}_m$ decreases sharply from a high value and asymptotically tends to the value 10 (approx.) as W → ∞. It is interesting to note that this asymptotic value for $\bar{\lambda}_m$ agrees with the corresponding value obtained by Rayleigh [10] in his study of the capillary instability of a liquid jet. Of course this result is to be expected physically since when W → ∞, surface tension dominates over the inertia force as in the capillary instability of a liquid jet. Figure 4 further reveals that for a fixed value of $\bar{h}$, the sheet is always stable if W < 2.5 (approx.). It can be seen from Fig. 5 that for a fixed value of $\bar{h}$, the maximum growth rate of instability increases nonlinearly with increase in W. Thus we would expect that when the surface tension is not too small (such that W > 2.5), for a sheet of given thickness moving with a fixed velocity, increase in surface tension tends to enhance the growth rate of instability. Variation of $\bar{\lambda}_m$ with $\bar{h}$ for W = 30.00 is shown in Fig. 6. It is clear that $\bar{\lambda}_m$ increases slowly but monotonically with $\bar{h}$.

References

1 Colbourn, A. J., and Heath, H. H., "Swirl Atomizer Sprays in Partial Vacuum," National Gas Turbine Establishment Memorandum 86, 1950.

2 Simons, A., and Goffe, C. R., "Photographs of Sprays from Pressure Jets," Aeronautical Research Council R. and M. No. 2343, 1950.

3 Dombrowski, N., and Johns, W. R., "The Aerodynamic Instability and Disintegration of Viscous Liquid Sheets," *Chem. Engr. Sci.*, Vol. 18, 1963, p. 203.

4 Squire, H. B., "Investigation of Instability of a Moving Liquid Film," *Brit. J. Appl. Phys.*, Vol. 4, 1953, p. 167.

5 York, J. L., Stubbs, H. E., and Tek, M. R., "The Mechanism of Disintegration of Liquid Sheets," ASME Paper No. 53-S-40, 1953, p. 1279.

6 Hagerty, W. W., and Shea, J. F., "A Study of Stability of the Plane Fluid Sheets," ASME *Journal of Applied Mechanics*, Vol. 22, 1955, p. 509.

7 Clark, C. J., and Dombrowski, N., "Aerodynamic Instability and Disintegration of Inviscid Liquid Sheets," *Proc. R. Soc.* (London), Vol. A 329, 1972, p. 467.

8 Fraser, R. P., Eisenklam, P., Dombrowski, N., and Hasson, D., "Drop Formation from Rapidly Moving Liquid Sheets," *A.I.Ch.E Journal*, Vol. 8, 1962, p. 672.

9 Dombrowski, N., Hasson, H., and Ward, D. E., "Some Aspects of Liquid Flow through Fan Spray Nozzles," *Chem. Engr. Sci.*, Vol. 12, 1960, p. 35.

10 Rayleigh, L., *Theory of Sound*, The Macmillan Comp. Ltd., London, 1894, reprinted by Dover, N.Y., Vol. 2, 1945, p. 351.

11 Taylor, G. I., "The Dynamics of Thin Sheets of Fluid," *Proc. Roy. Soc.* (London), Vol. 253A, 1959, pp. 289–321.

N. T. Obot
Assistant Professor.
Mem. ASME

K. Adu-Wusu
Graduate Student.

Department of Chemical Engineering,
Clarkson University,
Potsdam, New York 13676

The Flow Pattern in a Scalene Triangular Duct Having Two Rounded Corners

Experiments were carried out to determine the pressure drop characteristics and mean velocity distributions in a scalene triangualr duct having two rounded corners. The present data for friction factor are adequately represented by the circular pipe line for laminar flow, but fall below the latter for turbulent flow. The mean flow field is highly asymmetric, the degree of asymmetry being more accentuated along lines parallel to the altitude than parallel to the base.

1. Introduction

The characteristics of the flow field in triangular passages have been the subject of experimental study by a number of researchers [1–8], especially in connection with design of compact heat exchange equipment. However, virtually all of the available data were obtained with ducts of isosceles or equilateral cross-section. There has been almost no investigation with the scalene configuration. The particular industrial application which motivated this study was that of possible future design of flow passages for advanced aircraft gas turbine blades.

The complex nature of the flow field in narrow isosceles channels was first detailed by Eckert and Irvine [1]. They found that, even at relatively large Reynolds numbers, the flow in a duct of small apex angle consisted of two regimes: a laminar flow zone in the apex region of the duct, the size of which decreased with increasing Re, and a turbulent flow which prevailed over the remainder of the duct. Also, their results indicated that the Re value at which the flow was laminar throughout the entire channel was much lower than the critical Re usually quoted for circular tubes. Later, in [2], measurements of friction factor characteristics were made in which the apex angle was varied between 4.01 and 38.8 deg. Their finding was that, although the experimental data, when reduced to the hydraulic diameter, showed monotonic increase of friction factor with apex angle, the results for any particular apex angle were substantially lower than those for circular tubes, regardless of whether the flow was laminar or turbulent. This has been verified experimentally by other investigators who used ducts of similar design [3–8].

Using a birefringent flow visualization technique, Hanks and Brooks [3] presented results that were at variance with the findings in [1]. Specifically, they reported that, in the process of transition from laminar to turbulent flow, the prime region of turbulence initiation occurred in the vicinity of the apex, and that this resulted in a bifurcated flow over a small Re range. Also, with the aid of a birefringent fluid, they attempted to show that the presence of a smoke or dye injecting probe, as was the case in [1], resulted in patterns of light and shade that were indicative of a disturbed flow. Their conclusion therefore was that the existence of a dual flow regime was entirely the result of the influence of the smoke injecting probe on the flow and not due to any physical phenomenon occurring in the duct.

That the above conclusion by Hanks and Brooks was not necessarily correct has been demonstrated by Bandopadhayay and Hinwood [7], who also established quite convincingly that the coexistence of laminar and turbulent flow is an inherent feature of fluid flow in narrow triangular ducts. The laminar flow zone was found to consist of a greatly thickened viscous sublayer formed by interaction of the boundary layers on the side walls of the duct.

A comprehensive investigation, which involved measurements and prediction of the mean flow properties and turbulence quantities in an equilateral duct, was carried out by Aly et al. [8]. Their turbulent friction factor data were generally lower than those calculated using the Blasius equation, in line with the findings of other investigators. Also, the isovels were found to be somewhat dependent on Reynolds number, especially for the central portion of the duct where local velocities decrease with increasing Reynolds number.

The primary objective of our research program was to determine heat transfer rates in smooth and roughened scalene triangular ducts [9, 10]. The need to gain better understanding of the complex heat transfer trends, especially in the case of the roughened duct, prompted extension of the work to include measurements of pressure drop and mean velocity. The flow Reynolds number was varied between 800 and 40,000. Although mean velocity or heat transfer measurements did not cover the laminar flow region, pressure drop data were, for the sake of completeness, obtained for this region.

2 Experimental Apparatus and Test Procedures

The test facility consisted of a blower which delivered air through one of two rotameters (depending on the Re range), a 50.8 mm square plexiglas plenum chamber containing aluminum honeycomb and fine mesh screens, and through a $97D_e$ entrance length of a triangular passage which terminated in a flange for attachment of the test section. The inlet to the

Contributed by the Fluids Engineering Division for publication in the JOURNAL OF FLUIDS ENGINEERING. Manuscript received by the Fluids Engineering Division, September 17, 1984.

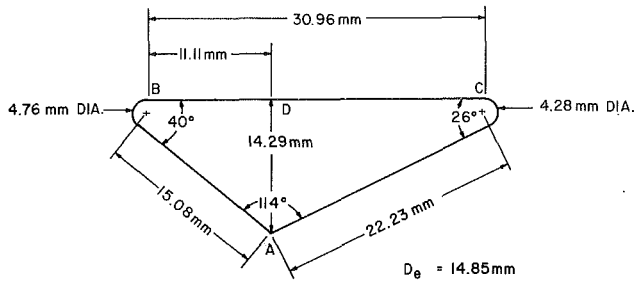

Fig. 1 Cross section of scalene duct

triangular duct was sharp-edged, the choice of which was made with the objective of facilitating the establishment of fully developed mean flow conditions prior to the test section. The latter was 400 mm long. The cross-section of the duct is illustrated in Fig. 1. As to its fabrication, the oblique sides including the two rounded corners were machined from one block of plexiglas, while the base was simply a flat section of appropriate dimension.

In order to obtain pressure distributions along the middle of each side of the entrance section, flush mounted taps (0.8 mm I.D.) were installed 152.4 mm apart. Since preliminary measurements with a duct of similar design showed significant variation in static pressure at a given cross-section especially at low Re, each of the upstream and downstream pressure values used in the computation of friction factor was averaged from the readings for 18 taps, i.e., 9, 6, and 3 on sides BC, CA, and AB (Fig. 1). For each side, the taps were equally spaced over the length indicated in Fig. 1. Also, taps, spaced 25.4 mm apart, were provided along the middle of each side of the test section.

Static pressures were measured by two Statham unbonded strain gauge differential transducers (ranges: ± 1.0 and ± 6.9 kPa). The smaller range transducer of greater sensitivity was used for low flow rates corresponding to values of Re in the range 800 to 10,000, while the other sensed pressures for the $5{,}000 \leq \text{Re} \leq 40{,}000$ range. For the overlapping region, the readings for the two transducers were almost identical. A 48 port scanivalve, equipped with interchangeable connectors, facilitated switching amongst the static taps located in the duct. The transducer output was recorded on a Hewlett Packard 3466A digital voltmeter. Air temperature, which differed only slightly from that of the laboratory, was measured using fine gauge chromel-alumel thermocouple.

Mean velocity distributions were determined from measurements with a cylindrical Pitot-static tube (1.7 mm O.D.). The probe was connected to a pressure transducer and the outpout was recorded on a digital voltmeter. The traversing mechanism on which the probe was attached consisted of two micrometer screws which were mounted on a sliding device and then fastened rigidly to a support. By this arrangement distances could be measured precisely in increments of 1.2 mm and 0.64 mm in the vertical and horizontal directions, respectively. Velocity measurements were made at about $1.3D_e$ from the duct exit, i.e., at about $124D_e$ from the sharp-edged inlet. Owing to the unique configuration of the duct, more detailed velocity profiles, such as are presented subsequently, could not be obtained at locations farther upstream from the exit. Additional information on the experimental apparatus is available in [11].

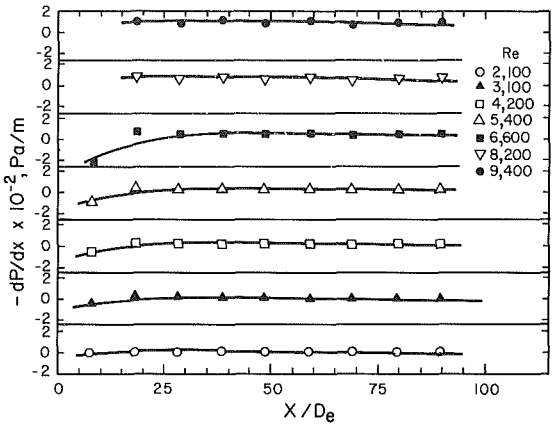

Fig. 2 Mean pressure gradient in entrance section

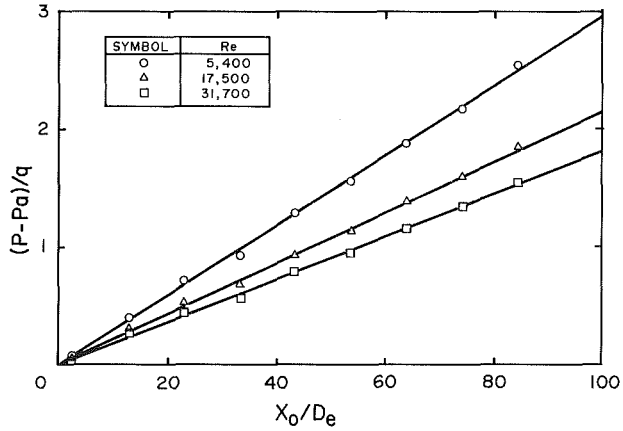

Fig. 3 Mean pressure distribution in entrance section

As to the uncertainties on measured variables, friction factor data were reproducible to within ± 2 percent. With the present instrumentation, velocities were obtained with a high degree of accuracy, and it was established that measurement errors are about 1–2 percent for the central portion of the duct. In the vicinity of the wall, the error in measured velocities should be expected to be higher due to the influence of the wall on the probe and the large level of turbulent velocity fluctuations, but these do not have any significant effect on the interpretation of some of the gross effects on the mean flow observed in the present tests.

3 Results and Discussion

3.1 Pressure Drop. The flow development was examined through pressure drop measurements, typical results of which are shown on Figs. 2 and 3. The results on both figures were prepared from the average pressure data as measured along the middle of the three sides. The abscissa in Fig. 2 is measured from the duct inlet while that in Fig. 3 is taken from

Nomenclature

A = duct cross-sectional area
a = height
b = base
D_e = equivalent or hydraulic diameter ($4A/P_w$)
f = Fanning friction factor [$(\Delta P/2\rho\bar{V}^2)\cdot D_e/L$]
L = distance between pressure taps
m = mass flow rate
P = mean static pressure
P_a = atmospheric pressure
P_w = wetted perimeter
q = average dynamic head ($\rho\bar{V}^2/2$)
Re = Reynolds number ($mD_e/A\mu$)
U = local mean velocity
$\bar{V}$ = bulk mean velocity
X = distance from duct inlet
X_0 = distance from duct exit
Y = location from base along the height
Z = location along the base
μ = fluid viscosity

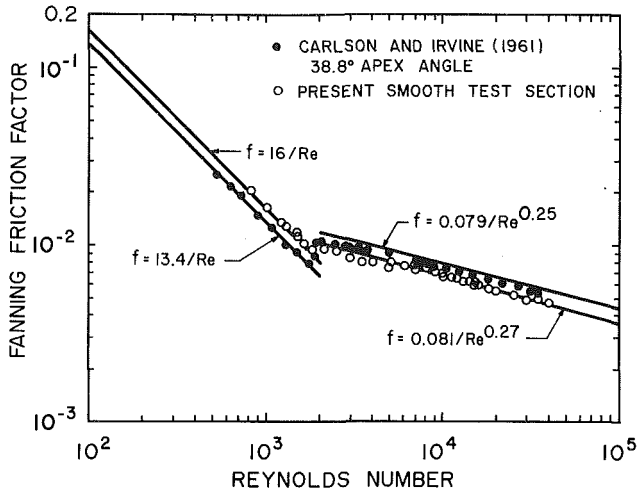

Fig. 4 Variation of friction factor with Reynolds number

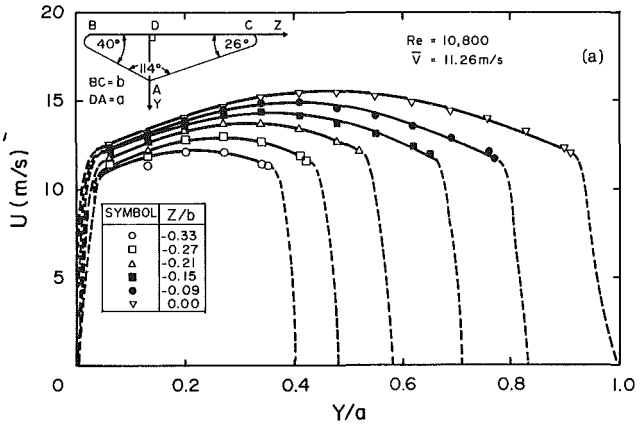

Fig. 5(*a*)

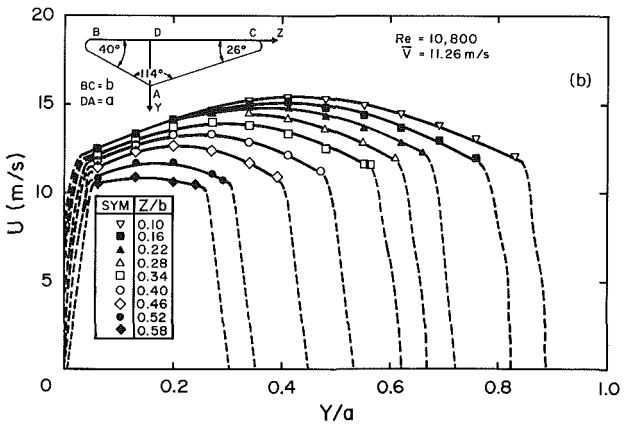

Fig. 5(*b*)

Fig. 5 Velocity distributions along lines parallel to altitude

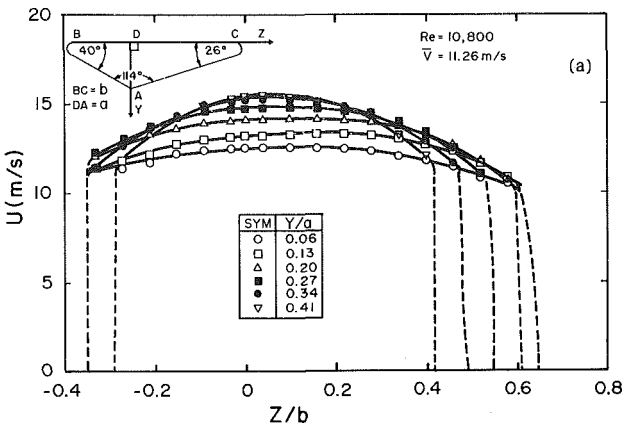

Fig. 6(*a*)

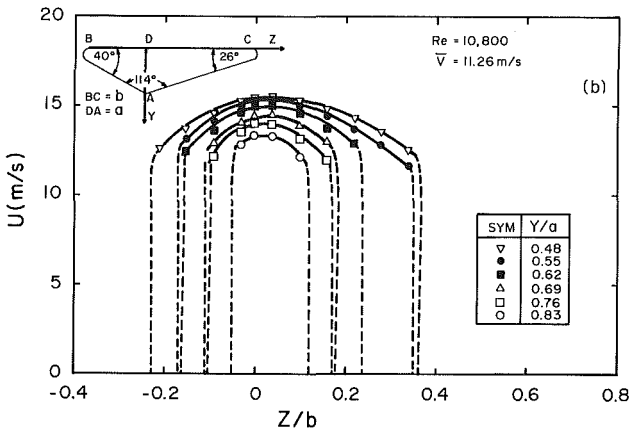

Fig. 6(*b*)

Fig. 6 Velocity distributions along lines parallel to base

the exit. The reason for presenting the results differently will become quite evident from the subsequent discussion of the results. It may be noted that the gradient or difference was calculated between consecutive taps and the value was plotted over the location midway between the taps. Also, it should be emphasized that, in view of the already noted cross-sectional variation in static pressure and the fact that a large number of taps would be required to obtain representative mean pressures for the entrance section, a higher accuracy for mean static pressure was neither possible nor considerd to be of great importance. This is not expected to have significant effect on the qualitative interpretation of the trends on both figures.

Figure 2 shows that, with a sharp-edged inlet, the near constancy of streamwise pressure gradient is realized by about $25D_e$ for Re $\leq$ 9,400. Also, the consequence of introducing a sharp-edged inlet is clearly evident in that, at the smallest X/D_e of 7.5 for which data were available, pressure gradient is positive for each of the Re tested. For Re $\geq$ 10,000 profiles for the $0 \leq X/D_e \leq 30$ region exhibited no systematic variation with Re or X/D_e and, for some of the Re values tested, the presence of several maxima and minina was not uncommon. Although similar results available elsewhere for the isosceles geometry are for Re < 7,000 [1, 6], one can readily infer from the trends, especially those of [1] for comparable inlet geometry to the duct, that a systematic trend for the $X/D_e < 30$ region is less likely to occur with increasing Re. It was therefore considered more logical, at least insofar as the approach to fully developed mean flow is concerned, to examine the alternative representation which is shown in Fig. 3. Note that the data for Re = 5,400 is common to both Figs. 2 and 3, and that the variation with X_0/D_e is fairly linear for $0 \leq X_0/D_e \leq 80$. However, for Re = 17,500 and 31,700, the data for $X_0/D_e > 80$ were off the scale. From Figs. 2 and 3 the conclusion amounts to this: a length of about $25D_e$ represents the minimum which is required for the establishment of fully developed mean flow conditions when the duct inlet is sharp-edged, but a much larger length would probably be needed for fully developed turbulence.

The pressure drop data for the test section, expressed as the Fanning friction factor, are shown in Fig. 4 for laminar and

turbulent flow. For the purpose of comparison with the literature, the well known laminar and turbulent flow expressions for smooth circular tubes together with the isosceles duct results of [2] are also shown. The relation, $f = 0.081\ \mathrm{Re}^{-0.27}$, represents the logarithmic best fit through the present data for $\mathrm{Re} \geq 5{,}000$.

Figure 4 shows that, for $\mathrm{Re} \leq 1700$, the scalene duct data are adequately represented by the circular tube line, with transition from laminar to turbulent occurring in the range of Re between 1,700 and 1,900. However, beyond Re = 2,000, the present results deviate markedly from the Blasius relation and are the lower set by about 17 percent. For laminar flow, the present results are about 14 percent higher than the 38.8 deg apex angle results of [2], with about an average difference of about 10 percent for turbulent flow, the latter being the higher set. Since fully developed turbulent friction factor for the isosceles cross-section decreases with decreasing apex angle [2], it is to be expected that the data for this scalene configuration would be quite close to the results which were obtained with very narrow ducts. This was verified from comparison of the present results with those in [2] for 7.96 and 12 deg apex angles. Consistent with this agreement, the Re range for transition from laminar to turbulent flow is also very close to that for narrow isosceles ducts. The speculation is that, as with the isosceles configuration, the scalene duct friction factor would depend on the numerical values for the enclosed angles. Additional experiments would be required to establish this observation.

3.2 Mean Velocity Distributions. Typical mean velocity distributions are presented in Figs. 5 and 6 for Re = 10,800. Several ways of presenting the results were attempted, and those to be described here were considered to be most helpful in examining the salient features of the mean flow as well as the heat transfer trends [9, 10]. Figure 5(*a*) shows results of vertical traverses from BD towards BA while, for clarity, the same basic information but for traverses from DC to AC is displayed in Fig. 5(*b*). The negative and positive values of Z/b lie to the left and to the right of the altitude (DA), respectively. Each value of Z has been scaled with $BC(=b)$ which has a value of 30.96 mm while the normalizing factor for Y is $DA(=a)$ and has a value of 14.29 mm (Fig. 1).

An alternative perspective for viewing the same experimental data is through plots of profiles at locations parallel to the base (BC). Such plots are presented in Fig. 6. Here, the desire to clarify rather than confuse the presentation has also prompted breaking the plots into two (Figs. 6(*a*) and (*b*)). As with Fig. 5, both figures must be viewed simultaneously. It is pertinent to note that the smaller the Y/a value, the closer the location to the base of the triangle. In other words, with increasing Y/a value, one is moving from the base along the altitude toward A. It is also of some interest to note that the setup is such that the flow direction is outwards from the page.

Examination of Figs. 5 and 6 reveals several interesting features the prominence of which depend, to some extent, on the way the data are plotted. The first, and perhaps the most obvious, is that the flow is asymmetric, this being more pronounced in Fig. 5 than in Fig. 6. In other words, the degree of asymmetry is more accentuated along lines parallel to the altitude than parallel to the base. One clear consequence of this flow imbalance is that, although all profiles show marked increase in velocity as one moves from the base towards the oblique sides, velocities are somewhat higher for the region adjacent to BA than CA. It is also especially noticeable in Fig. 5 that there is a crowding of the velocity profiles for the $Y/a < 0.2$ region. This is entirely the result of lack of strong variation in velocity in the region adjacent to the base, a fact that is best illustrated by the $0.06 \leq Y/a < 0.3$ profiles in Fig. 6.

Near the base and under the influence of the nearby flat surface, typical profiles are reasonably flat over most of the central portion of the channel. With increasing distance from the base, the profiles become more peaked, with some crossing of the profiles in clear evidence for regions nearest to the walls. This consequence of continuity is in fact expected because, since the volumetric flow rate is constant for a given Re, modifications which bring about higher velocities over the central region must necessarily be compensated by lower values close to the walls. All of the trends which have been noted in this paragraph have also been shown to exist for isosceles ducts [1].

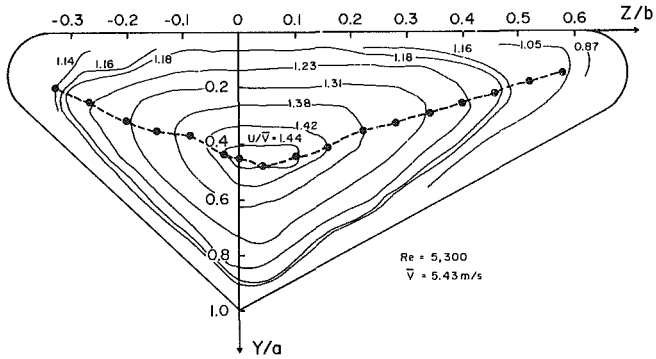

Fig. 7 Velocity contour diagram for Re = 5,300

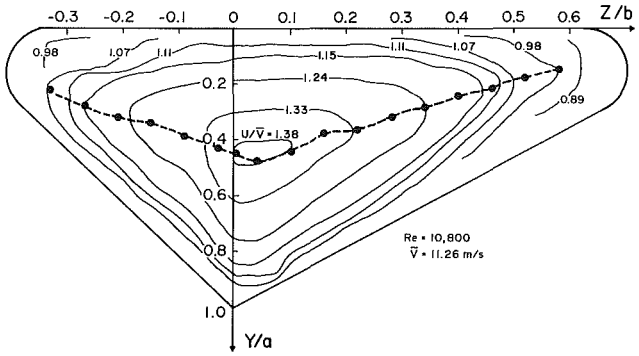

Fig. 8 Velocity contour diagram for Re = 10,800

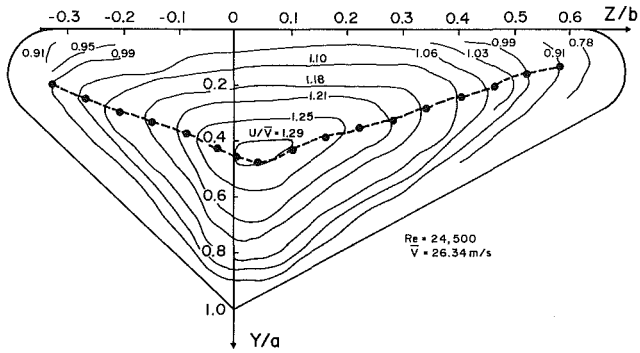

Fig. 9 Velocity contour diagram for Re = 24,500

Better insight into the nature of the mean flow as well as its effect on heat transfer may be gained by considering faired velocity contour diagrams which are presented in Figs. 7–9 for three values of Re. A typical contour line on each of these figures represents the locus of points having almost the same velocity, and each line has been scaled with the appropriate bulk mean velocity, $\bar{V}$, and hence corresponds to a constant value of $U/\bar{V}$. The additional information on these figures deals with the location of maximum velocity at each traverse station. These locations have been connected using dashed lines.

Since the contour diagrams were prepared from the mean velocity data, typical results of which have already been discussed, all features detailed earlier must also appear on this alternative representation. The fact that there is only a gradual change in velocity over the central portion of the duct is also strikingly apparent from the widely spaced trend in the contour lines. The closely spaced nature of the contour lines near the oblique walls, an expected trend, is consistent with the more rapid change in velocity as these walls are approached. The asymmetric nature of the mean flow, discussed in connection with Figs. 5 and 6, is clearly noticeable in each of Figs. 7 through 9. In the first place, the contour lines are more closely spaced to the left of the altitude than to the right. Also, the $U/\bar{V}$ values for the region enclosed by the 40° angle are generally higher than those which are observed to occur in the vicinity of the 26 deg angle. Note that all of the above observations are clearly in evidence for all Re tested.

A closer examination of Figs. 7-9 reveals that the mean flow field does exhibit several trends that are dependent on Re. The first involves the dependence of the contour spacings on Re, most noticeably over the central portion of the duct. Thus, one observes closely spaced isovels for Re = 5,300, more widely space curves for Re = 10,800, but for Re $\geq$ 14,800, one is back again to a contour representation that is not significantly different from that for Re = 5,300. It should, however, be mentioned that, although not included here, mean velocity profiles were obtained for Re = 14,800. This dependence is attributed to the existence of transitional flow for $1700 < \text{Re} < 14{,}800$. Indirect support for this observation comes from the smooth and roughened duct heat transfer data which indicated two distinct trends with increasing Re: a nearly constant heat transfer enhancement factor for the $4{,}000 \leq \text{Re} \leq 12{,}000$ range, the value of which was signficantly higher than that for Re > 12,000 [10]. As noted in the introductory section, a similar dependence of the isovel spacing on Re was reported for an equilateral duct [8].

Another Re effect deals with the ratio of $U/\bar{V}$. In this regard the results show the generally expected trend of $U/\bar{V}$ decreasing with increasing Re. Although the precise values of $U_{max}/\bar{V}$ cannot be determined from the available data, these are believed to be very close to the highest values which are indicated on these figures. It is of interest to note that, for the largest Re of 24,500, the $U/\bar{V}$ value of 1.29 is not significantly different from the circular pipe $U_{max}/\bar{V}$ value of 1.25 that can be deduced from the graphical presentation in [12]. Although each maximum velocity line moves outwards from the altitude towards the two rounded corners, there is hardly a Reynolds number effect on its location. It is also of some interest to note that a steady shift of the point of maximum velocity away from the altitude towards the corners was also reported for equilateral channels [5].

To carry the discussion one step further, one may wish to inquire whether the coexistence of laminar and turbulent flow is discernable for the range of Re tested or could be expected for scalene triangular ducts. In this connection it must not be forgotten that, between these two limiting flow regimes, there must necessarily exist a transitional flow regime. From the general shapes of the profiles in Figs. 5 and 6, the straightforward conclusion is that, for Re $\geq$ 5,300, there is no evidence in support of a laminar flow zone, although this has been shown to exist in a narrow duct at a comparable Re [1]. However, the trends evident from Fig. 6 appear to suggest that the existence of several flow regimes is quite possible at lower values of Re. In this regard it may be noted that, for each of the 5 Re values tested, the velocity profiles are almost flat near the base, but become more peaked with increasing distance from the base. This effect of the nearby flat surface should be almost the same with decreasing Re below that considered here. In fact, this observation can also be inferred from the results given in [1]. Since the velocity profiles of this study do exhibit intermediate and fuller shapes, similar to the expected trends for transitional and turbulent flows, a valid conclusion is that transitional and turbulent flows prevail over most of the duct cross-section.

Although the nature of the flow in the vicinity of the 26 deg angle is not laminar, the fact that the local Re in this region can be much lower than the bulk Re suggests, though not conclusively, that transitional flow may exist here. The same reasoning seems to dictate a marginal chance for the presence of a transitional flow near the 40 deg region. In the region enclosed by the 114 deg angle there is no evidence whatsoever in support of a regime other than turbulent flow for Re $\geq$ 5,300.

4 Conclusion

Experiments were carried out to establish the pressure drop characteristics and mean flow pattern for flow of air in a scalene triangular duct having two rounded corners and small hydraulic diameter. The data for friction factor, when reduced to the hydraulic diameter, are adequately represented by the circular tube line for laminar flow, but are about 17 percent lower than the values that are calculated from the Blasius relation for turbulent flow.

The mean flow pattern in a scalene triangular duct is asymmetric, the degree of asymmetry being more pronounced along lines parallel to the altitude than parallel to the base. The location of maximum velocity moves outwards from the altitude towards the two rounded corners which are enclosed by angles of 26 and 40 deg. For any particular Reynolds number, local velocities are generally higher in the 40 than the 26 deg region.

Acknowledgments

The Division of Research of Clarkson University provided funds for fabrication of the test-rig. K.A. was supported as a Teaching Assistant by the Chemical Engineering Department.

References

1 Eckert, E. R. G., and Irvine, T. F., "Flow in Corners of Passages with Noncircular Cross Sections," *Trans. ASME*, Vol. 78, 1956, pp. 709-718.

2 Carlson, L. W., and Irvine, T. F., "Fully Developed Pressure Drop in Triangular Shaped Corners," ASME Journal of Heat Transfer, Vol. 83, 1961, pp. 441-444.

3 Hanks, R. W., and Brooks, J. C., "Birefringent Flow Visualization of Transitional Flow Phenomena in an Isosceles Triangular Duct," *AIChE Journal*, Vol. 16, No. 3, 1970, pp. 483-489.

4 Hanks, R. W., and Cope, R. C., "Laminar-Turbulent Transitional Flow Phenomena in Isosceles Triangular Cross-Section Ducts," *AIChE Journal*, Vol. 16, No. 4, 1970, pp. 528-535.

5 Cope, R. C., and Hanks, R. W., "Transitional Flow in Isosceles Triangular Ducts," *Ind. Eng. Chem. Fundam.*, Vol. 11, No. 1, 1972, pp. 106-117.

6 Tung, S. S., and Irvine, T. F., "Experimental Study of the Flow of Viscoelastic Fluid in a Narrow Isosceles Triangular Duct," in *Studies in Heat Transfer*, Hemisphere Pub. Corp, New York, 1978, pp. 309-329.

7 Bandopadhayay, P. C., and Hinwood, J. B., "On the Coexistence of Laminar and Turbulent Flow in a Narrow Triangular Duct," *J. Fluid Mech.*, Vol. 59, 1973, pp. 775-783.

8 Aly, A. M. M., Trupp, A. C., and Gerrard, A. D., "Measurements and Prediction of Fully Developed Turbulent Flow in an Equilateral Duct," *J. Flud Mech.*, Vol. 85, Part 1, 1978, pp. 57-83.

9 Obot, N. T., "Heat Transfer in a Smooth Scalene Triangular Duct with Two Rounded Corners," *Int. Comm. Heat Mass Transfer*, Vol. 12, #3, 1985, pp. 251-258.

10 Obot, N. T., "Local and Average Heat Transfer Characteristics in Smooth and Roughened Scalene Triangular Channels," FHM Report #04, Dept. of Chem Eng., Clarkson University, 1984.

11 Adu-Wusu, K., "Pressure Drop and Velocity Distributions in a Scalene Triangular Channel," M.S. thesis, Clarkson University, Potsdam, NY, 1983.

12 Perry, J. H., *Chemical Engineers' Handbook*, 4th Edition, McGraw-Hill, NY, 1963, pp. 5-8.

J. W. Jacobs

A. Bunster

I. Catton

M. S. Plesset

Nuclear Energy Laboratory,
School of Engineering
and Applied Science,
University of California,
Los Angeles, Calif. 90024

Experimental Rayleigh-Taylor Instability in a Circular Tube

The Rayleigh-Taylor instability of an air-water system has been investigated experimentally. The instability was produced by accelerating a slug of water down a vertical circular tube of 6.25 in. inside diameter employing a pressure differential. Accelerations from 3 to 25 times gravitational acceleration with fluid depths from 5 to 20 centimeters were studied. The disturbances first observed were purely axisymmetric with wave numbers corresponding closely to the fastest growing values given by linear theory. Later stages of planform development were characterized by a series of transitions which cannot be predicted by linear theory. These transitions were correlated with disturbance height.

I Introduction

Rayleigh-Taylor instability occurs on the interface between two immiscible superposed fluids of different densities when the lighter fluid is accelerated toward the heavier one. Chandrasekhar [1] has presented the analytical results found using linear stability theory. Emmons et al. [2] addressed the nonlinear aspects of the stability problem by obtaining higher-order solutions. This phenomena was later recognized as being a singular perturbation problem, and because this was not taken into account in their analysis, Emmons et al. obtained results which were not valid in the neighborhood of the cutoff wave number and were valid only for a short period of time for wave numbers greater than the cutoff wave number. Rajappa [3, 4] solved the singular perturbation problem; however, his results contained an error. Finally, Nayfeh [5] and Kiang [6] obtained correct solutions.

Lewis [7] was the first to investigate this phenomenon experimentally. He obtained data for circumstances in which surface tension and viscosity should be relatively unimportant, and he obtained results which verified the linear theory. Allred and Blount [8] performed experiments under circumstances where surface tension and viscosity should be important. They had a considerable amount of scatter in their data and found that their measured initial growth rates were, on the whole, less than predicted by linear theory. Later, Emmons et al. [2] did experiments in which they found good agreement with linear theory for the case in which the disturbance wave number was less than the cutoff wave number. However, for the case of wave number greater than the cutoff value, they observed a condition of over-stability which is not predicted by theory. This phenomena might have been caused by imperfections in their experimental apparatus [5]. More recently, experimental results have been reported by Ratafia [9], Cole and Tankin [10], and Popil and Curzon [11]. It may be remarked that neither the apparatus nor the results of these investigations differ significantly from earlier investigations.

Contributed by the Fluids Engineering Division for publication in the JOURNAL OF FLUIDS ENGINEERING. Manuscript received by the Fluids Engineering Division, October 1, 1984.

The theoretical work done to date focuses on Rayleigh-Taylor instability in two dimensions. Linear theory can easily be generalized to three dimensions as well as to other geometries such as the axisymmetric case; however, the results obtained from nonlinear analysis cannot. In addition, the experimental work done so far has examined Rayleigh-Taylor instability in thin rectangular enclosures with the hope of isolating the two-dimensional phenomena. Thus the work reported here differs from previous work in that a three-dimensional instability is investigated. The experimental apparatus used in this study is similar to those used by Lewis [7] and Allred and Blount [8] with the difference that our test section is circular.

Another difference between this study and previous work is that in our experiments the system was not given an initial disturbance in the form of forced standing waves which has been the standard procedure. This approach limits the usefulness of our results when the instability is viewed as an initial value problem; however, we feel that interesting information can be obtained from this procedure. We will assume that the instability evolves from some sort of random excitation. This approach implies that the system is allowed to choose the mode with the largest growth rate from what is initially present in the system in the form of noise.

In the discussion that follows we will first give some results from linear theory regarding the instability in a cylindrical domain. The experimental apparatus will then be described followed by a presentation of some results of our experimental investigation.

II Linear Theory

Consider a system consisting of two immiscible fluids in an infinite region separated by a flat interface located in $z=0$. If both fluids are taken to be inviscid, irrotational and incompressible, and in addition it is assumed that the density of one of the fluids is much greater than the other (a reasonable assumption for a gas-liquid system), then the linearized equa-

tions governing the evolution of a small disturbance to this system (in cylindrical coordinates) are

$$\frac{1}{r}\frac{\partial}{\partial r}\left(r\frac{\partial\phi}{\partial r}\right)+\frac{1}{r^2}\frac{\partial^2\phi}{\partial\theta^2}+\frac{\partial^2\phi}{\partial z^2}=0 \qquad \begin{matrix} 0\le r<\infty \\ 0\le\theta<2\pi \\ -\infty<z\le 0 \end{matrix}$$

with boundary conditions

$$\frac{\partial\eta}{\partial t}-\frac{\partial\phi}{\partial z}=0$$

$$\frac{\partial\phi}{\partial t}-a\eta-\frac{\alpha}{\rho}\left[\frac{1}{r}\frac{\partial}{\partial r}\left(r\frac{\partial\eta}{\partial r}\right)+\frac{1}{r^2}\frac{\partial^2\eta}{\partial\theta^2}\right]=0 \quad z=0$$

$$\phi \to 0 \text{ as } z\to-\infty$$

Here, η is the perturbed surface elevation and ϕ is the velocity potential of the denser fluid, defined by

$$\mathbf{v}=\nabla\phi.$$

Also, α is the surface tension, ρ is the density of the heavier fluid, and a is the acceleration of the system relative to a free failing reference frame (positive when directed in the negative z direction). An arbitrary solution for surface height can be constructed from a series of the form

$$\eta(r,\theta)=\sum_k\sum_n A(k,n)e^{\sigma t}\cos(n\theta)J_n(kr) \tag{1}$$

where n is an integer and k is a wave number. The growth rate, σ, of the instability is given by the following dispersion relation

$$\sigma^2=ak-\alpha\frac{k^3}{\rho} \tag{2}$$

Using equation (2) it can easily be shown that the wave number with the maximum growth rate is given by

$$k_d=\left(\frac{\rho a}{3\alpha}\right)^{1/2}. \tag{3}$$

If k is large enough, σ will be imaginary and thus in the context of linear theory the system is stable. The value of wave number which divides stable solutions from unstable solutions is called the cutoff wave number and is given by

$$k_c=\left(\frac{\rho a}{\alpha}\right)^{1/2}. \tag{4}$$

Now if we restrict our interest to fluids contained in a circular tube of radius R, the set of allowable wave numbers is restricted. Only values of k satisfying the condition

$$\frac{d}{dr}[J_n(kr)]\,|_{r=R}=0 \tag{5}$$

are then acceptable. If the component we are interested in has m complete radial waves contained in the interval $0\le r\le R$ then k is found from the relation

$$k=\frac{j'_{n,2m+1}}{R} \tag{6}$$

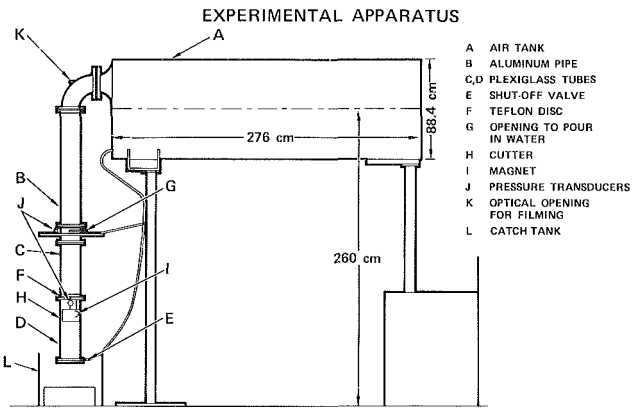

Fig. 1 The experimental apparatus

where $j'_{n,i}$ is the ith zero of the derivative of the Bessel function J_n.

Suppose now that at $t=0$ the disturbances are described as white noise of infinitesimal amplitude. If the amplitudes of these disturbances are small enough the solutions should be accurately governed by linear theory for an appreciable length of time. By the time the system reaches the point where linear theory no longer adequately describes the phenomena, only the component with wave number closest to k_d should be present.

III Experimental Apparatus and Procedure

In the experiments that comprise this study a column of water is accelerated down the length of a tube by imposing a pressure differential across it. Since we are primarily interested in Rayleigh-Taylor instability in which the acceleration is constant, it is important that the apparatus is designed so that this condition is closely satisfied. There are two considerations which will insure that this requirement is met. First, the pressure differential must be fairly constant. This condition is assured by employing a large enough high pressure reservoir and also by minimizing the flow losses in the delivery system. A second consideration is that the friction losses of the water slug are kept to a minimum. Unfortunately, not much can be done to reduce the drag of the water on the tube wall. However, in our experiments a disk is used to insure that the lower liquid surface remains flat. In this case a careful choice of materials will reduce the friction between this disk and the tube wall.

Figure 1 is a schematic drawing of the apparatus used for the experiment. A 1700 liter air tank, A, mounted 2 m above ground feeds into an aluminum pipe, B of 15.88 cm (6.25 in.) inside diameter and 122 cm long which extends vertically downwards. Two circular plexiglass tubes, C and D, of the same inside diameter as the pipe and having lengths of 53 cm each, are bolted on to the bottom of the aluminum pipe to constitute the test section. Aluminum foil diaphragms are inserted in the joint between C and D and at the bottom end of the test section to create two separate chambers (the upper chamber consists of sections A, B, and C while the lower

Nomenclature

A = amplitude function
a = virtual acceleration
g = gravitational acceleration
J_n = Bessel function
$j'_{n,i}$ = ith zero of the derivative of the Bessel function J_n
k = wave number
k_c = cutoff wave number
k_d = fastest growing wave number
m = number of radial waves
n = azimuthal wave number
r, θ, z = spatial coordinates
R = tube radius
t = time
$\mathbf{v}$ = velocity
α = surface tension
ρ = density
σ = growth rate
η = surface wave height
ϕ = velocity potential

top view

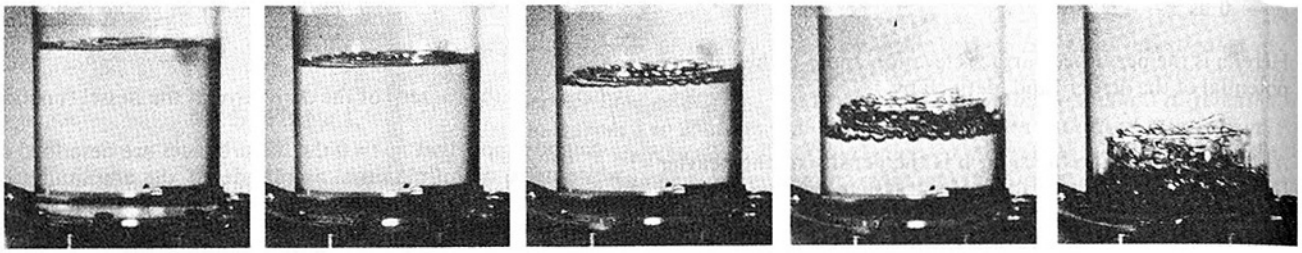

side view

Fig. 2 A consecutive series of photographs of the instability taken from the films of run 19

chamber is the plexiglass tube D). They are sandwiched together between flanges with 3.2 mm (1/8 in.) rubber gaskets in order to ensure a good seal. The bottom chamber is connected via a shut-off valve, *E*, to *A* by means of a tygon tube, so that it can be isolated from the upper chamber. A 3.4 cm thick teflon disk, *F*, hollowed out from the bottom and rendered water tight by a circular metal cover rests on the upper diaphragm. The disk fits snugly within the test section, but can nevertheless slide freely up and down with minimal friction.

Water is poured on top of the disk through an opening, G, in the aluminum pipe. A cutter, H, made of steel pipe 15.24 cm (6 in.) in diameter with 32 mm (1/8 in.) wall thickness and 10 cm long and with razor blades taped around its bottom edge, is held immediately below the upper diaphragm by means of a U-shaped magnet, I, placed against the outer wall of the test section. Two pressure transducers, J, are employed in the experiment. One is located on B and the other at the top of D. Their output is fed via an amplifier to a computer to enable pressures to be recorded during the experiment. In order to minimize vibration, the test section is braced at its center with two steel tubes at right angles to each other, which are clamped to nearby solid benches. Half of a 55 gallon drum, L, situated under the exit of the test section acts as a container to catch the ejected water. This tank is partially filled with polystyrene foam in order to absorb the impact of the cutter and disk.

A pair of high speed cameras were used to film the development of the Rayleigh-Taylor instability. One is placed directly above the water surface, for which an optical opening, K, is provided at the top of the aluminum pipe B. The other camera is aimed horizontally at the test section from about four feet away. One hundred-foot rolls of black and white Kodak 4X 7277 reversal film were employed for the photography. The speed setting of the cameras was 1000 frames per second. Lighting was provided by three 500-watt floodlights located behind the test section with a 32 mm (1/8 in.) thick white plastic screen placed in the light path in order to diffuse the light. Three additional 1000-watt tungsten lights illuminated the test section from the front and sides at a height slightly above the initial level of the water surface. With the aperture in both cameras set between f4 and f5.6, the arrangement produced reasonable exposure. In order to synchronize the photography with the acceleration of the slug of water and with the recording of pressure, use was made of a switch incorporated in the side camera to activate the analog to digital converter in the computer in conjunction with the ignition of a flash bulb. This switching mechanism can be made to function at any time after the camera is started. In our particular case the switch was made to operate after about 25 ft of film had been exposed by which time the camera had reached a steady speed.

Once the water has been introduced and the cameras loaded, the experimental procedure is as follows. The system is pressurized until the pressure necessary to produce the desired acceleration is attained. This is achieved by allowing compressed air to flow into tank A with shut-off valve E open, thus pressurizing sections C and D equally. The shut-off valve is then closed to isolate chamber D, and the cameras are started simultaneously. When the analog to digital converter is activated (about a second later), pressure recording begins and at the same instant the flashbulb lights, signaling an operator to pull the magnet away from the test section. The cutter is then free to fall and an instant later breaks the bottom diaphragm causing a sharp release of pressure. The pressure differential thus created between C and D, in turn causes the disk and water to suddenly break through the upper diaphragm with the prescribed acceleration.

A single sheet of 0.00762 mm (0.0003 in.) thick aluminum foil was used for the upper diaphragm, whereas for the bottom standard commercially available material proved adequate.

IV Discussion of Results

Runs were first made in order to determine the effect of liquid depth on the resulting instability. These consisted of runs

Table 1 Planform observations

RUN	a/g	LIQUID HEIGHT	RADIAL WAVES		AZIMUTHAL WAVES		LOSS OF SYMMETRY	LOSS OF PERIODICITY	COMMENTS
			Time of Appearance	m	Time of Appearance	n			
13	8.0	5 cm	37 ms	6–8	40 ms	36–40*o*	45 ms	70 ms	Small ring amplitude, not very circular Azimuthal waves only at tube wall
14	9.0	10 cm	24 ms	7–8½	35 ms	48 *o*	45 ms	70 ms	Good ring structure, Azimuthal waves not well defined in center
15	8.6	15 cm	28 ms	6½–8½	38 ms	48–52 *o* 16 *i*	45 ms	65 ms	Good ring structure, Azimuthal waves not well defined in center
16	9.3	20 cm	18 ms	7–9	33 ms	48–52 *o*	40 ms	60 ms	Good axial and Azimuthal wave structure
18	3.3	15 cm	----	4–5	62 ms	26–32 *o*	----	125 ms	Ring structure poor, small amplitude in center Azimuthal waves only near tube wall
19	9.1	15 cm	11 ms	7½–9	26 ms	48–50 *o* 40 *i*	33 ms	50 ms	Good structure
20	15.0	15 cm	11 ms	9½–10½	20 ms	52–60 *o* 36 *i*	25 ms	40 ms	Good structure
21	24.2	15 cm	12 ms	10–13½	17 ms	60–64 *o* 36 *i*	22 ms	38 ms	Good structure

made with depths of 5, 10, 15, and 20 centimeters. All were accelerated at approximately 10 times gravitational acceleration. Next, runs were made with a 15 cm fluid layer and were accelerated at approximately 3, 10, 15, and 25 times gravity in order to determine the effect of varying acceleration. Table 1 gives observations made in viewing the films of eight of these runs. Figure 2 is a photographic record of the evolution of the instability obtained from the films of run 19. It contains consecutive views from the top and side corresponding to times of 20, 25, 30, 40, and 50 milliseconds after the start of the acceleration. This run is typical in that the general behavior observed in Fig. 2 was found in all the runs.

The acceleration of the liquid slug was measured by recording the location of the disk as a function of time off the film. A rule attached to the side of the test section was used in taking these measurements. After the measurements were corrected for parallax, the square root of the displacement of the disk from its initial position was plotted versus time. If the acceleration is constant, this data will fall on a straight line. The slope of this line is then proportional to the square root of the acceleration. Figure 3 is a typical plot of these data along with the line fit to this data. The good correlation between the data and the line is an indication that the acceleration is very nearly constant.

A. Plan View. When viewed from the top the instability exhibited several distinct stages of development. With an initially flat interface, a short time after the system was impulsively started purely axisymmetric waves in the form of concentric rings were observed. The first two frames of Fig. 2 give a typical view of this kind of disturbance. These waves continued to grow until a point was reached where azimuthal waves became visible. The third frame of Fig. 2 is a typical view of this stage. As the instability continued to evolve, the troughs of the waves began to form into bubbles, and at this point the surface structure degenerated to a point where symmetry was lost. This stage is characterized by the radial waves (rings) becoming wavy or noncircular. Additionally, as the bubbles evolved, some grew at the expense of others so that the number of radial waves contained in the tube appeared to decrease. Finally, as the instability was viewed in its later stages, the periodicity of the phenomena vanished, and the system became one of apparent chaos.

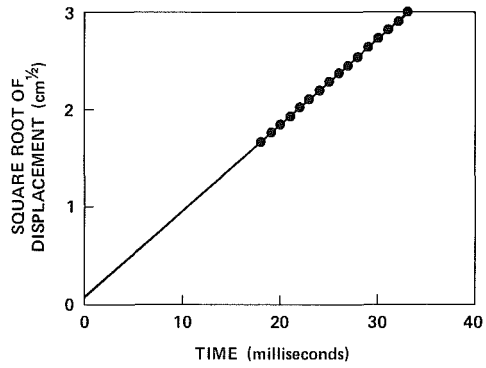

Fig. 3 Typical plot of the square root of disk displacement

Some observations of the runs made in this investigation are summarized in Table 1. Given in this table are approximate times of onset of the different regimes mentioned above. These values represent the time elapsed from the start to the instant the new stage of development first became evident. The observed transitions were not always sharp so that these numbers are very rough. There are large differences in this data between the runs when the liquid depth was varied which intuitively should not occur. The time of appearance of the radial waves should not be affected by liquid depth. Even the shallowest liquid layer used in this situation can be assumed to be of infinite depth on the basis of linear theory. In addition there is a large difference in the onset times between runs 15 and 19 even though the accelerations of these two runs were very nearly the same and the liquid layer depths were identical. However, since we do not have control over initial disturbances it is possible that the differences in the onset times are due to the fact that different runs contained initial disturbances of largely different amplitude. Nevertheless, when looking at the runs for which acceleration is varied, the times behave as would be expected, decreasing as acceleration is increased.

Table 1 also contains measured values of the number of radial and azimuthal waves observed in each run. Here m is the number of complete radial waves counted from the center to the wall along a radius and n is the number of azimuthal waves counted in a complete circle at a fixed radius. The letter

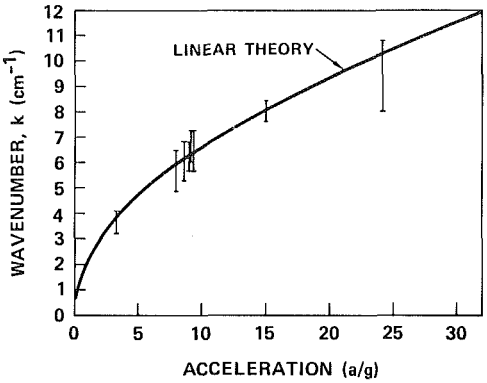

Fig. 4 Measured wave number plotted along with the curve for the fastest growing wave number found from linear theory

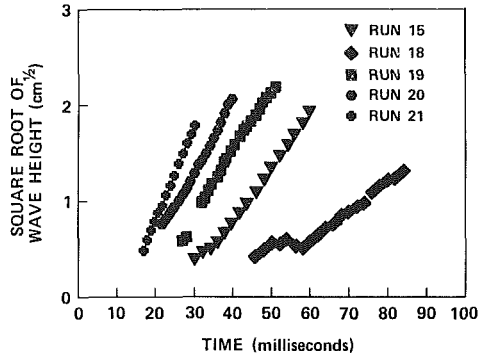

Fig. 5 Square root of the disturbance height for the runs with a liquid depth of 15 cm

"o" refers to the number of azimuthal waves counted on the outermost ring ($r=R$) and "i" refers to the number at some intermediate radius ($r\cong R/2$). The error in these measurements is indicated by the fact that the observed wave lengths were not uniform. For the case of radial waves, different numbers were obtained by counting along different radii. As for the azimuthal waves, for much of the time the view was such that sharp definition was lacking in a complete circle so that these numbers are largely estimates.

In the runs with either low acceleration or small liquid depth the unstable disturbance was predominantly confined to the region near the tube wall. In runs 13 and 18 the radial waves never reached appreciable size in the center portion of the tube. Thus, the measurements for m in these runs are estimates. In addition, for the cases of low acceleration and small depth, the azimuthal waves only appear adjacent to the wall. As depth or acceleration was increased the wave structure became homogeneous throughout the tube cross-section. It is not clear what causes this behavior; however, these results are consistent with observations made by Emmons et al. [2]. In their experiments Emmons et al. made a few runs in which they induced no initial perturbation. In those runs they observed that the disturbance that evolved was primarily confined to the edges of their enclosure. Since they made no runs with acceleration greater than approximately 6 g their experiments qualify as being of low acceleration in terms of our present experiments.

We have stated that according to linear theory the solution for surface shape has the form

$$\eta=\sum_k\sum_n A(k,n)e^{\sigma t}\cos(n\theta)J_n(kr) \tag{7}$$

where the summations are over sequences of n and k satisfying a periodicity condition in θ and a boundary condition at $r=R$. Further, provided that the initial perturbation can reasonably be described as white noise of infinitesimal amplitude, at a time sufficiently large the solution can be approximated by

$$\eta=A(t)\ \cos\ (n\theta)J_n(kr) \tag{8}$$

where the values of n and k are such that maximize the growth rate, σ. Equation (7) represents a two parameter family of solutions of which one is singled out as the most likely to dominate the final solution. In every experimental run made we observed that initially the disturbance was purely axisymmetric. This means that in all cases the first disturbance that became visible was a mode in which $n=0$. It is highly unlikely that in all these runs a mode with $n=0$ represented the component with the largest growth rate. On the contrary given any set of parameter values it is usually the case that a mode with $n\neq 0$ can be found with a corresponding growth rate larger than all possible modes with $n=0$. A likely explanation for this absence of azimuthal waves is that in our experiments the nonaxisymmetric modes may have been missing (or at least present but with amplitudes much smaller than the axisymmetric modes) from the initial perturbations. Another explanation is that nonlinear effects may have become important prior to the time that the instability first became visible.

Wave numbers of the observed axisymmetric disturbances can easily be calculated from the data in Table 1 and using equation (6). In Fig. 4 this wave number data are plotted versus acceleration. Figure 4 also contains a curve representing the fastest growing wave number calculated using equation (3). As can be seen, the measured wave numbers agree very well with what is predicted by linear theory. Thus, although the initial instability we observed appeared to be restricted in some way (i.e., not as general as predicted by linear theory), the wave numbers selected correspond well with the fastest growing wave numbers. This implies that the assumption that there is an equal opportunity for initial disturbances of all wave numbers to develop is satisfied at least for the case of axisymmetric modes.

In runs where the azimuthal waves appeared uniformly over the surface, the value of n decreased as radius decreased. In fact, it appeared that the wave lengths of these disturbances, not their number, was more or less constant. This observation is in disagreement with linear theory which gives, according to equation (8), a fixed value of n. However, in the linear solution the radial dependence is affected by the value of n. In our experiments we initially saw a purely axisymmetric wave form so that the radial dependence was then fixed in terms of J_0. When the azimuthal waves appeared it was too late to change the radial structure. If waves of large n were superposed on the initial axisymmetric waveform, it would mean that the effective azimuthal wave lengths would be very short near the center and thus below the cutoff wave length. This effect is accounted for in the linear solution by the fact that, for large n and small r, $J_n(kr)<<1$. Also the effective wave lengths in $J_n(kr)$ increase as n increases.

Linear theory falls short of explaining some important aspects of our experimental observations. Clearly a nonlinear analysis is needed to predict the appearance of the azimuthal disturbances we observed. This could have been guessed beforehand from the fact that the initial axisymmetric disturbances have grown to appreciable size before the azimuthal waves first appear. In addition, it is possible that the transition from a purely axisymmetric disturbance to a fully three-dimensional one represents a bifurcation in the associated stability problem. Further investigation into these nonlinear topics would certainly aid in the understanding of these phenomena.

B. Side View. The most interesting side views of the instability occur later in the run. The last two frames of Fig. 2 are typical of this stage. At this point the axial ring-like waves have evolved into concentric cylindrical sheets. These are the three-dimensional analogs to the "spikes" described in ex-

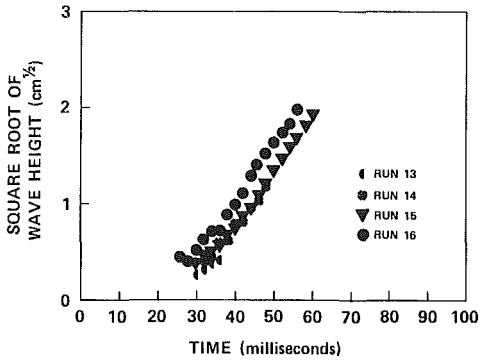

Fig. 6 Square root of the disturbance height for the runs accelerated at approximately 10 g

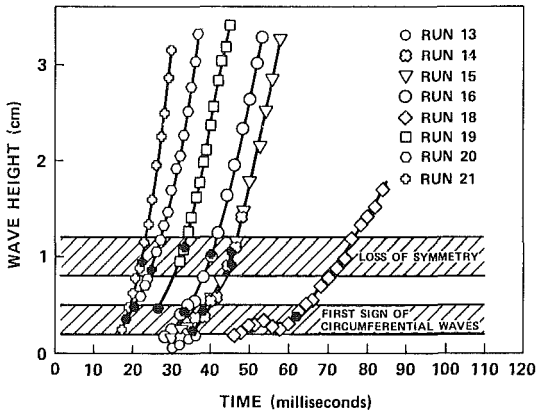

Fig. 7 Planform transition points plotted on the disturbance height curves

periments dealing with the two-dimensional phenomenon. In close examination of these pictures it appears that the azimuthal waves are predominantly confined to the troughs or bubbles of the axial disturbances. Not much azimuthal dependence is evident in the spike portion of the instability in this view. In addition, the outermost trough is seen to be much larger than its interior counterparts. This is obviously due to the effect of the tube wall on the instability.

The displacement of the free surface from its original planar position can be found by taking the difference between the measured displacement of the disk and the distance traveled by the position of interest on the free surface. This method was used along with measurements taken from the film to obtain wave heights. However, error in these results may be substantial due to the fact that in this method two fairly large measurements with associated error are subtracted to obtain a small result. Thus, measurements of wave height when the disturbance amplitudes are very small (less than 2 mm) will not be very accurate.

Figure 5 is a plot of the square root of wave height versus time for the runs where liquid depth was 15 cm. The heights represent the amount by which a selected wave extends above the initially flat interface. In each run the wave we chose to measure was one which was clearly defined on the film and thus was easy to measure throughout its development. In these measurements the error bounds are approximately $\pm$ 2 mm, thus the earliest measurements are not very accurate. In addition, there is error in the measurement of time associated with the inaccuracy in the determination of the instant the process began. This error is estimated to be $\pm$ 2 ms. The first thing one may notice in Fig. 5 is that the trajectories plotted are nicely arranged in order of decreasing acceleration which should be expected. However, one bothersome point is that the spacing between these curves is not consistent. The differences between the wave heights of runs 15 and 19 is considerable; however these runs were accelerated at very closely the same rate (8.6 g and 9.1 g, respectively). This fact is not consistent with the relative spacings between other runs (such as runs 19 and 20 where accelerations were 9.1 g and 15 g, respectively). These inconsistencies agree with the observations in the previous section regarding the relative times at which processes become noticeable. The explanation given there is applicable here; that is, because we have relinquished control over initial disturbances in these experiments we must accept the fact that large discrepancies (i.e., scatter) may occur in growth rate results.

Figure 6 is a plot of the square root of wave height versus time for the runs where the acceleration was approximately constant and the liquid depth was varied. In this plot it appears that there might be a weak connection between growth rate and liquid depth with which growth rate increases with depth. However, because of the apparent scatter observed in Fig. 5 this conclusion cannot be made. In both Figs. 5 and 6 the trajectories approach straight lines as time increases. This corresponds to the wave crests accelerating at a constant rate. This behavior has been observed by previous experimenters and can as well be predicted by theory (when surface tension is neglected). The slopes of these lines can be measured to obtain estimates of the value of acceleration. This was done and we found that the spike acceleration was approximately 80 percent of the acceleration of the liquid slug for all runs made except for run 18. In this run the spike acceleration turned out to be approximately 30 percent of the slug acceleration. Thus, in the later stages of most of the runs made the spikes were very nearly in free fall. The exception was the run of lowest acceleration. Emmons et al. [2] performed their experiments with accelerations in the range of 2 g to 6 g and found that in the latter stages of development their spikes were accelerating at roughly 1/3 free fall. This is consistent with our result for run 18.

The wave height curve for run 18 is odd in that it has a dip in it very early in its growth. Since the wave height is so small in the neighborhood of this point, it is not clear whether this peculiarity is real or whether it is the result of error in taking measurements.

Figure 7 is a plot of wave height versus time for all the runs in Table 1. On each curve is marked the approximate location of the first two transitions noted in the previous section. The solid hexagons mark the points of first appearance of azimuthal waves. The solid crosses mark the location where the rings started to lose their circular form and become distorted. The corresponding wave heights at these points can easily be ascertained. It is apparent that these transitions are correlated very nicely in terms of wave height. The transition points fall into bands of wave height which does not occur when correlating in terms of transition time. Thus, for the experiments run in this investigation, the transition from a purely axisymmetric disturbance to one with azimuthal dependence occurs when the wave crests reach a height of approximately 2 mm to 5 mm. Likewise the degeneration of the symmetric circular structure occurs when the instability waves reach a height of approximately 0.8 to 1.2 centimeters. The next transition (transition to chaos) occurs after the point of termination of wave height measurements; however, if these measurements are extrapolated this process can be found to occur when wave height reaches approximately 4 to 7 centimeters.

V Conclusions

We have investigated experimentally the Rayleigh-Taylor instability of an air-water system in a circular tube. The system was not artificially given an initial disturbance so that precise initial conditions could not be determined. This lack of data is a shortcoming in that certain types of quantitative information cannot be obtained from our experiments. In particular,

we have seen that uncertainties with the initial conditions have led to inconsistencies in our measurements of wave heights as functions of time. Nevertheless, some quantitative as well as a lot of interesting qualitative information has been obtained.

We have found that in the absence of artificially induced initial free surface shape a purely axisymmetric disturbance first develops. Although the disturbance is not as general as the exact solutions found from linear theory, the measured wave numbers are in good agreement with the fastest growing wave numbers obtained from that analysis. We have also observed the evolution of the instability to higher levels of complexity. We have broken this process into four regimes: axisymmetric, fully three-dimensional, nonsymmetrical but still periodic, and chaotic. We have recorded the approximate locations of the transitions from one regime to the next. The first transition is fairly sharp and because of this fact may be an indication of a bifurcation phenomena; however, the next two transitions are not so distinct. Finally, we have found that these transitions points can be correlated fairly well by considering the disturbance amplitude associated with the time of transition from one regime to the next.

Acknowledgments

The authors gratefully acknowledge the financial support provided by the National Science Foundation, No. MEA 81-05542. We would also like to acknowledge James I. Jenkins who had the major role in the design and construction of the experimental apparatus.

References

1 Chandrasekhar, S., *Hydrodynamic and Hydromagnetic Stability*, Clarendon Press, Oxford, England, 1960, Chapter X.

2 Emmons, H. W., Chang, C. T., and Watson, B. C., "Taylor Instability of Finite Surface Waves," *J. Fluid Mech.*, Vol. 17, 1960, p. 177.

3 Rajappa, N. R., "Non-Linear Theory of Taylor Instability of Superposed Fluids," *J. Phys. Soc., Japan*, Vol. 28, 1970, p. 219.

4 Rajappa, N. R., "On the Instability of Fluid Surfaces When Accelerated Perpendicular to Their Planes," *Acta Mechanica*, Vol. 10, 1970, p. 193.

5 Nayfeh, A. H., "On the Non-Linear Lamb-Taylor Instability," *J. Fluid Mech.*, Vol. 38, 1969, p. 619.

6 Kiang, R. L., "Nonlinear Theory of Inviscid Taylor Instability Near the Cutoff Wavenumber," *Phys. Fluids*, Vol. 12, 1969, p. 1333.

7 Lewis, D. J., "The Instability of Liquid Surfaces When Accelerated in a Direction Perpendicular to their Planes. II," *Proc. Roy. Soc.*, Series A 202, 1950, p. 81.

8 Allred, J. C., and Blount, G. H., "Experimental Studies of Taylor Instability," Los Alamos Scientific Laboratory Report LA-1600, 1954.

9 Ratafia, M., "Experimental Investigation of Rayleigh-Taylor Instability," *Phys. Fluids*, Vol. 16, 1973, p. 1207.

10 Cole, R. L., and Tankin, R. S., "Experimental Study of Taylor Instability," *Phys. Fluids*, Vol. 16, 1973, p. 1810.

11 Popil, R., and Curzon, F. L., "Climbing Water Films in Experiments on Rayleigh-Taylor Instabilities," *Phys. Fluids*, Vol. 23, 1980, p. 1718.

Numerical Solution of Two-Dimensional Turbulent Separated Flows Using a Reynolds Stress Closure Model

M. C. Celenligil
Department of Aeronautics,
Imperial College,
London SW7 2BY, England

G. L. Mellor
Professor,
Mechanical and Aerospace Engineering Department,
Princeton University,
Princeton, N.J. 08544
Mem. ASME

Turbulent boundary layer separation is studied using the turbulence closure model suggested by Mellor and Yamada. An explicit central finite-differencing scheme is used to solve the governing transport equations. Three flow problems are considered: separation on a flat surface, separation and reattachment over a backward-facing step, and turbulent free shear layer with streamwise curvature. In the problem of separation behind a backward-facing step, nearly cyclic vortex shedding is obtained whereas the other two problems are stationary. The computed results for both mean and turbulence quantities are in fairly good agreement with experimental data.

Introduction

Separation of turbulent boundary layers is observed in many fluid devices such as airfoils, diffusers, and turbomachines. Flow separation produces significant losses in the performance of the machines and naturally has been of great interest to engineers for many years. In the separation zone the mean flow changes direction, requiring the use of directionally-sensitive instruments for reliable measurements. Unfortunately, most of the well-established techniques such as hot-wires are not directionally-sensitive limiting their use to measurements taken before separation. However, useful experimental information in the separation zone has become available with the introduction of the laser-Doppler anemometry.

Theoretical studies of turbulent separated flows are not easy. Turbulence is, itself, complicated and the problem becomes more difficult with flow separation. For example, the boundary-layer equations are not valid for separated flows, nor does the law-of-the-wall hold near the separation point. Separation also prevents the application of some turbulence closure models which are widely used for simpler flows. Close to the separation region the experimentally observed mixing lengths [1-3] become smaller than those predicted by mixing length models and in the separation region the eddy viscosity can be negative.

In this study, the full Reynolds stress closure model suggested by Mellor [4] and by Mellor and Yamada [5] is applied to two-dimensional (planar), incompressible turbulent separated flows. Three flow problems are considered. In the first problem, separation on a flat surface is studied. The flow is stationary and the prevailing pressure gradient is the most important factor in the determination of the overall flow configuration. In the second problem, separation and reattachment behind a backward-facing step is studied. In this problem nearly cyclic vortex shedding is obtained. In the third problem, a free shear layer with streamwise curvature is studied. In this problem separation is prevented by boundary layer suction. The flow is stationary and is like a jet near the walls.

For the three problems under study, the turbulence model and the modeling constants are not modified. The results are compared with the experimental data presented at the 1980-81 AFOSR-HTTM-Stanford Conference on Complex Turbulent Flows, Comparison of Computation and Experiment [6].

The Governing Differential Equations

In this study, the vorticity-stream function approach is used. The ensemble mean stream function equation,

$$\frac{\partial^2\psi}{\partial x^2}+\frac{\partial^2\psi}{\partial y^2}=-\xi, \tag{1}$$

is obtained from the definition of the stream function $(U, V) \equiv (\partial\psi/\partial y, -\partial\psi/\partial x)$ and the mean vorticity, $\xi \equiv \partial U/\partial y - \partial V/\partial x$; (U, V) is the mean velocity vector. The transport equation for the mean vorticity,

$$\frac{D\xi}{Dt}=\frac{\partial^2(-\overline{uv})}{\partial x^2}-\frac{\partial^2(\overline{v^2}-\overline{u^2})}{\partial x\partial y}-\frac{\partial^2(-\overline{uv})}{\partial y^2}, \tag{2}$$

is derived by taking the curl of the mean momentum equation. The material derivative, $D(\ )/Dt \equiv \partial(\ )/\partial t + U\partial(\ )/\partial x + V\partial(\ )/\partial y$, contains the local time derivative and the advective space derivatives.

For the Reynolds stresses that appear in equation (2), we use the closure model suggested by Mellor et al. [4, 5]:

Contributed by the Fluids Engineering Division for publication in the JOURNAL OF FLUIDS ENGINEERING. Manuscript received by the Fluids Engineering Division, December 13, 1982.

$$\begin{bmatrix} \frac{D\overline{u^2}}{Dt} \\ \frac{D\overline{v^2}}{Dt} \\ \frac{D\overline{\omega^2}}{Dt} \\ \frac{D\overline{uv}}{Dt} \end{bmatrix} = \frac{\partial}{\partial x} K \begin{bmatrix} 3\frac{\partial \overline{u^2}}{\partial x} \\ \frac{\partial \overline{v^2}}{\partial x} + 2\frac{\partial \overline{uv}}{\partial y} \\ \frac{\partial \overline{\omega^2}}{\partial x} \\ \frac{\partial \overline{u^2}}{\partial y} + 2\frac{\partial \overline{uv}}{\partial x} \end{bmatrix} + \frac{\partial}{\partial y} K \begin{bmatrix} \frac{\partial \overline{u^2}}{\partial y} + 2\frac{\partial \overline{uv}}{\partial x} \\ 3\frac{\partial \overline{v^2}}{\partial y} \\ \frac{\partial \overline{w^2}}{\partial y} \\ \frac{\partial \overline{v^2}}{\partial x} + 2\frac{\partial \overline{uv}}{\partial y} \end{bmatrix} - \frac{q}{3A_1 l} \begin{bmatrix} \overline{u^2} - \frac{q^2}{3} \\ \overline{v^2} - \frac{q^2}{3} \\ \overline{\omega^2} - \frac{q^2}{3} \\ \overline{uv} \end{bmatrix}$$

$$+ C_1 q^2 \begin{bmatrix} 2\frac{\partial U}{\partial x} \\ 2\frac{\partial V}{\partial y} \\ 0 \\ \frac{\partial U}{\partial y} + \frac{\partial V}{\partial x} \end{bmatrix} + \begin{bmatrix} -2\overline{u^2}\frac{\partial U}{\partial x} - 2\overline{uv}\frac{\partial U}{\partial y} \\ -2\overline{uv}\frac{\partial V}{\partial x} - 2\overline{v^2}\frac{\partial V}{\partial y} \\ 0 \\ -\overline{u^2}\frac{\partial V}{\partial x} - \overline{v^2}\frac{\partial U}{\partial y} \end{bmatrix} - \frac{2}{3}\frac{q^3}{B_1 l} \begin{bmatrix} 1 \\ 1 \\ 1 \\ 0 \end{bmatrix} \tag{3}$$

where we define $K \equiv 3lqS_q/5$, $q^2 \equiv \overline{u^2} + \overline{v^2} + \overline{w^2}$, $A_1 = 0.92$, $B_1 = 16.6$, $C_1 = 0.08$ and $S_q = 0.2$.

The length scale, l, in equation (3) is modeled by another transport equation,

$$\frac{D(q^2 l)}{Dt} = \frac{\partial}{\partial x}\left[qlS_l \frac{\partial (q^2 l)}{\partial x}\right] + \frac{\partial}{\partial y}\left[qlS_l \frac{\partial (q^2 l)}{\partial y}\right] - \frac{q^3}{B_1}\left[1 + E_2\left(\frac{l}{\kappa L}\right)^2\right] + E_1 l\left[-\overline{uv}\left(\frac{\partial U}{\partial y} + \frac{\partial V}{\partial x}\right) - \overline{u^2}\frac{\partial U}{\partial x} - \overline{v^2}\frac{\partial V}{\partial y}\right], \tag{4}$$

where a wall proximity length scale, L, is defined according to

$$L^{-1}(\mathbf{x}) \equiv \frac{1}{\pi}\oint \frac{ds}{|\mathbf{x} - \mathbf{x}_w|^2}, \tag{5}$$

$\mathbf{x}$ is any point in the fluid domain bounded by solid wall at $\mathbf{x}_w$, and $ds = |d\mathbf{x}_w|$. The modeling constants in equation (4) are $E_1 = 1.8$, $E_2 = 1.33$, $S_l = 0.2$; $\kappa = 0.41$ is Von Karman's constant.

Numerical Technique

The local time derivative and advective space derivative parts of the left sides of (2)–(4) are differenced by explicit central differencing and leapfrog schemes respectively. Equation (1) is also centrally differenced and is solved using an alternating-direction implicit (ADI) method.

Initially, the flow is irrotational and the Reynolds stresses and length scale are set to small arbitrary values. Then (2)–(4) are used to update the vorticity, stress components and length scale to the next time level. Boundary values will be stipulated in the following discussion for each of the three problems. After the updated vorticity distribution is obtained, equation (1) is solved for the stream function. The time stepping process is repeated until either a steady-state solution or cyclically repeating solutions are obtained.

Nomenclature

A_1, B_1, C_1 = modeling constants
B^+ = parameter used in wall layer model
C_{f0} = skin friction coefficient ($= \tau_w / \frac{1}{2}\rho U_0^2$)
C_f = skin friction coefficient ($= \tau_w / \frac{1}{2}\rho U_\infty^2$)
C_P = static pressure coefficient, $(P - P_0)/\frac{1}{2}\rho U_0^2$
$D(\ )/Dt$ = material derivative
E_1, E_2 = modeling constants
f = frequency
H = reference length, m
L = wall proximity function
l = turbulence length scale
P = static pressure
P_0 = static pressure at the entrance
q^2 = twice the turbulent kinetic energy
S_l, S_q = modeling constants
T = nondimensional time
U, V = mean velocities
u, v, w = fluctuating velocities
u', v', w' = turbulence intensities, $(u' = \sqrt{\overline{u^2}})$
u_τ = friction velocity, $(= \sqrt{|\tau_w|/\rho})$
U_0 = reference velocity, m/s
U_∞ = freestream velocity
$\mathbf{x}$ = position vector
x_R = reattachment location
α = parameter used in wall layer model
β = corner vorticity parameter
δ = boundary layer thickness
κ = Von Karman constant, (=0.41)
ν = kinematic viscosity
ξ = vorticity
ξ_c = corner vorticity
ρ = density
τ = total shear stress
τ_w = shear stress at the wall
ψ = stream function
$< >$ = notation for cycle averaged quantities

To maintain computational stability, an explicit diffusion is added to the transport equations. This is a fraction of the artificial diffusion term inherent in the upwind forward scheme. In each flow problem, the minimum value is used for this fraction which introduces artificial viscosities of the order of Δx^2 and Δy^2, respectively, and the second order accuracy of the scheme is preserved (p. 66 [7]).

Turbulent Boundary Layer Separation on a Flat Surface

Although flow separation on a flat surface is the simplest geometry to study, until recently very little quantitative information has been available due to lack of proper instrumentation. Recently Simpson et al. [1–3] obtained useful data in the separation zone using directionally-sensitive laser-Doppler anemometry. The schematic sideview of the wind tunnel they used in their experiments is shown in Fig. 1. At sections A, B, and C there is boundary layer suction and high momentum fluid supply to prevent separation at the top wall.

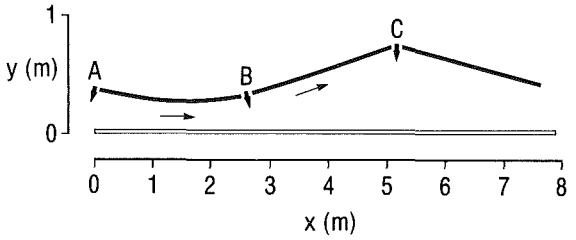

Fig. 1 Schematic of experimental apparatus

Computations for this case were on a 45×45 grid located between $x = 2.197$ m and $x = 4.34$ m in the horizontal direction and between $y = 0$ and $y = 0.328$ m in the vertical direction. The purpose of the computations was to simulate the flow structure of the turbulent boundary layer under the effect of an adverse pressure gradient. Therefore, experimental data were used only in defining the entrance conditions and for specifying the freestream velocity at the top boundary. At the entrance section, ξ (assuming $\partial V/\partial x = 0$), ψ, $\overline{u^2}$, $\overline{v^2}$ and $\overline{uv}$ were obtained from the data. Since data were not available for $\overline{w^2}$ and l, $\overline{w^2}$ was assumed to be $\overline{w^2} = \overline{v^2}$ and l was obtained by assuming an equilibrium turbulent boundary layer at the entrance. At the exit section, we let $\partial^2\psi/\partial x^2 = 0$, $\partial\xi/\partial x = 0$, $\partial \overline{u_i u_j}/\partial x = 0$ and $\partial q^2 l/\partial x = 0$. At the wall, $\psi = l = 0$; Neuman boundary conditions, $\partial\overline{u^2}/\partial y = \partial\overline{v^2}/\partial y = \partial\overline{w^2}/\partial y = 0$, were used for the turbulence intensities. At the top open boundary $\partial\xi/\partial y = 0$, $\partial \overline{u_i u_j}/\partial y = 0$, $\partial q^2 l/\partial y = 0$ boundary conditions were used and the freestream velocity was obtained from the data.

The turbulence model does not include the viscous sublayer, i.e., the model calculates the "outer function" which must be matched to an "inner wall function" which, in the case of non-separating flows, is the law-of-the-wall. The numerical mechanics are that, given a calculated velocity, U, at the point nearest the wall, y, the wall function must supply the wall shear stress. Although the straight law-of-the-wall function does work operationally we have found that the wall model suggested by Mellor [8][1] yields results in closer agreement with data. This model had been shown to compare well with data close to separation; its capability of coping with fully separated flow has not been established.

The model may be cast in the form $U/u_\tau = f(yu_\tau/\nu, \tau/\tau_w)$ where τ_w is the wall (kinematic) stress ($|\tau_w| = u_\tau^2$) and U and τ are the mean velocity and stress at y. Specifically, outside of the viscous sublayer the model yields when τ_w and τ have the same sign:

$$\frac{U}{u_\tau \text{sign}(\tau_w)} = B^+ + \frac{1}{\kappa}\ln\left[\frac{yu_\tau}{\nu}\frac{4}{\left\{\left|\frac{\tau}{\tau_w}\right|^{1/2}+1\right\}^2}\right] + \frac{2}{\kappa}\left[\left|\frac{\tau}{\tau_w}\right|^{1/2}-1\right], \quad (6)$$

or when τ_w and τ have opposite signs:

$$\frac{U}{u_\tau \text{sign}(\tau_w)} = B^+ - \frac{2}{\kappa}\left[\left|\frac{\tau}{\tau_w}\right|^{1/2}+1\right] + \frac{1}{\kappa}\ln\left[\frac{yu_\tau}{\nu}\frac{4}{\left|\frac{\tau}{\tau_w}\right|+1}\right] + \frac{2}{\kappa}\tan^{-1}\sqrt{\left|\frac{\tau}{\tau_w}\right|}, \quad (7)$$

where $\text{sign}(\tau_w) \equiv \tau_w/|\tau_w|$ and B^+ depends on the nondimensional parameter $\alpha \equiv (\tau/\tau_w - 1)/(yu_\tau/\nu)$. As $\tau/\tau_w \to 1$, the wall model asymptotes to the conventional law-of-the-wall relation. Also $B^+ \to 4.9$ as $\tau/\tau_w \to 1$.

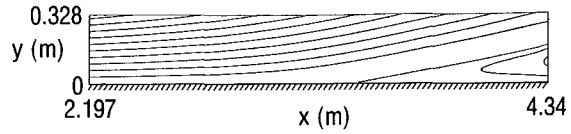

Fig. 2 The streamlines for the separated flow on a flat surface

By numerically integrating the transport equations for a time $\sim 40\ H/U_0$ ($H = 2$ m, $U_0 = 20.43$ m/sec) a stationary, separated flow configuration is obtained. The streamlines of the stationary flow are shown in Fig. 2. The mean velocity U, turbulence intensity u', turbulent shear stress uv are plotted in Fig. 3, 4 and 5, respectively. The measured boundary layer thicknesses are marked at each location. The skin friction coefficient, $C_f = \tau_w/\frac{1}{2}\rho U_\infty^2$, is plotted in Fig. 6. All of these quantities are nondimensionalized with respect to the *local* freestream velocities.

The detachment point which is defined as the location where C_f is zero is around $x = 3.267$ m. In the experimental data, the location where C_f is zero is not available and reliable C_f data were originally presented only upto $x = 3.048$ m. This is due to the fact that C_f data, obtained by Simpson et al. [9] using the law-of-the-wall, were not considered reliable and were excluded from the Stanford data set. However, the C_f values were small as are the values that one would roughly obtain from Fig. 6. Subsequently, Simpson [10] deduced a C_f value in the separated region and this is also included in Fig. 6 where $x = 4.34$ m.

The deviation of the computed results from the experimental data in the region close to the exit section is caused partly by the coarseness of the mesh and partly by the exit boundary conditions. We have, however, tried several different boundary conditions at the exit section. The experimental data was used as the exit boundary condition for the stream function. The results were very close to the previous results except near the exit section where comparison with the data was less favorable. In one of our runs, we reduced the backflow velocities at the exit by half; but this had very little effect on the results in the separation region away from the exit section. This supports the hypothesis that the reverse flow in the

[1] This wall layer model is based on an effective viscosity which asymptotes to the molecular viscosity near the wall and the Prandtl relation $\kappa^2 y^2 |dU/dy|$ far from the wall and a linear variation of the total shear stress close to the wall. It may also be shown that equations (3) and (4) asymptote to the Prandtl relation close to wall. Thus, in the parlance of singular perturbation theory, we numerically calculate the outer function which is matched to an inner, analytical function represented by equations (6) and (7).

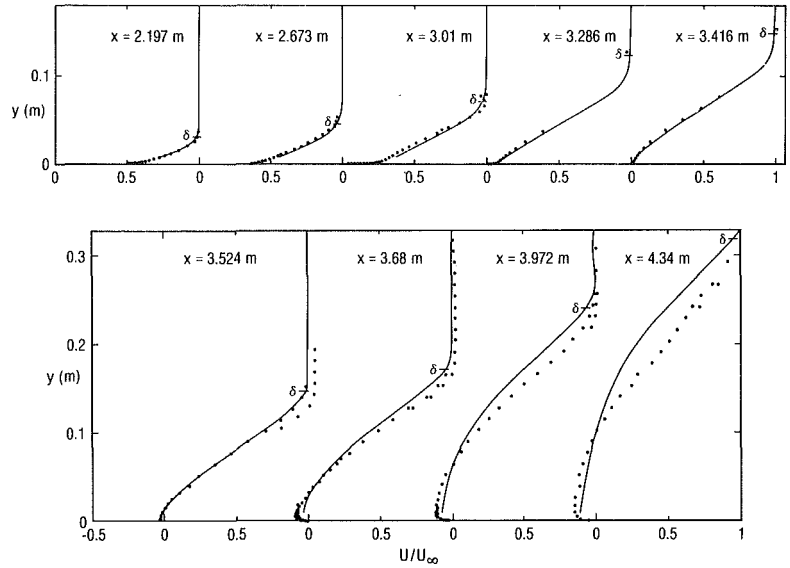

Fig. 3 U/U_∞ profiles at various locations

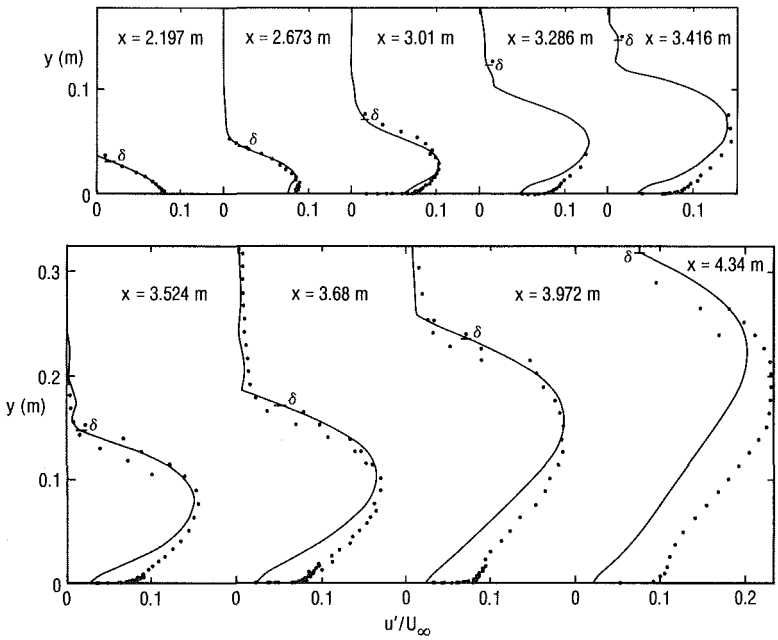

Fig. 4 u'/U_∞ profiles at various locations

separation region is not unduly sensitive to disturbances in the mean backflow far downstream as had been demonstrated experimentally by Simpson et al.

The results are found to be insensitive to various wall boundary conditions for the turbulence intensities, u', v', w'. However, the results improved considerably when the wall shear stress is obtained using the modified wall layer model $U/u_\tau = f(yu_\tau/\nu, \tau/\tau_w)$ instead of the conventional logarithmic law-of-the-wall. When the latter is used, the detachment point is moved upstream 16 percent of the length of our computational domain.

Our results are found to be sensitive to the prevailing external pressure gradient. It is found that perturbing the freestream velocity distribution by 5 percent can move the separation point downstream 25 percent of the length of the computational domain. No other boundary conditions exerted this much effect on the results.

As can be seen from Figs. 3, 5, and 6, the mean flow and uv are predicted fairly well whereas the u' in Fig. 4 shows deviations from the experimental data close to the wall and near the exit. In order to improve the results, the mesh size was reduced by one half, but this changed the results very little. A staggered mesh system with an equal number of grid points in the entrance and exit boundary layers is unsuitable for the elliptic scheme used, as δ grows by a factor of 10 requiring very small Δy near the entrance and hence very small Δt for computational stability.

Recently, Simpson [10] has correlated his near wall velocity data downstream of separation in the form, $U/|U_N| = f(y/N)$, where U_N is the maximum backflow velocity and N is the distance from the wall to the maximum velocity. Figure 7 is Simpson's data correlation. The dashed line is equations (6) and (7) whereas the solid line is a numerical solution which extends through the viscous region to the wall as described by Mellor [8]. The case plotted is for $\alpha = -0.1$. There is a difference between the correlation and the model in the range $0.02 < y/N < 0.5$ such that, for a given $U/|U_N|$, the value of the calculated y/N is about twice the observational value. This would indicate that the wall model provides the values of τ_w that are small by roughly a factor of two. This error only

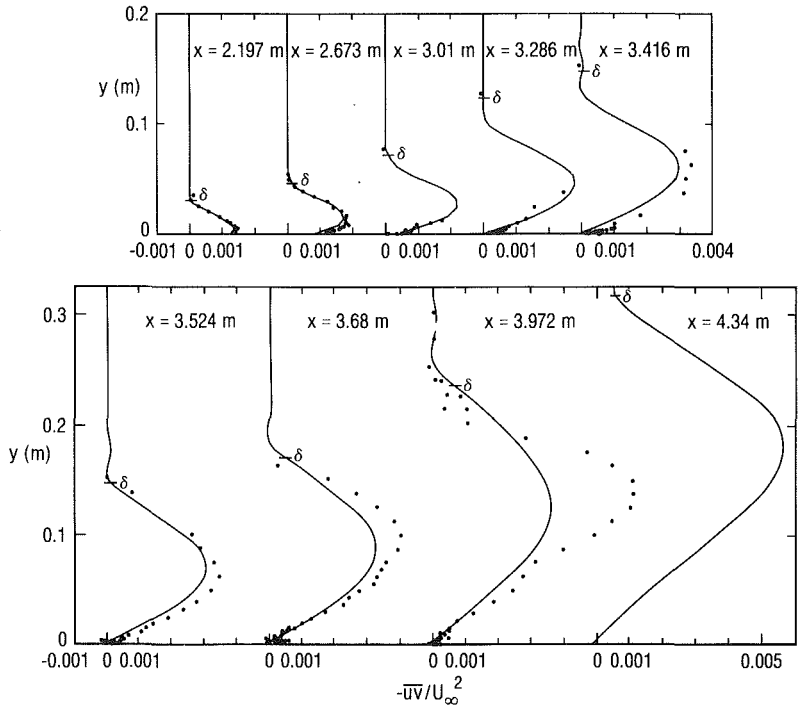

Fig. 5 $-\overline{uv}/U_\infty^2$ profiles at various locations

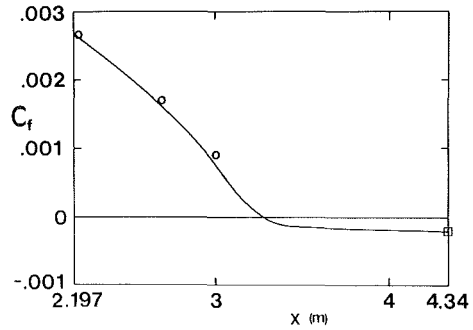

Fig. 6 C_f distribution. The positive data (shown with circles) are from [1], whereas the negative datum (shown by a square) is from [10].

prevails for "large" values of α where τ_w is small. With the help of Simpson's data, it seems likely that the wall model can be improved in the future.

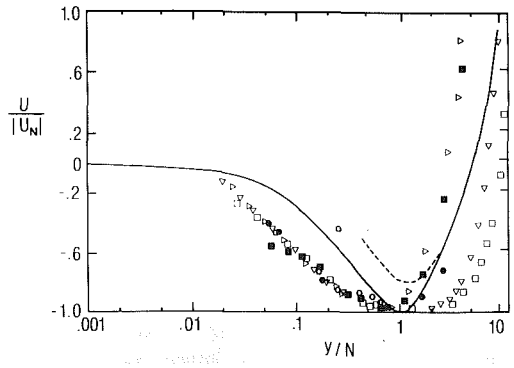

Fig. 7 The data points are Simpson's "universal correlation" of the velocity profile in separated flow. The solid line is numerically calculated according to the wall model of Mellor [8] for a value $\alpha = -0.1$ (an average value for Simpson's separated flow). The dashed line is obtained from (6) and (7).

Separation and Reattachment of Turbulent Flows Over a Backward-Facing Step

The flow over a backward-facing step has been of great importance to aeronautical engineers because of its close connection to the flow about bluff bodies. In the past, there have been a number of experiments performed on low-speed flows over a backward-facing step [11–15]. The data with which we compare our results were obtained by Kim, Kline, and Johnston [14]. The cross-sectional view of the test section is shown in Fig. 8.

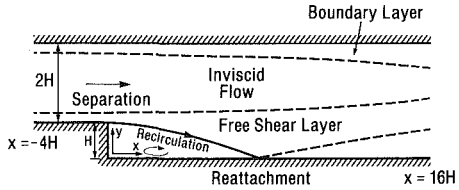

Fig. 8 Side view of the test area

The computations were performed on a 31×31 grid located between $x/H = -4$ and $x/H = 16$ in the horizontal direction and $y = 0$ and $y/H = 3$ in the vertical direction ($U_0 = 18.2$ m/s, $H = 0.0381$ m). The calculations were then repeated using a 61×61 grid with half mesh sizes but very little change was observed.

The boundary conditions are similar to those used in the previous problem. The stream functions on opposite walls differ by an amount determined by volume flow rate. At 90 deg corner, the wall vorticity is evaluated using the method suggested by Briggs et al. [16] which ensures that the streamlines remain parallel to their original direction after leaving a 90 deg corner. The corner vorticity is defined by $\xi_c = -\beta \partial U/\partial y$ where the parameter β is of order 1. β is modified slightly at each time step if the stream function at the first grid point downstream of corner deviates from that at the corner.

In our computations, an unsteady flow structure is obtained and the flow becomes nearly cyclic in time. The nondimensional cycling time is approximately $\Delta T = 10$. The time se-

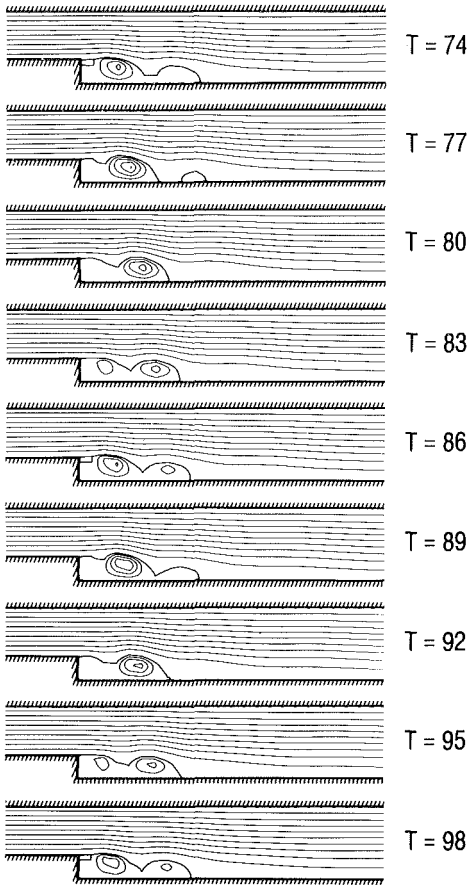

Fig. 9 The streamlines during two cycles. $T = U_0 t/H$ is the nondimensional time.

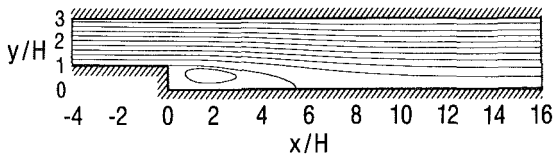

Fig. 10 The averaged streamlines, $<\psi>$

quence of the streamlines during two cycles are shown in Fig. 9. The shedding of vortices during these cycles can also be observed from the vorticity contours (p. 103 [17]).

In order to compare our results with the time averaged experimental data, the computational results are averaged over an integral number of cycles. The cycle averaged quantities are denoted by an angle bracket, e.g., $\langle U \rangle$. Figures 10 and 11 show the streamlines and the mean velocity $\langle U \rangle / U_0$, respectively, after averaging between $T = 170$ and $T = 190$. Clearly, the flow structure returns to ordinary turbulent boundary state quite slowly after reattachment.

For the Reynolds stresses, one has to add $(U_i - \langle U_i \rangle)(U_j - \langle U_j \rangle)$ to $\langle u_i u_j \rangle$ in order to include the effect of mean velocity variations around $\langle U_i \rangle$ to obtain the total values. Figures 12 and 13 show the turbulence intensity $\langle \overline{u^2} \rangle + \langle (U - \langle U \rangle)^2 \rangle$ and the turbulent shear stress $\langle \overline{uv} \rangle + \langle (U - \langle U \rangle)(V - \langle V \rangle) \rangle$ along with $\langle u^2 \rangle$ and $\langle uv \rangle$. It can be seen that the flow unsteadiness makes considerable contribution to the total stresses in the recirculation region downstream of the step. Before the separation and after the reattachment, the flow unsteadiness has very little effect.

The unsteadiness of the flow has been observed in the experiments of Kim et al. [14] also. They reported that the reattachment point moves forward and backward continuously around seven step heights downstream of the step in a fluctuating band of two step heights, i.e., $x_R = 7H \mp H$. In the experiments performed by others [18] the Reynolds stress data shows large scatter in the recirculation region due to flow unsteadiness. Consequently, in the recirculation region reliable data are not available for the Reynolds stresses, and no data are shown at $x/H = 1.333, 2.667, 5.333$ in Figs. 12 and 13.

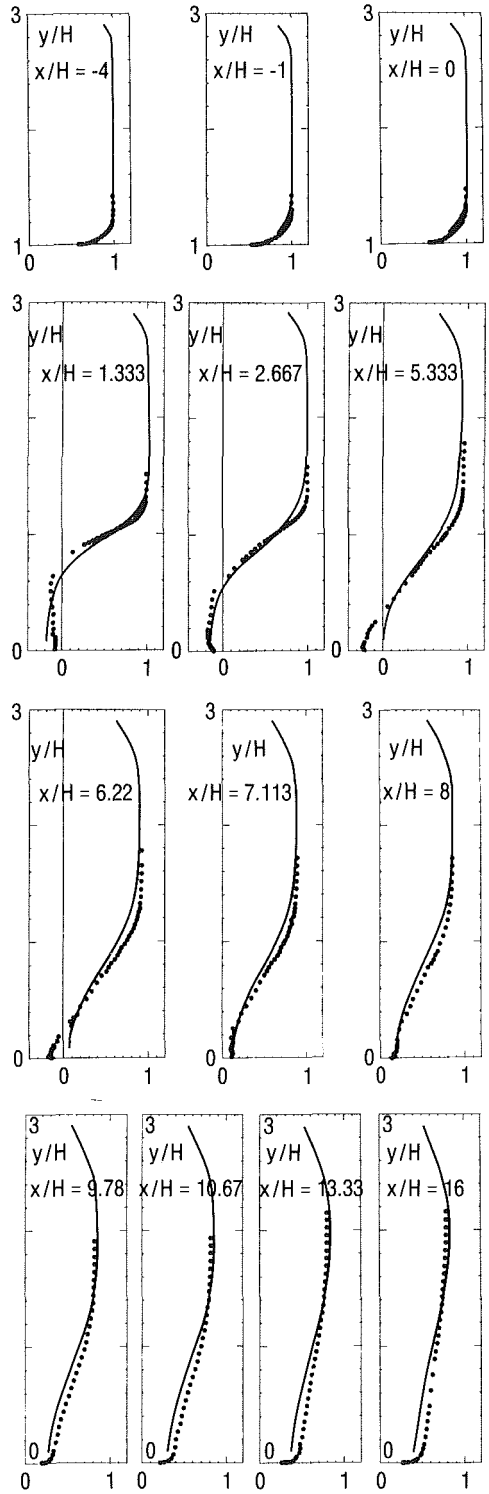

Fig. 11 $<U>/U_0$ at various locations

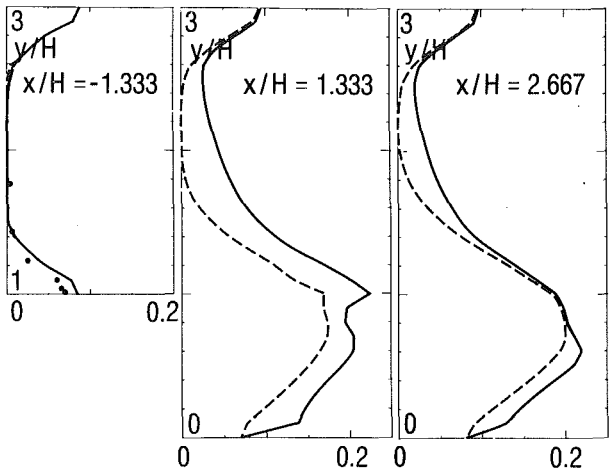

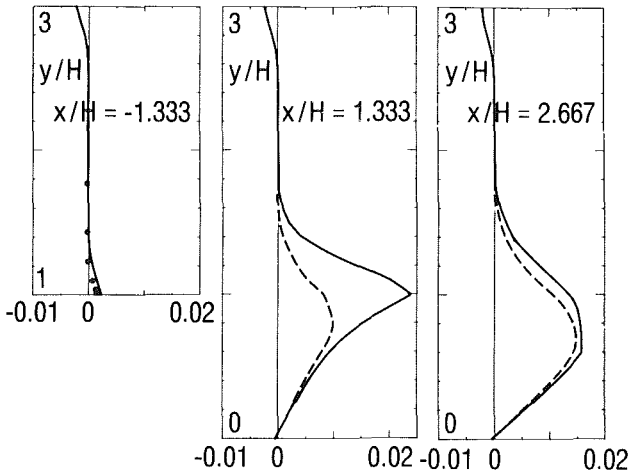

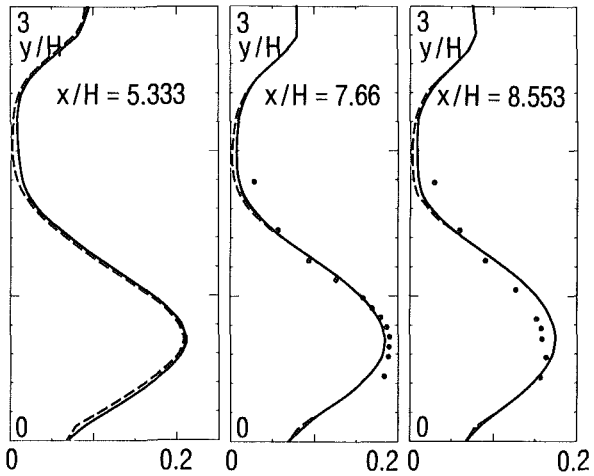

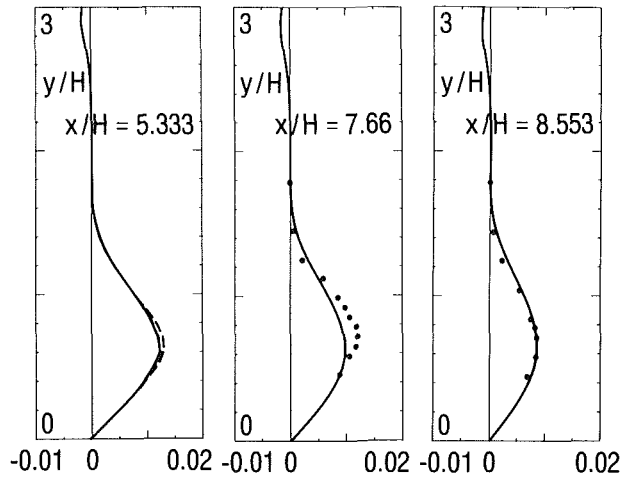

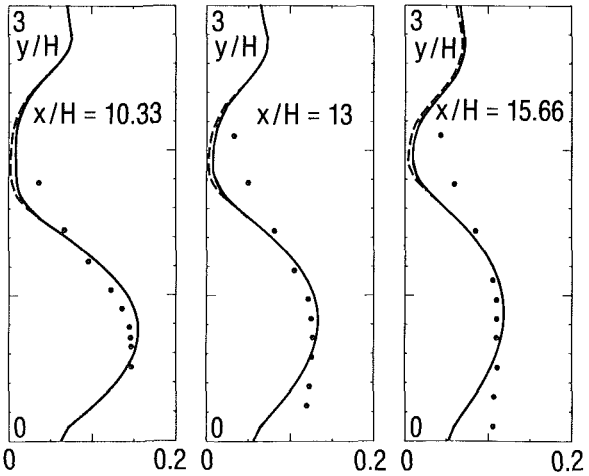

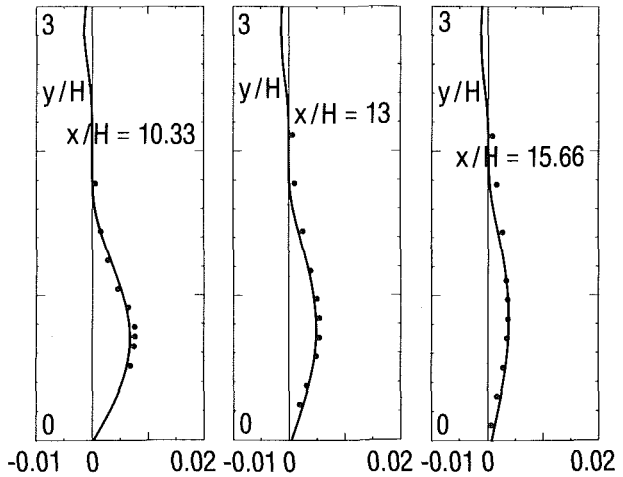

Fig. 12 Turbulence intensity in x-direction
—— $\sqrt{<\overline{u^2}> + <(U - <U>)^2>}/U_0$
— — — $\sqrt{<\overline{u^2}>}/U_0$

Fig. 13 Turbulent shear stress
—— $[<\overline{uv}> + <(U - <U>)(V - <V>)>]/U_0^2$
— — — $<\overline{uv}>/U_0^2$

The power spectrum data obtained from the reattaching turbulent shear layers behind a backward-facing step show that a considerable fraction of turbulence fluctuations occur at low frequencies (at nondimensional frequencies, fH/U_0, less than 0.1) [19]. In our computations, the nearly cyclic vortex shedding has a nondimensional frequency of 0.1 which is in good agreement with the data. However, the computed vortex shedding is at a nearly discrete frequency instead of a band of frequencies. Interestingly, for the flow behind a circular cylinder, the Strouhal number based on the cylinder radius is 0.105 at high Reynolds numbers.

In our results the reattachment point fluctuates around the location $x/H = 7.89$ which is a couple of grid points downstream of the location $x/H = 5.40$ where the stream function on the first grid point adjacent to the wall is zero. With the finer grid (61×61) these two locations are at $x/H = 7.75$ and $x/H = 5.81$, which is a slight improvement. The thin

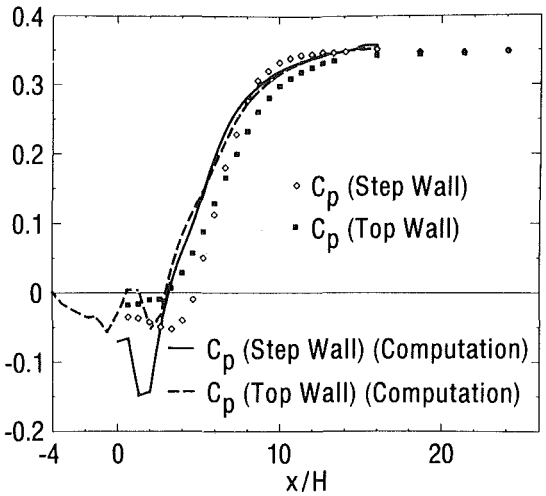

Fig. 14 C_p distribution

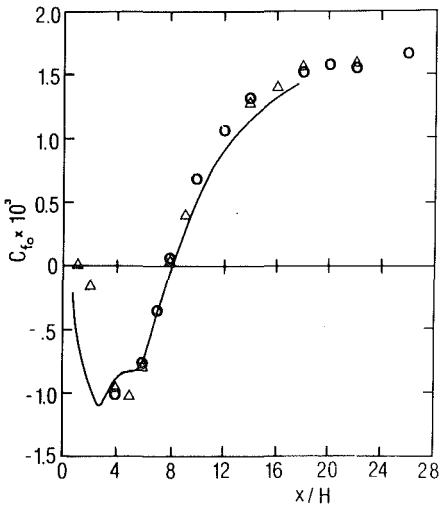

Fig. 15 The pulsed wall probe measurements of Westphal et al. [20] are the data points. The solid lines are calculated values.

reverse flow close to the wall between these two locations can only be detected from the skin friction results and not from Figs. 10 and 11. It does, however, seem unrealistic as the two locations should be much closer to each other.

For this problem, we also computed the pressure coefficient, C_p, by diagnostically solving the momentum equation once the solution is obtained. The results for C_p are in good agreement with the data (Fig. 14) except at the point where the step wall intersects the bottom wall. This is possibly related to the relative coarseness of the grid in this region of rapid change.

Westphal et al. [20] have made an additional observation using a "pulsed wall probe" designed to measure skin friction in separating flow. Their measurements are shown in Fig. 15, along with the calculated $C_{f0} = \tau_w / 1/2\rho U_0^2$ values. The salient feature of both the measured and calculated values in the separated region is their large magnitudes which are associated with the large scale unsteadiness in the detached flow region.

Turbulent Free Shear Layer With Streamwise Curvature

Flows with large streamwise curvature in the plane of mean shear have been studied by Guitton [21] in a wall jet, Wyngaard et al. [22] in a mixing layer, So and Mellor [23] in a boundary layer, and Castro and Bradshaw [24] in a free shear layer. In all these experiments, it was observed that the turbulence structure was changed significantly by the curvature of the flow field. In the experiments performed by So and Mellor [23] the strong stabilizing effect of a convex wall was shown where the shear stress was observed to vanish in the middle of the boundary layer.

In this study a turbulent free shear layer with large streamwise curvature is studied and our results were compared with the data obtained by Castro and Bradshaw [24]. The cross-sectional view of the test area is shown in Fig. 16. Boundary layer suction at the lower corner prevents flow separation. A stagnation point is close to the suction slot.

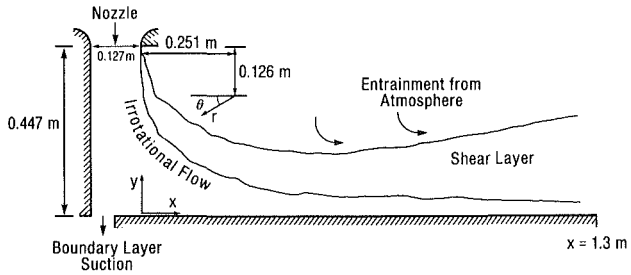

Fig. 16 Schematic of the test area

The computations were done using a 87×23 grid located between $x = -0.127$ m and $x = 0.783$ m in the horizontal direction, and $y = 0$ and $y = 0.447$ m in the vertical direction ($U_0 = 33$m/s). The results are presented in polar coordinates in the curved portion of the flow, and in rectangular coordinates in the downstream recovery region.

The turbulence model we use automatically includes the effects of curvature [25]. The boundary conditions are very similar to those used in the previous two problems with the exception that at the top open boundary and at the exit section the boundary condition, $\partial\psi/\partial n = 0$, was used (instead of $\partial^2\psi/\partial n^2 = 0$ used at the exit sections of the other problems). Also at the top open boundary, the flow was assumed to be irrotational with negligible turbulence. The corner wall vorticity at the entrance ($x = 0$, $y = 0.447$ m) was determined the same way as in the step problem.

Integrating the transport equations, a stationary flow structure is obtained. The streamlines of the flow are shown in Fig. 17. At various sections (shown in Fig. 18), the mean flow in the streamwise direction and the turbulent shear stress are plotted (Figs. 19 and 20, respectively).

As can be seen from the streamline pictures, the flow is like a jet near the walls. The results show discrepancies with the experimental data in the upstream portion of the flow. However, comparison with data improves in the recovery region farther downstream. At the entrance where the initial shear layer is poorly resolved, only the nominal tunnel exit speed (33 m/s) and the longitudinal turbulence intensity (0.1 percent) are available as entrance data. Insufficient information provided at the entrance section and the coarse grid size are thought to be the major sources of error in the upstream section.

The results are extremely sensitive to the boundary conditions applied at the top section. When the computations were repeated assuming a wall to be present at the top section, unsteady vortex shedding was observed as in the step problem.

Summary and Conclusions

This study concentrates on the prediction of incompressible planar turbulent separated flows using the Reynolds stress closure model suggested by Mellor et al. [4, 5]. The transport equations are integrated numerically using a fully elliptic algorithm and the unsteady flow structure is obtained by marching forward in time. The wall boundary condition for mean velocity is supplied by the law-of-the-wall, modified to include effect of normal shear stress gradient; near separation, this

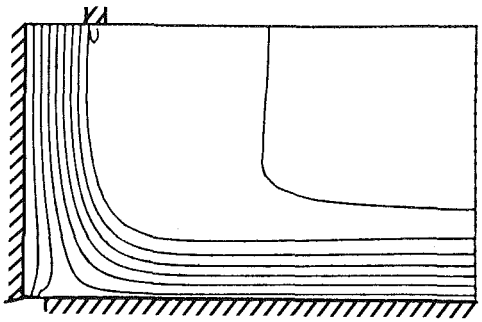

Fig. 17 The computed streamlines

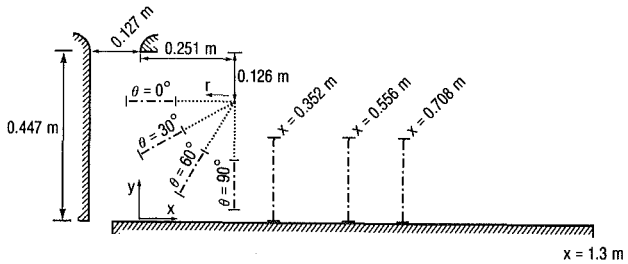

Fig. 18 The sections (indicated by dashed lines) where data were obtained

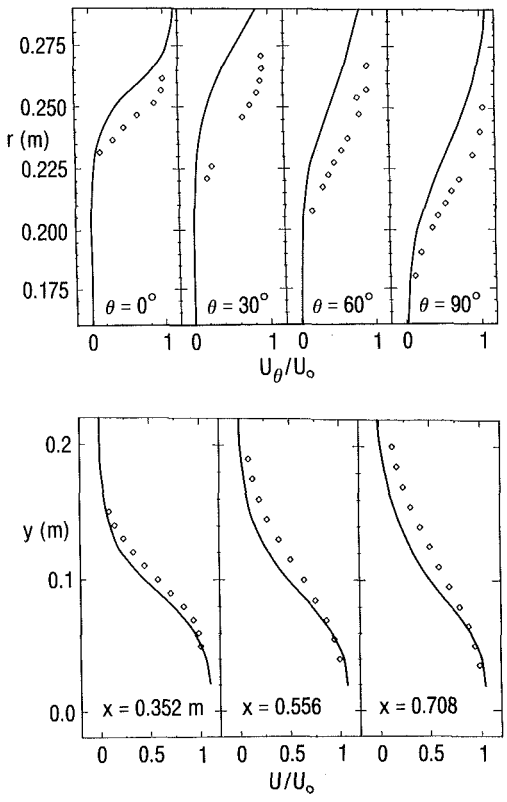

Fig. 19 Mean velocity profiles

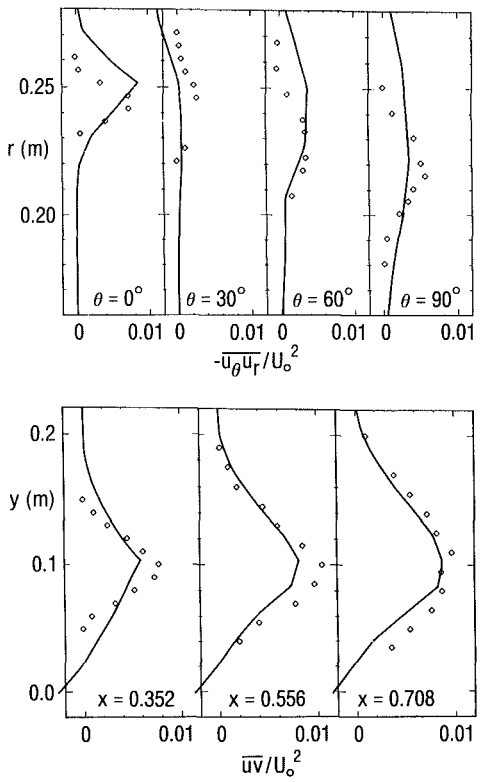

Fig. 20 Turbulent shear stress profiles

was an improvement over the unmodified law-of-the-wall. Considering Simpson's near wall velocity data, some error is evident and, thus, the wall boundary condition is a subject for further improvement.

Three flow problems are considered: separation on a flat surface, flow over a backward-facing step and a free shear layer with streamwise curvature. In the first problem, the pressure gradient is found to be the most important factor to determine the overall structure. Also, our results support the hypothesis that the reserve flow in the separation region is not sensitive to disturbances farther downstream. In the step problem, an eddy shedding is obtained and the flow becomes nearly cyclic in time. The flow unsteadiness has significant effect on the flow structure only in the recirculation region downstream of the step. In the problem of free shear layer with streamwise curvature, the flow is stationary and is like a jet near the walls. The results are quite sensitive to the boundary conditions applied at the open top boundary.

The corner boundary condition of the step problem should not be mainly responsible for the eddy shedding since using the very same boundary condition a stationary flow develops in the curved shear layer problem. Unsteady vortex shedding does occur when a wall is stipulated instead of top open boundary; however, this is consistent with the step problem since the wall geometries expand abruptly in both cases. Roache (p. 169 [7]) suggests several methods for the determination of corner vorticity and argues that neither of them should be ruled out because of the singular nature of the corner. In this study, the effect of other corner boundary conditions have not been investigated though this should be looked at in the future.

The flow problems studied in this research have been investigated by other researchers using different turbulence models and different numerical techniques [15, 16, 26, 27]. Comparing our results with the experimental data and other computations, we see that our turbulence model predicted the mean flows reasonably well except in regions where thin shear layers are not sufficiently resolved by the numerical grid. The turbulence intensities are also predicted fairly well. There are, however, noticeable errors in u' near the wall and downstream of Simpson's separated boundary layer.

There are, of course, many possibilities for extension of the work described in this paper. For example, a more flexible computational grid, adaptable to curved surfaces would be desirable. Further application to other flows should include wake flow behind bluff bodies when the two-dimensional,

oscillatory flow structure should be amplified relative to that found in the case of the backward-facing step.

Acknowledgments

This research was supported by the Air Force Office of Scientific Research under grant AFOSR-79-0118. The computations were performed on the ASC computer at the Geophysical Fluid Dynamics Laboratory of Princeton University.

References

1 Simpson, R. L., Chew, Y.-T., and Shivaprasad, B. G., "The Structure of a Separating Turbulent Boundary Layer. Part 1. Mean Flow and Reynolds Stresses," *Journal of Fluid Mechanics*, Vol. 113, 1981, pp. 23–51.

2 Simpson, R. L., Chew, Y.-T., and Shivaprasad, B. G., "The Structure of a Separating Turbulent Boundary Layer. Part 2. Higher-Order Turbulence Results," *Journal of Fluid Mechanics*, Vol. 113, 1981, pp. 53–73.

3 Shiloh, K., Shivaprasad, B. G., and Simpson, R. L., "The Structure of a Separating Turbulent Boundary Layer. Part 3. Transverse Velocity Measurements," *Journal of Fluid Mechanics*, Vol. 113, 1981, pp. 77–90.

4 Mellor, G. L., "Analytic Prediction of the Properties of Stratified Planetary Surface Layers," *Journal of Atmospheric Sciences*, Vol. 30, No. 6, 1973, pp. 1061–1069.

5 Mellor, G. L., and Yamada, T., "Development of a Turbulence Closure Model for Geophysical Fluid Problems," *Reviews of Geophysics and Space Physics* (to be published) 1982.

6 Mellor, G. L., and Celenligil, M. C., "Some Calculated Elliptical Turbulent Flow Cases (0331, 0421, 0431) for Submission to the Stanford Conference on Complex Turbulent Flows," *Proceedings of the 1980–81 AFOSR-HTTM-Stanford Conference on Complex Turbulent Flows: Comparision of Computation and Experiment*, Stanford, Calif., Sept. 1981.

7 Roache, P. J., *Computational Fluid Dynamics*, Hermosa Publishers, 1976.

8 Mellor, G. L., "The Effects of Pressure Gradients on Turbulent Flow Near a Smooth Wall," *Journal of Fluid Mechanics*, Vol. 24, Part 2, 1966, pp. 255–274.

9 Simpson, R. L., Strickland, J. H., and Barr, J. W., "Features of a Separated Turbulent Boundary Layer in the Vicinity of Separation," *Journal of Fluid Mechanics*, Vol. 79, 1977, pp. 553–594.

10 Simpson, R. L., "A Model for the Backflow Mean Velocity Profile," *AIAA Journal*, Vol. 21, 1983, pp. 142–143.

11 Tani, I., Iuchi, M., and Komoda, H., "Experimental Investigation of Flow Separation Associated With a Step or a Groove," Aeronautical Research Institute, Report No. 364, Vol. 27, No. 4, 1961, pp. 119–137.

12 Abbott, D. E., and Kline, S. J., "Theoretical and Experimental Investigation of Flow Over Single and Double Backward-Facing Steps," Report MD-5, Thermosciences Division, Dept. of Mech. Eng., Stanford University, June 1961.

13 Bradshaw, P., and Wong, F. Y. F., "The Reattachment and Relaxation of a Turbulent Shear Layer," *Journal of Fluid Mechanics*, Vol. 52, Part 1, 1972, pp. 113–135.

14 Kim, J., Kline, S. J., and Johnston, J. P., "Investigation of Separation and Reattachment of a Turbulent Shear Layer: Flow Over a Backward-Facing Step," Report MD-37, Thermosciences Division, Dept. of Mech. Eng., Stanford University, 1978.

15 Ashurst, W. T., Durst, F., and Tropea, C., "Two-Dimensional Separated Flow: Experiment and Discrete Vortex Dynamics Simulation," Report SAND79-8830, 1980.

16 Briggs, M., Mellor, G. L., and Yamada, T., "A Second Moment Turbulence Model Applied to Fully Separated Flows," *Turbulence in Internal Flows* 249–276, S. M. B. Murthy, ed., Hemisphere Pub. Corp., 1977.

17 Celenligil, M. C., "Numerical Solution of Incompressible Planar Turbulent Separated Flows," Ph.D. thesis, Mechanical and Aerospace Engineering, No. 1548-T, Princeton University, June 1982.

18 Eaton, J. K., and Johnston, J. P., "An Evaluation of Data for the Backward-Facing Step Flow: Report Prepared for the 1980/81 Conferences on Complex Turbulent Flows," Jan. 1980.

19 Eaton, J. K., and Johnston, J. P., "Low-Frequency Unsteadiness of a Reattaching Turbulent Shear Layer," *Proceedings of the Third International Symposium on Turbulent Shear Flows*, Davis, Calif., Sept. 1981.

20 Westphal, R. V., Eaton, J. K., and Johnston, J. P., "A New Probe for Measurement of Velocity and Wall Shear Stress in Unsteady, Reversing Flow," ASME JOURNAL OF FLUIDS ENGINEERING, Vol. 103, 1981, pp. 478–382.

21 Guitton, D. E., Ph.D. thesis, McGill University, Montreal, 1970.

22 Wyngaard, J. C., Tennekes, H., Lumley, J. L., and Margolis, D. P., "Structure of Turbulence in a Curved Mixing Layer," *Physics of Fluids*, Vol. 11, 1968, p. 1251.

23 So, R. M. C., and Mellor, G. L., "Experiment on Convex Curvature Effects in Turbulent Boundary Layers," *Journal of Fluid Mechanics*, Vol. 60, Part 1, 1973, pp. 43–62.

24 Castro, I. P., and Bradshaw, P., "The Turbulence Structure of a Highly Curved Mixing Layer," *Journal of Fluid Mechanics*, Vol. 73, Part 2, 1976, pp. 265–304.

25 Mellor, G. L., "A Comparative Study of Curved Flow and Density-Stratified Flow," *Journal of Atmospheric Sciences*, Vol. 32, No. 7, 1975, pp. 1278–1282.

26 Pletcher, R. H., "Prediction of Incompressible Turbulent Separating Flow," ASME JOURNAL OF FLUIDS ENGINEERING, Vol. 100, 1978, pp. 427–433.

27 Gibson, M. M., and Rodi, W., "Reynolds-Stress Closure Model of Turbulence Applied to the Calculation of a Highly Curved Mixing Layer," *Journal of Fluid Mechanics*, Vol. 103, February 1981, pp. 161–182.

Adaptive Grid Generation by Mean Value Relaxation[1]

P. R. Eiseman
Columbia University,
New York, NY 10027

A grid movement algorithm has been developed for the purpose of adaptively resolving numerical solutions to physical problems and, in addition, for grid clustering on arbitrary surfaces. Both the solutions and the arbitrary surfaces are represented by grid point data with a continuous definition provided by interpolation between points. Movement is applied relative to this representation. The algorithm comes from a local mean value construction to produce a finite difference molecule for movement. The mean value weights are of a general enough nature to provide for a generous number of clustering possibilities. The movement molecule is executed within an interative cycle in the spirit of point Jacobi or Gauss-Seidel, and as a consequence, corresponds to the solution of some elliptic partial differential equation which satisfies a maximum (minimum) principle due to the mean value construction. From this principle, the movement will always preserve nonsingularity for the continuous transformation. For the discrete representation in the form of a grid, local geometric constraints are established to maintain this preservation.

Introduction

The salient physical quantities in fluid dynamic phenomena often vary widely over short distances and moreover such variations can occur with a complicated spatial configuration which continually changes. In the numerical simulation, a discrete approximation is usually made to a system of partial differential equations which describe the particular phenomena. When the discretization is done with a fixed mesh, the accurate simulation can be jeopardized if the large solution variations occur on a scale that is too small for the mesh. To assure that the solution is well modeled, various strategies have been proposed in order to adapt the mesh in some way to the solution (e.g., [1]–[8]).

The essential character of the solution is expressed as a surface formed by the salient physical quantities which may vary widely over short distances. These quantities generally form a vector which depends upon both time and the pointwise locations in the physical region. At any instant of time, the pointwise evaluations throughout the region collectively form a surface over the region. If the evaluations are systematically done with respect to coordinates on the physical region, then corresponding coordinates are defined on the surface given that there is only one vector for each physical point. In particular, the spatial dimension of both the physical region and the surface are the same. When the vector of salient quantities is lengthened by the addition of a component for each coordinate direction on the physical region, a Euclidian space which contains the surface in embedded form is obtained. When the significant variations of given quantities do not conflict with each other, they may also be represented as a single quantiy by means of a scalar function. This reduces the dimensionality of the embedding space and thereby represents a simplification. The resulting surface then provides a simple monitor of solution behavior and accordingly is called a monitor surface.

When the monitor surface is uniformly covered with a grid of points, the significant solution gradients are implicitly resolved. The surface, however, may remain unresolved if it bends too rapidly for the pointwise distribution. To include the resolution of bends, surface curvature is employed within a general weight function that multiplies the element which produces uniform conditions. The elements used herein are cell volumes. When the weight increases from a constant value, points are clustered relative to a volume measure of uniformity. Other measures of uniformity along with the various choices for curvature are discussed in Eiseman [3] and [9] together with the formative aspects of monitor surfaces.

Using monitor surfaces, a solution adaptive grid generation scheme has been developed in a manner which has a number of favorable characteristics: grid control is directly inserted; the transformation is always nonsingular; the algorithm is simple; the algorithm is independent of any particular numerical method; the number of user-specified quantities is minimized; the technique works well in any number of spatial dimensions; and the results are also applicable to grid generation on arbitrary surfaces.

Mean Value Relaxation

All of the above characteristics have been obtained with a local geometric construction on the monitor surface to form a global scheme by means of pointwise iteration in the sense of Jacobi or Gauss-Seidel. The resulting grids are surface grids which are usually projected back onto the underlying physical region. The local construction is based upon a mean value strategy for each coordinate direction, which in the global context leads to an underlying system of elliptic partial differential equations that possess a maximum (minimum) princi-

[1]Research supported by AFOSR Grant AFOSR-82-0176.
Contributed by the Fluids Engineering Division for publication in the JOURNAL OF FLUIDS ENGINEERING. Manuscript received by the Fluids Engineering Division, September 7, 1983.

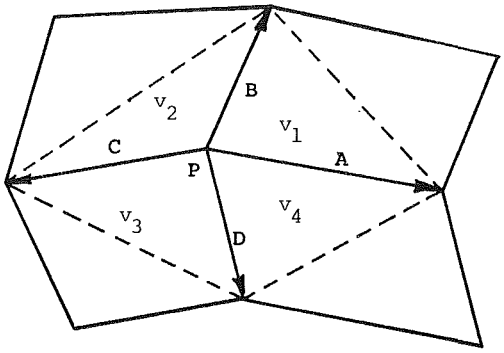

Fig. 1 Difference molecule for grid movement algorithm on the monitor surface

ple. There is no need, however, to explicitly derive the elliptic system since it is not of any practical use in our situation. Instead, we proceed locally with our development.

First suppose that we are given a nonsingular coordinate grid either initially or from a previous cycle. For clarity, we first examine the two-dimensional case. The higher dimensional cases are just straightforward extensions which retain all of the desired properties.

In two dimensions, we have two curvilinear coordinates s and t which under uniform discretization yield a grid on the monitor surface. By setting the vector of solution monitoring quantities to zero while retaining the physical space locations, a corresponding projected grid is obtained on the underlying physical region. Our fundamental objective is to move the grid points on the surface into positions which more accurately represent the surface. From the perspective of the projected grid on the physical region, the surface is more highly resolved. From the applications viewpoint, the accuracy of a numerical solution procedure is enhanced.

The movement algorithm is constructed from the existing monitor surface grid. From a surface grid point **P**, vectors pointing to the nearest surface grid points in the s-direction are denoted by **A** and **C**, respectively, in the positive and negative directions. Similarly, in the t-direction nearest grid points in the positive and negative directions are denoted by **B** and **D**, respectively. The point **P** together with vectors **A**, **B**, **C**, and **D** are illustrated in Fig. 1. In addition, volumes v_1, v_2, v_3, and v_4 are indicated for each quadrant and are respectively equal to the quadrant area up to the dashed line. Here, each is the area of a triangle.

On the basic grid molecule, the volumes are used to form weights that pull **P** along the respective coordinate curves. The pull is between positive and negative directions due to the total weight on either side of the other coordinate curve. The total weight of any side is just a sum of the two weights that are centered in the adjacent quadrant volumes. For triangles, the volume centers are the barycenters and are computed from **P** as one-third of the sum of the corresponding two sides. The respective centers for each quadrant are then given by

$$\begin{aligned}
\mathbf{b}_1 &= \mathbf{P} + \frac{1}{3}\mathbf{A} + \frac{1}{3}\mathbf{B} \\
\mathbf{b}_2 &= \mathbf{P} + \frac{1}{3}\mathbf{B} + \frac{1}{3}\mathbf{C} \\
\mathbf{b}_3 &= \mathbf{P} + \frac{1}{3}\mathbf{C} + \frac{1}{3}\mathbf{D} \\
\mathbf{b}_4 &= \mathbf{P} + \frac{1}{3}\mathbf{D} + \frac{1}{3}\mathbf{A}
\end{aligned} \tag{1}$$

In the case of direction **A**, weights w_1 and w_4 for the adjacent volumes v_1 and v_4 are determined at centers $\mathbf{b}_1$ and $\mathbf{b}_4$ and yield the weight center $\mathbf{C}_A$ for side **A** which is given by the linear combination

$$\mathbf{C}_A = \frac{w_1}{w_1 + w_4}\mathbf{b}_1 + \frac{w_4}{w_1 + w_4}\mathbf{b}_4 \tag{2}$$

On substitution from equation (1), the center can be written as

$$\mathbf{C}_A = \mathbf{P} + \frac{1}{3}\mathbf{A} + \frac{1}{3}\left\{\frac{w_1}{w_1 + w_4}\mathbf{B} + \frac{w_4}{w_1 + w_4}\mathbf{D}\right\} \tag{3}$$

The distance d_A along **A** is simply given by the projection

$$d_A = (\mathbf{C}_A - \mathbf{P}) \cdot \frac{\mathbf{A}}{\|\mathbf{A}\|} \tag{4}$$

or, by using equation (3), by

$$d_A = \frac{1}{3}\|\mathbf{A}\| + \frac{1}{3}\left\{\frac{w_1}{w_1 + w_4}\mathbf{B} + \frac{w_4}{w_1 + w_4}\mathbf{D}\right\} \cdot \frac{\mathbf{A}}{\|\mathbf{A}\|} \tag{5}$$

Since negative distances represent the direction corresponding to the opposite side, the distance d_A is truncated at 0 by using $\max\{d_A, 0\}$. In many circumstances, however, the last term in equation (5) is small relative to the first since the grid must be highly distorted for it to give a reasonably significant projection along **A**. As a consequence, the first term is usually a good approximation to the sum and, moreover, it is always positive. In the other directions the same reasoning is also used. Altogether, the maximum distances for movement along the respective **A**, **B**, **C**, and **D** directions are then approximated by

Nomenclature

$\mathbf{A}$ = vector in positive s-direction
$\mathbf{b}_1, \ldots, \mathbf{b}_4$ = barycenter locations for 4 quadrants
$\mathbf{B}$ = vector in positive t-direction
$\mathbf{C}$ = vector in negative s-direction
$\mathbf{C}_A$ = weight center in **A**-direction
$\mathbf{D}$ = vector in negative t-direction
$\mathbf{E}_s, \mathbf{E}_t, \mathbf{E}_{st}$ = grid points corresponding unit increments in s, t and (s,t)
d_A, d_B, d_C, d_D = maximum distances along **A**, **B**, **C**, **D**, respectively
d_s, d_t = distances in s and t directions
f = test function
M_j = magnitude for clustering to jth quantity
m = exponent
min = minimum
max = maximum
$\mathbf{P}$ = point at center of grid molecule
$\mathbf{P}_{\text{new}}$ = update for **P**
$\mathbf{P}_s$ = new position is s
$\mathbf{P}_t$ = new position in t
(s,t) = two-dimensional curvilinear coordinates
v = general quadrant volume
$v_1, \ldots, v_4$ = quadrant volume
w = general quadrant weight
$w_1, \ldots, w_4$ = quadrant weights
$w_A, \ldots, w_D$ = weights for directions **A**, . . . ,**D**
(x,y) = two-dimensional Cartesian coordinates
α = magnitude of increment in s
α_j = scale factor of M_j
β = magnitude of increment in t
$\| \ \|$ = magnitude of a vector

$$d_A = \frac{1}{3}\|\mathbf{A}\|$$

$$d_B = \frac{1}{3}\|\mathbf{B}\| \tag{6}$$

$$d_C = \frac{1}{3}\|\mathbf{C}\|$$

$$d_D = \frac{1}{3}\|\mathbf{D}\|$$

In the four directions, the weights are just the total weights on the corresponding sides and are given by

$$w_A = w_1 + w_4$$

$$w_B = w_1 + w_2 \tag{7}$$

$$w_C = w_2 + w_3$$

$$w_D = w_3 + w_4$$

On the coordinate curve in s, movement can vary from d_C units in the negative direction of **C** up to d_A units in the positive direction of **A**. The grid point **P** now corresponds to the number 0 within the interval of distances from $-d_C$ up to d_A. With weights w_C and w_A at the respective ends, the weighted mean value of distance d_s is given by

$$d_s = \frac{w_C(-d_C) + w_A d_A}{w_C + w_A} \tag{8}$$

When d_s is positive, we go in the direction of **A**; when negative, in the direction of **C**; and when 0, no movement at all. Analytically these possibilities can be combined to express the new point $\mathbf{P}_s$ in the form

$$\mathbf{P}_s = \mathbf{P} + \frac{\mathbf{C}}{\|\mathbf{C}\|}\max\{-d_s,0\} + \frac{\mathbf{A}}{\|\mathbf{A}\|}\max\{d_s,0\} \tag{9}$$

As d_s changes sign, it is clear that $\mathbf{P}_s$ flips between directions **A** and **C** and thus remains on the curve. In a parallel manner, the new position $\mathbf{P}_t$ along the coordinate curve in the t variable is given by

$$\mathbf{P}_t = \mathbf{P} + \frac{\mathbf{D}}{\|\mathbf{D}\|}\max\{-d_t,0\} + \frac{\mathbf{B}}{\|\mathbf{B}\|}\max\{d_t,0\} \tag{10}$$

where

$$d_t = \frac{w_B d_B - w_D d_D}{w_B + w_D} \tag{11}$$

While the same quadrant weights can be used directly, a directionally biased motion can be imposed when distinct quadrant weights are used for each direction. From this vantage point, the weights in the above equations are interpreted as a component of some weight vector.

For the new positions along the s and t coordinate curves, the corresponding curvilinear coordinate values are determined so that the original or previous transformation can be applied to obtain the new position for **P**. The transformations here are given in discrete form and are defined between the grid points by local bilinear interpolation. This means that along coordinate curves, the curvilinear increment is determined linearly. Without loss of generality, the Cartesian grid of curvilinear variables (s,t) is assumed to have unit spacing between points so that all increments will vary between -1 and 1. In the s and t directions, the increments from the (s,t)-value for P are then given by proportions

$$\Delta s = \frac{\min\{d_s,0\}}{\|\mathbf{C}\|} + \frac{\max\{d_s,0\}}{\|\mathbf{A}\|}$$

and (12)

$$\Delta t = \frac{\min\{d_t,0\}}{\|\mathbf{D}\|} + \frac{\max\{d_t,0\}}{\|\mathbf{B}\|}$$

respectively. The quadrants for Δs and Δt are clearly in a one-to-one correspondence with the transformed quadrants illustrated in Fig. 1.

As an alternative strategy, increments in s and t can also be determined from the difference molecule in (s,t)-space rather than directly on the monitor surface. The molecule of Fig. 1 then becomes specialized to the situation where **A**, **B**, **C**, and **D** are all of unit length and the successive angles between them are all 90 degrees. The weights, however, are determined by using volumes on the monitor surface instead of in Cartesian (s,t)-space where all four of them would be equal. In effect, the simple specialized molecule has weights which include the Jacobian as a factor. The result of simplification is evident upon an examination of our original discussion. In the direction **A**, the weight center $\mathbf{C}_A$ is given, as before, by equation (3). Since the last term in equation (3) is perpendicular to **A**, the distance d_A of equation (5) reduces to the one-third rule of equation (6) without any approximation. Due to the unit length of **A**, the distance is just one-third. Altogether, the maximum movement distances of equation (6) reduce to

$$d_A = d_B = d_C = d_D = \frac{1}{3} \tag{13}$$

With the weights of equation (7), the distances d_s and d_t of equations (8) and (11) are just the respective increments Δs and Δt. Altogether, they are given by

$$\Delta s = \frac{w_A - w_C}{3w} \tag{14}$$

$$\Delta t = \frac{w_B - w_D}{3w}$$

where

$$w = w_A + w_C = w_B + w_D = w_1 + w_2 + w_3 + w_4$$

is the total weight. Due to the colinearity of **A** and **C** and of **B** and **D**, the splitting of equation (12) about **P** is removed and is a simplification. The original distance weighting of equations (8) and (11), however, favors longer sides. For example, with equal weights in the s-direction, equation (14) yields $\Delta s = 0$ while equation (8) reduces to $d_s = 1/2(d_A - d_C)$ which yields a generally nonzero increment from equation (12).

Next, with either strategy, the new position is computed from **P**. From the signs of Δs and Δt, a quadrant is selected and the transformed volume is determined by 4 mesh points including **P**. Let $\mathbf{E}_s$, $\mathbf{E}_t$, and $\mathbf{E}_{st}$ be the other grid points corresponding to the unit sized increments in s, t and (s,t). Then for $\alpha = |\Delta s|$ and $\beta = |\Delta t|$, the new position $\mathbf{P}_{\text{new}}$ is given by the bilinear interpolant

$$\mathbf{P}_{\text{new}} = (1-\alpha)[(1-\beta)\mathbf{P} + \beta\mathbf{E}_t] + \alpha[(1-\beta)\mathbf{E}_s + \beta\mathbf{E}_{st}] \tag{15}$$

It is important to note that the influence of the diagonally opposite point $\mathbf{E}_{st}$ to **P** has been inserted at this stage. As a consequence, the movement of **P** to $\mathbf{P}_{\text{new}}$ conforms more closely to the previous grid structure as is reasonably expected from using the transformation itself. In the Cartesian space of curvilinear variables, the possible regions for movement subject to the maximum distances of equations (6) or (13) are illustrated in Fig. 2. The shaded regions represent the set of potential new variable locations. Due to the piecewise bilinear definition of the transformation, the one-third rule for equation (6) is pulled back to the (s,t)-space. By contrast, the one-third rule for equation (13) is already there. With a potential movement of one-third for each grid point, it is clear from the figure that there is an extra third left over as a buffer zone between points and their potential new positions. As a consequence, either point Jacobi or Gauss-Seidel iteration can be employed to take our local coordinatewise mean value development into a global transformation of elliptic type. Had there been no buffer zone, then point Jacobi would not have been generally possible. That is, since point Jacobi here deter-

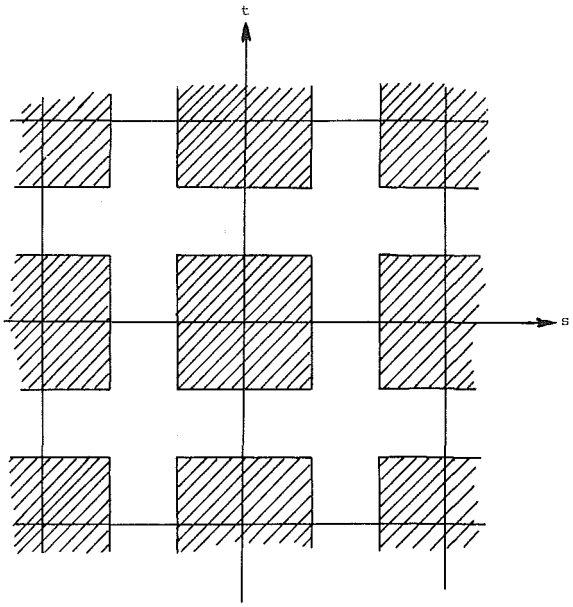

Fig. 2 Regions for new locations in the space of curvilinear variables s and t

mines new grid points $\mathbf{P}_{new}$ only from old information, a region overlap would yield the possibility for neighboring points to interchange positions in the curvilinear variable space, and thereby, to cause a singularity for the curvilinear variable space grid. Under the bilinear mapping of equation (15), this singularity is sent onto a corresponding singularity on the monitor surface and on the projection to the physical region. By contrast, Gauss-Seidel uses all available current information which in this context means that the underlying "previous" transformation is continually being updated. Thus, a potential grid overlap from previous movements would be eliminated in the space of curvilinear varibles even if the potential pointwise movement were expanded to the full triangle defined by $\alpha+\beta \leq 1$ in equation (15) rather than the one-third rule as in Fig. 2. This happens because the curvilinear space grid is reset to a Cartesian grid immediately after each point is moved. The effect on the monitor surface grid is that the distances from neighboring points have been suitably shrunk by previous movements. This means that points cannot interchange positions along the coordinate curves at any stage in the iteration. However, this does not prevent an overlap between neighboring curves as illustrated in Fig. 3.

While the new position in Fig. 3 is contained within a quadrilateral patch from the bilinear mapping of equation (15), the new curve represented by the dashed line segments overlaps the curve beneath it. This can occur only when the region defined by the full nine point molecule is concave with respect to positions on the monitor surface. The distortion of the monitor surface in its embedding space is not relevant for this purpose. In an analytical sense, the geodesic curvature would have to be examined for sign changes as the boundary of the full molecule is traversed: such changes correspond to inflection points of the boundary curve within the surface. In a simpler sense, the plane tangent to the surface at the point **P** can be defined, the molecule can then be projected into it, and finally the points of concavity can be detected by standard planar constructions. A still simpler but coarser approximation can also be done by taking the projection into the underlying physical region. By any of these methods the grid points where there is concavity can be systematically detected on any given nine point movement molecule. A point of concavity is depicted directly beneath **P** in the molecule displayed in Figs. 3 and 4. To prevent the new (dashed) coordinate curve from overlapping the segment entering the concave point from

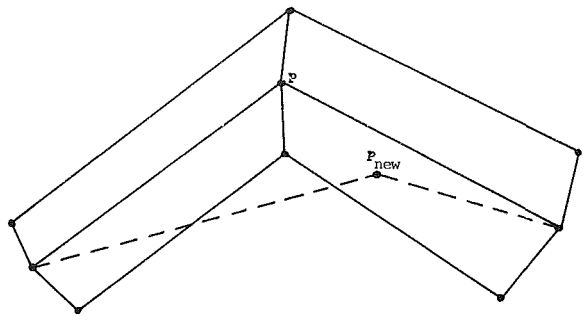

Fig. 3 Possible overlap with neighboring concave curve

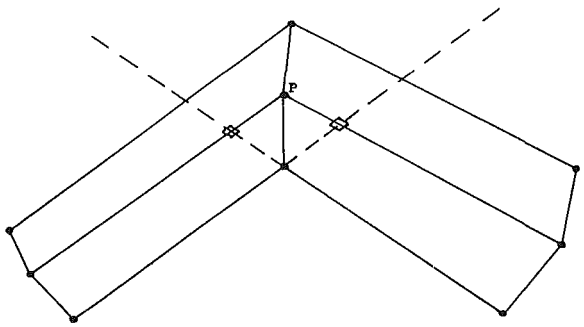

Fig. 4 Movement barriers to prevent overlap with a neighboring concave curve: the point P cannot be moved through the dashed curve

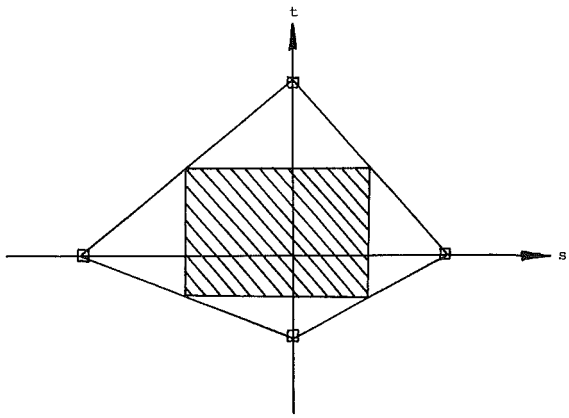

Fig. 5 The region of possible movements that are free from grid overlap of any sort on the monitor surface

the left as it does in Fig. 3, that segment must be extended to form a barrier beyond which **P** cannot be moved. The dashed extension on the right-hand side of Fig. 4 represents this barrier. Similarly, the other side of the concave point gives rise to a motion barrier which is depicted by the remaining dashed extension. When the same planar projections that can be used to detect concavity are used for establishing such barriers, the overlap of segments is just an intersection of line segments. In Fig. 4, these intersections are denoted by small boxes. In the more precise sense where the actual surface molecule is used to establish the barriers, the boxes represent the two locations on the coordinate curve which are nearest to their respective barriers. The overlap of segments here is just the mutually perpendicular distance between them. Once barriers are established along each coordinate curve where they are needed, the corresponding constraints on displacements in s and t are simply obtained from the linearity of the interpolation mapping in equation (15). The maximum allowable displacements are then determined by the minimum of each constraint and the corresponding previous maximum. In Fig. 5, such adjusted maxima are represented by small boxes along the s and t axes. By connecting them together, a diamond

shaped region is established where the bilinear mapping of equation (15) will not produce a grid overlap on the monitor surface. For systematic applications, however, a rectangular region is preferable. The largest inscribed rectangle is displayed by the shaded region in Fig. 5 and is defined by taking half of the maximum possible displacements along each axis. The rectangular corners, however, are on the diamond shaped border where the bilinear transformation just starts its problems. By uniformly shrinking this rectangle, a slight amount, some safety margin can be established. With the shrunk rectangle, new maximum displacement distances are just the new axial intersections in curvilinear space. On the monitor surface, the linearity of equation (15) along each coordinate curve establishes the required maximal displacements for equations (5) or (6).

With the earlier buffer zones of Fig. 2 and the further restrictions from the movement barriers, each Jacobi or Gauss-Seidel sweep through the mesh takes a nonsingular grid into another nonsingular grid. By repetition, any finite number of sweeps clearly preserves nonsingularity. Since the new grid results from a finite number of sweeps, the adaptive grid which is initially nonsingular is then guaranteed to always be. On reflection, this guarantee is analytically an interesting consequence of a maximum (minimum) principle which is built into the mean value formulation (equations (8) and (11) or (14)) in the local movement molecule of Fig. 1. On a discrete level, it is maintained by using motion barriers to establish a safe range for the mean value process on each molecule.

The Choice of Weights

To apply the algorithm, suitable quadrant weights w must be given for each volume v in the local molecule. When $w = v$, the grid converges towards uniform conditions on the monitor surface since points **P** then move towards their surface area centers of gravity. Uniformity on the monitor surface means that solution gradients are automatically resolved in the grid projection onto the physical domain. When a suitable resolution of surface quantities is desired, the definition of w is extended to provide for the required clustering. Denoting the magnitude of the jth quantity by M_j, the general weight is taken as

$$w = \left(1 + \sum_j \alpha_j M_j\right) v \tag{16}$$

where the coefficients α_j are non-negative real numbers. Each α_j gives the level of clustering attached to the jth property relative to the other properties and to uniformity which is now represented by the 1 in equation (16). As an example, curvature clustering is achieved by taking $j = 1$ and M_1 as the magnitude of curvature. A development which leads to a reasonable selection of curvature measure is given in Eiseman [3]. With a suitable measure, points are then attracted to higher curvature regions as α_1 increases from 0. Such coordinates represent a generalization of the one-dimensional camp-polytropic coordinates of Ablow and Schecter [1], and the spherical-normal image clustering of Eiseman [10], both of which reduce to the arc length scheme of White [4] when $\alpha_1 = 0$. As yet another example, we may directly generate the grid on the problem domain rather than the solution surface and cluster with M_1 and M_2 for the magnitude of gradients and Laplacians, respectively. Here, the 1 in equation (16) represents uniformity in the physical space relative to which gradient and Laplacian clustering is controlled by the sizes of α_1 and α_2. In this context, the Laplacian as a rough approximation to mean curvature is for curvature attraction. This example can also be viewed as a generalization of the method of Dwyer et al [5]. With such a direct insertion of control, the various possibilities for clustering to desired quantities are virtually without limit.

Generality of Application

In any of the possible examples, the mesh generation strategy here is clearly independent of the method in which the solution is generated. The only presumption is that there is a surface defined in the form of a grid on which the grid generator can be applied to achieve a better pointwise description. When the surface is generated from some solution algorithm the better pointwise description leads to an improvement in accuracy with a fixed number of grid points for the next or current solution step. The timing depends upon whether the grid generator is applied simultaneously or prior to the solution step or steps. When the solution step is replaced by analytic evaluations of an arbitrarily prescribed function over a gridded domain, the resulting surface grid while possibly smoother is indistinguishable. Consequently, the mesh generator can also be considered as a surface mesh generator. Moreover, it can be applied to surfaces of a more general description than those which are defined by functions over a given domain. That is, surfaces defined in a general parametric fashion can be considered.

Higher Dimensions

Whether the application is for monitor surfaces or for general surfaces, the grid generator is readily extended to any number of spatial dimensions without any loss of its fundamental properties. As with two dimensions, the process is applied to each coordinate direction to determine the local curvilinear values from which the new position can be found by application of the currently given transformation. In n-dimensions, the transformation is locally defined by n-linear interpolation between grid points. The surface which separates positive and negative sides for a given coordinate direction (as in Fig. 1) are now $(n-1)$-dimensional. On each side, there are 2^{n-1} volumes v_i on which weights w_i are formed. Here, each v_i is a general n-simplex [11]. In two dimensions, they are triangles; in three dimensions, tetrahedrons; . . . . General maximum distances of the form in equation (5) can be derived and can be well approximated as in equation (6), but now with the general barycentric coordinate value which is distance divided by $n+1$. With total weight, assigned to each side, the local distance mean value is determined as in equation (8) and (11) and is used as in equation (12) to get the curvilinear increments. Similarly, the alternative construction in curvilinear variables can also be extended. With either construction, the increments for each coordinate direction give the new location in the space of curvilinear variables. On application of the transformation, the new surface point location is determined.

Applications

The movement algorithm is applied to adapt a grid to surface data and weights that are given with respect to the grid itself. For the movement to be smooth, both the surface and the weights must also be smooth. Otherwise, ripples in either the surface or the weights will be translated into ripples in the grid and most likely into an unstable situation. As a consequence, a smoothing step or steps is recommended if the gridded data is not already smooth. In the overall solution adaptive context, movement is first applied to conform more closely to initial conditions, and subsequently, to resolve the solution as it evolves. The evolutionary cycle falls into the general sequential pattern which usually consists of a solution step, surface generation, surface smoothing, weight construction, weight smoothing, and then movement. In the adaptation to initial conditions, the cycle is modified by replacing the solution step with evaluation at the initial conditions. The smoothing steps in the cycle can be accomplished by a short iteration on local averages to filter out small fluctuations in the data while retaining its basic character. Among the numerous alternatives, one of the simplest is to consider

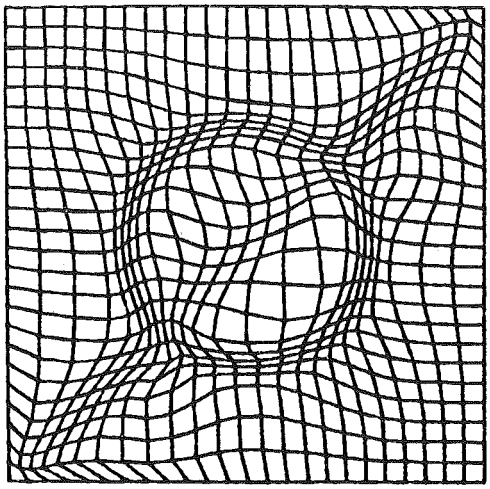

Fig. 6 Grid adapted to a disturbance on a line and a circle

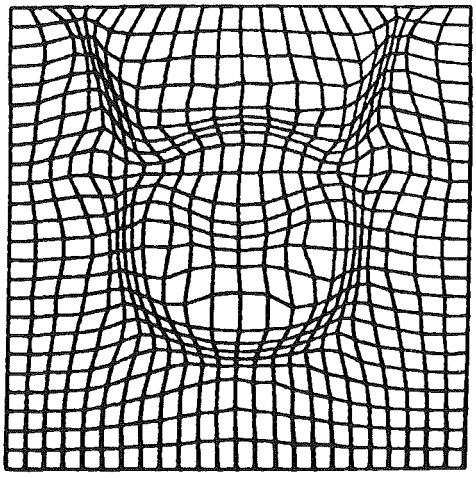

Fig. 7 Grid adapted to a disturbance on a parabola and a circle

smoothing as a diffusion process and to apply the heat equation to the data for several time steps.

The basic part of the solution adaptive process is the grid movement scheme which is employed. To test the scheme that has been developed here, a sequence of test cases has been chosen to examine the movement without outside interference from a particular problem or numerical method. Since the main purpose of adaptivity is to cluster points in regions where there are disturbances, a method for artificially and smoothly inserting such disturbances is required. As a basic building block, the hyperbolic tangent formula

$$T(r) = A \tanh D\, r \tag{17}$$

is used. At $r=0$, T represents a disturbance in the form of a jump from $-A$ to $+A$ with a jumping rate which is increased with D. In the example cases, sufficiently severe disturbances were obtained with a rate of $D=3$ and an amplitude of 2 by setting $A=1$. In terms of Cartesian coordinates (x,y), disturbances on the unit circle and on the polynomial curve $y=x^m$ are obtained by setting $r = x^2+y^2 - 1$ and $r=y-x^m$, respectively. Altogether, the function

$$f(x,y) = T(x^2+y^2-1) + T(y-x^m) \tag{18}$$

is used in place of the solution step. This function gives a smooth surface definition everywhere except at the origin where there is a very small conical peak due to truncation of the hyperbolic tangent asymptotic behavior at unit distance. The weights for the test cases were chosen to be just surface area elements. In each case, a 25×25 initial grid was adapted

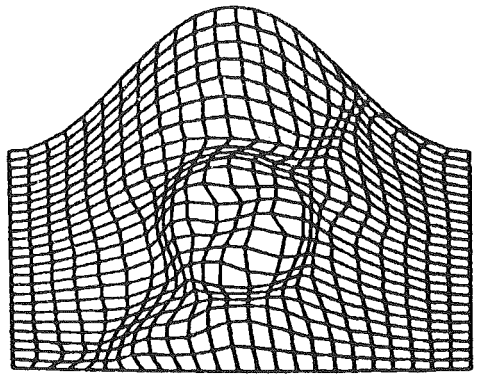

Fig. 8 Grid adapted to a disturbance on a line and a circle under a cosine curve

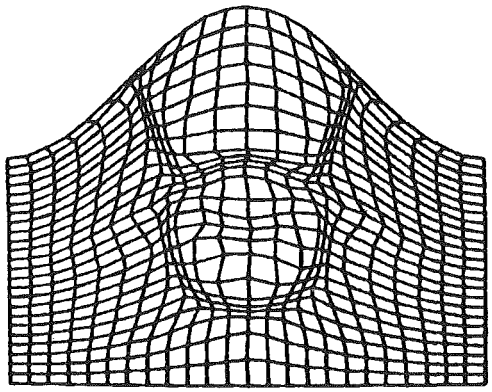

Fig. 9 Grid adapted to a disturbance on a parabola and a circle under a cosine curve

to the given surfaces with 25 Gauss-Seidel iterations of the movement molecule. The molecule was applied without motion barriers on both the solution surface and on the space of curvilinear variables. The results between the two locations of application did not, however, exhibit any appreciable difference in the sequence of test cases. The resulting grids displayed here come from the molecule on the surface and are indistinguishable from the parallel cases on the space of curvilinear variables. In the first case, the initial grid was Cartesian on the square defined from -2 to $+2$ in both x and y. The disturbance was taken to be on the circle and the line $y = x$ by setting $m = 1$ in equation (18) for the surface. With movement on only interior points, the adapted grid was generated and is displayed in Fig. 6. From the Gauss-Seidel iteration on lexigraphically ordered points, a slight asymmetry about the line $y = x$ results and can be observed upon a careful examination of the grid. By replacing the line with a parabola ($m = 2$ in equation (18)), the grid of Fig. 7 was obtained. In each of these cases, effective grid clustering capabilities have been demonstrated. In physical terms, the circle could represent a large vortex detectable by velocity magnitudes; the line or parabola, a shock wave detectable by pressure values. The adaptive method is also directly applicable to situations where there are curved boundaries. This is demonstrated by repeating the first two cases on a region with a curved upper boundary given by a cosine curve. From the sheared initial grid defined by

$$\begin{aligned} x &= s \\ y &= (4+\cos s)t - 2 \end{aligned} \tag{19}$$

movement was applied to the same disturbances as before. The results are presented in Figs. 8 and 9. In each of the four cases considered so far, there was no boundary movement and, as a consequence, some grid distortion has occurred at locations where the disturbances impinge upon the bound-

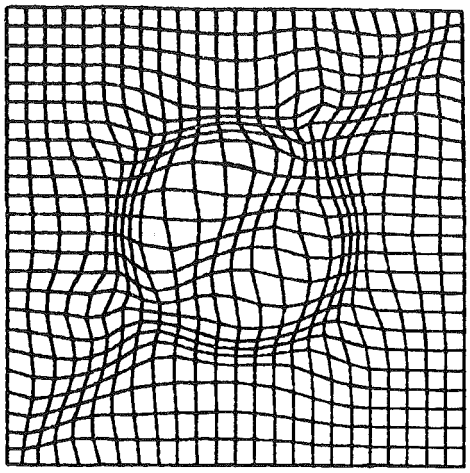

Fig. 10 Grid adapted to a disturbance on a line and a circle with movement along boundaries

aries. This can be observed in the resultant grids. Movement along the boundaries is obtained in a straightforward manner by setting transverse movement to 0 and applying a reduced movement molecule where weights exist on only one side. By repeating the first case with boundary movement, the grid in Fig. 10 was obtained and is readily seen to have less distortion at the boundaries. In each example, the rates of convergence were observed by repeating the cases with 50 iterations as opposed to 25. With 25, each point is just influenced by all the others. With 50, the effect is doubled. The grids, however, did not substantially change with the additional 25 iterations. More accurately, the movement in an iteration can be measured by calculating the average movement distance or a root mean square of distances over all grid points. With either measure, the iteration can be dynamically stopped when global movement falls below a specified value.

Conclusion

A robust and general adaptive grid scheme has been developed by mean value relaxation and has been effectively demonstrated on a sequence of two-dimensional test cases which accurately reflect many common types of disturbance. The scheme is applicable in higher dimensions, on curved boundaries, and on arbitrary surfaces.

References

1 Ablow, C. M., and Schecter, S. (1978), "Campolytropic Coordinates," *J. Comput. Phys.*, Vol. 27, pp. 351–362.

2 Ablow, C. M. (1982), "Equidistant Mesh for Gas Dynamic Calculations," *Numerical Grid Generation*, Ed. by J. F. Thompson, North-Holland, pp. 859–864.

3 Eiseman, P. R. (1983), "Alternating Direction Adaptive Grid Generation," AIAA Comput. Fluid Dyn. Conf., 6th, pp. 339–348; *AIAA J.*, Vol. 23, No. 4, (1985), pp. 551–560.

4 White, A. B., (1982), "On the Numerical Solution of Initial Boundary-Value Problems in One Space Dimension," *SIAM J. Numer. Anal.*, Vol. 19, pp. 683–697.

5 Dwyer, H. A., Smooke, M. D., and Kee, R. J. (1982), "Adaptive Gridding for Finite Difference Solutions to Heat and Mass Transfer Problems," *Numerical Grid Generation*, Ed. by J. F. Thompson, North-Holland, pp. 339–359.

6 Anderson, D. A., and Rai, M. M. (1982), "The Use of Solution Adaptive Grids in Solving Partial Differential Equations," *Numerical Grid Generation*, Ed. by J. F. Thompson, North-Holland, pp. 317–338.

7 Brackbill, J., and Saltzman, J. S. (1982), "Adaptive Zoning for Singular Problems in Two Dimensions," *J. Comput. Phys.*, Vol. 46, pp. 342–368.

8 Gnoffo, P. A. (1982), "A Vectorized, Finite-Volume, Adaptive-Grid Algorithm for Navier-Stokes," *Numerical Grid Generation*, Ed. by J. F. Thompson, North-Holland, pp. 819–836.

9 Eiseman, P. R. (1985), "Grid Generation for Fluid Mechanics Computations," *The Annual Review of Fluid Mechanics*, Vol. 17, pp. 487–522.

10 Eiseman, P. R. (1979), "A Multisurface Method of Coordinate Generation," *J. Comput. Phys.*, Vol. 33, pp. 118–150.

11 Singer, I. M., and Thorpe, J. A. (1967), *Lecture Notes in Elementary Topology and Geometry*. Scott Foresman, and Co.

Yutaka Tsuji
Associate Professor.

Yoshinobu Morikawa
Professor.

Osamu Mizuno[1]
Graduate Student.

Department of Mechanical Engineering,
Faculty of Engineering,
Osaka University,
Suita, Osaka, 565 Japan

Experimental Measurement of the Magnus Force on a Rotating Sphere at Low Reynolds Numbers

The Magnus force on a rotating sphere at low Reynolds numbers was obtained from trajectories of the sphere which impinged on an inclined plate and bounced. An empirical expression for the lift coefficient which is proportional to the angular velocity was deduced by comparing measurements of the range of flight with the solutions of the equation of motion.

1 Introduction

The effect of Magnus force on a rotating sphere dates back to the 17th century, era of I. Newton [1]. This means that the discovery of the Magnus force on the sphere was two centuries older than that of the rotating cylinder which was discovered by Magnus [2]. However, there have been few reports dealing with the measurement of Magnus force on the sphere. Rubinow et al. [3] obtained the Magnus force theoretically at very low Reynolds numbers. Macoll [4], Davies [5], Tani [6], Taneda [7], and Barkla et al. [1] showed their experimental results of the force at very large Reynolds numbers. The above results are briefly reviewed here.

Let us consider that a sphere of diameter d is spinning at an angular velocity ω in an uniform flow field, as shown in Fig. 1. When the relative velocity between the flow and sphere is u_r, the lift coefficient C_L is defined by

$$F_L = C_L \tfrac{1}{2}\rho_f u_r^2 S \tag{1}$$

where ρ_f is the fluid density and S is the projected sectional area of the sphere. The solution of Rubinow et al. [3] is expressed by

$$C_L = 2\Gamma \tag{2}$$

where Γ is the ratio of the surface velocity of the sphere to the relative velocity, that is,

$$\Gamma = \tfrac{1}{2} d\omega / u_r \tag{3}$$

Γ is called nondimensional angular velocity in this paper. Existing results concerning the Magnus force on the sphere are collected in Fig. 2, a part of which is cited from reference [8]. The Reynolds number in the figure is defined by

$$\mathrm{R_e} = u_r d/\nu \tag{4}$$

The drag coefficient C_D is defined by

$$F_D = C_D \tfrac{1}{2}\rho_f u_r^2 S \tag{5}$$

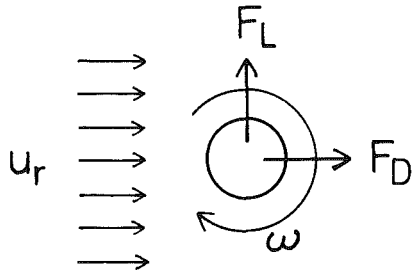

Fig. 1 Fluid-dynamic forces acting on a rotating sphere

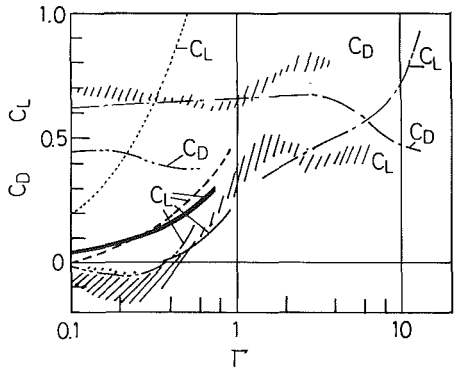

Fig. 2 Drag and lift coefficients of the rotating sphere

References		$\mathrm{R_e}$
Macoll [4]		$4.6 \times 10^4 \sim 1.1 \times 10^5$
Wooden sphere	Tani [6]	1×10^5
Baseball	Tani [6]	1×10^5
Barkla et al. [1]		2×10^3
Davies [5]		9×10^4
Rubinow et al. [3]		<1
The present result		$550 \sim 1600$

and is also shown in Fig. 2. The drag coefficients C_D is found not to be significantly influenced by the rotation. What is interesting in the results of Macoll [4] is that the lift force is negative at a low value of Γ. Taneda [7] attributed this negative force to the laminar-turbulent transition of the boun-

[1] Present address: Matsushita Electronic Industrial Company Ltd., Osaka, Japan.

Contributed by the Fluids Engineering Division for publication in the JOURNAL OF FLUIDS ENGINEERING. Manuscript received by the Fluids Engineering Division, September 29, 1984.

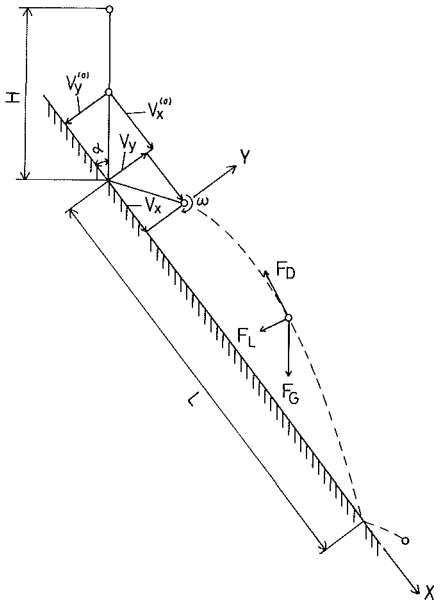

Fig. 3 Collision between the sphere and plate

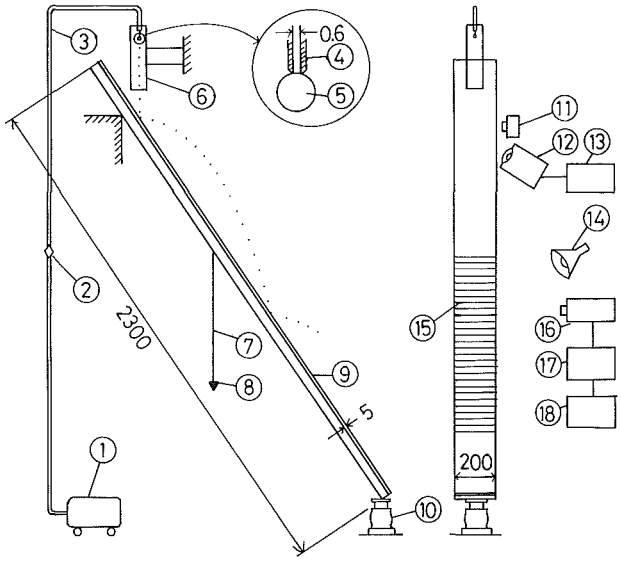

Fig. 4 Experimental equipment ①: Vacuum cleaner, ②: Glass valve, ③: Vinyl tube, ④: Metal tube, ⑤: Sphere, ⑥: Acrylic pipe, ⑦: Thread, ⑧: Weight, ⑨: Acrylic plate, ⑩: Jack, ⑪: Camera, ⑫: Stroboscope ⑬: Oscillator, ⑭: Light, ⑮: Marked line, ⑯: Video camera, ⑰: Video tape recorder, ⑱: Monitor TV

Table 1 Experimental results of translation velocities in the X and Y directions

H (cm)	α (deg)	$\bar{V}_x$ (Average) (m/s)	σ_x (S. D.) (m/s)	$\frac{\sigma_x}{\bar{V}_x}$	$\bar{V}_y$ (Average) (m/s)	σ_y (S. D.) (m/s)	$\frac{\sigma_y}{\bar{V}_y}$	N (Number)
20	30	1.566	0.044	0.028	0.788	0.040	0.051	49
	45	1.150	0.057	0.050	1.116	0.038	0.034	61
	60	0.663	0.033	0.050	1.388	0.032	0.023	62
30	30	1.875	0.044	0.023	0.958	0.023	0.024	50
	45	1.313	0.050	0.038	1.371	0.044	0.032	50
	60	0.799	0.046	0.058	1.694	0.052	0.031	30

Table 2 Experimental results of the angular velocity

H (cm)	α (deg)	$\bar{\omega}$ (Average) (rad/s)	σ_ω (S. D.) (rad/s)	$\frac{\sigma_\omega}{\bar{\omega}}$	N (Number)
20	30	216.8	41.46	0.191	49
	45	293.4	51.37	0.175	61
	60	353.6	35.33	0.100	62
30	30	270.0	31.60	0.117	50
	45	429.3	55.74	0.130	50
	60	440.1	35.72	0.081	30

dary layer on the sphere. As is shown in Fig. 2, most of the previous experimental results were obtained for Reynolds numbers higher than 10^4. The work by Barkla et al. [1] is only one example of the previous experiments where the Reynolds number is lower than 10^4. The reason the scarcity of data of the Magnus force at low Reynold numbers (but higher than those for creeping motion) is that it is difficult to obtain results theoretically and experimentally.

The motivation of the present work is to get fundamental data which are necessary to calculate motion of particles conveyed pneumatically in a pipeline. Motion of solid particles in the pipe causes rotation due to collision with the pipe wall. In pneumatic conveying of coarse particles, the Reynolds number R_e is usually not so low as to apply the Stokes and Oseen treatments nor so high as to make use of the previous results at the Reynolds number higher than 10^4. Moreover, the results of low and high Reynolds numbers show different tendencies, as is seen in Fig. 2. Therefore we lack the knowledge required to estimate the Magnus force at intermediate Reynolds numbers. In this paper, experimental procedures and results at the Reynolds numbers of 550 to 1600 are presented.

2 Experimental Arrangements

Most of the previous experimental workers referred to in Introduction of this paper used a method where a sphere was rotated by an electric motor via a support and the Magnus force was measured directly by detecting the force acting on the support. However such a method is difficult for cases of the Reynolds number lower than 10^4, because the size of the sphere is too small for the support and the force is too small to detect. Thus, an indirect method was adopted in the present work. That is, a small sphere was made to collide with an in-

Nomenclature

C = coefficient defined by (11)
C_D, C_L = drag and lift coefficients
d = diameter of sphere
F_D, F_L = drag and lift forces
F_D, F_L = drag and lift forces
g = acceleration due to gravity
H = initial height of position of the sphere
I = moment of inertia of the sphere
L = range of flight of the sphere
R_e = Reynolds number, $u_r d/\nu$
$R_{e\omega}$ = Reynolds number, $(d/2)^2\omega/\nu$
S = projected sectional area of the sphere
T = torque on the sphere due to the viscosity
u_r = relative (slip) velocity between the sphere and fluid
V_X, V_Y = components of the sphere velocity in the X and Y directions immediately after collision between the sphere and plate, see Fig. 3
X, Y = coordinates, see Fig. 3
α = inclined angle, see Fig. 3
Γ = nondimensional angular velocity, $\frac{1}{2}d\omega/u_r$
ν = kinematic viscosity of the fluid
ρ_f, ρ_s = densities of the fluid and sphere
$\sigma_X, \sigma_Y, \sigma_\omega, \sigma_L$ = standard deviations corresponding to V_X, V_Y, ω and L
ω = angular velocity of rotation

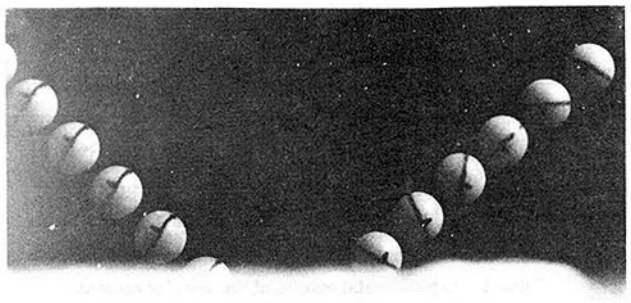

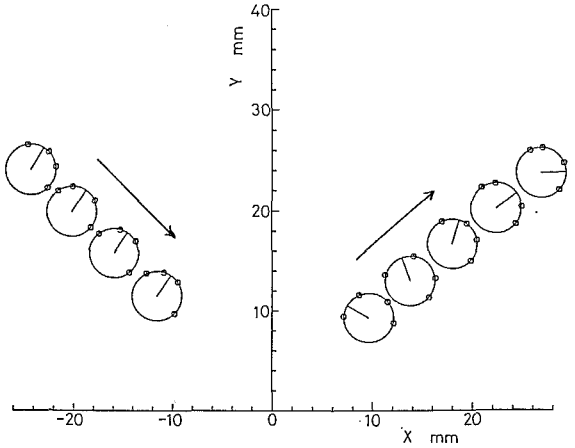

Fig. 5 Motion of the sphere near the plate ($H = 20$cm, $\alpha = 45$ deg) (*a*) Photograph (*b*) Reproduced picture

clined flat plate, as is shown in Fig. 3, and both the range of flight L and the rotational rate of the sphere was measured. The Magnus force was determined by comparing the measured range with the solution of the equation of motion which is described later. Figure 4 shows the outline of the equipment used. The sphere used in this work was a plastic one, 5 mm in diameter and 1040 kg/m^3 in density, which was manufactured as a chemical-proof bearing ball.

2.1 Measurements of Sphere Velocities and Rotational Rates After Collision. Symbols concerning the velocities before and after the collision are defined in Fig. 3. At first, the sphere was held at the end of a small tube (0.6 mm I.D.) by suction air of a vacuum cleaner, as is shown in an enlarged illustration in Fig. 4. When the valve ② was shut, the suction air stoped, which made the sphere fall down without rotation. After the sphere collided with the plate, it began to rotate. Consecutive pictures of the sphere were taken by stroboscopic photography, from which the velocities of the sphere were obtained. A line segment was marked on a part of the sphere surface. The angular velocity (rotation rate) was obtained by measuring the rate of change in angle of the line, which was due to the rotation.

The parameters which were varied in the present experiment were the height of an initial position of the sphere (H) and the inclined angle of the plate (α). Measurements were made for the cases of $H = 20$ and 30 cm and $\alpha = 30$, 45, and 60. The frequencies of the stroboscope light were set at $f = 300$ Hz for $H = 20$ cm and $f = 400$ Hz for $H = 30$ cm. Although the sphere used in this experiment had very good sphericity, data were inevitably scattered. This is common to experiments dealing with collision. Therefore averaging the results of many trials were needed to improve the accuracy of the results. The present authors used a digitizer connected to a microcomputer for the sake of preciseness and efficiency in film

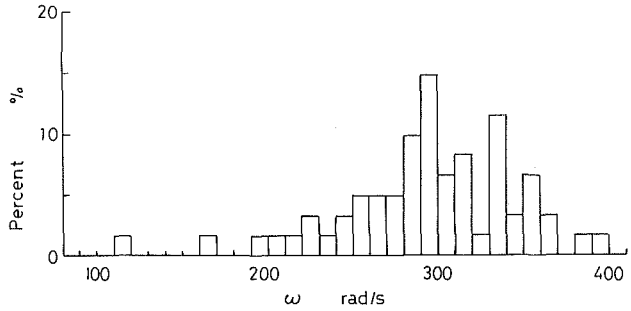

Fig. 6 Histogram of the angular velocity ($H = 20$cm, $\alpha = 45$ deg)

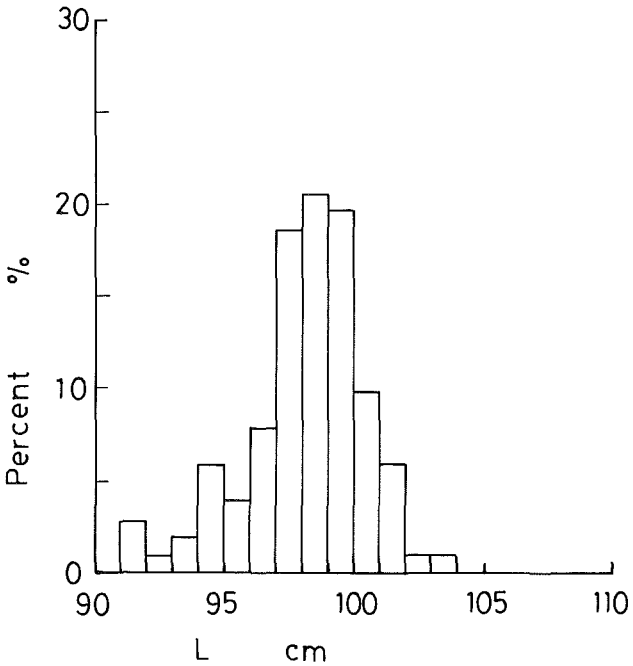

Fig. 7 Histogram of the range of flight ($H = 30$cm, $\alpha = 45$ deg)

readings. A negative film of the picture was enlarged ten times by a film enlarger and projected directly on the plate of the digitizer which digitized the coordinates of any point of the picture. Although three points on the circumference are enough to determine the center of the circle (sphere), four points were plotted on the projected circles. The coordinate of the center was determined by repeated calculations so that the circle calculated had these four points on its circumference as nearly as possible. The preciseness of coordinate readings was ±0.01 mm.

2.2 Measurements of Range of Flight. The range of flight of a bouncing sphere was measured in the following way. A number of lines were marked on the plate at intervals of 2 cm. Motion of the sphere was recorded by a video tape recorder. The position at which the sphere contacted the plate was obtained from the reproduced image on CRT by referring to the marked lines. The preciseness of these position readings was ± 2 mm. The data of the range were also significantly scattered. Therefore, measurements of the range under the same conditions were repeated more than 100 times.

3 Experimental Results

Figure 5 shows the motion of the sphere when it collided with the plate in the direction from left to right. Figure 5(*a*) is a photograph, while Fig. 5(*b*) is the result reproduced by the digitizer. Four points on each circumference indicate the

Table 3 Experimental results of the range of flight

H (cm)	α (deg)	$\bar{L}$ (Average) (m)	σ_L (S.D.) (m)	$\sigma_L/\bar{L}$	R_e	N (Number)
20	30	0.882	0.023	0.026	622 – 1406	111
	45	0.696	0.017	0.024	568 – 1198	106
	60	0.453	0.009	0.020	545 – 924	110
30	30	1.254	0.036	0.029	747 – 1640	111
	45	0.980	0.024	0.024	673 – 1405	102
	60	0.679	0.017	0.025	664 – 1099	109

Table 4 Coefficients in equation (8)

R_e	K_1	K_2	K_3
$R_e < 0.1$	0	24	0
$0.1 \leq R_e \leq 1.0$	3.69	22.73	0.0903
$1.0 \leq R_e \leq 10$	1.222	29.1667	-3.889
$10 \leq R_e \leq 10^2$	0.6167	46.5	-116.67
$10^2 \leq R_e \leq 10^3$	0.3644	98.33	-2778.0
$10^3 \leq R_e \leq 5\times10^3$	0.3571	148.62	-47500.0

points from which the center of the sphere was determined. The rotating motion of the sphere is clearly observed by the change of angle of the line segment marked on the sphere. Although the rate of change is given discretely in the picture, it was confirmed in a preliminary experiment that there was no possibility of aliasing error for the frequencies of the stroboscope.

Figures 6 and 7 present histograms of angular velocities and ranges of flight. The data are scattered widely as shown in the figures. Not only the angular velocity and range of flight but also the translation velocity showed a large scatter. Therefore, all the results are presented in numerical tables where averaged values, standard deviations σ and numbers of data N are given. The Reynolds number R_e varied during the flight due to the accelerating motion of the sphere. The range of variation of R_e is also shown in Table 3.

4 Equation of Motion

The equation of motion of a sphere which moves in a fluid at rest is generally given by

$$m\frac{d\mathbf{V}}{dt} = -m\left(1-\frac{\rho_f}{\rho_s}\right)g\mathbf{k} - (C_D\mathbf{V} - C_L\mathbf{e}\times\mathbf{V})\tfrac{1}{2}\rho_f|\mathbf{V}|S \quad (6)$$

where m is the mass of the sphere ($m=\rho_s\pi d^3/6$), $\mathbf{k}$ the unit vector in the vertical direction, e the unit vector perpendicular to $\mathbf{V}$ and g the acceleration due to gravity. The term of the virtual mass due to accelerated motion is neglected in (6). The gravitational constant constant g has the following local value,

$$g = 9.7973\text{m/s}^2 \quad (7)$$

It is assumed that the drag coefficient C_D is not influenced by the rotation and the empirical equation given by Morsi et al. [9] is applied to C_D

$$C_D = K_1 + \frac{K_2}{R_e} + \frac{K_3}{R_e^2} \quad (8)$$

Values of K_1 to K_3 are shown in Table 4. This simplification can be expected from the previous experiments, which show that C_D is not affected by rotation (Fig. 2).

The rotating motion of the sphere given by collision decays due to the fluid viscosity during the flight. The angular velocity changes according to the equation

$$I\frac{d\omega}{dt} = -T \quad (9)$$

where I is the moment of inertia of the sphere and T is the torque acting on the sphere. In this work, the result by Dennis et al. [10] was applied to T,

$$T = \tfrac{1}{2}\rho_f(\tfrac{1}{2}d)^5\omega^2(6.45/\sqrt{R_{e\omega}} + 32.1/R_{e\omega}) \quad (10)$$

$$R_{e\omega} = (\tfrac{1}{2}d)^2\omega/\nu$$

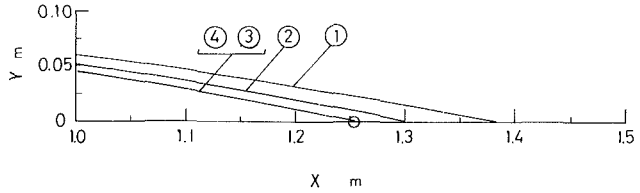

Fig. 8 Trajectories of the sphere ($H=30$cm, $\alpha=30$ deg, ①: All the fluid-dynamic forces are neglected. ②: Only the drag force is considered. ③: Both the drag and Magnus forces are considered. ④: Decay of the rotation due to the viscosity is considered in addition to the drag and Magnus forces. 0: Average value of measurements)

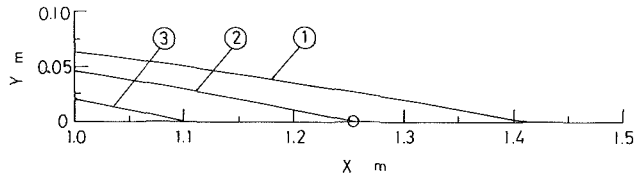

Fig. 9 Trajectories of the sphere ($H=30$cm, $\alpha=30$ deg ①: C_L by Macoll is used. ②: C_L of equation (11) with $C=0.4$ is used. ③: C_L by Rubinow et al. is used. 0: Average value of measurements

With respect to the expression for the Magnus lift coefficient C_L, the authors assumed the following form

$$C_L = C\times\Gamma \quad (11)$$

The reason for the above expression is that the present Reynolds numbers are not high enough to consider the negative lift and the theoretical result at low Reynolds numbers shows that C_L is proportional to Γ. In the equation of motion (6) where the unknown variable is $\mathbf{V}$, all the parameters are known except for C. Therefore, a locus and range of the sphere can be obtained by integrating (6) and (9) where the translation and angular velocities immediately after the collision are given as the initial conditions. The value of C which gives the best agreement with measurements of the range was obtained by trial and error.

5 Comparison Between Measurements and Calculations

Several calculated loci are compared in Fig. 8 to see the effects of fluid-dynamic forces. The region for X larger than 1 m is presented in the figure to emphasize the place where the sphere contacts the plate. The round circles plotted in the abscissa is an experimental point. Curve ① represents the case where all the fluid-dynamic forces are neglected, and curve ②, the case where only the fluid-drag is taken into consideration. Both drag and lift forces are considered in curve ③, where the coefficient C_L is assumed $C = 0.4$. In curve ④, the viscous decay of rotation is considered in addition to the drag and lift forces, but the difference between ③ and ④ is too small to recognize in the figure. Figure 8 indicates that the Magnus force obviously influences the locus of the sphere and that the value of $C = 0.4$ gives good agreement with the experimental point. In the following calculated results, all the fluid-dynamic forces are taken into consideration as in ④.

Loci based on the lift coefficient given by Macoll [4] and Rubinow et al. [3] are shown in Fig. 9, where the curve ① is the case of C_L by Macoll, the curve ②, the case of C_L of (11) with $C = 0.4$, and the curve ③, the case of C_L by Rubinow et al. The lift coefficients by Macoll and Rubinow et al. do not explain the measured point. This tendency was common to conditions other than Fig. 9 and thus it is certain that C_L which compares well with the present measurements lies between the results by Macoll and Rubinow et al.

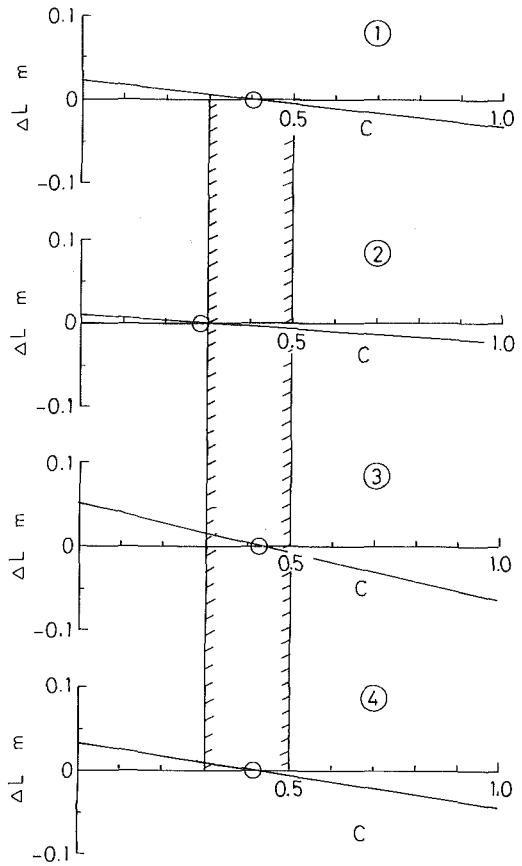

Fig. 10 Relation between ΔL and C (①: $H = 20$cm, $\alpha = 30$ deg, ②: $H = 20$cm, $\alpha = 45$ deg, ③: $H = 30$cm, $\alpha = 30$ deg, ④: $H = 30$cm, $\alpha = 45$ deg)

In order to determine the best value of C, the authors changed the value of C systematically and investigated the difference in the range between calculations and experiments, $\Delta L = L_{cal} - L_{exp}$. Figure 10 shows the relation between ΔL and C, where the circle point indicates the value corresponding to $\Delta L = 0$. Results at $\alpha = 60$ deg are omitted in the figure, because the difference due to C did not appear in ΔL, i.e., the values of $C = 0 \sim 1.0$ gave almost the same result $\Delta L = 0$ at $\alpha = 60$ deg. It is found in Fig. 10 that C corresponding to $\Delta L = 0$ takes the value

$$C = 0.4 \pm 0.1 \tag{12}$$

for different values of α and H.

If the value of C should be adjusted differently according to the experimental conditions, it would be questionable to assume the equation (11) and to neglect the effect of the rotation on C_D. Fortunately, as was seen, C has the same value for various conditions and thus equations (11) and (12) are justified. However we must notice that equations (11) and (12) are confirmed under the condition that

$$\left.\begin{aligned} R_e &= 550 \sim 1600 \\ \Gamma &< 0.7 \end{aligned}\right\} \tag{13}$$

Barkla et al. [1] made an experiment under the same range of the Reynolds number as the present one. They obtained the lift coefficient from the orbit of a rotating sphere which was suspended as a pendulum. In their experiment, Γ was larger than 1, and C_L increased monotonically with increasing Γ unlike the results of Macoll [4] (see Fig. 2). The values of Γ in this experiment are limited to less than 0.7, but the curve of the present result is approximately connected with that of Barkla et al., as is found in Fig. 2.

6 Conclusions

The Magnus force F_L on a rotating sphere (diameter $d = 5$ mm) was obtained from trajectories of the sphere which impinged on an inclined plate. Translation and angular velocities and ranges of flight after impingement were measured in a number of trials by the use of a camera, VTR and digitizer. Comparing measurements of the range of flight with the solutions of the equation of motion, it was found that the lift coefficient C_L defined by $F_L = C_L \frac{1}{2}\rho_f u_r^2 S$ is given by $C_L = (0.4 \pm 0.1)\Gamma$, where Γ is the nondimensional angular velocity $\Gamma = \frac{1}{2}d\omega/u_r$, ω the angular velocity and u_r is the relative velocity between the fluid and sphere. The present result was obtained under the condition that the Reynolds number $R_e = u_r d/\nu = 550 \sim 1600$ and Γ was less than 0.7.

The authors should like to thank Mr. Toshihumi Sano for his assistance in the present experiment. This work was supported by the Grant-in-Aid for Co-operative Research in Japan, Grant No. A-58350008.

References

1 Barkla, H. M., and Auchterlonie, L. J., "The Magnus or Robins Effect on Rotating Spheres," *J. Fluid Mechanics*, Vol. 47, Part 3, 1971, pp. 437–448.

2 Magnus, G., "Über die Abweichung der Geschlosse, und eine auffallende Erscheinung bei rotierenden Körpern," *Poggendorfs Annalen der Physik und Chemie*, Vol. 88, 1853, p. 1.

3 Rubinow, S. I., and Keller, J. B., "The Transverse Force on a Spinning Sphere Moving in a Viscous Fluid," *J. Fluid Mechanics*, Vol. 11, 1961, pp. 447–459.

4 Macoll, J. H., "Aerodynamics of a Spinning Sphere," *J. Roy. Aero. Soc.*, Vol. 32, 1928, pp. 777–798.

5 Davies, J. M., "The Aerodynamics of Golf Balls," *J. Appl. Phys.*, Vol. 20, 1949, pp. 821–828.

6 Tani, I., "Baseball's Curved Balls," *Kagaku*, Vol. 20, 1950, pp. 405–409 (in Japanese).

7 Taneda, S., "Negative Magnus Effect," Rep. Res. Inst. Appl. Phys. Kyushu University, Vol. 20, 1957, pp. 123–128.

8 Clift, R., Grace, J. R., and Weber, M. E., *Bubbles, Drops, and Particles*, Academic Press, 1978, p. 262.

9 Morsi, S. A., and Alexander, A. J., "An Investigation of Particle Trajectories in Two-Phase Flow Systems," *J. Fluid Mechanics*, Vol. 55, Part 2, 1972, pp. 193–208.

10 Dennis, S. C. R., Singh, S. N. and Ingham, D. B., "The Steady Flow due to a Rotating Sphere at Low and Moderate Reynolds Numbers," *J. Fluid Mechanics*, Vol. 101, Part 2, 1980, pp. 257–279.

C. D. Tropea
Research Assistant.

R. Gackstatter
Student.

Lehrstuhl fur Strömungsmechanik,
University of Erlangen-Nürnberg,
Egerlandstr. 13, 8520 Erlangen,
Federal Republic of Germany

The Flow Over Two-Dimensional Surface-Mounted Obstacles at Low Reynolds Numbers

The flow over a fence and a block mounted in a fully developed channel flow is experimentally investigated as a function of the Reynolds number, blockage ratio and length-to-height ratio using a laser-Doppler-anemometer. The information obtained includes the location and size of the primary and secondary recirculation zones, and profiles of the mean streamwise velocity component. The experiments were carried out in a channel for a Reynolds number in the range $150 < Re_H < 4500$. *Comparisons are drawn between the obstacle flow and the backward-facing step flow.*

1 Introduction

The flow over obstacles, hills, and steps has in the past been the subject of numerous investigations, partially because of its relevance in a multitude of engineering applications and partially because these simple geometries lend themselves well as a proving stone on which theoretical or numerical models can be tested. The role of experimental investigations of these flows is to establish general trends and relations between the relevant parameters, and subsequently to provide detailed verification data of the velocity field for comparison with numerical predictions. These goals also served the present study, in which the flow over a sharp-edged obstable was examined.

Previous experience with the backward-facing step in internal flows has shown that the Reynolds number and the blockage ratio, i.e., the ratio of the obstacle height to the channel height, h/H, both influence the flow significantly [1]. Furthermore, it is expected in the case of flow over an obstacle that the length-to-height ratio of the obstacle, l/h, will also be a relevant parameter. In particular two limiting cases can be identified; for $l/h \to \infty$ we obtain a forward-facing step followed by a backward-facing step, with no interaction between the "two" flows. For decreasing l/h this interaction increases, presumably reaching a maximum for the flow over a fence, i.e. for $l/h \to 0$. A prime object of the work reported here was, therefore, to examine the flow as a function of these three nondimensional parameters; Re, h/H and l/h.

Although a considerable number of experiments have been carried out in the past on the obstacle flow [2–8], none of these have dealt with the low Reynolds number range and none have looked at an obstacle submerged in a fully developed channel flow. One reason for the latter is that many studies were directly related to modelling structures in the atmospheric boundary layer, and as such the influence of the normalized boundary layer thickness parameter, δ/h, was of prime interest. Castro [5] showed for instance that in the range $0.34 < \delta/h < 0.80$, the reattachment length decreases with decreasing δ/h.

Contributed by the Fluids Engineering Division for publication in the JOURNAL OF FLUIDS ENGINEERING. Manuscript received by the Fluids Engineering Division, October 4, 1984.

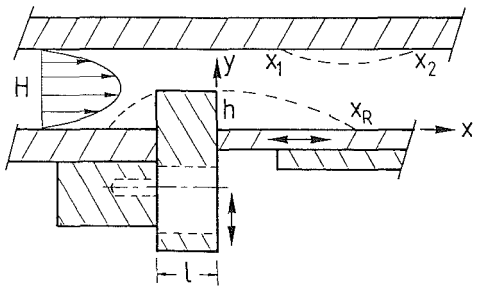

Fig. 1 The geometry of the surface-mounted obstacle

At least one study [7] has systematically looked at the mean reattachment length behind the obstacle, x_R/h, as a function of increasing l/h ratio for an obstacle submerged in a boundary layer. In their investigation Bergeles and Athanassiadis [7] show that the flow reattaches on the top surface of the obstacle for $l/h > 4$, and accordingly the reattachment length behind the obstacle experiences a sudden decrease from $x_R/h = 11$ to $x_R/h = 3$. Castro [8] however, shows that this behavior is very sensitive to the oncoming boundary layer. In one study performed in a rough wall boundary layer he found that even for a length ratio of $l/h = 1$, the shear layer separating from the leading edge of the obstacle reattached onto the top surface for values of l/h and h/H similar to the smooth wall measurements where no reattachment had occurred.

Durst and Rastogi [6] investigated the effect of varying the blockage ratio from 0.5 to 0 (open test section) while keeping l/h constant. A strong variation of x_R/h from 5 to 14–16 was found, the exact values again depending on the length ratio l/h in the same manner as indicated in [7]. Two important results can be derived from their measurements. Firstly the blockage ratio appears to be influential for values above 0.04, which is in good agreement with results for the flow over backward-facing steps [1]. Secondly, they showed that the length-to-height ratio of the obstacle, l/h, has no significant influence on the mean reattachment length for values less than 0.33. This result, which essentially prescribes how thin an obstacle must be to be classified as a fence, is also of use in the present study. Interestingly, Durst and Rastogi found that a fence that

was bevelled to a sharp edge consistently resulted in longer reattachment lengths. Therefore, although the ratio l/h has little influence on x_R/h at low values ($l < .33$), the shape of the separating edge appears to be important. This influence was however not investigated any further in the present work.

Despite the fact that all of the above investigations were performed at a channel Reynolds number above 5000 some similarities to the present results can be identified in the following sections.

2 Apparatus and Procedure.

Experimental Apparatus. The measurements were performed in a channel of cross-section 1 cm × 18 cm ($H \times W$) with an inlet section identical to that described by Armaly et al. [9]. The obstacle was placed 70 cm downstream of the channel inlet and thus in a region of fully developed channel flow for all investigated Reynolds numbers. A universal mount allowed positioning of the obstacle at any desired height in the channel and a movable wall on the obstacle side permitted obstacles of varying length to be installed (see Fig. 1).

The air supply to the channel was a composite of a radial fan and compressed air used for particle seeding and were brought together in a large mixing chamber prior to the test rig. Both supplies were continuously monitored, the fan with a tachometer and the compressed air line with a water-filled U-tube manometer. The long time stability of the inlet mass flow rate was experimentally determined to be within 4 percent.

The velocity measurements were obtained using a one-component laser-Doppler anemometer operated in the forward scatter mode. Reverse flow regions and regions of large velocity fluctuations were resolved using frequency shifting of up to 2 MHz by means of a double Bragg cell module. The control volume dimensions were approximately ϕ 220 μm × 2.6 mm. Particle seeding was achieved using olive oil in an atomizer and a separator, producing particles in the size range 0.5 μm–5 μm. Point-wise traversing of the flow was carried out by leaving the LDA-system stationary and traversing the test section. A mechanical gauge was used to measure the relative y-position to within 10 μm, and simple machine rules provided accuracy of ±.5 mm in the x and z movements.

The signal processing used in this study was based on the digital acquisition of individual, bandpass filtered Doppler bursts using a transient recorder (Datalab DL 1080, 20 MHz). The digitized bursts were transferred to the host computer (HP A700) and an on-line evaluation of the burst frequency was performed according to methods outlined by Tropea [10]. The computed results consisted of mean and RMS flow velocity using arithmetic averages, and the probability density distribution of the samples. This information was directly stored on disk for subsequent evaluation. Since this system is capable of processing only about 20 doppler bursts per second, it falls into the category of "controlled processor" in the terminology of Erdmann and Tropea [11], (and in most regions of the flow can be considered a one-shot processor). The turbulence-induced normalized bias of the mean velocity in this case was shown in [11] to be a minimum reaching typical values of $0.10\,\eta^2$ for $\eta \sim .3$ where η^2 is the square of the normalized variance of the local velocity fluctuations. However, in the recirculation zones where very low particle rates occur and local turbulent levels are high ($\eta \sim 1.0$), this error can reach absolute values of up to $.06\,\eta^2$.

Experimental Procedure. The location of the flow separation and reattachment were determined by directly measuring the velocity distribution in the vicinity of the required point. In this manner, the line on which $\bar{U} = 0$ could be extrapolated to the wall. Thus the separation and reattachment points presented in the following corresponded to points at which the mean streamline $\Psi = 0$ intersects the wall. Errors in this method occur both in the determination of the true y-position of the measurement volume and in the velocity measurement itself, especially in regions of high turbulence intensity and low particle rates. The uncertainty of these positions was estimated to be ±1 mm. Secondary recirculation zones appearing on the wall opposite the obstacle were also identified using this technique. It should however be remarked that the dimensions of these regions were very small at their onset or disappearance with changing Reynolds number. In such cases the measurement uncertainty of the mean separation or reattachment point could increase considerably up to ±2.5 mm.

Preliminary measurements with and without the obstacle were performed to check the spanwise uniformity of the channel flow. The mean velocity was found to be uniform to within 0.5 percent in the central 2/3 portion of the channel, for channel Reynolds numbers in the range of 75 to 6000. Subsequent measurements were restricted to the channel centerline. The flow rate as obtained by integrating the mean velocity profiles showed scatter within about 3 percent with the obstacle mounted, occasionally attaining somewhat higher values, but with no identifiable trend with regards to the x-position.

Test Conditions. In order to characterize the flow in laminar, transitional, and turbulent regimes, analogous to the backstep flow, initial measurements of the mean reattachment length were performed over a large range of geometric and dynamic parameters. Two obstables were used, a fence of 1 mm thickness (i.e., $l = 1$ mm), and a 20 mm block. These were each placed at three heights in the channel corresponding to a blockage ratio, h/H, of 0.25, 0.50, and 0.75. The ratio of the channel width to obstable height therefore varied between 24 and 72. The Reynolds number based on the centerline velocity of the approaching flow, U_0, and on the channel half-width, $H/2$, was varied between 150 and 4500.

Following this initial survey of the flow more detailed velocity profiles were obtained for selected Reynolds numbers in the fully laminar range. Although not all of this information is explicitly presented in this paper, the complete set of these conditions is summarized in Table 1. Results are presented for the boxed in conditions. A complete report of all measurements obtained can be found in [12].

Nomenclature

ER = $H/(H-h)$ Expansion ratio
H = channel height (H = 1 cm)
h = height of obstacle
l = length of obstacle
$\mathrm{Re}_H = \dfrac{U_0 H/2}{\nu}$ channel Reynolds number
Re_h = $U_g h/\nu$ (for laminar flow $\mathrm{Re}_h = \mathrm{Re}_H \times 1.32\,(\mathrm{ER}-1)$)
$\bar{U}$ = mean velocity at a point
U_0 = maximum channel velocity on the centerline upstream of obstacle
U_g = mean profile average velocity in the plane above the obstacle (gap velocity)
x_R = mean reattachment length
x_1, x_2 = separation and reattachment position of secondary recirculation zone
δ = boundary layer thickness
η^2 = $\sigma^2/\bar{U}^2$ reduced variance of velocity fluctuations
ν = kinematic viscosity of working fluid

Table 1 Summary of test conditions for which detailed velocity profiles were obtained

	$l=20$ mm			$l=1$ mm		
h/H	Channel $\mathrm{Re}_H=\frac{U_0 H/2}{\nu}$					
.25	111	395	770	–	–	–
.50	144	463	–	120	218	773
.75	177	387	–	82	142	766

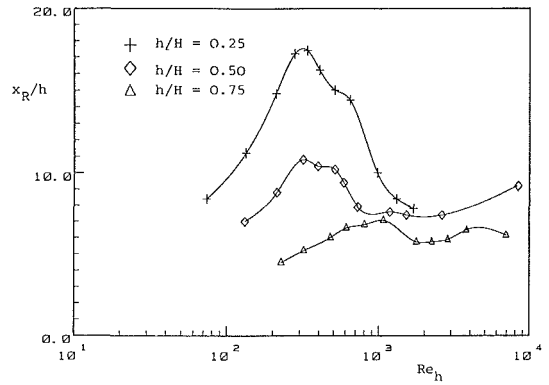

Fig. 2 Reattachment length as a function of Reynolds number for the fence obstacle (l-1 mm). (Uncertainty in Re_h: ±4.5 percent and x_R/h: less than ± 6 percent.)

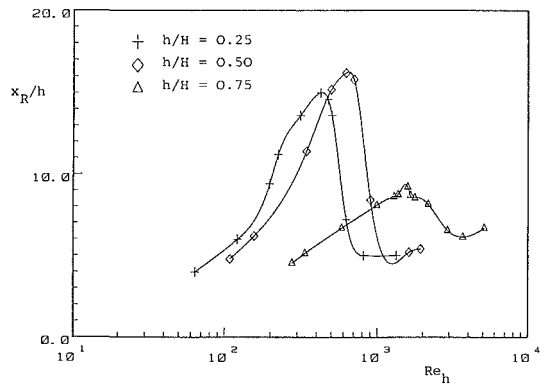

Fig. 3 Reattachment length as a function of Reynolds number for the block obstacle (l-20 mm). (Uncertainty in Re_h: ±4.5 percent and x_R/h: less than ±6 percent.)

3 Experimental Results

Positions of Separation and Reattachment. The main results of this part of the investigation are contained in Figs. 2 and 3, showing the reduced reattachment length, x_R/h, plotted as a function of the step-height Reynolds number $\mathrm{Re}_h = U_g h/\nu$, where U_g is the spatial mean velocity in the gap above the obstacle. The choice of length and velocity scales on which to base the Reynolds number is somewhat arbitrary, however reference is made here to experience with the backward-facing step in which the variations in x_R/h for different blockage ratios are well correlated to Re_h. Inspection of Figs. 2 and 3 indicate that this correlation is not as strong for the obstacle flow. On the other hand the choice of the gap velocity U_g, allows direct comparison with results obtained for the backward-facing step geometry.

The dependence of x_R/h on Reynolds number as shown in these figures follows the general pattern common to the backward-facing step flow. Three regions can be identified;

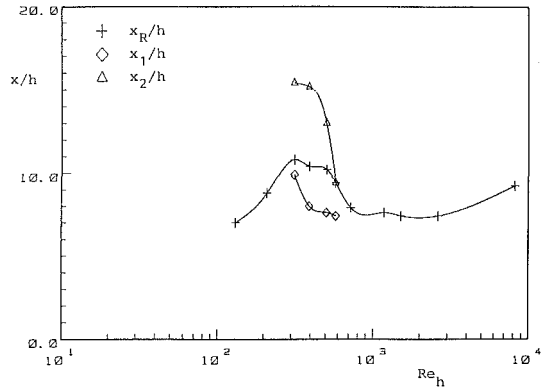

Fig. 4 The secondary recirculation zone for the h/H-0.5 fence. (Uncertainty in Re_h ±4.5 percent and x_R/h: less than ±6 percent.)

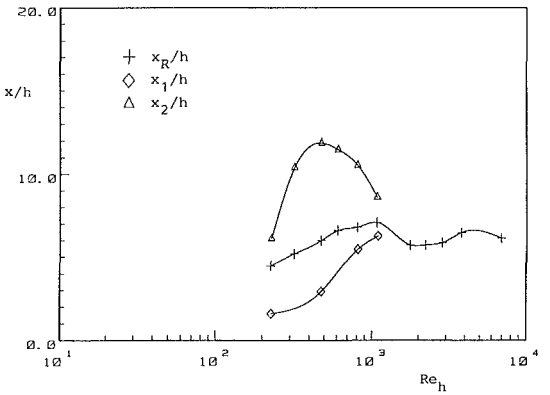

Fig. 5 The secondary recirculation zone for the h/H-0.75 fence. (Uncertainty in Re_h: ±4.5 percent and x_R/h: less than ±6 percent.)

the laminar region with a steady increase of x_R/h with Reynolds number; the transitional region marked by an abrupt drop in x_R/h and in some cases, a partial recovery; and a turbulent region in which x_R/h is not expected to vary much but which was not achieved with the present test rig. For both the fence and the block geometry the transitional region occurred in the Reynolds number range $400 < \mathrm{Re}_h < 4000$, the exact values depending on the blockage ratio. For comparison purposes, the range found for the backward-facing step flow with an expansion ratio of $\mathrm{ER} = H/(H-h) = 2.0$ was $1000 < \mathrm{Re}_h < 10{,}000$.

Figure 2 shows clearly the effect of the blockage ratio on x_R/h for the fence geometry. Strictly, the length ratio l/h has also been varied in this diagram, however from the previous results of Durst and Rastogi [6] this should have little influence for this range of l/h. It can be seen that the reattachment length drops significantly with increasing blockage, at least for the laminar and transitional conditions investigated here. Although the turbulent range has not been investigated, the indication from Fig. 2 is that this influence would be somewhat weaker at higher Reynolds numbers.

One reason for the very strong changes of x_R/h with blockage ratio is the appearance of a secondary recirculation zone on the wall opposite the fence. In Figs. 4 and 5 the separation point, x_1, and the position of mean reattachment, x_2, of the secondary recirculation region are shown for the $h/H = 0.5$ and the $h/H = 0.75$ fence, respectively. No such region was found for the $h/H = 0.25$ fence. While the interaction between the pressure field and the velocity field are not fully understood in regions of separation, it is evident that the recirculation zone in Figs. 4 and 5 is a result of a strong rise in the static pressure due to the sudden expansion behind the

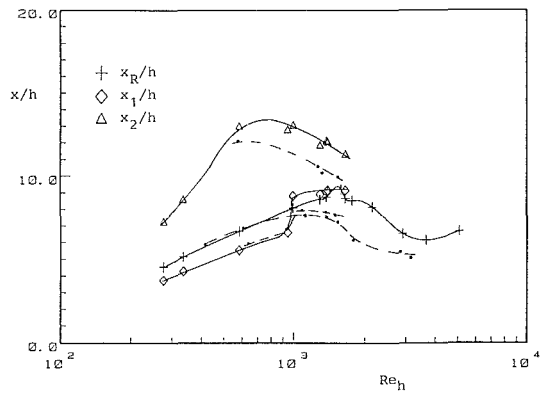

Fig. 6 The secondary recirculation zone for the *h/H*-0.75 obstacle. (Uncertainty in Re_h: ±4.5 percent and x_R/h: less than ±6 percent.)

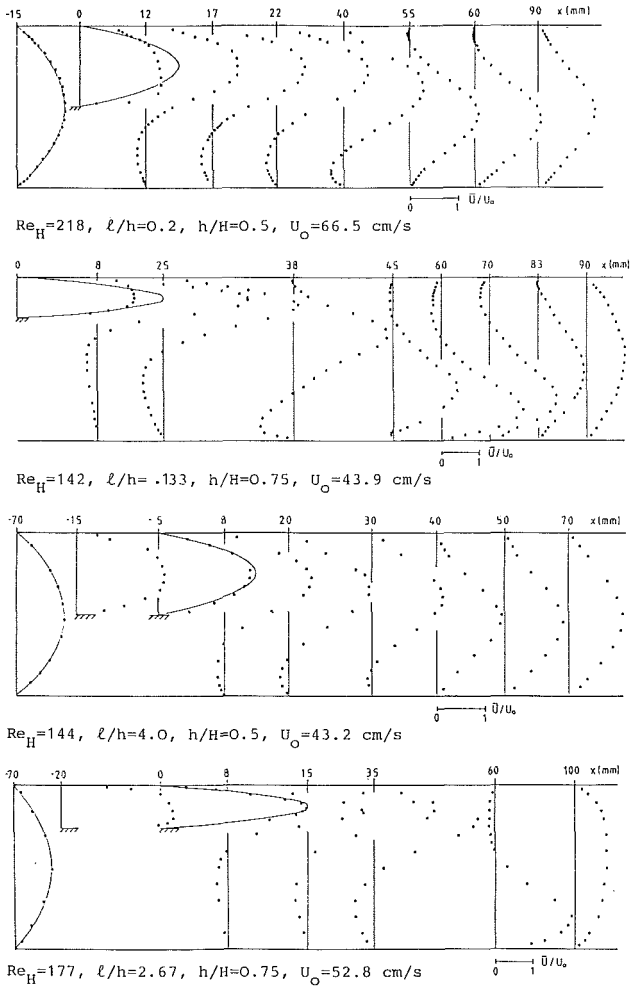

Fig. 7 Measured mean velocity profiles. (Uncertainty in *x*: ±.50 mm and *h*: ± .05 mm and U_0: 4 percent. Uncertainty in *U*: outside recirculation areas ± .1 cm/s, within recirculation areas ± .50 cm/s.)

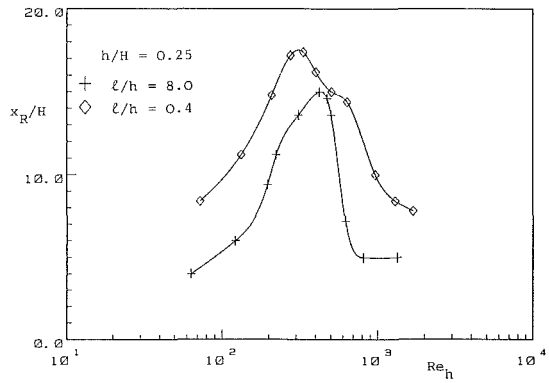

Fig. 8 The mean reattachment length at a blockage ratio of *h/H*-0.25. (Uncertainty in Re_h: ±4.5 percent and x_R/h: less than ±6 percent.)

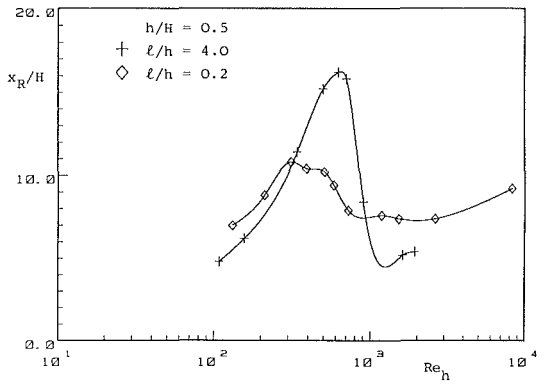

Fig. 9 The mean reattachment length at a blockage ratio of *h/H*-0.50 (Uncertainty in Re_h: ±4.5 percent and x_R/h: less than ± 6 percent.)

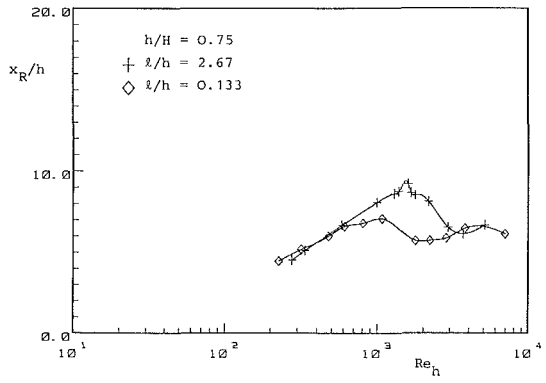

Fig. 10 The mean reattachment length at a blockage ratio of *h/H*-0.75 (Uncertainty in Re_h: ±4.5 percent and x_R/h: less than ±6 percent.)

obstacle. The flow, having been accelerated through the gap above the obstacle can no longer transfer enough of its *U*-momentum in the *y*-direction to overcome the pressure rise.

A similar behavior of the flow was observed for the obstacle geometry as shown in Fig. 6. In this case however, a secondary recirculation region was only found in the case of the $h/H = 0.75$ obstacle. Hence the blockage ratio effect as shown in Fig. 3 was most predominant for this obstacle height. The reasons for this difference between the obstacle and the fence flow appear to be straightforward. The accelerated flow in the gap above the obstacle has a length of channel within which it can "relax," i.e., the *U*-momentum can redistribute itself somewhat before encountering the sharp rise in pressure following the trailing edge of the obstacle. In the case of the $h/H = 0.5$ obstacle, this "relaxation" is apparently sufficient to prevent separation on the upper channel wall.

In addition, Fig. 6 indicates that the secondary recirculation zone experiences an abrupt decrease in size with increasing Reynolds number. This occurs in a manner such that the separation point, x_1, no longer lies before the reattachment on the opposite wall, x_R. In checking the repeatability of this result another feature of the flow was brought to light. Although the solid curves in Fig. 6 could be repeated many times on different occasions, the results indicated by the dashed curves were equally likely, although no alternating be-

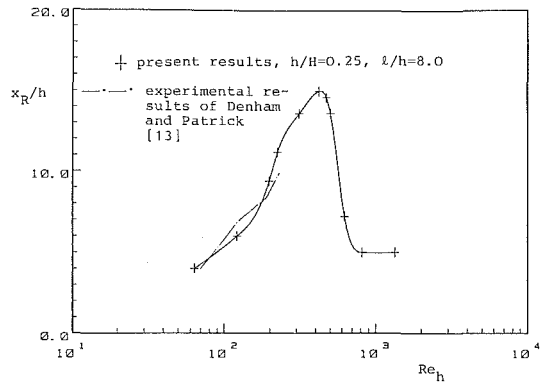

Fig. 11 Comparison of present results with those of Denham and Patrick [13]. (Uncertainty in Re_h: ±4.5 percent and x_R/h: less than ±6 percent.)

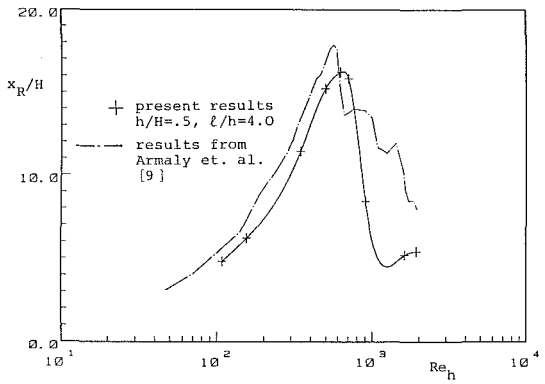

Fig. 12 Comparison of present results with those of Armaly et al. [9] (Uncertainty in Re_h: ±4.5 percent and x_R/h: less than ±6 percent.)

tween the two was observed while the channel was running. In spite of the fact that this behavior was not observed for any of the other geometries studied, such a duality in flow states immediately cast doubts, on for instance, the inlet flow control, seeding, or the presence of hysteresis effects in the channel. Therefore all such influences were once again investigated, yielding no systematic correlation, at least within the accuracy to which all parameters could be controlled. It appears, therefore, that there exist two quite stable flow conditions for this particular geometry. Interestly, the abrupt change in size of the secondary recirculation zone remains in both cases.

Velocity Profiles. A selection of the measured mean velocity profiles is shown in Fig. 7 for the fence and obstacle geometries at a channel Reynolds number of approximately 150. The corresponding RMS of the fluctuating velocity component was also measured, however it is of little value for comparison purposes with numerical predictions of laminar flows. On the other hand the RMS velocity profile at the last downstream station indicated clearly that although the mean velocity profile had taken on a parabolic shape, the flow had not yet reached an undisturbed state, since the RMS profile were still highly distorted from its inlet condition.

The profiles in Fig. 7 have been corrected for the nonuniform mass flowrate as obtained by integrating the U-velocity profile across the channel. The scatter of 0–5 percent with reference to the inlet profile was removed by a simple uniform scaling of all points. This was done only out of convenience for comparison to numerical predictions, which of course conserve mass exactly.

In Fig. 7 parabolas are drawn in over the measured inlet flow profile and at the separating edge for purposes of comparison. Characteristic of all the flows is the velocity overshoot near the upper surface of the obstacle. This again illustrates the inability of the flow to transfer enough of it U-momentum in the y direction following the forward-facing step to yield a symmetric profile. It is also interesting to note that there exists no significant recirculation zone on the obstacle surface. This appears to be a major distinction between internal and open flow situations. Since near wall RMS values remained below three percent of the maximum channel velocity it is assumed that the flow remained laminar throughout the contraction for all cases presented here.

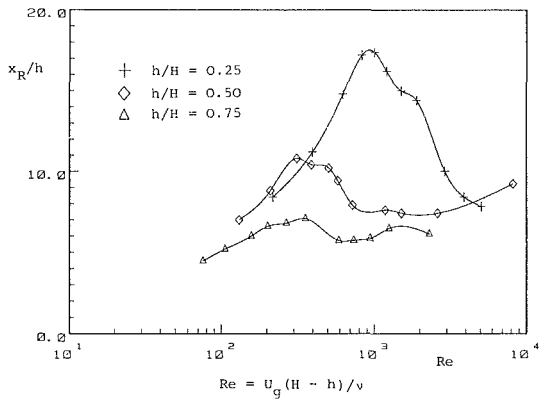

Fig. 13 Reattachment length as a function of Reynolds number for the obstacle (l–20 mm). (Uncertainty in Re_h: ±4.5 percent and x_R/h: less than ±6 percent.)

Discussion

One object of the present study is to directly compare the fence flow with the obstacle flow, under otherwise similar conditions. This is done in Figs. 8–10, in which the data of Figs. 2 and 3 is reploted for constant blockage ratios, but for different l/h, whereby one set of results in each diagram can be considered a fence flow.

It is seen that at low blockage ratios the fence geometry results consistently in longer reattachment lengths. This compares well with results at higher Reynolds numbers from Bergeles and Athanassiadis [7], and Durst and Rastogi [6], the general explanation being that the flow separates from the fence with an appreciable positive V-velocity component, thus prolonging the reattachment. At higher blockage ratios however, this pattern is reversed and the obstacle begins to show longer reattachment lengths. For the blockage ratio $h/H = 0.5$ this is no doubt due to the appearance of the secondary recirculation zone for the fence and not for the obstacle. At a blockage ratio of 0.75, the secondary recirculation is smaller in dimensions for the obstacle than for the fence.

In the limit of $l/h \to \infty$ the obstacle flow must revert to the backward-facing step flow and although the results in Fig. 7 show that this point is not yet fully reached in terms of the separating velocity profile, a comparison of reattachment lengths can still be drawn. Figure 11 shows the x_R/h results of the $h/H = 0.25$ obstacle with results obtained by Denham and Patrick [13] for a backstep with expansion ratio ER = 1.5. Although the expansion ratio in the present case was only ER = 1.33 good agreement can be seen between the two investigations. A further comparison is shown in Fig. 12 in the which the x_R results of the $h/H = 0.5$ obstacle are shown with results taken from Armaly et al. [9] for a backstep flow with an expansion ratio of ER = 2.0. Similarities are seen not only in the magnitude of x_R/h, but also in the Reynolds number range distinguishing the transitional state of the flow. The difference between the two curves, namely that the obstacle flow consistently yielded lower reattachment lengths, could be due to the nonfully developed velocity profile at separation. In [14] for instance, it was shown using a combination of ex-

perimental and numerical results, that a stronger velocity gradient at separation leads to shorter mean reattachment lengths.

Finally it was the purpose of this investigation to study the influence of the blockage ratio on the flow over obstacles. One effect had already been discussed; the shortening of the main recirculation zone with increasing blockage ratio, largely due to the appearance of secondary recirculation zones. From Figs. 2 and 3 however, it is also apparent that the onset of the transitional region occurs at higher Reynolds numbers for higher blockage ratios. Physical explanations for this are not readily apparent and in fact the data may be deceptive due to the choice of the Reynolds number definition. If for instance the sudden drop in the reattachment length with increasing Reynolds number is associated with the physical process of the separating, laminar shear layer becoming turbulent prior to reattachment, as has been postulated by many authors for the backstep flow [1], [15], then it may be more appropriate to choose length and velocity scales for the Reynolds number, which are more characteristic of the velocity gradient at separation. Thus the Reynolds number using the mean velocity above the obstacle and the gap height would be appropriate. The results of Fig. 3 are replotted in Fig. 13 using this Reynolds number. In this presentation of the results the onset of transition occurs at lower Reynolds numbers with increasing blockage ratio. This suggests that the ability of the separated shear layer to remain laminar is negatively influenced by either the higher acceleration of flow through the gap, or the stronger pressure rise after the obstacle in the case of higher blockage ratio.

Acknowledgments

The authors would like to thank J. C. F. Pereira, several of whose measurements appear in the results presented. Also the financial support of the Deutsche Forschungsgemeinschaft under Project Tro 194/1-1 is gratefully acknowledged.

References

1 Durst, F., and Tropea, C., "Flows Over Two-Dimensional Backward-Facing Steps," *Structure of Complex Turb. Flows IUTAM Symposium*, Marseille, 1982, Ed. Dumas, Fulachier, Berlin, Springer Verlag, 1982.

2 Good, M. C., and Joubert, P. N., "The Form Drag of Two-Dimensional Bluff-Plates Immersed in Turbulent Boundary Layers," *J. Fluid Mech.*, Vol. 31, 1968, p. 547.

3 Cenedese, A., Iannetta, S., Mele, P., and Pietrogiacomi, D., "Non-Stationary Analysis of Velocity Field Around a Square Section Bluff Body," *Turb. Shear Flows 1* (Ed. Durst et al.), Berlin, Springer Verlag, 1977.

4 Crabb, D., Durao, D. F. G., and Whitelaw, J. H., "Velocity Characteristics in the Vicinity of a Two-Dimensional Rib," *Proc. 4th Brazilian Cong. of Mech. Eng.*, Paper B-3, 1977.

5 Castro, I. P., "Measurements in Shear Layers Separating From Surface-Mounted Bluff Bodies," *J. Wind Eng. and Ind. Aero.*, Vol. 7, 1981, p. 253.

6 Durst, F., and Rastogi, A. K., "Turbulent Flow over Two-Dimensional Fences," *Turb. Shear Flow 2* (Ed. Bradbury et al.), Berlin, Springer Verlag, 1979.

7 Bergeles, G., and Athanassiadis, N., "The Flow Past a Surface-Mounted Obstacle," ASME JOURNAL OF FLUID ENGINEERING, Vol. 105, 1983, p. 461.

8 Castro, I. P., "Relaxing Wakes Behind Surface-Mounted Obstacles in Rough Wall Boundary Layers," *J. Fluid Mech.*, Vol. 93, 1979, p. 631.

9 Armaly, B. F., Durst, F., Pereira, J. C. F., and Schönung, B., "Experimental and Theoretical Investigation of Backward-Facing Step Flow," *J. Fluid Mech.*, Vol. 127, 1983, p. 473.

10 Tropea, C., "Die turbulente Stufenströmung in Flachkanälen und offenen Gerinnen," diss., Universität Karlsruhe, 1982.

11 Erdmann, J. C., and Tropea, C., "Turbulence-Induced Statistical Bias in Laser Anemometry," *Proc. 7th Bi. Symp. on Turb.*, Rolla, 1981.

12 Gackstatter, R., "Experimentelle Untersuchungen der abgelösten Strömung über zweidimensionale Hindernisse mittels Laser-Doppler-Anemometrie," Diplomarbeit, Lehrstuhl für Strömungsmechanik, Universität Erlangen-Nürnberg, FRG, 1984.

13 Denham, M. K., and Patrick, M. A., "Laminar Flow Over a Downstream-Facing Step in an Two-Dimensional Flow Channel," *Trans. Instn. Chem. Eng.*, Vol. 52, 1974, p. 361.

14 Atkins, D. J., Maskell, S. J., Patrick, M. A., "Numerical Prediction of Separated Flows," Internal Report, Dept. of Chem. Eng. and Math., Univ. of Exeter, Devan U. K.

15 Lurz, W., "An Experimental Study of the Effect of a Backward-Facing Step in the Flat Plate upon the Laminar Boundary Layer," Report No. 80-A!, Series A, Helsinki, Univ. of Tech., Lab. of Aero., 1980.

Flow in an Open Tank With a Free Surface Driven by the Spinning Bottom

Jae Min Hyun[1]
Department of Mechanical Engineering,
Clarkson University,
Potsdam, New York 13676
Mem. ASME

An investigation is made of flows of a viscous incompressible fluid inside a circular cylindrical tank. The flow is driven by the spinning bottom endwall disk of the tank. Numerical solutions of the Navier-Stokes equations were obtained over a range of rotational Reynolds number and of aspect ratio (cylinder height/radius) using two kinds of boundary condition at the top: a closed tank with a rigid lid and an open tank with a free surface. We provide descriptions of flow details for these two boundary conditions at the top. For small aspect ratios, the nature of the azimuthal flow is distinctly different depending on the type of the top boundary condition, i.e., a Couette flow under a rigid lid and a solid-body rotation under a free surface. These qualitative flow patterns are insensitive to the Reynolds number. For flows with a finite aspect ratio and at small Reynolds numbers, the change in the top boundary condition has little impact on the flow. For flows with a finite aspect ratio and at large Reynolds numbers, the prevailing flow patterns are of boundary layer-type. At a given vertical level, the angular velocity attains a larger value under a free surface than under a rigid lid.

1 Introduction

The flow of a viscous fluid inside a rotating disk-cylinder arrangement has drawn much attention lately (e.g., see [1–8]). Specifically, consider a circular cylindrical tank (radius a, height H) at rest, whose central axis is aligned in the vertical direction Z, filled with an incompressible fluid of kinematic viscosity ν. The bottom endwall disk of the tank rotates steadily about the cylinder axis with a constant angular velocity Ω. This induces azimuthal and meridional circulations inside the tank, and the determination of this internal flow constitutes the present problem. The rotating disk-cylinder apparatus is an important laboratory tool to model the flows that occur in certain technological and geophysical applications, e.g., centrifuge, fluid machinery, chemical mixers. Also, from a theoretical viewpoint, the study of this flow can throw light on the fundamental dynamics involved in rotating fluids. Due primarily to the inherent complexity of the flow, the majority of past investigators tackled the problem by seeking numerical solutions to the Navier-Stokes equations [1–6, 8].

It appears that, all of the previously published work dealt with the flow in a closed tank with a stationary rigid lid at the top, which is in direct contact with the fluid. The rigid lid boundary condition places a strong constraint on the flow; both the azimuthal and meridional velocities vanish at the lid. No papers have appeared in the literature which address the question of the flow in an open tank with a free surface, driven by the spinning bottom. The replacement of a rigid lid by a free surface enables us to focus on the influence of the top surface on the internal flow in the tank. Mathematically, the problem is that of having a stress-free boundary condition at the top. This flow configuration serves as a useful physical model for the rotating flows inside a spin-stabilized rocket or shell partially filled with a liquid. Several types of chemical mixers operate with the fluid exposed to the atmosphere. Knowledge of rotating flows with a free surface is needed to model the motions of geophysical fluid systems. In view of the theoretical significance and practical relevance, we propose in this paper to examine the flow of a viscous fluid in an open tank. For a definition sketch of the physical system, the reader is referred to Fig. 1 of Alonso [4].

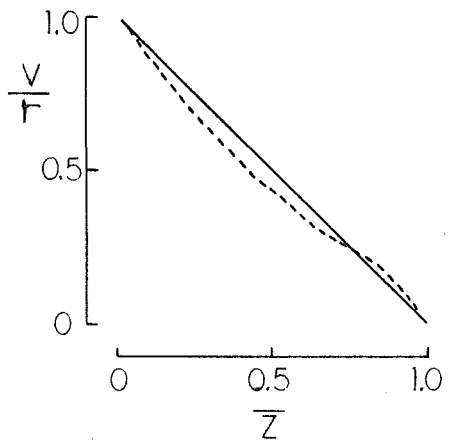

Fig. 1 Representative comparison of the present results (——) with the measurements (····) of [13] for a rigid-lid closed tank. $\bar{z} = 1 - z$. Re = 139, $h = 0.19$, $r = 0.58$.

[1]Present address: Department of Mechanical Engineering, Korea Advanced Institute of Science and Tech., Seoul, Korea.

Contributed by the Fluids Engineering Division for publication in the JOURNAL OF FLUIDS ENGINEERING. Manuscript received by the Fluids Engineering Division, November 7, 1984.

In line with the approach taken by previous studies, flow data were acquired by numerically integrating the full Navier-Stokes equations. Our purpose is to describe the azimuthal and meridional flow details inside the tank over a range of rotational Reynolds number and for varying aspect ratios. Emphasis is placed on depicting the distinct features of the flow as the top boundary condition changes from a rigid lid to a free surface.

2 Formulation

The Navier-Stokes equations used are referred to an axisymmetric cylindrical frame (R, θ, Z), with (U, V, W) denoting the velocity components. The vorticity-stream function expressions are, in dimensionless form, (see [1, 2])

$$u\frac{\partial \Gamma}{\partial r}+w\frac{\partial \Gamma}{\partial z}=(\mathrm{Re})^{-1}\left(\nabla^2\Gamma-\frac{2}{r}\frac{\partial \Gamma}{\partial r}\right), \tag{1}$$

$$u\frac{\partial \zeta}{\partial r}+w\frac{\partial \zeta}{\partial z}-\frac{u\zeta}{r}-\frac{2\Gamma}{r^3}\frac{\partial \Gamma}{\partial z}=(\mathrm{Re})^{-1}\left(\nabla^2\zeta-\frac{\zeta}{r^3}\right), \tag{2}$$

$$\nabla^2\psi-\frac{2}{r}\frac{\partial \psi}{\partial r}=r\zeta, \tag{3}$$

where

$$r=R/a,\ z=Z/a,$$

$$u=U/a\Omega,\ v=V/a\Omega,\ w=W/a\Omega,$$

$$\Gamma=vr,\ \zeta=\frac{\partial u}{\partial z}-\frac{\partial w}{\partial r},$$

$$\mathrm{Re}=\frac{\Omega a^2}{\nu},\ \nabla^2=\frac{\partial^2}{\partial r^2}+r^{-1}\frac{\partial}{\partial r}+\frac{\partial^2}{\partial z^2},$$

$$u=r^{-1}\frac{\partial \psi}{\partial z},\ w=-r^{-1}\frac{\partial \psi}{\partial r}.$$

The boundary conditions are

at $r=0,\ \psi=0,\ \Gamma=0,\ \zeta=0;$ (4)

at $r=1,\ \psi=0,\ \Gamma=0,\ \zeta=\frac{1}{r}\frac{\partial^2\psi}{\partial r^2};$ (5)

at $z=0,\ \psi=0,\ \Gamma=r^2,\ \zeta=\frac{1}{r}\frac{\partial^2\psi}{\partial z^2};$ (6)

at $z=h[\equiv H/a],\ \psi=0,\ \partial\Gamma/\partial z=0,\ \zeta=0$ (for a free surface); (7*a*)

at $z=h,\ \psi=0,\ \Gamma=0,\ \zeta=\frac{1}{r}\frac{\partial^2\psi}{\partial z^2}$ (for a rigid lid). (7*b*)

The free surface boundary conditions, equation (7*a*), need some discussion. The determination of the exact shape and location of the free surface of a rotating liquid is, in general, a very complex problem. The steady-state free-surface equation for a rigidly rotating liquid is given as by Gerber [9]

$$z=\omega^2 a\, r^2/2\, g+K,$$

where ω is the angular velocity of the liquid. The constant K is determined by conservation of mass. Gerber [9] presented a diagram of all possible free-surface configurations, which depend on the relative values of ω, a, and h. The determination of the time-dependent shape of free surface for large Re during the spin-up period was considered by Goller and Ranov [10]. The main purpose of this paper is to obtain a qualitative understanding of the character of internal flows of a rotating fluid capped by a free surface. For this purpose, we confine attention to situations where the centrifugal acceleration is much smaller than the gravitational acceleration, i.e., the Froude number $\Omega^2a^2/g\,H << 1$. Consequently, the deflection of the free surface from the horizontal can be ignored. This is equivalent to stating that the free surface in the present problem is treated in the same way as a free slip rigid contact lid [11]. It is true that, by adopting this restriction, the present analysis is limited in parameter ranges, and it does not cover the cases in which the rotation rate is very large. However, in reality, the condition, $\Omega^2a^2/g\,H << 1$, can be satisfied reasonably well in most geophysical fluid modeling experiments even when the rotational Reynolds number is high. For common geophysical fluid dynamics laboratory experiments using water, the parameters are typically (see, e.g., [4, 6, 10]) $a \sim 10$ cm, $H \sim 10$ cm, $g \sim 980$ cm s^{-2}, $\nu \sim 0.01$ cm^2 s^{-1}. Even for a high value of Re, e.g., Re $= 10^4$, Ω is of the order of 1 rad s^{-1}, then $\Omega^2\,a^2/g\,H$ ($\cong 0.01$) is still much smaller than one. Based on these considerations, [11] used equation (7*a*) in a systematic investigation of thermally driven flows in a rotating annulus. The physical meaning of equation (7*a*) can be explained as follows: the normal velocity component vanishes along all boundary surfaces, yielding $\psi = 0$; the tangential stresses on the free surface must vanish, requiring $\partial\Gamma/\partial z = 0$, $\partial^2\psi/\partial z^2 = 0$, therefore the vorticity $\zeta = 0$ (see [11]).

The governing equations and the boundary conditions were finite-differenced on a stretched, nonuniform mesh. The grid network was generated by the following formula [4]:

$$r_i=(i-1)/(i_{\max}-1)+r_s\sin[\pi(i-1)/(i_{\max}-1)],$$

$$z_j=(j-1)/(j_{\max}-1)-z_s\sin[\pi(j-1)/(j_{\max}-1)], \tag{8}$$

in which $(i_{\max}, j_{\max})$ are the total number of grid points and (r_s, z_s) are the grid stretching factors. Central-differencing was applied to the diffusion terms, and upwind differencing was used for the convective terms. The finite-difference equations were solved by a line-by-line alternating direction implicit iterative method [12]. It was found that underrelaxation was needed to attain convergence. The present procedure has adopted

$$\left|\psi_{ij}^{n+1}-\psi_{ij}^{n}\right|_{\max}\Big/\left|\psi_{ij}^{n}\right|_{\max}<10^{-4}$$

as the convergence criterion, where n is the iteration index. Most of the calculations were implemented on a (41×41) grid. Sensitivity of the results to grid size was tested for two trial runs. Several hundred iterations were usually required to yield a converged solution. Employing a (41×41) grid, the computer time was typically ½ ~ 1 hour on an IBM 4341 Computer, depending on the parameters.

3 Results and Discussion

To validate the numerical results, calculations were made on several cases of rigid-lid tank flows for which laboratory measurements [13] or numerical solutions [1, 2, 5] were available. Comparisons of the present numerical results with these available data indicated satisfactory agreement. Figure 1 shows one such comparison.

Computations were performed for the Reynolds number ranging $1.0 \le \mathrm{Re} \le 1000.0$ and for the aspect ratios $0.1 \le h \le 1.0$. Only the specific results illuminating the distinct flow characteristics will be presented.

(*a*) $h = 0.1$. A series of calculations was conducted using the aspect ratio $h = 0.1$. These are representative of the flows of a shallow layer of fluid. Viscous diffusion is the primary mechanism, and the induced flows fill much of the vertical extent of the fluid layer.

Figure 2 displays the plots of meridional stream function (ψ) and of azimuthal velocity (v) at Re $= 1.0$. The fluids near the rotating disk are driven radially outward and the fluids in the interior are drawn toward the rotating disk. The meridional flows form a counter-clockwise circulation in the axial plane. Since Re is small, the magnitudes of the meridional flows are

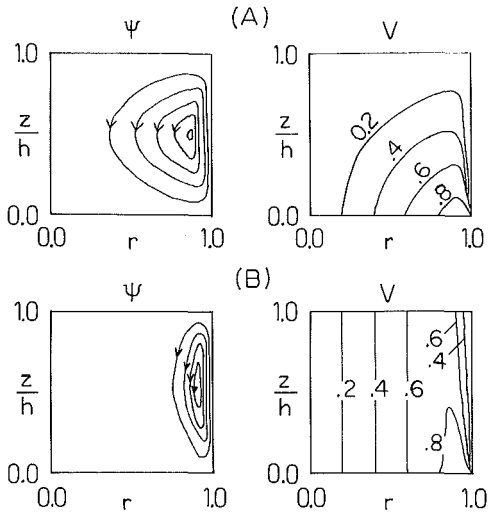

Fig. 2 Plots of meridional stream function (ψ) and of azimuthal velocity (v) for $h = 0.1$, Re = 1.0
(A) rigid lid at the top. $\psi_{max} = 0.182 \times 10^{-5}$, and contour increment $\Delta\psi = 0.4 \times 10^{-6}$;
(B) free surface at the top. $\psi_{max} = 0.199 \times 10^{-5}$, $\Delta\psi = 0.4 \times 10^{-6}$.

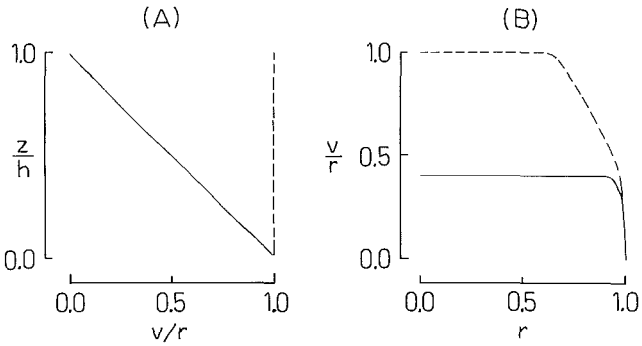

Fig. 3 Profiles of angular velocity v/r for $h = 0.1$, Re = 1.0. ——, rigid lid; ···, free surface.
(A) along the vertical cut at $r = 0.4$;
(B) along the horizontal cut at $z/h = 0.4$.

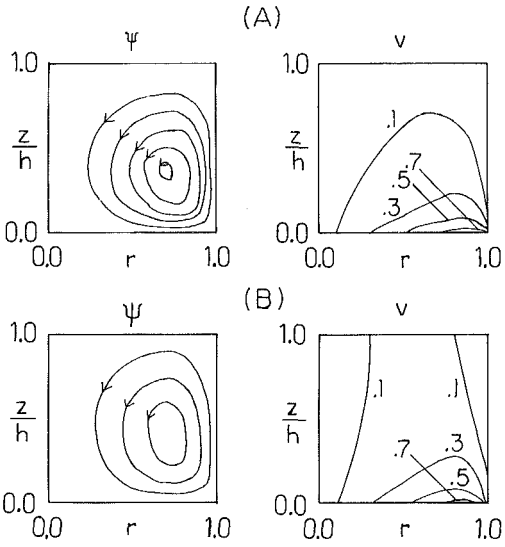

Fig. 4 Plots of meridional stream function (ψ) and of azimuthal velocity (v) for $h = 0.5$, Re = 100.0.
(A) rigid lid at the top. $\psi_{max} = 0.311 \times 10^{-2}$, $\Delta\psi = 0.6 \times 10^{-3}$;
(B) free surface at the top. $\psi_{max} = 0.365 \times 10^{-2}$, $\Delta\psi = 0.1 \times 10^{-2}$.

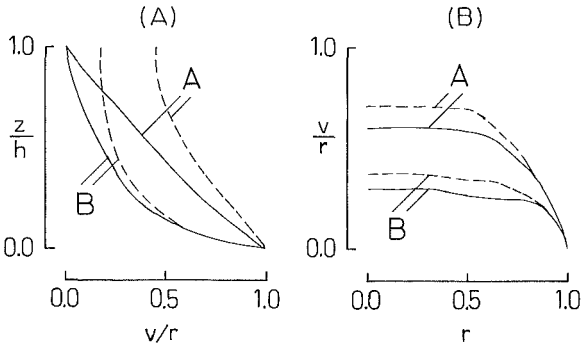

Fig. 5 Profiles of v/r for $h = 0.5$. Curves A are for Re = 1.0, and curves B are for Re = 100.0. ——, rigid lid; ···, free surface.
(A) along the vertical cut at $r = 0.4$;
(B) along the horizontal cut at $z/h = 0.4$.

vanishingly small, indicating that the advective effects are all but negligible.

In the case of a rigid lid [see Fig. 2(A)], the top surface acts as a momentum sink. Thus, the viscously controlled azimuthal velocity in a shallow layer of fluid decreases almost linearly with height from its maximum (dimensional) value of $R\Omega$ at the rotating disk to zero at the rigid lid. Hence, a Couette flow-like azimuthal velocity distribution is established in the bulk of the flow field, except in the region adjacent to the stationary sidewall.

When a shallow layer of fluid underlies a free surface [see Fig. 2(B)], there is no momentum sink at $z = h$. Consequently, the azimuthal flows under overwhelming viscous influence are substantially uniform in the axial direction in the main body of flow field, maintaining essentially a solid-body rotation with (dimensional) angular velocity Ω. At large radii, the axial uniformity is not fully sustained due to the presence of the sidewall.

In an effort to gain further insight into the flows of a shallow layer of fluid, the profiles of the angular velocity, v/r, are shown in Fig. 3. The profiles along a vertical cut near mid-radius [Fig. 3(A)] are consistent with the characterizations stated above, i.e., a Couette flow-like behavior under a rigid lid, and a solid-body rotation under a free surface. Figure 3(B) clearly indicates that the angular velocities are substantially uniform in the horizontal direction in the region away from the sidewall.

It is useful to make a first approximation to the shape of the free surface based on the calculated angular velocity field shown in Figs. 2 and 3. The form of the free surface for a rigidly rotating liquid is given as

$$z = \omega^2 a\, r^2/2\, g + (h - \omega^2 a/4\, g),$$

where ω is the angular velocity of the liquid. For shallow fluids, $\omega \cong \Omega$. Thus, the maximum deflection of the free surface from the horizontal is $0.25\ \Omega^2\ a/g$ at the central axis. As was pointed out earlier, for typical geophysical fluid modeling experiments $\Omega^2\ a/g << 1$; this provides justification to the use of the free surface boundary conditions, equation (7*a*).

The flow patterns depicted in Figs. 2 and 3 at Re = 1.0 remain essentially unchanged as Re increases. Viscous diffusion is still the principal mechanism. One parameter to measure the importance of viscous diffusion is the Reynolds number based on the height, $Re^* = \Omega H^2/\nu$ [$\equiv h^2$ Re]. Even when the rotational Reynolds number Re is increased to 10^3, Re^* is still 10 for $h = 0.1$, suggesting that the flow is profoundly influenced by viscous diffusion. However, as Re increases, the meridional flows increase in magnitude. This is consistent with the fact that, for flows under dominant viscous influence, Γ is in-

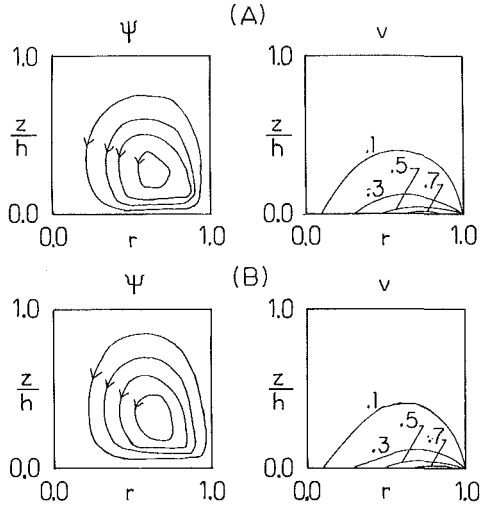

Fig. 6 Plots of meridional stream function (ψ) and of azimuthal velocity (v) for h = 1.0, Re = 1.0.
(A) rigid lid at the top. $\psi_{max} = 0.893 \times 10^{-4}$, $\Delta\psi = 0.2 \times 10^{-4}$;
(B) free surface at the top. $\psi_{max} = 0.924 \times 10^{-4}$, $\Delta\psi = 0.2 \times 10^{-4}$.

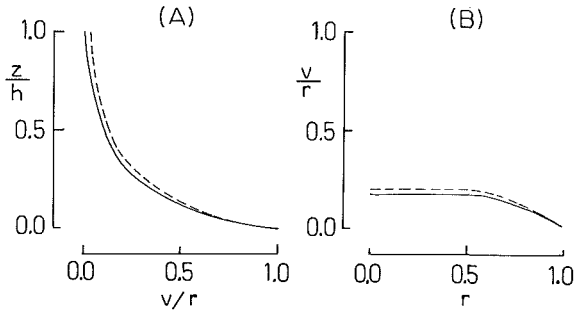

Fig. 7 Profiles of v/r for h = 1.0, Re = 1.0. ——, rigid lid; ···, free surface.
(A) along the vertical cut at r = 0.4;
(B) along the horizontal cut at z/h = 0.4.

dependent of Re* and ψ and ζ are linearly proportional to Re* (see [1]). However, even at Re = 1000.0, the largest Reynolds number considered in the present study, the meridional circulation is still very weak, and, consequently, the advective effects are quite minimal compared to the diffusive effects.

(b) h = 0.5. Figures 4 and 5 exemplify the flows for an intermediate aspect ratio. The overall patterns of the ψ and v plots shown in Fig. 4 do not change as Re varies. The meridional flows increase in magnitude as Re increases, as was pointed out before.

Figure 5 shows the profiles of angular velocities in the region away from the sidewall. When Re is small [see curves for Re = 1.0], the flows are controlled chiefly by viscous diffusion. Under a rigid lid, therefore, the v/r profile is similar to a Couette flow. When a free surface overlies the fluid, however, a solid-body roation at Ω is no longer attainable; the influence of the rotating disk decays noticeably because the depth is large. The azimuthal flows decay less rapidly with height under a free surface than under a rigid lid. We note that the angular velocities near the free surface are appreciable.

As Re increases [see curves for Re = 100.0 in Fig. 5], the meridional flows intensify, and the advective effects are enhanced. The flow gradients increase especially in the region near the rotating disk. The azimuthal flows decay rapidly with height in a narrow region close to the rotating disk [say, within $z/h \lesssim 0.1$ in Fig. 5(A)], but away from the rotating disk [$z/h \gtrsim 0.1$] the azimuthal flows decrease less rapidly with height.

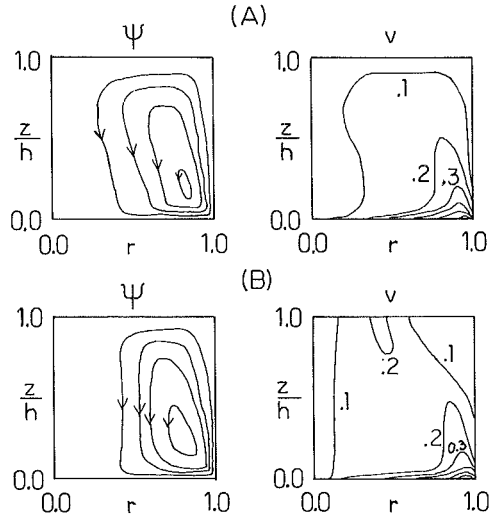

Fig. 8 Plots of meridional stream function (ψ) and of azimuthal velocity (v) for h = 1.0, Re = 1000.0.
(A) rigid lid at the top. $\psi_{max} = 0.798 \times 10^{-2}$, $\Delta\psi = 0.2 \times 10^{-2}$;
(B) free surface at the top. $\psi_{max} = 0.832 \times 10^{-2}$, $\Delta\psi = 0.2 \times 10^{-2}$.

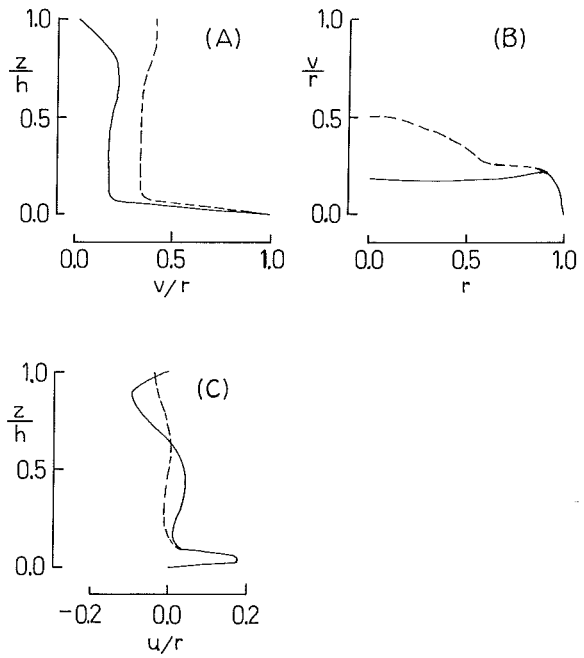

Fig. 9 Velocity profiles for h = 1.0, Re = 1000.0. ——, rigid lid; ···, free surface.
(A) vertical profile of v/r along r = 0.4;
(B) horizontal profile of v/r along z/h = 0.4;
(C) vertical profile of u/r along r = 0.4.

This points to the formation of a boundary layer. The boundary layer-type flow characteristics will become more apparent as both Re and h increase (see Fig. 9). The angular velocities are fairly uniform in the horizontal direction in the region away from the sidewall.

(c) h = 1.0. The flows in the tank of aspect ratio unity will now be examined. Pao [2] gave an extensive account of the flow in a rigid-lid tank with aspect ratio unity.

Figures 6 and 7 present the results for a small Reynolds number. The viscous diffusion has major influence on the flow. The meridional flows are small in magnitude, and, consequently, the advective effects are minimal. The influence of

the rotating disk diminishes sharply because the depth is large. The motions that are induced by the rotating disk can penetrate only up to a fraction of the fluid layer; the azimuthal flows are confined to a relatively small region close to the rotating disk. As is clearly discernible in Fig. 6, the azimuthal velocity is less than 0.1 in the region $z/h \gtrsim 0.5$. In the vicinity of the top surface $z = h$, the azimuthal flows have diminished sufficiently to a very small value. This leads to the observation that the precise form of the boundary condition at $z = h$ has little effect on the nature of the flow in the tank. Figures 6 and 7 demonstrate that the flow is indeed insensitive to the change in the boundary conditions at the top. For both a rigid lid and a free surface condition, the angular velocities decay rapidly with height, therefore, the overall magnitudes of the angular velocities near the top tend to be very small.

Figures 8 and 9 pertain to the flow at a large Reynolds number. The flow is characterized by the presence of distinct boundary layers. The meridional flows are appreciable in strength, pointing to significant advective effects. Strong gradients of the meridional flows are evident near the corner. The existence of the Ekman boundary layer near the rotating disk is clearly seen in the profiles of v/r and of u/r. The direct effect of viscosity is concentrated in this layer. In the region away from the bottom Ekman layer, the flow is mainly determined by the inviscid advective effects. The horizontal velocities in the inviscid core are uniform in the direction parallel to the rotation axis, which can be predicted by the well-known Taylor-Proudman theorem. The flow behavior near the top is determined primarily by the top boundary condition. If there is a rigid lid, another Ekman layer, although weak in strength, is required to adjust the velocities to zero at the top. On the other hand, if the fluid is capped by a free surface, no boundary layer exists near the top. The angular velocity at a given vertical level under a free surface is notably larger than that under a rigid lid.

Before closing, it is of interest to note the significance of the bottom corner region where the rotating disk joins the stationary sidewall. When Re is large, [14] showed that such corner disturbances are localized to a small area $0(\mathrm{Re}^{-1/2} \times \mathrm{Re}^{-1/3})$. When Re is small, [7, 8] demonstrated that the character of the flow in the main body of fluid is substantially unaffected by the corner disturbances.

4 Conclusions

When the aspect ratio is small, the boundary condition at the top has major influence on the nature of the flow, i.e., a Couette flow profile for a rigid lid, and a solid-body rotation for a free surface. These qualitative flow structures remain unchanged as Re varies.

For the flows with a finite aspect ratio, the character of the flow depends on the Reynolds number. At small Reynolds numbers, the overall flow patterns are insensitive to the change in the boundary conditions at the top. At large Reynolds numbers, boundary layer-type flow patterns prevail. The angular velocities in the region away from the boundary layers are substantially uniform in the axial direction. The angular velocities are appreciably larger for the case of free surface than for a rigid lid.

References

1 Pao, H.-P., "A Numerical Computation of a Confined Rotating Flow," ASME *Journal of Applied Mechanics*, Vol. 37, 1970, pp. 480–487.

2 Pao, H.-P., "Numerical Solutions of the Navier-Stokes Equations for Flows in the Disk-Cylinder System," *The Physics of Fluids*, Vol. 15, 1972, pp. 4–11.

3 Lugt, H. J., and Haussling, H. J., "Development of Flow Circulation in a Rotating Tank," *Acta Mechanica*, Vol. 18, 1973, pp. 255–272.

4 Alonso, C. V., "Steady Laminar Flow in a Stationary Tank with a Spinning Bottom," ASME *Journal of Applied Mechanics*, Vol. 42, 1975, pp. 771–776.

5 Bertela, M., and Gori, F., "Laminar Flow in a Cylindrical Container with a Rotating Cover," ASME JOURNAL OF FLUIDS ENGINEERING, Vol. 104, 1982, pp. 31–39.

6 Dijkstra, D., and Van Heijst, G. J. F., "The Flow between Two Finite Rotating Disks Enclosed by a Cylinder," *Journal of Fluid Mechanics*, Vol. 128, 1983, pp. 123–154.

7 Kim, M.-U., "Slow Rotation of a Disk in a Fluid-filled Circular Cylinder," *Journal Physical Society of Japan*, Vol. 50, 1981, pp. 4063–4067.

8 Hyun, J. M., "Flow near a Slowly Rotating Disk in a Finite Cylinder," *Journal Physical Society of Japan*, Vol. 53, 1984, pp. 3808–3813.

9 Gerber, N., "Properties of Rigidly Rotating Liquids in Closed Partially Filled Cylinders," ASME *Journal of Applied Mechanics*, Vol. 42, 1975, pp. 734–735.

10 Goller, H., and Ranov, T., "Unsteady Rotating Flow in a Cylinder with a Free surface," ASME *Journal of Basic Engineering*, Vol. 90, 1968, pp. 445–454.

11 Williams, G. P., "Thermal Convection in a Rotating Fluid Annulus: Part 1. The Basic Axisymmetric Flow," *Journal of the Atmospheric Sciences*, Vol. 24, 1967, pp. 144–161.

12 Patankar, S. V., *Numerical Heat Transfer and Fluid Flow*, McGraw-Hill, New York, 1980, p. 65.

13 Bien, F., and Penner, S. S., "Velocity Profiles in Steady and Unsteady Rotating Flows for a Finite Cylindrical Geometry," *The Physics of Fluids*, Vol. 13, 1970, pp. 1665–1671.

14 Bennetts, D. A., and Jackson, W. D. N., "Source-sink Flows in a Rotating Annulus: a Combined Laboratory and Numerical Study," *Journal of Fluid Mechanics*, Vol. 66, 1974, pp. 689–705.

A Semipotential Flow Theory for the Dynamics of Cylinder Arrays in Cross Flow

M. P. Paidoussis
Fellow ASME

S. J. Price
Mem. ASME

D. Mavriplis

Department of Mechanical Engineering,
McGill University, Montreal,
Quebec, Canada

This paper presents a semianalytical model, involving the superposition of the empirically determined cross flow about a cylinder in an array and the analytically determined vibration-induced flow field in still fluid, for the purpose of analyzing the stability of cylinder arrays in cross flow and predicting the threshold of fluidelastic instability. The flow field is divided into two regions: a viscous bubble of separated flow, and an inviscid, sinuous duct-flow region elsewhere. The only empirical input required by the model in its simplest form is the pressure distribution about a cylinder in the array. The results obtained are in reasonably good accord with experimental data, only for low values of the mass-damping parameter (e.g., for liquid flows), where fluidelastic instability is predominantly caused by negative fluid-dynamic damping terms. For high mass-damping parameters (e.g., for gaseous flows), where fluidelastic instability is evidently controlled by fluid-dynamic stiffness terms, the model greatly overestimates the threshold of fluidelastic instability. However, once measured fluid-dynamic stiffness terms are included in the model, agreement with experimental data is much improved, yielding the threshold flow velocities for fluidelastic instability to within a factor of 2 or better.

1 Introduction

Arrays of tubular cylinders subjected to cross flow are frequently used in a variety of heat exchange equipment, e.g., in heat exchangers, steam generators, and condensers. A number of flow-induced vibration problems are known to arise therein, in which the cylinders are excited by the cross flow to vibrate at large amplitudes – leading to fatigue and fretting failures [1]. The so-called fluidelastic instability is by far the most damaging; once a certain threshold cross-flow velocity is exceeded, the vibration amplitude often grows to the point where inter-cylinder clashing occurs.

Fluidelastic instability was established as a distinct phenomenon – radically different from vibration induced by "vortex-shedding," with which it had theretofore been confused – in the 1960s by Roberts [2] and Connors [3]. Connors' model especially, perhaps because of the convenient simplicity of the final result, gained widespread acceptance. Connors obtained the following expression for the critical flow velocity, U_c, for the onset of fluidelastic instability of a single row of cylinders in air-flow:

$$\frac{U_c}{fD} = K\left\{\frac{m\delta}{\rho D^2}\right\}^{1/2} \tag{1}$$

where ρ is the fluid density, D the diameter and m the mass per unit length of the cylinders, f the frequency, and δ the logarithmic decrement of cylinder vibration. In the mid-1970s, Blevins [4, 5] extended the analysis to deal with multirow arrays of cylinders, the final result once more reducing to the form of equation (1), but with a different proportionality factor, K.

Ever since then, a great deal of effort was expended trying to empirically determine values of K, which would serve as design guidelines for different types of array, e.g., [6]. In some cases, equation (1) was modified by separating the two dimensionless quantities, δ and $m/\rho D^2$, and placing exponents on each, different than ½, and so on [7–12]. These various efforts were only partially successful: if the system being analyzed was sufficiently close to the experimental data base on which the empirical expression being used was based, then prediction of fluidelastic instability was found to be reasonably good; otherwise, discrepancies of up to one order of magnitude were found be possible [1, 11, 12]. This led to a new series of studies in the 1980s, where attention was once more focused on *the fluid mechanics* of the problem – leading to four distinct new analytical models for fluidelastic instability.

Chen [13, 14] undertook an ambitious analytical formulation of the fluid mechanical forces, some of which cannot be obtained analytically. However, if these latter are taken from measured quantities (e.g., from Tanaka and Takahara's measurements [15]), very good agreement with experiment is obtained. Nevertheless, to apply this model, it is necessary to measure the unsteady fluid-dynamic forces on an oscillating cylinder and at least its immediate neighbours, for a range of reduced velocities and amplitudes, and for each geometrical arrangement to be analyzed, which is a difficult and time-consuming task.

An analytical model requiring less empirical input was developed by Price and Paidoussis [16–19]. This is a quasi-

Contributed by the Fluids Engineering Division for publication in the JOURNAL OF FLUIDS ENGINEERING. Manuscript received by the Fluids Engineering Division, July 27, 1984.

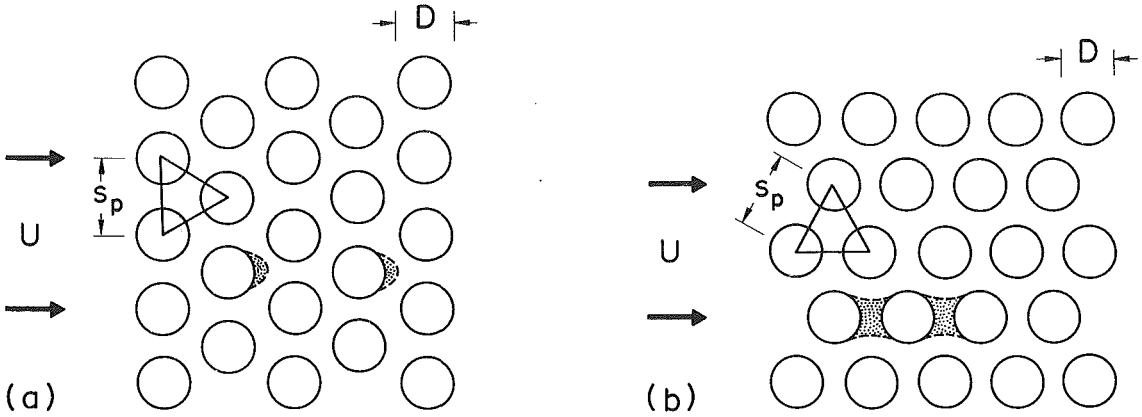

Fig. 1 The two types of staggered cylinder array in cross flow, analyzed in this paper: (*a*) "normal," and (*b*) "parallel," or "rotated," equilateral triangular array. The dimensionless pitch ratio, s_p/D, is defined, and the separated (rotational) flow regions are sketched in, behind two cylinders in each case.

static model, requiring measurement of the fluid-dynamic stiffness (displacement-dependent) terms only, and incorporating fluid-dynamic damping terms in the manner of Den Hartog's model for the analysis of iced transmission lines. In its latest version, the model incorporates phase-lag between cylinder motion and motion-induced forces in the manner proposed by Simpson and Flower [20]. This theory has been found to be in reasonably good agreement with a wide range of experimental data [18, 19].

Another model, requiring even less empirical input, was developed by Lever and Weaver [21], in which fluidelastic instability is presumed to be governed by interstitial flow redistribution associated with, and lagging behind, motions of any one cylinder in the array. The results obtained agree remarkably with Chen's [14], despite fundamental differences in the two analytical models, as well as with experimental results.

Another model was proposed by Paidoussis, Mavriplis, and Price [22], which analyzes the system by means of potential-flow theory – in a manner similar to Chen's earlier work [23]. This, apparently unreasonable approach, is based on the observation that, for some array geometries, the wakes (regions of rotational flow) are quite small [24, 25]. This model also incorporates a heuristically-introduced phase lag between cylinder displacements and displacement-dependent forces. Although it is recognized at the outset that potential flow theory is not the best fluid-mechanical tool for analyzing such systems, the model gives some interesting insights into the mechanism of fluidelastic instability and achieves prediction of the critical flow velocities within a factor of three or better. This model requires but one empirical input – namely, the aforementioned phase lag betweeen cylinder displacements and displacement-dependent forces. Considering the drastic simplifications in this theoretical model, the most serious of which is to ignore the existence of wakes, the results were considered to be sufficiently encouraging to warrant pursuing this line of work, leading to the present paper.

In this paper, the mean flow is considered to be made up of two regions: the potential-like flow outside the wakes, which may be analyzed by inviscid flow theory, and the rotational flow regions within the wakes. Making certain simplifying assumptions concerning the latter, a composite mean flow is constructed, on which the unsteady, vibration-induced flow field is then superposed. The fluid-dynamic forces on the cylinders may then be formulated analytically, if only the measured pressure distribution on a cylinder within the array is available. Thus, this analytical model falls within the category of the attempts designed to predict fluidelastic instabilities with minimum empirical input.

2 The Nature of the Flow Field

Rudimentary flow visualization experiments [25] were performed in a kerosene-vapour smoke tunnel, for both the normal and rotated triangular arrays of Fig. 1. A set of surface pressure measurements on centrally located cylinders in the array was also undertaken in a wind tunnel, to complement the flow visualization experiments. For the inter-cylinder spacings tested, it was found that the regions of rotational flow, i.e., the wakes, are of limited extent, as sketched in Fig. 1. The remainder of the flow field appeared to be a fully-developed turbulent corridor- or duct-like flow meandering through the cylinder array.

In order to assess the nature of this duct-like flow, an electrical potential analogue was constructed, so as to test whether this flow may be modelled by means of potential flow theory [25]. With the electrical analogue apparatus, involving electrical conducting paper, cut in the shape of a portion of the duct-like flow passage, it was possible to obtain surface pressure distributions on the cylinder, outside the wake. Then, by comparing these pressure distributions to those measured in the wind tunnel, it was concluded that the duct flow may adequately be modelled by potential flow theory.

Hence, in the absence of cylinder motion, the flow field consists of rotational wake regions and duct-like flow regions. The former are difficult to model and will simply be considered here as "dead" regions, in which the mean flow velocity is null; the latter will be modelled by means of potential flow. Superimposed on this flow field is the flow generated by cylinder motions. The method of superposition of the two flow fields is discussed in the next Section.

3 Formulation of the Analytical Model

The incorporation of the effect of flow separation and the superposition of inviscid and viscous flows into a single self-consistent analytical model are difficult to achieve. However, examples of relatively successful attempts do exist: e.g., Kelly's [26] analysis of the flow about slender bodies at oblique angles of attack, involving the combination of an empirically determined cross flow and an analytically determined axial flow; also, Paidoussis and Wong's [27] analysis of cross-flow-induced flutter of thin cylindrical shells, where the vibration-induced unsteady potential flow was superposed on the steady viscous cross flow.

Here it will be attempted to superimpose the vibration-induced flow field on the mean steady flow, which itself is composed of two flow regions, the wake and the duct-like flow, as discussed earlier. As the model is formulated in the context of linear stability theory, cylinder vibrations are con-

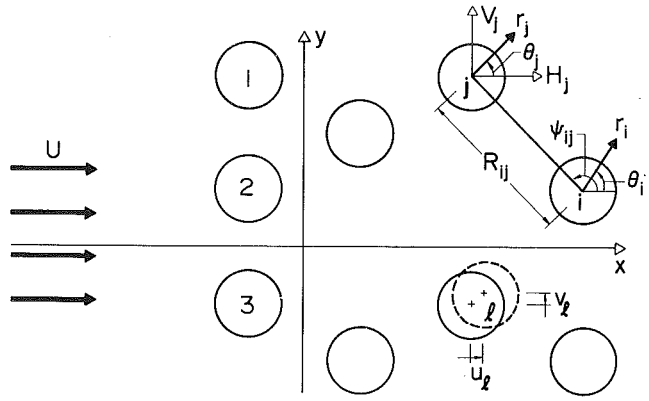

Fig. 2 The system under consideration, showing the coordinate systems (x,y), (r_i,θ_i) and the displacements of the lth cylinder, u_l and v_l, as well as the fluid forces acting on cylinder j, H_j, and V_j

sidered to be small; hence, it is assumed that no flow separation takes place, insofar as the vibration-induced flow is concerned. The cross-flow field is obtained empirically, in terms of the surface pressure distributions on a cylinder in the midst of a large stationary array, as described earlier.

3.1 The General Approach. Consider the flow field in a vibrating array of cylinders to be represented by a potential function, Φ, such that

$$\Phi(r,\theta,t)=\phi_0(r,\theta)+\phi(r,\theta,t), \tag{2}$$

where ϕ_0 is the potential due to the steady cross flow in the stationary array and ϕ is the potential due solely to cylinder vibrations. (Of course, it is understood that the viscous cross flow cannot be represented by a potential function; however, this hypothetical ϕ_0 is introduced here as an aid to understanding the general approach taken.)

Consider the array to be composed of k cylinders, and let (r_i, θ_i) be the polar coordinate system centered on cylinder i, as shown in Fig. 2. For each nonvibrating cylinder, the condition of impermeability at the cylinder surface dictates that the radial surface flow velocity, V_r, be zero. Hence, on a cylinder vibrating with velocities $\partial u_i/\partial t$ and $\partial v_i/\partial t$, in the x- and y-direction, respectively,

$$V_r\Big|_{r_i=R_i}=\frac{\partial\Phi}{\partial r_i}\Big|_{r_i=R_i}=\frac{\partial u_i}{\partial t}\cos\theta_i+\frac{\partial v_i}{\partial t}\sin\theta_i,$$

$$i=1,2,\ldots,k. \tag{3}$$

For a nonvibrating cylinder the tangential surface velocity, excluding any boundary-layer effects, is

$$V_\theta\Big|_{r_i=R_i}=(1/r_i)(\partial\phi_0/\partial\theta_i)\Big|_{r_i=R_i}=Uf_i(\theta_i),\ i=1,2,\ldots,k, \tag{4}$$

where U is the free-stream cross-flow velocity; $f_i(\theta_i)$ is determined experimentally, for a certain range of Reynolds numbers, by converting measured surface pressure distributions to surface velocity distributions *via* Bernoulli's equation. Similarly, for a vibrating cylinder

$$V_\theta\Big|_{r_i=R_i}=Uf_i(\theta_i)+\frac{1}{r_i}\frac{\partial\phi}{\partial\theta_i}\Big|_{r_i=R_i},\ i=1,2,\ldots,k. \tag{5}$$

To obtain the unsteady pressure distributions on a vibrating cylinder, the unsteady form of Bernoulli's equation may be used, i.e.,

$$\left[\frac{P}{\rho}+\tfrac{1}{2}V^2+\frac{\partial\phi}{\partial t}\right]_{r_i=R_i}=P_{\text{const}},\ i=1,2,\ldots,k, \tag{6}$$

where V is the vectorial sum of V_r and V_θ, and P_{const} is an appropriate stagnation pressure.

By integrating these pressure distributions, the fluid-dynamic forces on cylinder i may be obtained,

$$H_i=-\int_0^{2\pi}P\Big|_{r_i=R_i}R_i\cos\theta_i d\theta_i \text{ and}$$

$$V_i=-\int_0^{2\pi}P\Big|_{r_i=R_i}R_i\sin\theta_i d\theta_i, \tag{7}$$

in the x- and y-direction, respectively.

All cylinders are supposed to be identical, with flexural rigidity EI, mass per unit length m, and an equivalent viscous damping coefficient $c=2mf\delta$, f being the cylinder natural frequency and δ the logarithmic decrement of mechanical damping in vacuum. The equations of motion are then given by

$$EI\frac{\partial^4u_i}{\partial z^4}+C\frac{\partial u_i}{\partial t}+m\frac{\partial^2u_i}{\partial t^2}=H_i,\ EI\frac{\partial^4v_i}{\partial z^4}+C\frac{\partial v_i}{\partial t}+m\frac{\partial^2v_i}{\partial t^2}=V_i,$$

$$i=1,2,\ldots,k. \tag{8}$$

Solution of these equations permits the assessment of stability of the system for any given value of U.

3.2 The Unsteady Potential Function. The unsteady potential function due to motions of all the cylinders in otherwise still fluid must clearly satisfy Laplace's equation, $\nabla^2\phi=0$, subject to the boundary conditions $\phi\to0$ as $r\to\infty$ and equation (3). The method of solution, having already been obtained [28, 29], will not be presented here again. Denoting by ϕ^i the form of ϕ expressed in terms of a coordinate system centered on cylinder i, the solution may be expressed as follows [29]:

$$\phi^i=\sum_{n=1}^{\infty}\frac{R^{n+1}}{r_i^n}[a_{in}\cos n\theta_i+b_{in}\sin n\theta_i]$$

$$+\sum_{j=1}^{k^*}\sum_{n=1}^{\infty}\sum_{m=0}^{\infty}\left\{\frac{(-1)^n(n+m-1)!R^{n+1}r_i^m}{m!(n-1)!R_{ij}^{m+n}}\right\}\times$$

$$\{a_{jn}\cos[m\theta_i-(m+n)\psi_{ij}]-b_{jn}\sin[m\theta_i-(m+n)\psi_{ij}]\}, \tag{9}$$

where R_{ij} and ψ_{ij} are defined in Fig. 2, a_{in} and b_{in} are of the form

$$a_{in}=\sum_{l=1}^{k}\left\{\alpha_{inl}\frac{\partial u_l}{\partial t}+\gamma_{inl}\frac{\partial v_l}{\partial t}\right\},$$

$$b_{in}=\sum_{l=1}^{k}\left\{\delta_{inl}\frac{\partial u_l}{\partial t}+\beta_{inl}\frac{\partial v_l}{\partial t}\right\},$$

$$i=1,2,\ldots,k;\ n=1,2,\ldots,\infty, \tag{10}$$

and the starred sumation excludes $j=i$. The α_{inl}, β_{inl}, γ_{inl}, δ_{inl} are obtained by solving a set of linear nonhomogeneous equations given in reference [29].

3.3 The Initial Form of the Fluid-Dynamic Forces. Substituting equations (3) and (5) into (6) and thence into (7), one obtains, to first-order approximation,

$$H_i=\rho R\int_0^{2\pi}\frac{\partial\phi}{\partial t}\Big|_{r_i=R}\cos\theta_i d\theta_i$$

$$+\rho UR\int_0^{2\pi}\frac{1}{R}\frac{\partial\phi}{\partial\theta_i}\Big|_{r_i=R}f_i(\theta_i)\cos\theta_i d\theta_i$$

$$+\tfrac{1}{2}\rho U^2R\int_0^{2\pi}f_i^2(\theta_i)\cos\theta_i d\theta_i,$$

$$V_i=\rho R\int_0^{2\pi}\frac{\partial\phi}{\partial t}\Big|_{r_i=R}\sin\theta_i d\theta_i$$

$$+\rho UR\int_0^{2\pi}\frac{1}{R}\frac{\partial\phi}{\partial\theta_i}\Big|_{r_i=R} f_i(\theta_i)\sin\theta_i d\theta_i$$

$$+\tfrac{1}{2}\rho U^2 R\int_0^{2\pi} f_i^2(\theta_i)\sin\theta_i d\theta_i, \tag{11}$$

where the superscript i on ϕ (as in equation (9)) has been suppressed, and the fact that $R_i = R$, $i = 1,2, \ldots, k$, has been utilized.

Now, in view of the form of equations (9) and (10), it is easily seen that: (i) the first terms in H_i and V_i, in equations (11), are proportional to cylinder accelerations, i.e., they are *fluid-dynamic inertia terms;* (ii) the second terms, proportional to cylinder velocities, are *fluid-dynamic damping terms;* and (iii) the third set of terms are the *steady drag and lift* on the cylinders; the absence of *fluid-dynamic stiffness terms* should be noted here.

This last omission arises from the fact that ϕ does not contain any displacement-dependent terms, whereas fluid-dynamic stiffness terms are known to exist and to play an important role in precipitating instability [13, 14, 16–19]. However, such forces may be introduced empirically, by measuring the steady drag and lift on a cylinder as a function of displacement and then taking the slope of the resultant terms about the point of zero displacement [17]; thus,

$$C_{Di} = C_{Di}^0 + \sum_{l=1}^{k}\frac{\partial C_{Di}}{\partial u_l}u_l + \sum_{l=1}^{k}\frac{\partial C_{Di}}{\partial v_l}v_l \tag{12}$$

and similarly for C_{Li}. Hence, it is clear that equations (11) may be rewritten in the following functional form:

$$\begin{aligned} H_i &= \sum_{l=1}^{k}\{\rho\pi R^2(A_{il}\ddot{u}_l + B_{il}\ddot{v}_l) + \rho UR(C_{il}\dot{u}_l \\ &\quad + D_{il}\dot{v}_l) + \rho U^2 R(E_{il}u_l + F_{il}v_l)\} + \rho U^2 RC_{Di}^0, \\ V_i &= \sum_{l=1}^{k}\{\rho\pi R^2(A'_{il}\ddot{u}_l + B'_{il}\ddot{v}_l) + \rho UR(C'_{il}\dot{u}_l + D'_{il}\dot{v}_l) \\ &\quad + \rho U^2 R(E'_{il}u_l + F'_{il}v_l)\} + \rho U^2 RC_{Li}^0, i = 1,2, \ldots, k, \end{aligned} \tag{13}$$

where the constants $A_{il}, \ldots, D_{il}$ may be determined analytically and E_{il}, F_{il} empirically, and similarly for the primed quantities; the dot denotes differentiation with respect to time.

4 Elaboration of the Analytical Model

The analytical model, as developed in Section 3, suffers from a number of problems, which will be discussed next. It is rather difficult to appreciate the reasons for the modifications to be introduced here, without having the foregoing framework of the overall model at hand; this explains what, at first sight, might appear a circuitous route to the final form of the analytical model.

A simple test, perhaps the simplest, was first made by analyzing the following problem: a single cylinder moving with uniform velocity U *in purely inviscid* quiescent fluid, in the x-direction. In this case, $\dot{u} = U$, $\dot{v} = 0$, $\ddot{u} = \ddot{v} = 0$, and $V_r = U\cos\theta$, $V_\theta = U\sin\theta$ on the cylinder surface. Using the full unsteady Bernoulli equation, the pressure around the cylinder is found to be

$$P|_{r=R} = -\tfrac{1}{2}\rho U^2 + \text{constant}, \tag{14}$$

which is clearly wrong. By solving analytically the classical problem of a doublet in uniform flow, or the equivalent problem of a doublet moving uniformly in still fluid, the correct pressure distribution is found to be

$$P|_{r=R} - P_\infty = \tfrac{1}{2}\rho U^2(1 - 4\sin^2\theta). \tag{15}$$

The source of the error is associated with the $\partial\phi/\partial t$ term in Bernoulli's equation, which in the present form of the analytical model yields inertia terms only, whereas in the proper moving-doublet analysis it yields other terms as well. The reason for the erroneous result was identified to be the following: the change in position of the coordinate frame (r,θ), fixed on the vibrating cylinder, has not been taken into account. Although this error has also been identified in conjunction with the purely potential flow analysis of reference [22] and properly corrected through the use of a moving reference frame, it is not possible to do so in this case, simply because the function $f_i(\theta_i)$ is known only in terms of a fixed coordinate system (i.e., it is not known how $f_i(\theta_i)$ changes with motion of the cylinder itself, let alone with motion of adjacent cylinders).

Hence, the only option available is to apply Bernoulli's equation in *steady flow* (except for the calculation of inertia forces, which are correctly handled by the analysis as it stands [22]), thus exploiting the equivalence of a cylinder subject to uniform cross flow to a cylinder moving with constant velocity in still fluid. In other words, a velocity equal and opposite to that of the cylinder must be superimposed on the mean flow velocity, thereby recasting the problem in a moving reference frame and bringing the cylinder to rest. Thus, superimposing the velocity

$$-\dot{u}\hat{i} = -(\dot{u}\cos\theta)\hat{e}_r + (\dot{u}\sin\theta)\hat{e}_\theta,$$

where $\hat{i}$, $\hat{e}_r$, $\hat{e}_\theta$ are the unit vectors in the x-, r-, and θ-direction, respectively, yields $V_r = 0$, $V_\theta = 2\dot{u}\sin\theta$. Then, utilizing these modified flow velocities in Bernoulli's equation, the correct pressure distribution of equation (15) may be obtained.

Hence, generalizing the above for the problem at hand requires that ϕ be modified, such that

$$\tilde{\phi}^i = \phi^i - \dot{u}_i r_i\cos\theta_i - \dot{v}_i r_i\sin\theta_i \tag{16}$$

in the calculation of the velocity-dependent terms, yielding

$$\begin{aligned} H_i &= \rho R\int_0^{2\pi}\frac{\partial\phi}{\partial t}\Big|_{r_i=R}\cos\theta_i d\theta_i \\ &\quad + \rho UR\int_0^{2\pi}\frac{1}{R}\frac{\partial\tilde{\phi}}{\partial\theta_i}\Big|_{r_i=R} f_i(\theta_i)\cos\theta_i d\theta_i \\ &\quad + \rho U^2 R\sum_{l=1}^{k}(E_{il}u_l + F_{il}v_l) \\ &\quad + \tfrac{1}{2}\rho U^2 R\int_0^{2\pi} f_i^2(\theta_i)\cos\theta_i d\theta_i \end{aligned} \tag{17}$$

and a similar expression for V_i. Similar changes would be necessary in equations (13), where now $\tilde{C}_{il}$ replaces C_{il}, and so on, so that

$$\tilde{C}_{il} = C_{il} + \delta_{il}\int_0^{2\pi} f_i(\theta_i)\sin\theta_i\cos\theta_i d\theta_i, \tag{18a}$$

$$\tilde{D}_{il} = D_{il} - \delta_{il}\int_0^{2\pi} f_i(\theta_i)\cos^2\theta_i d\theta_i, \tag{18b}$$

for instance, where δ_{il} is Kronecker's delta.

This problem has been solved, however, only at the expense of creating another, albeit smaller one: by effecting the correction of equation (16), new velocities were effectively imposed on cylinders adjacent to cylinder i; nevertheless, since the forces acting on a cylinder are mainly generated by its own motion, as opposed to motion of adjacent cylinders, the problem may be considered to have been minimized.

Another modification which has to be introduced may be elucidated by considering the pressure distribution around a stationary cylinder in the viscous flow field, which is found to be

$$P|_{r=R} - P_\infty = \tfrac{1}{2}\rho U^2[1 - f^2(\theta)];$$

it is recalled that the tangential velocity on the cylinder surface is $Uf(\theta)$. Consider now the superposition of this mean-flow field on the vibration-induced one. On the one hand, $f(\theta) = 0$ must be taken in the wake, in accord with the assumption that the mean flow velocity in the wake is zero. On the other hand, if $f(\theta) = 0$ is applied to the pressure expression above, this would imply that the pressure in the wake is equal to the stagnation pressure, which is known to be incorrect.

This problem arises because of the manner of linking the empirical viscous flow to the potential, vibration-induced flow: although the superposition of the vibration-induced flow velocity, $(1/R)(\partial\tilde{\phi}/\partial\theta)$, on the mean tangential flow velocity, $Uf(\theta)$, is admissible in regions of irrotational flow, it is inadmissible in the wake; i.e., the same Bernoulli equation cannot be used across the free (separated) shear layer.

Hence, the two flow regions must be treated separately, through the use of *two* unsteady Bernoulli equations:

$$\frac{P}{\rho} + \tfrac{1}{2}V^2 + \frac{\partial\phi}{\partial t} = P_{st} \text{ and } \frac{P}{\rho} + \frac{\partial\phi}{\partial t} = P_b(t), \qquad (19)$$

valid outside and inside the wake, respectively, where $V = 0$ was taken in the latter region; P_{st} is the stagnation pressure at the front of the cylinder and P_b is the base pressure, which is taken to be constant through the wake, but time-varying, as will be shown later.

Hence, the fluid-dynamic forces are given by

$$H_i = \int_{\text{o.w}} \left\{\tfrac{1}{2}\rho V^2 + \frac{\partial\phi}{\partial t} - P_{st}\right\} R\cos\theta_i d\theta_i + \int_{\text{i.w.}} \left\{\frac{\partial\phi}{\partial t} - P_b\right\} R\cos\theta_i d\theta_i,\ i = 1,2,\ldots,k, \qquad (20)$$

and an equivalent expression for V_i, where o.w. and i.w. stand for *o*utside and *i*nside the *w*ake, respectively; the fluid-dynamic stiffness terms have been omitted from equation (20), for simplicity. Next, making use of the fact that if P_{st} were exerted all around the circumference of the cylinder, no net force would have resulted, this expression may be re-written as

$$H_i = \int_0^{2\pi} \rho \frac{\partial\phi}{\partial t}\bigg|_{r_i=R} R\cos\theta_i d\theta_i + \int_{\text{o.w.}} \tfrac{1}{2}\rho V^2 R\cos\theta_i d\theta_i + \int_{\text{i.w.}} (P_{st} - P_b) R\cos\theta_i d\theta_i,\ i = 1,2,\ldots,k. \qquad (21)$$

It must be noted at this stage that, although the base pressure *coefficient* is a constant, $P_{st} - P_b$ is generally not.

Next, an assumption must be made regarding the base pressure; it will be taken to be equal to the surface pressure at separation, denoted by P_{se}, so that

$$P_{st} - P_b = P_{st} - P_{se} = \tfrac{1}{2}\rho V_{se}^2. \qquad (22)$$

This assumption seems reasonable, upon inspection of experimental pressure profiles about a cylinder in cross flow, e.g., Roshko's [30], where $P \simeq P_{se}$ is observed beyond separation.

With this modification, the final form of the equations for the fluid-dynamic forces may now be obtained. Thus, writing

$$V^2 = \left\{Uf_i(\theta_i) + \frac{1}{R}\frac{\partial\tilde{\phi}}{\partial\theta_i}\bigg|_{r_i=R}\right\}^2 \simeq U^2 f_i^2(\theta_i) + \frac{2U}{R} f_i(\theta_i)\frac{\partial\tilde{\phi}}{\partial\theta_i}\bigg|_{r_i=R},$$

the following expressions for the fluid-dynamic forces are obtained:

$$H_i = \int_0^{2\pi} \rho \frac{\partial\phi}{\partial t}\bigg|_{r_i=R} R\cos\theta_i d\theta_i + \rho UR\int_0^{2\pi}\left[\frac{f_i(\theta_i)}{R}\frac{\partial\tilde{\phi}}{\partial\theta_i}\bigg|_{r_i=R}\right]^* \cos\theta_i d\theta_i + \rho U^2 R\sum_{l=1}^{k}(Eu_{il} + F_{il}v_l) + \rho U^2 RC_{Di}^0, \qquad (23)$$

$$V_i = \int_0^{2\pi} \rho \frac{\partial\phi}{\partial t}\bigg|_{r_i=R} R\sin\theta_i d\theta_i + \rho UR\int_0^{2\pi}\left[\frac{f_i(\theta_i)}{R}\frac{\partial\tilde{\phi}}{\partial\theta_i}\bigg|_{r_i=R}\right]^* \sin\theta_i d\theta_i + \rho U^2 R\sum_{l=1}^{k}(E'_{il}u_l + F'_{il}v_l) + \rho U^2 RC_{Li}^0, \qquad (23)$$

where the starred bracket indicates that the term within takes a constant value in the wake, equal to that at the separation point.

This represents the final form of the analytical model, in which (i) two Bernoulli equations have been utilized, one inside and the other outside the wake, and (ii) they have been applied in such a manner, that if cylinder i were moving alone, the correct pressure distribution and forces thereon would be obtained. The fluid-dynamic stiffness terms were not elaborated upon, since they are determined empirically; in the following, their importance will be assessed by first conducting calculations without these terms, and then with them.

5 Calculations, Results, and Discussion

The equations of motion were first linearized and then nondimensionalized, whereby the following dimensionless parameters emerged: the mass parameter, $m/\rho D^2$; the *in vacuo* logarithmic decrement of mechanical damping of the cylinders, δ; the reduced velocity, U/fD, where f is the *in vacuo* first-mode frequency, in Hz; the frequency ratio $\xi_p = f_p/f$, where f_p is the actual frequency of the pth mode.

The equations are then solved by modal-analysis techniques and by transformation into the form of a standard eigenvalue problem. *Ad hoc* computer programs [25] yield the system eigenfrequencies for any given U; by incrementing U gradually, it is thus possible to determine U_c, the critical flow velocity for the onset of fluidelastic instability.

Calculations were conducted for an array of only seven cylinders ($k = 7$), with $s_p/D = 1.375$, involving one central cylinder and another six clustered arount it in a circle. Some calculations were also done with twelve-cylinder arrays and the results were found to be sufficiently close to those with $k = 7$ (within 1 percent for U_c) to conclude that the seven-cylinder array adequately models much larger systems. In the calculations for ϕ, the summations in equation (9) were truncated at $n = m = 10$; truncating at $n = m = 12$, resulted in differences of less than 0.01 percent.

For the rotated triangular array (Fig. 1(*b*)), the portion of the wake which is reattached to the front of each cylinder was not treated as a constant pressure zone similar to the wake at the rear. This is because this forward region is delimited by two stagnation points, between which the pressure drops toward the base pressure (of the upstream cylinder) near the leading edge of the cylinder; hence, the flow in this region is neither inviscid nor isobaric, but is composed of a type of shear layer about each stagnation-separation streamline. Hence, the flow field in rotated triangular arrays is rather complex and, for this reason, the analytical model is considered to be better suited for normal triangular arrays.

The results for the threshold of instability are shown in Figs. 3 and 4 for the rotated and normal triangular arrays, respectively – both without and with the fluid-dynamic stiffness terms. The critical flow velocities are presented in terms of the so-called reference-pitch flow velocity, U_{pc}, for ease of comparison with the available data, where

$$U_{pc} = [s_p/(s_p - D)]U_c. \quad (24)$$

The experimental data in Figs. 3 and 4 are for various s_p/D. However, as these are in the range 1.3 to 1.5, it is supposed that comparing them with the theoretical ones, for which $s_p/D = 1.375$, would provide a reasonable test for the theory. The same applies to δ, which in the theoretical calculations has been taken to be $\delta = 0.01$, while in the experiments it covers a wide range. Indeed, in the experimental data, δ was sometimes measured in air (essentially in vacuum), sometimes in still liquid, and sometimes in flowing fluid, rendering comparison with theoretical results problematical. The same applies to m and f, which are sometimes the values in air, sometimes in liquid (where applicable), and so on.

Considering Fig. 3 first, it is seen that, if the fluid-dynamic stiffness terms are omitted, then agreement between theory and experiment is not good, the main reason being that theory predicts a quasi-linear relationship between U_{pc}/fD and $m\delta/\rho D^2$, whereas the experimental data, for $m\delta/\rho D^2 > 1$ approximately, indicate something closer to a square-root relationship. The only range of reasonably close agreement is for low values of $m\delta/\rho D^2$, i.e., in liquid flows. On the other hand, if the fluid-dynamic stiffness terms are incorporated into the analysis, then reasonably good agreement is obtained for most of the range of $m\delta/\rho D^2$. This is not surprising, as it has been shown by Chen [13, 14] and by the authors [16–19] that for gaseous flows the fluid-dynamic stiffness terms are predominant, thereby controlling the precipitation of fluidelastic instability.

In the calculations, no phase lag was assumed to exist between cylinder displacements and displacement-dependent fluid forces – as was done, for instance, in different ways, in references [18, 19, 22]. By examining the effect of such phase lag in these other studies, it is clear that its inclusion would have diminished the theoretical U_{pc}/fD, thereby further improving agreement between theory and experiment, over most of the range of $m\delta/\rho D^2$.

Considering Fig. 4 next, it is seen that, in the absence of fluid-dynamic stiffness terms, agreement between theory and experimental data is poor through-out, for the same reasons noted in the foregoing. It is nevertheless noted that the theoretical critical flow velocities are higher, by a factor of approximately 2, than the corresponding ones for rotated triangular arrays, which agrees with Weaver and Yeung's observations [31]. Another interesting aspect of the theoretical stability curve is the discontinuity at low $m\delta/\rho D^2$. At first sight this appears to be of the same type as those obtained by many authors [14, 18, 19, 21], but may also be associated with a change in inter-cylinder modal pattern.

When the fluid-dynamic stiffness terms are included in the analysis, then the agreement between theory and experiment becomes quite good in this case also, except for the solitary experimental point at extremely low $m\delta/\rho D^2$. Excluding that last data point, it is seen that the theory provides a sensible minimum boundary to the experimental data points. Hence, as expected, this theory applies more successfully to normal than to rotated triangular arrays.

Incidentally, the results in both Figs. 3 and 4 also show how important are the fluid-dynamic stiffness terms for successful prediction of the instability threshold. Theories which either neglect these terms altogether or predict a conservative set of fluid-dynamic stiffness terms (and a correspondingly symmetric stiffness matrix) are considerably less successful [21,22] – especially at relatively high $m\delta/\rho D^2$ – than those that utilize the measured, nonconservative set of stiffness terms [13–19].

6 Conclusion

The analytical model developed represents an attempt to modify a purely potential-flow formulation of the fluid dynamic forces acting on a cylinder in an array [22], by developing a composite flow-field formulation involving (i) a viscous cross flow about a stationary cylinder in the array and (ii) a vibration-induced potential flow.

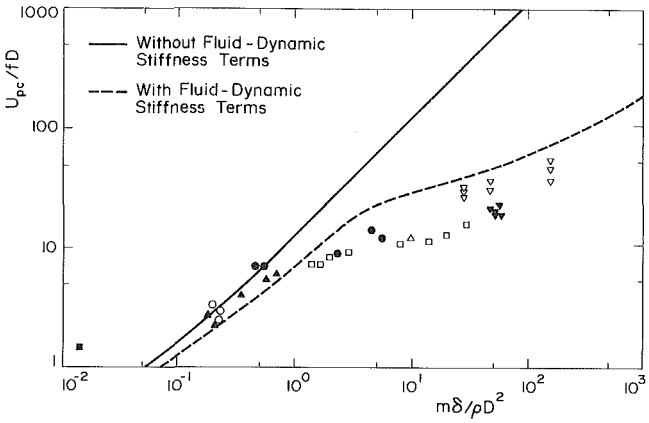

Fig. 3 Comparison between the critical flow velocities obtained by the semipotential theoretical model and available experimental data from various sources (refs. [10, 18, 22]), for *rotated triangular arrays*. For the theoretical results, $s_p/D = 1.375$, $\delta = 0.01$.

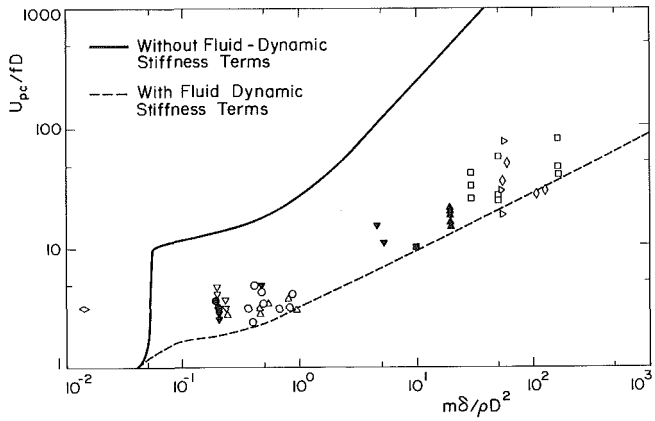

Fig. 4 Comparison between the critical flow velocities obtained by the semi-potential theoretical model and available experimental data from various sources (see references [10, 18, 22]), *for normal triangular arrays*. For the theoretical results, $s_p/D = 1.375$, $\delta = 0.01$.

Perhaps the greatest value of this work has been the elucidation of some of the difficulties and the pitfalls associated with the superposition of the two flow fields, as described in Section 4. These were only partially solved, (*a*) by dealing with regions of irrotational and rotational flow separately, in terms of obtaining the unsteady pressure distribution on the cylinders, and (*b*) by developing an approximate scheme for dealing with the application of Bernoulli's equation on a moving cylinder. This latter scheme suffers from the weakness that, whereas it correctly accounts for the component of the fluid forces associated with movement of the cylinder under consideration, it imposes "corrections" on the components due to motion of adjacent cylinders, which are fictitious and hence erroneous. Perhaps, if the analysis were applied to motions of a single cylinder in the array, as was successfully done elsewhere [19, 21], this last problem might be overcome, resulting in better agreement with experimental data.

It would, of course, also be possible to measure the pressure distribution on a cylinder in the array, not only in the equilibrium configuration, but also in statically deformed configurations, thereby (i) overcoming this last problem and (ii) obtaining fluid-dynamic stiffness terms in a different way. However, this would deflect from the original aim of this work, which was to develop a model for predicting fluidelastic instability with minimum empirical input.

Assessing the success of the analytical model, in terms of agreement with experimental data, it must be judged as poor – unless the empirically obtained fluid-dynamic stiffness terms are incorporated in the analysis. However, if that must be done, then the model of references [18, 19], requiring equal empirical input, must be judged superior. Hence, this analytical model is of limited practical interest, and the main contribution of this work lies in the probing of the fluid mechanical aspects of the problem and in the insights gained thereby into the underlying mechanism for fluidelastic instability.

Acknowledgments

This research was supported by grants from the Natural Sciences and Engineering Research Council of Canada and Le programme FCAC of Quebec. The authors also gratefully acknowledge the use of the facilities of Prof. Newman's Low Speed Aerodynamics Laboratory.

References

1 Paidoussis, M. P., "Flow-Induced Vibrations in Nuclear Reactors and Heat Exchangers: Practical Experiences and State of Knowledge", in *Practical Experiences with Flow-Induced Vibrations* (eds. Naudascher, E. and Rockwell, D.), pp. 1–81. Springer-Verlag, Berlin, 1980.

2 Roberts, B. W., "Low Frequency, Aeroelastic Vibrations in a Cascade of Circular Cylinders," *Mechanical Engineering Science Monograph No. 4*, I. Mech. E., London, 1966.

3 Connors, H. J., Jr., "Fluidelastic Vibration of Tube Arrays Excited by Cross Flow," in *Flow-Induced Vibration in Heat Exchangers* (ed. Reiff, D. D.), pp. 42–56. ASME, New York, 1970.

4 Blevins, R. D., "Fluidelastic Whirling of a Tube Row," ASME *Journal of Pressure Vessel Technology*, Vol. 96, 1974, pp. 263–267.

5 Blevins, R. D., "Fluidelastic Whirling of Tube Rows and Tube Arrays," ASME JOURNAL OF FLUIDS ENGINEERING, Vol. 99, 1977, pp. 457–460.

6 Soper, B. M. H., "The Effect of Tube Layout on the Fluid-Elastic Instability of Tube Bundles in Crossflow," ASME *Journal of Heat Transfer*, Vol. 105, 1983, pp. 744–750.

7 Pettigrew, M. J., Sylvestre, Y., and Campagna, A. O., "Vibration Analysis of Heat Exchanger and Steam Generator Designs," *Nuclear Engineering and Design*, Vol. 48, 1978, pp. 97–115.

8 Weaver, D. S., and El-Kashlan, M., "The Effect of Damping and Mass Ratio on the Stability of a Tube Bank," *Journal of Sound and Vibration*, Vol. 76, 1981, pp. 283–294.

9 Nicolet, J. B., Sagner, M. and Régis, G., "Vibrations de faisceaux de tubes sous excitation aérodynamique," *Revue générale de Thermique*, No. 128, 1976, pp. 869–891.

10 Chen, S. S., "Instability Flow Velocity of Tube Arrays in Crossflow," *Proceedings International Conference "Flow-Induced Vibrations in Fluid Engineering,"* pp. 233–254. BHRA, Cranfield, Beds, U.K., 1982.

11 Paidoussis, M. P., "Fluidelastic Vibration of Cylinder Arrays in Axial and Cross Flow: State of the Art," *Journal of Sound and Vibration*, Vol. 76, 1981, pp. 329–360.

12 Paidoussis, M. P., "A Review of Flow-Induced Vibrations in Reactors and Reactor Components," *Nuclear Engineering and Design*, Vol. 74, 1983, pp. 31–60.

13 Chen, S. S., "Instability Mechanisms and Stability Criteria of a Group of Circular Cylinders Subjected to Cross Flow. Part 1: Theory," ASME *Journal of Vibration, Acoustics, Stress and Reliability in Design*, Vol. 105, 1983, pp. 51–58.

14 Chen, S. S., "Instability Mechanisms and Stability Criteria of a Group of Circular Cylinders Subjected to Cross Flow. Part 2: Numerical Results and Discussions," ASME *Journal of Vibration, Acoustics, Stress and Reliability in Design*, Vol. 105, 1983, pp. 253–260.

15 Tanaka, H. and Takahara, S., "Fluid Elastic Vibration of Tube Array in Cross Flow," *Journal of Sound and Vibration*, Vol. 77, 1981, pp. 19–37.

16 Price, S. J. and Paidoussis, M. P., "Fluidelastic Instability of a Double Row of Circular Cylinders Subjected to a Cross-Flow," ASME *Journal of Vibration, Acoustics, Stress and Reliability in Design*, Vol. 105, 1983, pp. 59–66 (ASME Paper 81-DET-24).

17 Price, S. J. and Paidoussis, M. P., "A Theoretical Investigation of the Parameters Affecting the Fluidelastic Instability of a Double Row of Cylinders Subject to a Cross-Flow," *Proceedings 3rd International Conference "Vibration in Nuclear Plant,"* pp. 107–119. Keswick, U.K., 1982.

18 Price, S. J. and Paidoussis, M. P., "An Improved Mathematical Model for the Stability of Cylinder Rows Subject to Cross-Flow," *Journal of Sound and Vibration*, Vol. 97, 1984, pp. 615–640.

19 Price, S. J., and Paidoussis, M. P., "A Theoretical Investigation of the Fluidelastic Instability of a Single Flexible Cylinder Surrounded by Rigid Cylinders," *ASME Symposium on Flow-Induced Vibrations*, WAM 1984, New Orleans; Vol. 2, pp. 117–133.

20 Simpson, A., and Flower, J. W., "An Improved Mathematical Model for the Aerodynamic Forces on Tandem Cylinders in Motion with Aeroelastic Applications," *Journal of Sound and Vibration*, Vol. 51, 1977, pp. 183–217.

21 Lever, J. H. and Weaver, D. S., "A Theoretical Model for the Fluidelastic Instability in Heat Exchanger Tube Bundles," ASME *Journal of Pressure Vessel Technology*, Vol. 104, 1982, pp. 147–158.

22 Paidoussis, M. P., Mavriplis, D. and Price, S. J., "A Potential Flow Theory for the Dynamics of Cylinder Arrays in Cross Flow," *Journal of Fluid Mechanics*, Vol. 146, 1984, pp. 227–252.

23 Chen, S. S., "Crossflow-Induced Vibrations of Heat Exchanger Tube Banks," *Nuclear Engineering and Design*, Vol. 47, 1978, pp. 67–86.

24 Wallis, R. P., "Photographic Study of Fluid Flow between Banks of Tubes," *Engineering*, Vol. 148, 1939, pp. 423–426.

25 Mavriplis, D., "An Investigation of the Limitations of Potential Flow in Cross-Flow Induced Vibrations of Cylinder Arrays," *M. Eng. thesis, Department of Mechanical Engineering, McGill University*, May 1982.

26 Kelly, H. R., "The Estimation of Normal-Force, Drag, and Pitching-Moment Coefficients for Blunt-Based Bodies of Revolution at Large Angles of Attack," *Journal of the Aeronautical Sciences*, Vol. 2, 1954, pp. 549–555.

27 Paidoussis, M. P. and Wong, D. T.-M., "Flutter of Thin Cylindrical Shells in Cross Flow," *Journal of Fluid Mechanics*, Vol. 115, 1982, p. 411–426.

28 Chen, S. S., "Vibration of Nuclear Fuel Bundles," *Nuclear Engineering and Design*, Vol. 35, 1975, pp. 399–422.

29 Paidoussis, M. P., Suss, S., and Pustejovsky, M., "Free Vibration of Cylinders in Liquid-Filled Channels," *Journal of Sound and Vibration*, Vol. 55, 1977, pp. 443–459.

30 Roshko, A., "A New Hodograph for Free Streamline Theory," NACA Tech. Note 3136, 1954.

31 Yeung, H. C. and Weaver, D. S., "The Effect of Approach Flow Direction on the Flow-Induced Vibrations of a Triangular Tube Array," ASME *Journal of Vibration, Acoustics, Stress and Reliability in Design*, Vol. 105, 1983, pp. 76–82.

Flow Around Two Intersecting Circular Cylinders

M. M. Zdravkovich
Reader,
University of Salford, U.K.
Mem. ASME

One aspect of the flow around two intersecting cylinders, which has attracted little attention so far, is the structure of a three-dimensional near-wake behind the intersection. Some preliminary measurements of pressure distributions along the span were complemented by oil-film surface flow visualization. A strong secondary flow was found in the near-wake which extended spanwise more than three diameters from the intersection. The main feature was the formation of four symmetrically positioned pairs of swirling vortices which originated from the surface of the cylinders. The secondary flow caused an increase in the local drag coefficient.

Introduction

The interference of two parallel circular cylinders in close proximity has occurred in many practical applications [1] and has attracted a lot of research [2]. Two intersecting circular cylinders are also used as structural members in offshore engineering but have not attracted similar attention.

The interference of two circular cylinders in contact forming a cross produced a complex three-dimensional flow structure entirely different in both wakes [3]. The main feature of the secondary flow was a formation of two stationary pairs of swirling flows attached to the rear side of the upstream cylinder [3]. The local drag force along the span increased although the vortex shedding ceased.

The early measurements of drag forces on intersecting struts and circular cylinders were reported by Biermann and Herrnstein in 1933 [4]. They established that two intersecting cylinders forming a letter V with an angle ψ produced the same overall drag coefficient irrespective of the angle ψ in the range 90 deg $< \psi <$ 180 deg. A slight *decrease* in the overall drag coefficient was found for the intersecting angles 15 deg $< \psi <$ 90 deg for the three test Reynolds numbers: 6×10^4, 1.06×10^5 5×10^5. Contrary to that a significant *increase* in the overall drag coefficient was found for streamlined struts in the range 15 deg $< \psi <$ 90 deg. The maximum adverse interference took place for $\psi = 30$ deg.

The structure of turbulent wakes behind two intersecting cylinders at right-angles was investigated recently by Osaka et al. [5]. The profiles of time-averaged and fluctuating velocity components were measured at a Reynolds number $\mathrm{Re} = 8 \times 10^3$ over a wide range of downstream stations from $x/D = 3$ to 594. They found that "the decay rate of the centreline defect-velocity was considerably slower than that found in either two-dimensional or axisymmetric wakes. Even very far downstream, the wake did not behave as a simple combination of two perpendicular two-dimensional wakes." This could be explained by the existence of strong swirling flows along the wake visualized in [3].

"Subsequent analysis of the balance of turbulent energy production and dissipation [6] showed that the diffusion term was different from two-dimensional wakes." The secondary flow produced four pairs of streamwise vortices which were symmetric with respect to the boundaries, i.e., a pair in each quadrant. The origin of streamwise vortices and their effect on local surface pressure was not investigated by Osaka et al. [6]. This is the main object of this paper.

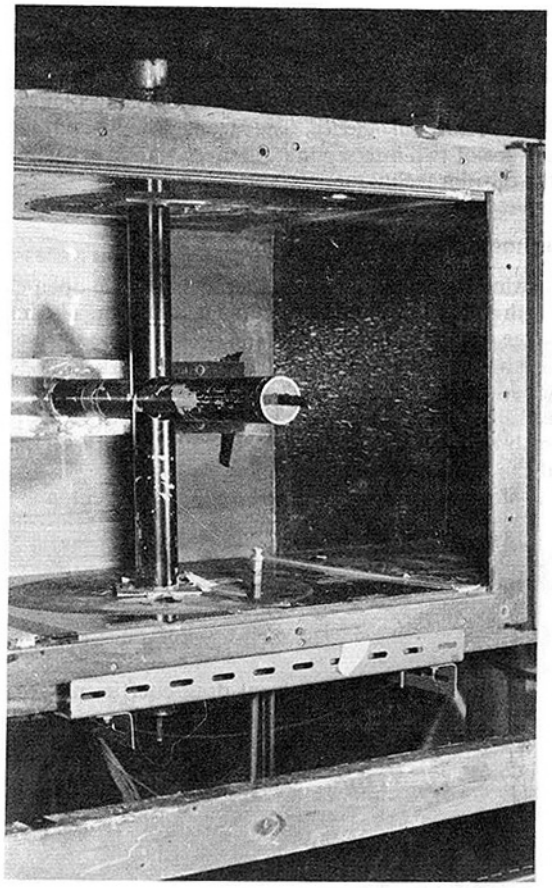

Fig. 1 Lay-out of intersecting cylinders

Contributed by the Fluids Engineering Division for publication in the JOURNAL OF FLUIDS ENGINEERING. Manuscript received by the Fluids Engineering Division, October 16, 1984.

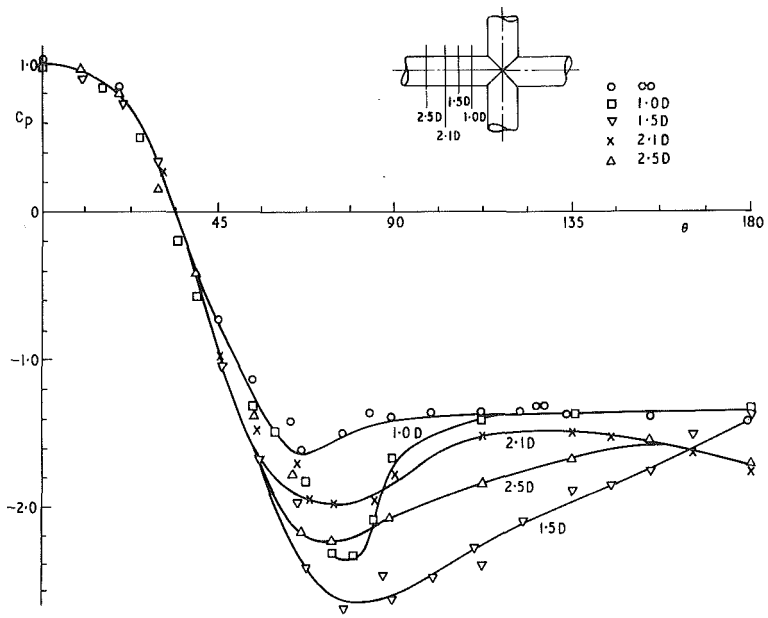

Fig. 2 Pressure distributions measured at $R_e = 9 \times 10^4$ (± 500) for $1 \leq Z/D \leq 2.5$ and for a single cylinder. (Uncertainty in $C_p = \pm 0.15$ in the separated region and $C_p = \pm 0.05$ elsewhere, in $Z/D = \pm 0.05$ and in $\theta = \pm 1.5$ deg at 20:1 odds.)

The present tests were deliberately limited to cylinders with a small aspect ratio of 9 coupled with a high blockage ratio of 22.6 percent as found in off-shore structures and planar grids used to generate turbulence. The strong secondary flow near the surface of two intersecting cylinders was visualized by using the oil-film technique.

Experimental Arrangement

The wind tunnel used in this experiment was an open-circuit type with a closed test section of 0.45m × 0.45m. The intensity of free stream turbulence was 0.4 percent. The scale of turbulence was not measured. A pair of circular cylinders of 50.8 mm diameter were machined and fitted to intersect at right angles. The cylinders spanned the test section horizontally and vertically and the centre of intersection coincided with the centre of the test section as seen in Fig. 1.

The blockage ratio amounted to 22.6 percent and two-dimensional corrections were not applied. The existing corrections developed for the two-dimensional wakes were inadequate for the three dimensional wake in the middle. The cross formed by the two cylinders in the square test section could be considered as an element of an off-shore structure or a grid where the tunnel walls could be thought of as "mirrors." The effects of blockage and aspect ratio could not be separated in the present tests.

The pressure tappings were drilled in one plane of one cylinder at 0, ± 65, ± 90, and 180 deg, and the pressure distribution was measured by rotating the cylinder in increments of 15 deg (± 1 deg). The three-dimensional pressure variation along the span was measured by displacing the monitored cylinder sidewise relative to the other fixed cylinder. The ends of both cylinders protruded through rubber-sealed holes outside the test section.

The Reynolds number range covered was from 4.1×10^4 to 9×10^4, which corresponded to the upper subcritical regime.

Nomenclature

B = the size of test section

$C_d = 2\int_0^{\pi} C_p \cos\theta d\theta$ local drag coefficient

$C_D = \dfrac{F_D}{\frac{1}{2}\rho V^2 DL}$ drag coefficient

$C_p = \dfrac{p - p_1}{\frac{1}{2}\rho V^2}$ local pressure coefficient

C_{pb} = base pressure coefficient in separated region

$\dfrac{dCp}{d\theta} < 0$ = favourable pressure gradient

$\dfrac{dCp}{d\theta} > 0$ = adverse pressure gradient

$\dfrac{d^2Cp}{d\theta^2} = 0$ = inflexion point corresponds to the separation point

D = outer diameter of cylinder

D/B = blockage ratio

F_d = local pressure drag force

F_D = average pressure drag force

L = length of cylinder

L/D = aspect ratio

p = local circumferential static pressure

p_1 = free stream static pressure

$R_e = \dfrac{VD}{\nu}$ = Reynolds number

V = free stream velocity

x = streamwise coordinate

x/D = nondimensional streamwise coordinate

Z = spanwise coordinate

Z/D = nondimensional spanwise coordinate

ν = kinematic viscosity of air

ψ = angle of intersection between cylinders

ρ = density of air

θ = circumferential angle

θ_s = angle of separation

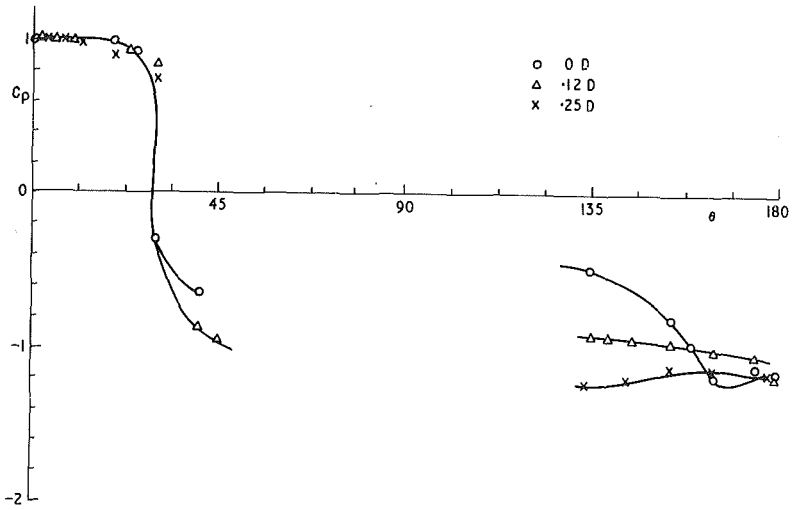

Fig. 3 Pressure distribution measured at $R_e = 9 \times 10^4$ (± 500) for $0 < Z/D < 0.5$ (Uncertainty in all parameters the same as for Fig. 2.)

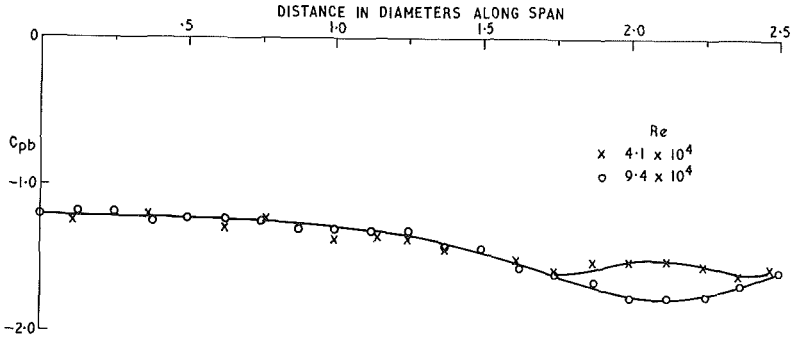

Fig. 4 Variation of base pressure coefficient along span for $R_e = 4.1 \times 10^4$ (± 500) and 8.9×10^4 (± 500). (Uncertainty in $C_{pb} = \pm 0.15$, in $Z/D = \pm 0.05$ and in $\theta = \pm 1.5$ deg at 20:1 odds.)

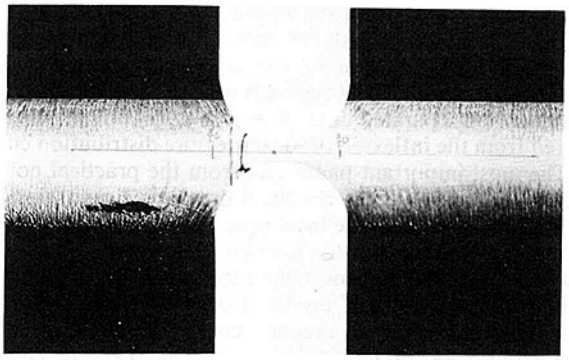

Fig. 5 Surface flow pattern along the horizontal cylinder; upstream view. $R_e = 4.1 \times 10^4$ (± 500.)

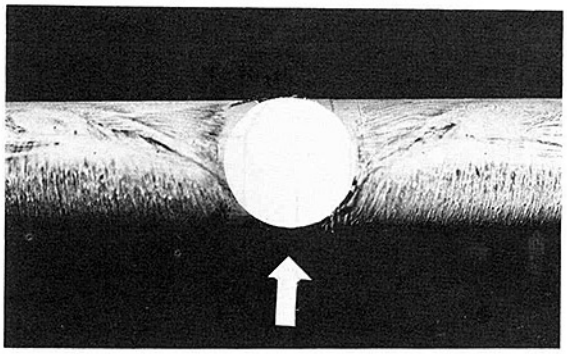

Fig. 7 The same as in Fig. 5: top view

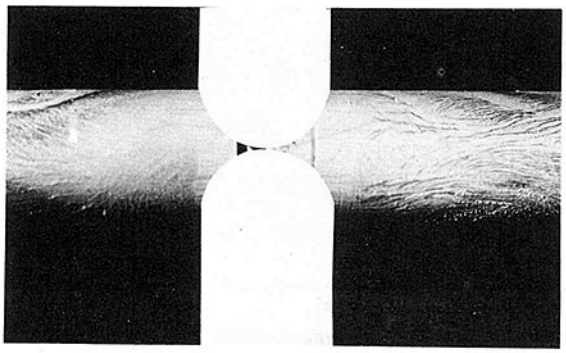

Fig. 6 The same as in Fig. 5: downstream view

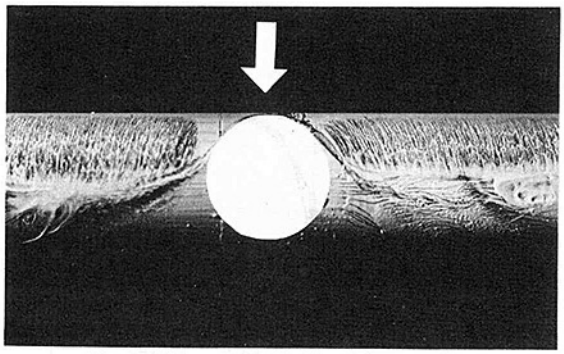

Fig. 8 The same as in Fig. 5: bottom view

The free-stream velocity was evaluated from the pressure difference measured at the beginning and end of the contraction preceding the test section.

Oil-film visualization was performed by spraying the matt-black cylinder surface with a mixture of fluorescent powder in light oil [7]. The surface-flow photographs were taken in ultraviolet light and revealed the powder patterns after about 20 minutes running time.

Experimental Results

The three-dimensional flow in the wake behind two intersecting cylinders is expected to be symmetrical relative to both cylinders' axes. The strongest interference is expected in the plane of mutual intersection and it should gradually decrease and approach a two-dimensional wake far away from the intersection.

A typical pressure distribution around a single, nominally[1] two dimensional circular cylinder is shown in Fig. 2 for comparison. The well-known features are the favorable pressure gradient up to 70 deg, adverse pressure gradient from 70–90 deg the inflexion point around 80 deg which corresponds to the separation point and a flat base pressure in the near-wake with $C_{pb} = -1.4$. There was a negligible difference between the pressure distribution measured at $R_e = 9.4 \times 10^4$ and $R_e = 4.2 \times 10^4$.

[1]There is always an interaction between the wall boundary layer and piercing cylinders which produces a three dimensional horse-shoe vortex, see Baker [8].

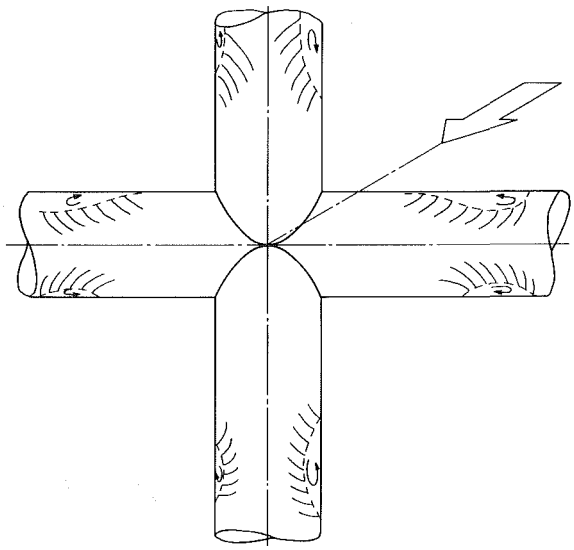

Fig. 9 Sketch of inferred flow pattern

The effect of interference is seen in Fig. 2 to spread even 2.5 diameters away from the centre of the intersection. The minimum C_{pmin} is -2.1, well in excess of -1.6 found for a nominally two dimensional cylinder. The region of the adverse pressure gradient extended from 75 to 140 deg with an estimated separation at 105 deg and $C_{pb} = -1.6$. At about 2 diameters from the intersection, $C_{pmin} = -2.0$, and the extent of the adverse pressure region was reduced from 140 to 115 deg with separation just beyond 90 deg. Nearer to the intersection, $C_{pmin} = -2.3$, the adverse pressure gradient became steep between 75 and 100 deg, the separation was 85 deg and $C_{pb} = -1.4$.

When the cross-section with pressure tappings was displaced towards the intersection at any distance less than ½ diameter some pressure tappings were covered by the other intersecting cylinder. Figure 3 shows these "incomplete" pressure distributions. There are two distinct features of these pressure distributions:

(*a*) The favorable pressure gradient becomes less steep at first indicating a stagnant region followed by an almost discontinuous fall in pressure coefficient. This is seen for all three spanwise stations where pressure was measured.

(*b*) The flat pressure distribution measured in the near-wake region showed consistently that the base pressure was higher than that found behind the nominally two-dimensional cylinder. The variation of C_{pb} along the span is shown in Fig. 4. There is a Reynolds number effect in the location of the C_{pbmin}.

The variation of local pressure in the separated region along the span indicates the existence of secondary flow. Figures 5–8 show the surface flow pattern produced by the secondary flow which considerably distorted separation lines. The "blobs" of accumulated powder, seen in Figs. 7 and 8, are located in the regions where the minimum base pressure was measured. The minimum base pressure induces a maximum local drag coefficient and it is evident in Figs. 6 and 8 that vigorous swirling flows surround the blobs. Hence it may be inferred that the blobs are imprints of the centers of streamwise vortices with concomitant minimum pressures. These two pairs of attached streamwise vortices on each cylinder are sketched in Fig. 9. This is in agreement with hot wire measurements in the far-wake [5]. The variation of the extent and location of the adverse pressure gradient region is seen to be closely related to the distorted separated lines. The separation points can be inferred from the inflexion of local pressure distribution curves.

The most important parameter from the practical point of view is the variation of the local drag coefficient along the span of the cylinder. The local drag coefficient was evaluated from the measured pressure distributions. Figure 10 shows the variation of local drag coefficient for two Reynolds numbers. The maximum value of the local drag coefficient coincided with the minimum base pressure coefficient shown in Fig. 4 and with the location of blobs seen in Figs. 6 and 8. The local minimum of drag coefficient around $Z/D = \pm 1$ for both Reynolds numbers cannot be explained.

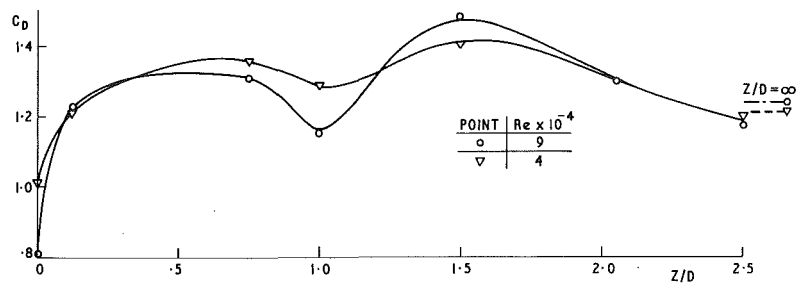

Fig. 10 Variation of local pressure drag coefficient along the span (*a*) $R_e = 4 \times 10^4$ and (*b*) $R_e = 9 \times 10^4$.

Conclusion

The combined measurement of pressure distribution around and along the cylinder and the application of the oil-film visualization techniques confirmed the existence of four pairs of streamwise vortices as found in [3] and [5]. These streamwise vortices originate at the surface of the cylinders in the near-wake region. The variation of local base pressure along the span of the cylinder was related to the secondary flows and resulted in a maximum local drag coefficient in the attachment region of streamwise vortices.

Acknowledgment

The author would like to give credit for experimental assistance to his former student Mr A. A. Qaisi.

References

1 Zdravkovich, M. M., "Review of Flow Interference Between Two Circular Cylinders in Various Arrangements," ASME JOURNAL FLUIDS ENGINEERING, Vol. 99, 1977, pp. 618–633.

2 Zdravkovich, M. M., "Classification of Flow Induced Oscillations of Two Parallel Circular Cylinders in Various Arrangements," in *ASME Symposium on Flow Induced Vibrations*, Ed. M. Paidoussis et al., Vol. 2, 1984, pp. 1–19.

3 Zdravkovich, M. M., "Interference Between Two Circular Cylinders Forming a Cross," *Journal of Fluid Mechanics*, Vol. 128, 1983, pp. 231–246.

4 Biermann, D., and Hernstein, W. H., "The Interaction Between Struts in Various Combinations," Nat. Adv. Comm. Aer. Tech. Rep. 468, 1933.

5 Osaka, H., Nakamura, Y., Yamada, H., Kuwata, Y., and Kageyama, Y., "The Structure of Turbulent Wake Behind a Cruciform Circular Cylinder," *Bulletin Japan Society Mechanical Engineers*, Vol. 26, 1983, pp. 351–358 and pp. 521–528.

6 Osaka, H., Yamada, H., and Nakamura, I., "Three-Dimensional Structure of the Turbulent Wake Behind an Intersecting Circular Cylinder," in IUTAM Symp. on Three-Dimensional Turbulent Boundary Layers, Springer-Verlag, Berlin 1983.

7 Square, L. C., "The Motion of a Thin Oil Sheet Under the Boundary Layer on a Body," in AGARD 70, Flow Visualization Using Indicators, 1962.

8 Baker, C. J., "The Turbulent Horse-Show Vortex," *Journal Wind Engineering and Industrial Aerodynamics*, Vol. 6, 1980, pp. 9–23.

An Investigation of Compressible Flow Characteristics of Butterfly Valves

A. L. Addy
Professor and Associate Head.
Fellow ASME

M. J. Morris
U.S. Department of Energy
Graduate Trainee.

J. C. Dutton
Associate Professor.
Mem. ASME

Department of Mechanical and Industrial Engineering,
University of Illinois at Urbana-Champaign,
Urbana, Ill. 61801

Compressible flow characteristics including mass flowrate, onset of "choked" flow, stagnation pressure loss, and static pressure recovery have been investigated for butterfly valves. A simplified sudden-enlargement in flow area theoretical model has been used to characterize the overall mass flowrate and pressure characteristics of the valve flow. A series of small-scale compressible flow experiments has also been conducted using sudden-enlargement configurations with different nozzle geometries and using geometrically similar model valves. These experiments provided a database for augmenting the simplified theoretical model with needed empirical information and for assessing the range of applicability of the theoretical model. This method can be used to predict the mass flow and pressure characteristics of full-scale valves based on model experiments and/or to determine the overall operating characteristics of full-scale valves from in situ pressure measurements.

Introduction

Under certain combinations of valve-disk opening angle and pressure difference across the valve, compressible flow effects can significantly alter the performance characteristics and flowfield of a butterfly valve. At these conditions, regions of transonic and supersonic flow can develop in the vicinity of the valve-disk and downstream of it. In addition, limitation of the mass flowrate through the valve may occur with the onset of "choked" flow, and complex systems of expansion and shock waves may develop at and downstream of the valve. In turn, these processes establish the pressure distribution through the downstream of the valve.

In design and performance analyses of valves which are to operate with compressible flow, the prediction of the mass flowrate and overall pressure characteristics is an important consideration. Separated flow regions form downstream of the valve-disk and can vary significantly in size depending on the valve-disk opening angle. These separated flow regions tend to behave as a sudden-enlargement in flow area to the flow passing between the valve-disk and seat. In this investigation, a simplified sudden-enlargement theoretical model has been chosen because it includes the essential features necessary to describe the overall operating characteristics of the valve. If an "effective" sudden-enlargement in area ratio can be determined from experiments for the valve, the theoretical model can be used to predict the mass flowrate and overall pressure characteristics of the valve. To demonstrate the method, experiments with model valves and a full-scale valve have been used to determine the "effective" sudden-enlargement area ratio for the valves as a function of valve-disk opening angle.

Contributed by the Fluids Engineering Division for publication in the JOURNAL OF FLUIDS ENGINEERING. Manuscript received by the Fluids Engineering Division, February 24, 1984.

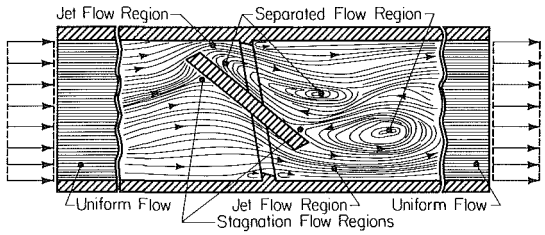

Fig. 1 Qualitative flowfield features in a partially open butterfly-type valve

Qualitative Nature of Butterfly Valve Flow

Based on flow visualization studies, the flowfield within a partially open valve is illustrated in Fig. 1. The flow changes speed and direction as it approaches the valve-disk because of the decreasing flow area and the orientation of the disk. On the upstream surface of the disk, a stagnation region forms; outside of this region, the flow direction is toward the periphery of the disk. The flow is accelerated as it passes between the wall and the valve-disk because of the decreasing flow area. Near the periphery of the disk, the flow separates and becomes a jet flow which is bounded on one side by the wall and on the other side by the separated flow region in the wake of the valve-disk. The separated flow region includes recirculating flows and a stagnation flow region on the downstream surface of the disk. The jet and separated flows interact, mix, and recompress downstream. Sufficiently far downstream of the valve-disk, the flow must again occupy the available flow area and approach a fully-developed flow (which is modeled one-dimensionally as being uniform).

The mass flowrate and pressure characteristics of the butterfly valve are strongly affected by the interaction between the jet and separated flows downstream of the valve-disk. The separation at the valve-disk effectively subjects the flow to a

sudden-enlargement in flow area. The nature and irreversibility of the flow through the valve are strongly dependent on the sudden-enlargement area relative to the flow area at separation. In particular for a compressible flow, transonic and supersonic regions can develop in the jet flow. As a result, choking of the flow through the valve can occur, relatively low pressures can occur in the separated flow region, and the flow can recompress to higher pressure levels far downstream.

In a valve, the size and structure of the separated flow region depend on the valve geometry and the valve-disk opening angle and, to a lesser extent, the local flow conditions. Qualitatively, the flow experiences a smaller sudden-enlargement area change when the valve is fully open than when the valve approaches the fully closed position. Thus, the sudden-enlargement area would be expected to vary continuously between these limits as a function of valve-disk opening angle.

Theoretical Analysis

Theoretical Flow Model. The simplified theoretical flow model selected to represent the flow through a butterfly valve is shown in Fig. 2. This flow model includes the essential features of the valve flow necessary to predict the mass flow and overall pressure characteristics, *viz.*, the jet flow, the sudden-enlargement in flow area, and the mixing and recompression to a uniform downstream state. In this model, flow from an ideal converging nozzle separates at the sudden-enlargement at station 1, and forms a separated flow region bounded by the mixing duct wall and the jet flow from the nozzle. These flows interact and mix within the duct and approach a uniform flow far downstream in the mixing duct.[1]

The compressible flow through a sudden-enlargement in flow area has been extensively investigated in the literature [1–9]. It has been shown that there is good agreement between predicted and experimentally determined flow characteristics for the discharge of a converging nozzle into a sudden-enlargement in flow area. The theory developed herein proposes to use this well known sudden-enlargement analysis to model the pressure and mass flow characteristics of the flow through butterfly valves. However, to relate the theoretical model and actual valve flows, "effective" nozzle-to-duct area ratios must be determined as a function of the valve-disk opening angle and the upstream and downstream flow conditions using model or full-scale valve experiments. In this way, some of the complexity of the valve flow is incorporated into the theoretical model via this empirical area ratio relationship. To the authors' knowledge, this is the first time the sudden-enlargement flow model has been applied to model the operating characteristics of the flow through valves.

Theoretical Formulation. The conservation principles are applied to the control volume indicated in Fig. 2 to analyze compressible flow through the sudden-enlargement in flow

[1]Experiments have shown that a uniform downstream flow is approached within the mixing duct for duct length-to-diameter ratios, L/D, in the approximate range: $8 < L/D < 12$.

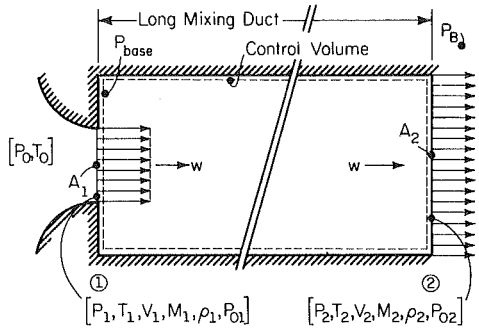

Fig. 2 Sudden-enlargement in flow area model

area. For steady and uniform flow at stations 1 and 2, the continuity equations becomes:

$$w = \rho_1 A_1 V_1 = \rho_2 A_2 V_2 \tag{1}$$

If shear stresses at the wall are neglected, the momentum equation becomes:

$$P_{base}(A_2 - A_1) + P_1 A_1 - P_2 A_2 = \rho_2 A_2 V_2^2 - \rho_1 A_1 V_1^2 \tag{2}$$

For compressible flow, $P_1 \geq P_{base}$. For the flow of a calorically perfect gas without shaft/shear work and heat transfer, the energy equation simplifies to:

$$T_0 = T_{01} = T_{02} \tag{3}$$

Equations (1)–(3) can be combined and simplified into the following equations which are convenient for computations. These equations are:

$$\frac{P_2}{P_1} = \frac{A_1}{A_2}\left[\frac{P}{P^*}(\gamma, M_2)\right]\left[\frac{P}{P^*}(\gamma, M_1)\right]^{-1} \tag{4}$$

and

$$\frac{P_{base}}{P_1} = (\gamma+1)\left[\frac{A_1/A_2}{1 - A_1/A_2}\right]\left[\frac{F}{F^*}(\gamma, M_2) - \frac{F}{F^*}(\gamma, M_1)\right]\left[\frac{P}{P^*}(\gamma, M_1)\right]^{-1} \tag{5}$$

The gas dynamic functions, P/P^* and F/F^*, are defined as:

$$\frac{P}{P^*}(\gamma, M) = M^{-1}\left[\left(\frac{2}{\gamma+1}\right)\left(1 + \frac{\gamma-1}{2}M^2\right)\right]^{-1/2} \tag{6}$$

and

$$\frac{F}{F^*}(\gamma, M) = M^{-1}[1+\gamma M^2][2(\gamma+1)\left(1 + \frac{\gamma-1}{2}M^2\right)]^{-1/2} \tag{7}$$

From equations (4) and (5), the base and downstream pressure ratios can be expressed in terms of the upstream stagnation pressure by:

$$\frac{P_2}{P_{01}} = \frac{P_2}{P_1} \cdot \frac{P}{P_0}(\gamma, M_1) \tag{8}$$

and

$$\frac{P_{base}}{P_{01}} = \frac{P_{base}}{P_1} \cdot \frac{P}{P_0}(\gamma, M_1) \tag{9}$$

Nomenclature

A	= area	T	= temperature	**Supscripts**	
C_F	= flow coefficient, w/w_{CN}	V	= velocity magnitude	0	= stagnation condition
D	= diameter	w	= mass flowrate	1,2	= flowfield locations
L	= length	α	= valve-disk opening angle	ATM	= atmosphere
M	= Mach number	γ	= ratio of specific heats	B	= back
P	= pressure	ρ	= density	base	= base region
R	= gas constant	$(A_1/A_2)_E$	= effective area ratio	CN	= ideal converging nozzle
s	= specific entropy	$(P_2/P_0)^*$	= pressure ratio for onset of choked flow	N	= actual converging nozzle
t	= valve-disk thickness			V	= valve

where the isentropic pressure ratio function, P/P_0, is defined by:

$$\frac{P}{P_0}(\gamma,M)=\left(1+\frac{\gamma-1}{2}M^2\right)^{-\gamma/(\gamma-1)} \tag{10}$$

The ratio of stagnation pressures at stations 1 and 2 is given by:

$$\frac{P_{02}}{P_{01}}=\left[\frac{P}{P_0}(\gamma,M_1)\right]\left[\frac{P}{P_0}(\gamma,M_2)\right]^{-1}\cdot\left[\frac{P_2}{P_1}\right] \tag{11}$$

where P_2/P_1 is obtained from equation (4).

For one-dimensional adiabatic flow, the specific entropy difference between stations 1 and 2 is given in terms of the stagnation pressure ratio by:

$$(s_2-s_1)/R=-\ln(P_{02}/P_{01}) \tag{12}$$

Thus the irreversibility in the flow between stations 1 and 2 is directly related to the ratio of the stagnation pressures at those stations.

Flow Regimes. In this one-dimensional analysis, there are two flow regimes which are distinguished by whether the flow is subsonic or sonic at station 1. For subsonic flow, the requirements are: $0 \le M_1 < 1$ and $P_{base}/P_1 = 1$. For sonic flow, the requirements are: $M_1 = 1$ and $P_{base}/P_1 \le 1$. The onset of choked flow occurs when $M_1 = 1$ and $P_{base}/P_1 = 1$.

This one-dimensional analysis will provide solutions in the range: $0 \le P_{base}/P_1 \le 1$. However, experiments have shown that the value of P_{base}/P_1 approaches a constant value greater than zero at low values of the back pressure ratio, P_B/P_0. When this occurs, the flow ceases to be one-dimensional in nature and becomes dominated by two-dimensional effects involving the attachment of the expanding jet flow to the wall, the entrainment by turbulent mixing of flow from the separated region, and the recompression of this entrained flow. This is the classic internal base-pressure problem discussed in References [7–9].

Application to Valve Flow. For a given gas flow, the ratio of the specific heats, γ, is known. If the area ratio, A_1/A_2, and the pressure ratio, P_2/P_{01} are known, the sudden-enlargement model can be used to determine the mass flow characteristics of the valve. From this analysis, the pressure ratio for the onset of choked flow, $(P_2/P_{01})^*$, can also be determined for a given value of A_1/A_2. For values of A_1/A_2, P_2/P_{01}, a value of P_{02}/P_{01} can be determined. The one-dimensional theoretical results for the flow of air with $\gamma = 1.4$ are presented in Figs. 5–7, 10, and 11. Regions in which one-dimensional solutions do not exist for the given conditions are identified in Figs. 6 and 10. The one-dimensional model predicts an unrealistic negative base pressure ratio for these conditions although, as just mentioned, it actually approaches a low constant value. These theoretical results can be related to actual butterfly valve flows by conducting experiments to determine the "effective" sudden-enlargement area ratio, $(A_1/A_2)_E$, as a function of valve-disk opening angle.

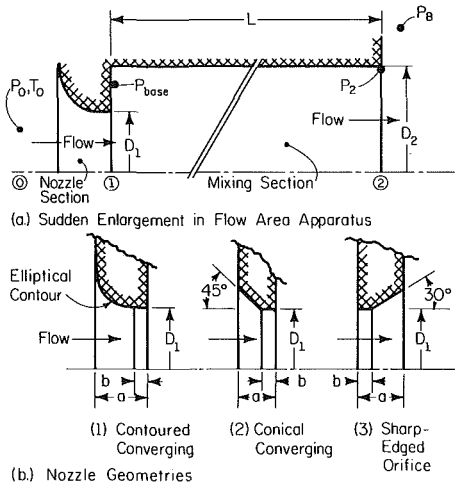

Fig. 3 Apparatus for sudden-enlargement experiments

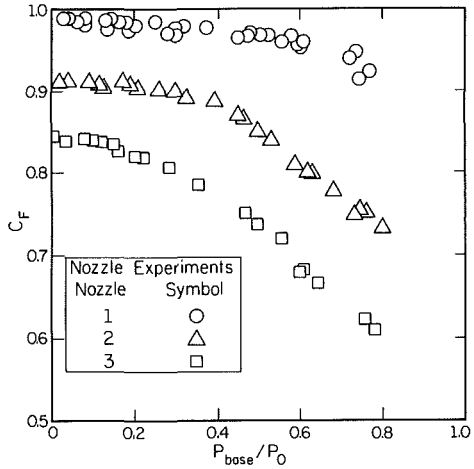

Fig. 4 Mass flowrate coefficients for the three nozzle geometries used in the sudden-enlargement experiments. (Uncertainty in C_F = ±2 percent and in P_{base}/P_0 = ±1 percent)

Table 1 Summary of geometries investigated in sudden-enlargement experiments

Nozzle Number	D_1 (mm)	a/D_1 (−)	b/D_1 (−)	D_2 (mm)	L/D_2 (−)	A_1/A_2 (−)
1	12.7	1.40	0.40	15.9	20	0.640
				19.1	20	0.444
				22.2	20	0.327
				28.6	10	0.198
	15.9	2.60	0.30	19.1	20	0.694
				22.2	20	0.510
				28.6	10	0.309
	19.1	1.80	0.0	22.2	20	0.735
				28.6	10	0.445
2	12.7	1.00	0.11	15.9	20	0.640
				19.1	20	0.444
				22.2	20	0.327
				28.6	10	0.198
3	12.7	0.55	0.11	15.9	20	0.640
				19.1	20	0.444
				22.2	20	0.327
				28.6	10	0.198

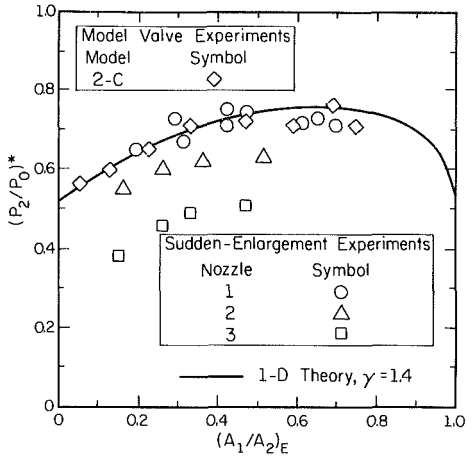

Fig. 5 Pressure ratio for the onset of "choked" flow as a function of the effective sudden-enlargement area ratio for the model valve; P_0 corresponds to P_{01}. (Uncertainty in $(P_2/P_0)^* = \pm 3$ percent and $(A_1/A_2)_E = \pm 3$ percent)

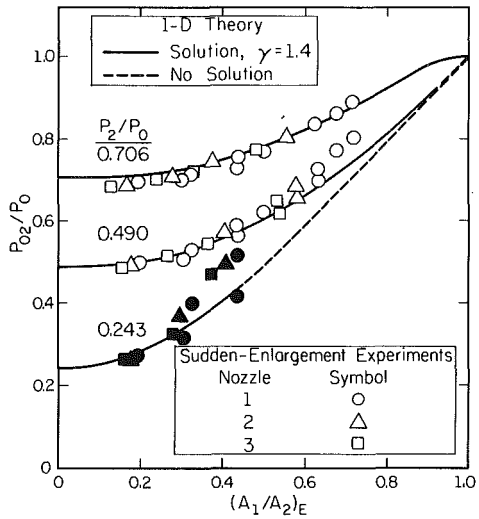

Fig. 6 Stagnation pressure ratio as a function of the effective sudden-enlargement area ratio for different nozzle geometries. (Uncertainty in P_{02}/P_0, $P_2/P_0 = \pm 1$ percent and $(A_1/A_2)_E = \pm 3$ percent)

Experimental Investigation

A series of small-scale, compressible flow experiments was conducted with sudden-enlargement configurations and model butterfly valves. The objectives of these experiments were to assess the applicability and limitations of the theoretical model and to develop the empirical database needed to use the theoretical model to analyze valve flow.

Based on one of the model valves, a full-scale valve was designed, built, and tested. Experimental results for this valve are presented and compared herein with model valve experimental data and theoretical predictions.

Sudden-Enlargement Experiments. The effects of nozzle geometry and nozzle-to-duct area ratio on the sudden-enlargement flow were investigated. Three nozzle geometries: (1) contoured converging, (2) conical converging, and (3) sharp-edged orifice, were used in these experiments to achieve different mass flowrate coefficients.[2] The experimental apparatus and the nozzle geometries are illustrated in Fig. 3 and the detailed dimensions are summarized in Table 1.

These experiments were conducted at several values of upstream stagnation pressure, P_0, while the downstream

[2]The nozzle mass flowrate coefficient is defined as the ratio of the mass flowrate through the actual nozzle to that of an ideal converging nozzle with the same exit area and pressure operating conditions, i.e., $C_f = w_N/w_{CN}$.

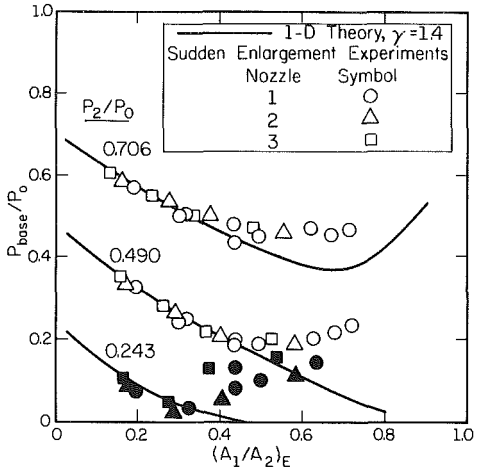

Fig. 7 Base pressure ratio as a function of the effective sudden-enlargement area ratio for different nozzle geometries; the solid symbols distinguish between pressure ratios. (Uncertainty in P_{02}/P_0, $P_2/P_0 = \pm 1$ percent and $(A_1/A_2)_E = \pm 3$ percent)

pressure was approximately atmospheric, $P_2 = P_B = P_{ATM}$. The range of operating pressure ratios for these experiments was approximately: $0.15 < P_2/P_0 < 0.90$. For the area ratios of Table 1 and the above range of pressure ratios, the base pressure ratio varied in the approximate range: $0.02 < P_{base}/P_0 < 0.85$. Corresponding to this range of pressure ratios, the Reynolds number based on the exit diameter of the nozzle varied in the approximate range: $10^5 < \mathrm{Re}_{D_1} < 10^6$.

In these experiments, the static and stagnation pressures were measured with pressure transducers, the temperatures were measured with thermocouples, and the mass flowrate was measured with standard VDI nozzle sections. These measurements were digitized, stored on magnetic tape, and reduced by computer. The overall accuracies of these measurements are estimated to be: ± 1, ± 1, and ± 2 percent, respectively.

For each configuration and operating pressure ratio, P_B/P_0, the following experimental results were obtained: C_F, P_2/P_0, P_{base}/P_0, and P_{02}/P_0.[3] The onset of choked flow was determined for each configuration by determining the pressure ratio, $(P_2/P_0)^*$, for which the mass flowrate became independent of P_2/P_0.

The nozzle flow coefficients, which were determined from these experiments, are presented in Fig. 4 for nozzle geometries 1, 2, and 3. The nozzle flow coefficients are seen to vary substantially. For nozzle geometries 2 and 3, the variation of their flow coefficients with pressure ratio is attributed, in part, to nonuniform flow effects occurring in the transonic flowfield near the nozzle exit [10, 11].

Similar to the approach proposed to analyze valve flow characteristics, an "effective" sudden-enlargement area ratio, $(A_1/A_2)_E$, can also be determined from these experiments; this area ratio is:

$$(A_1/A_2)_E = C_F \cdot (A_1/A_2). \tag{13}$$

The one-dimensional theoretical results and the experimentally determined pressure ratio data for the onset of choked flow, $(P_2/P_0)^*$, based on these "effective" area ratios, are given in Fig. 5 for the three nozzle geometries. In Fig. 5, the agreement between the experimental and theoretical results is seen to be good for nozzle geometry 1, only fair for nozzle geometry 2, and poor for nozzle geometry 3. The disagreement between the one-dimensional theoretical and experimental results for the latter two nozzle geometries is due to nonuniform transonic flow effects within these nozzles. These effects substan-

[3]In these experiments, $P_0 = P_{01}$ and $P_2 = P_B$.

[4]For these flows, $P_{01} = P_0$.

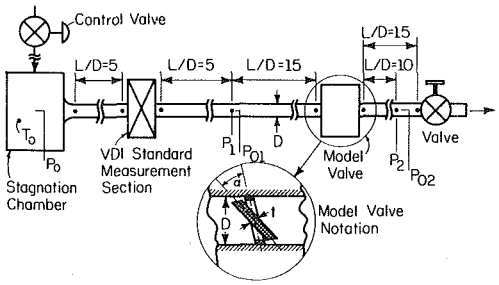

Fig. 8 Schematic of experimental apparatus for model valve experiments

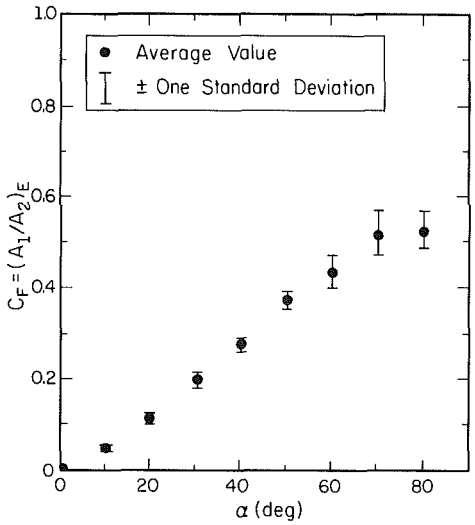

Fig. 9 Mass flowrate coefficient as a function of the valve-disk opening angle for model 2-A and operating pressure ratio range; 0.36 ≤ P_2/P_{01} ≤ 0.86. (Uncertainty is indicated within the figure.)

tially reduce the pressure ratio for choked flow through these nozzle geometries compared to that required for the contoured converging nozzle geometry by distorting the sonic line [10].

The experimental and theoretical values of the stagnation pressure ratio, P_{02}/P_0, and the base pressure ratio, P_{base}/P_0, are presented in Figs. 6 and 7 versus the "effective" area ratio for three values of the operating pressure ratio, P_2/P_0[4]. The "effective" area ratio correlates the experimental pressure ratio data in these figures reasonably well. The stagnation pressure ratio data are in good agreement with the theoretical predictions in Fig. 6. The base pressure ratio data are in good agreement with the one-dimensional theory in Fig. 7 over a part of the range of $(A_1/A_2)_E$. However, as previously mentioned, for each P_2/P_0, the base pressure becomes constant and the flow becomes two-dimensional in nature when the nozzle jet flow attaches to the sudden-enlargement wall. Consequently, the agreement with one-dimensional theory is expected to be poor over this range of conditions.

From the comparisons of Figs. 5, 6, and 7, the pressure ratio for the onset of choking is seen to be sensitive to the nozzle geometry while the stagnation and base pressure ratios are less sensitive to the nozzle geometry as demonstrated by the correlation achieved by utilizing the concept of the "effective" sudden-enlargement area ratio.

Model Valve Experiments. A series of experiments was conducted with two sets of model butterfly valves using the experimental apparatus illustrated in Fig. 8 and the instrumentation system previously described for the sudden-enlargement experiments. For the first set of valves, three nominal valve diameters (50.8, 76.2, and 101.6 mm) were selected and the valve-disks were scaled proportionately to maintain geometric similarity. These experiments were used to determine the effects of model valve scale. In a nondimensional representation of the valve characteristics, it was found that the two model valves with nominal diameters of 76.2 mm and 101.6 mm produced essentially the same flow characteristics. Based on these results, a second set of four model valves was designed with a nominal diameter of 76.2 mm. These model valves have similar valve-disk geometries but with different valve-disk thicknesses; the significant dimensions for these valves are summarized in Table 2.

Both sets of valves were investigated with compressible flow over a wide range of operating conditions and valve opening angles. In these experiments, the pressure ratio for the onset of

Table 2 Summary of model valve dimensions

Valve Set	D mm	t/D
1 – A	50.8	0.100
– B	76.2	0.100
– C	101.6	0.100
2 – A	76.2	0.144
– B	76.2	0.086
– C	76.2	0.075
– D	76.2	0.121

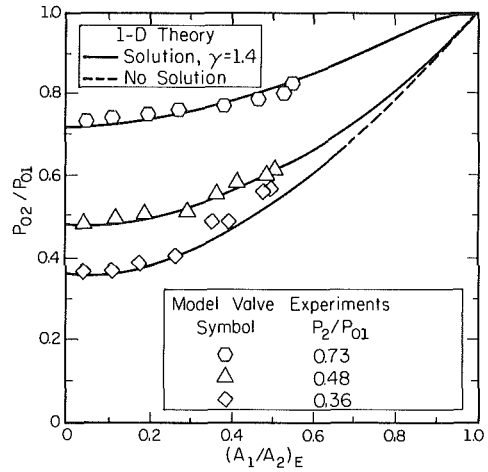

Fig. 10 Stagnation pressure ratio as a function of the effective sudden-enlargement area ratio for model 2-A. (Uncertainty same as Figs. 6 and 7.)

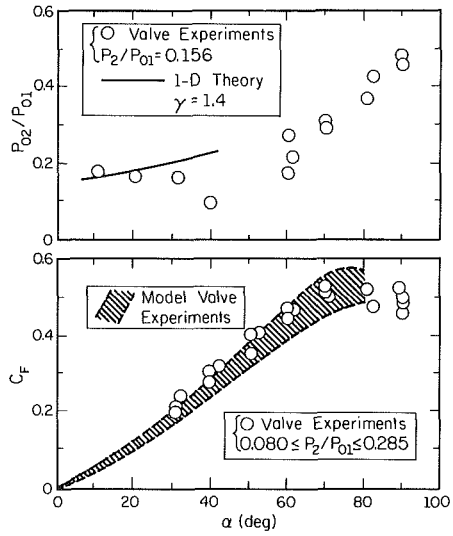

Fig. 11 Mass flowrate coefficient and stagnation pressure ratio as a function of valve-disk opening angle for a full-scale valve which was based on model 2-A. (Uncertainty in C_F = ±4 percent, P_{02}/P_{01} = ±3 percent, and α = ±0.5 percent.)

choked flow, $(P_2/P_0)^*$, was determined over the range of valve-disk opening angles. The mass flowrate characteristics of the model valves were expressed in terms of a flow coefficient which is defined as the ratio of the actual valve mass flowrate, w_v, to the mass flowrate, w_{CN}, through an ideal converging nozzle with a throat diameter equal to the nominal valve diameter and with the same pressure conditions as the model valve. The valve flow coefficient is:

$$C_F = w_v/w_{CN} \tag{14}$$

This flow coefficient definition is similar to that used to represent the flow performance of actual nozzles. For a valve, this flow coefficient approaches a valve somewhat less than unity when the valve is fully open and a valve of zero when the valve is nearly closed, i.e., $0 \leq C_F < 1$. This flow coefficient can also be interpreted as the ratio of the one-dimensional valve flow area to the nominal valve area or the "effective" sudden-enlargement area ratio for the valve; that is:

$$(A_1/A_2)_E = C_F \tag{15}$$

From experiments with a given model valve, the flow coefficient was found to be primarily a function of the valve-disk opening angle and to a much lesser degree a function of the upstream pipe Reynolds number.

Representative experimental and theoretical results are presented in Figs. 5, 9, and 10 for two members of the second set of model valves, models 2-A and 2-C; these experimental data are, however, typical of data obtained for all of the model valves. Mean values of the experimentally determined valve flow coefficient, C_F, are presented in Fig. 9 as a function of valve-disk opening angle, α. The range of variation in C_F for these experiments is also indicated in this figure and is attributed, in part, to the parametric variation in operating pressure ratio, P_2/P_{01}, during these experiments. The range in operating pressure ratio was: $0.358 < P_2/P_{01} < 0.855$. The experimentally determined values of the choking pressure ratio $(P_2/P_{01})^*$ are presented versus $(A_1/A_2)_E = C_F$ in Fig. 5. For comparison, this figure also includes the theoretical curve for one-dimensional flow. The agreement between the experimental and theoretical results is good. The effective sudden-enlargement area ratio model predicts the onset of choking better for the butterfly valve than for the conically convergent or sharp-edged orifice/sudden-enlargement geometries. The experimental and theoretical results for the stagnation pressure ratio, P_{02}/P_{01}, are presented in Fig. 10 as a function of $(A_1/A_2)_E = C_F$ for three parametric values of P_2/P_{01}. The agreement between these results is also good. The one-dimensional theoretical model represents the valve mass flow and overall pressure characteristics very well given the empirical relationship, C_F versus α, for the valve.

Full-Scale Valve Experiments. A full-scale valve with a nominal diameter of 304.8 mm was designed based on model valve 2-A [12]; the full-scale valve-to-model valve diameter ratio is four. One of the objectives of these experiments was to measure the mass flowrate and stagnation pressure ratio characteristics of this valve as a function of valve-disk opening angle for choked flow through the valve. These choked flow experiments were conducted over a range of operating pressure ratios: $0.080 < P_2/P_{01} < 0.285$.

The experimentally determined mass flowrate coefficient, C_F, was determined from these experiments as a function of valve-disk opening angle, α. These data are presented in the lower part of Fig. 11 along with the corresponding data for the model valve. The agreement between these experimental data for C_F is reasonably good and supports the scaling of the model valve data to design and analyze full-scale valves.

Experimental and theoretical results for the stagnation pressure ratio are presented in the upper part of Fig. 11 for a constant value of $P_2/P_{01} = 0.156$. As a result of the low value of P_2/P_{01}, the one-dimensional theoretical solution for P_{02}/P_{01} exists only over the indicated range. Due to geometric constraints, the downstream total-head probe could only be located 2.5 diameters downstream of the test valve. As a result, some of the variation in stagnation pressure data could be due to the total-head probe being affected by the separated flow in the wake of the valve disk.

Conclusions

This investigation demonstrates the usefulness of the one-dimensional sudden-enlargement flow model in understanding and predicting the overall performance characteristics of butterfly valve designs under various operating conditions. The sudden-enlargement analysis coupled with the empirical valve flow coefficient accurately relates the mass flow and overall pressure characteristics of the sudden-enlargement geometry to those of the valve flow; it also relates these operating characteristics for a model valve to those of a full-scale valve. This analysis provides a basis for evaluating the effects of compressible flow on valve performance. If the valve flow coefficient is known and an operating pressure ratio specified, the performance characteristics of the valve can be estimated. Conversely, the flow performance characteristics of a full scale valve *in situ* can be determined using the sudden-enlargement analysis with measured values of the static and the stagnation pressures upstream and downstream of the valve. Consequently, this analysis shows promise as a means to evaluate better valve design and to optimize valve performance.

Acknowledgment

This research was supported by the CLOW Corporation, Engineered Products Division, the Department of Energy Graduate Traineeship Program, and the Department of Mechanical and Industrial Engineering, University of Illinois at Urbana-Champaign.

References

1 Hall, W. B., and Orme, E. M., "Flow of a Compressible Fluid Through a Sudden-Enlargement in a Pipe," *Proc. of Inst. of Mech. Eng.*, Vol. 169, No. 49, 1955.

2 Crocco, L., "One-Dimensional Treatment of Steady Gas Dynamics," Section B of *Fundamentals of Gas Dynamics*, H. W. Emmons, ed., Vol. III, High Speed Aerodynamics and Jet Propulsion, Princeton University Press, 1958.

3 Benedict, R. P., Carlucci, N. A., and Swetz, S. D., "Flow Losses in Abrupt Enlargements and Contractions," ASME *Journal of Engineering for Power*, Vol. 88, 1966, pp. 73–81.

4 Shouman, A. R., and Massey, J. L. Jr., "Stagnation Pressure Losses of Compressible Fluids Through Abrupt Area Changes Neglecting Friction at the Walls," ASME Paper No. 68-WA/FE-46, 1968.

5 Benedict, R. P., Wyler, J. S., Dudek, J. A., and Gleed, R. A., "Generalized Flow Across an Abrupt Enlargement," ASME *Journal of Engineering for Power*, Vol. 98, 1976, pp. 327–334.

6 Benedict, R. P., *Fundamentals of Pipe Flow*, Wiley, 1980.

7 Wick, R. S., "The Effect of Boundary Layer on Sonic Flow Through An Abrupt Cross-Sectional Area Change," *J. Aero. Sci.*, Vol. 20, 1953, pp. 675–682.

8 Korst, H. H., "Comments on the Effect of Boundary Layer on Sonic Flow Through an Abrupt Cross-Sectional Area Change," *J. Aero. Sci.*, Vol. 21, No. 8, 1954, pp. 568–569.

9 Korst, H. H., Chow, W. L., and Zumwalt, G. W., "Research on Transonic and Supersonic Flow of a Real Fluid at Abrupt Increases in Cross Section," University of Illinois, ME Technical Report 392-5, Dec. 1959.

10 Thornock, R. L. and Brown, E. F., "An Experimental Study of Compressible Flow Through Convergent-Conical Nozzles, Including a Comparison with Theoretical Results," ASME *Journal of Basic Engineering*, Vol. 94, Dec. 1972, pp. 926–932.

11 Dutton, J. C. and Addy, A. L., "Transonic Flow in the Throat Region of Axisymmetric Nozzles," *AIAA Journal*, Vol. 19, No. 6, June 1981, pp. 801–804.

12 Felber, M. L., "Simultaneous Static Seismic Load and Flow Interruption Capability Tests of a 12-Inch Valve for the CLOW Corporation," Report No. 2-59700/1R-52972, Vought Corporation, Dallas, Texas, 15 Dec. 1981.

The Influence of Pipe Motion on Acoustic Wave Propagation

S. Stuckenbruck[1]
Mechanical Engineering Department,
Pontificia Universidade Catolica,
Rio de Janerio, Brasil

D. C. Wiggert
Department of Civil
and Sanitary Engineering,
Michigan State University,
East Lansing, Mich.

R. S. Otwell
McNamee, Porter and Seeley,
Ann Arbor, Mich.

It is well known that the magnitude of the acoustic wavespeed in piping is influenced by properties of the fluid and the pipe material. Traditionally, derivations have been based on a quasi-static control volume model, where the pipe deformation takes place in the time the liquid acoustic wave travels a known distance along the pipe. In actuality, dilation of the piping causes axial stress waves to propagate along the pipe wall at speeds greater than that of the acoustic wave. Such axial coupling between the liquid and piping has been reported by several investigators, including Walker and Phillips [4], *who developed a six-equation model with a three-wave family—radial and axial stress, and axial liquid. In the present study Walker and Phillips' model is simplified to a four-equation one by neglecting radial inertia, a valid assumption for many practical piping system transients. An eigenvalue analysis of the hyperbolic relations reveals two axial waves—in the liquid and in the pipe wall—which are modified by the coupling action. The traditional wave speed formulations with varied coupling constraints are reviewed in light of the present development. Numerical examples are presented which show the effects of such interaction for various combinations of liquid and piping.*

Introduction

Classical waterhammer theory is frequently used to compute the magnitude and velocity of propagation of a solitary pressure pulse in an inviscid, slightly compressible liquid contained in a thin, elastic pipe. In that theory, small effects due to radial fluid velocity and radial pressure gradients, as well as inertial forces in the pipe walls, are all neglected. The theory predicts that pressure waves in the fluid travel at the Joukowski [1] wavespeed.

$$a_f = \left[\frac{K/\rho_f}{1 + \psi \dfrac{dK}{eE}} \right]^{1/2} \tag{1}$$

where the coefficient $\psi = 1$.
For many decades this expression was used in the analysis of waterhammer problems. In recent years, however, higher order theories have been introduced in the study of transients occurring in the flow of fluid in piping system. In these analyses, improvments in the classical waterhammer theory are introduced through the inclusion of new terms which consider effects such as forces associated with radial motion of the fluid and radial and longitudinal motion of the pipe wall, as well as the motion of bends, valves, etc. [2–7]. All of these theories have led to a better understanding of the waterhammer problem, and have introdued new models capable of simulating more accurately some particular cases of this complex phenomenon.

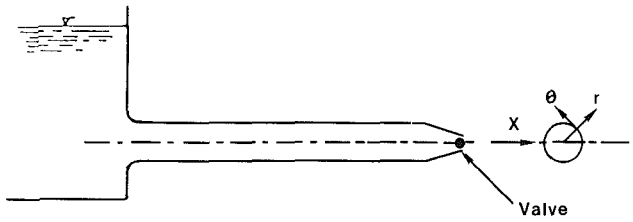

Fig. 1 Schematic of the pipe

Herein, the velocities of propagation of pressure waves in the liquid and stress waves in the pipe walls are obtained by including the equations of conservation of momentum and mass for the pipe wall material as well as for the liquid. The theoretical development is based on a more complete development provided by Walker and Phillips [4]. Since for most of the applied waterhammer problems the pulse lengths are quite long relative to the pipe diameter, inertial forces in the radial direction in the fluid and pipes are neglected [3, 4]. The analysis leads to a system of four linear, first-order, hyperbolic partial differential equations [6], whose eigenvalues give the wave velocities in the fluid and pipe wall.

Traditional Analysis of Wavespeeds

In the past there has been some discussion of the derivation of the velocity of propagation of pressure waves in liquids contained in elastic pipes when the traditional, simplified assumptions have been made. In 1955 Parmakian [8] noted that the longitudinal strain in the pipe wall could have some significant effect on the wave velocities and introduced so-called correction factors for the liquid wave velocity for three commonly used pipe supports. Actually, these support conditions define the type of restraint imposed on the axial strain in the pipe wall. Parmakian found that the coefficient ψ in equa-

[1] Visiting Professor, Department of Civil and Sanitary Engineering, Michigan State University.

Contributed by the Fluids Engineering Division and presented at the Pressure Vessels and Piping Conference and Exhibit, Cambridge, Mass., October 7–10, 1984 of The American Society of Mechanical Engineers. Manuscript received by the Fluids Engineering Division, September 4, 1984.

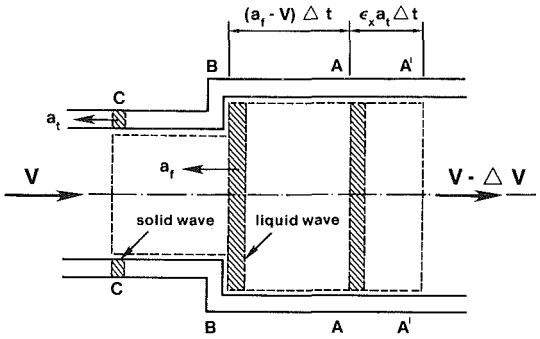

Fig. 2 The liquid and solid wave fronts

tion (1) was a function of the Poisson ratio and the restraint imposed on the axial strain in the pipe wall. Halliwell [9] presented a general expression for the wave velocity which allowed many types of pipe support for both thin- and thick-walled pipes. In a discussipn of Halliwell's article, Streeter [10], although agreeing on values of the coefficient for two cases of pipe support, obtained a different result from Halliwell for the case of no restraint on the axial strain. Unfortunately, this discrepancy still persists in recent publications [11, 12] and, for this reason the traditional analysis is reviewed herein.

Consider an elastic pipe fixed at the reservoir end, Fig. 1, but free to move or vibrate in its axial direction due to loads created, for instance, at a closing valve located at its downstream end. For this particular situation it is well known [2] that two waves propagate initially in the upstream direction (from the valve toward the reservoir): one in the fluid and another in the pipe wall. As these waves travel the pipe deforms in the axial and radial directions causing a continuous change in the pipe geometry as shown in Fig 2.

In order to obtain an expression for the velocity of the wave in the fluid the equations of conservation of mass and momentum are used. It is convenient to employ the integral formulation for the continuity equation [13], i.e.)

$$\frac{d}{dt}\int_{cv}\rho_f\, d\mathcal{V}+\int_{cs}\rho_f(\mathbf{V}-\dot{\mathbf{u}})\cdot d\mathbf{A}=0 \tag{2}$$

The momentum equation for this problem reduces to the Joukowski equation

$$\Delta p=\rho_f a_f \Delta V \tag{3}$$

where the velocities are considered positive when pointing in the positive x-direction.

By applying equations (2) and (3) to the control volume shown in Fig. 2 the following expression is obtained for the wave velocity in the liquid (details are given in the Appendix):

$$a_f=\left[\frac{K/\rho_f}{1+\dfrac{K}{A}\dfrac{\Delta A}{\Delta p}}\right]^{1/2} \tag{4}$$

This result demonstrates that, with the classical waterhammer theory assumptions, the velocity of propagation of a pressure pulse in the liquid is independent of the velocity of the stress waves on the pipe wall or, equivalently, independent of the velocity of deformation of the pipe wall in the axial direction. The formula can be applied to thin or thick-walled pipes since no assumptions were made in this regard, and for different types of pipe supports and materials. Ths expression agrees with that given by Wylie and Streeter [11], where it is applied to many different situations; hence herein no further analysis will be made.

Improved Analysis of Wavespeeds

Consider now the cases of transient flow of an inviscid, slightly compressible liquid contained in a thin, elastic pipes, under the assumption that radial and axial motions and forces on the fluid and pipe are relevant and the pipe. Also, by assuming that the liquid bulk modulus is constant, the liquid velocity is much smaller than the speed of sound in the pipe, and the flow is axisymmetric for moderately long pulses, then the fluid moition is governed by a three equation system given by Walker and Phillips [4] in the form:

$$\frac{1}{K}\frac{\partial p}{\partial t}+\frac{\partial V_r}{\partial r}+\frac{V_r}{r}+\frac{\partial V_x}{\partial x}=0 \tag{5}$$

$$\frac{\partial p}{\partial x}+\rho_f\frac{\partial V_x}{\partial t}=0 \tag{6}$$

$$\frac{\partial p}{\partial r}+\rho_f\frac{\partial V_r}{\partial t}=0 \tag{7}$$

In addition, the pipe motion is governed by the equations for the small deformation, elastic, stress problem:

$$\frac{\partial \sigma_x}{\partial x}-\rho_t\frac{\partial \dot{u}}{\partial t}=0 \tag{8}$$

$$\rho_t\,\mathrm{Re}\,\frac{\partial \dot{w}}{\partial t}-Rp_0+e\,\sigma_\theta=0 \tag{9}$$

$$\frac{\partial \sigma_x}{\partial t}-E^*\left(\frac{\partial \dot{u}}{\partial x}+\nu\frac{\dot{w}}{R}\right)=0 \tag{10}$$

$$\sigma_\theta-E^*\left(\frac{w}{R}+\nu\frac{\partial u}{\partial x}\right)=0 \tag{11}$$

Nomenclature

a, a^* = wavespeed, m/s
A = cross-sectional area, m^2
c = constants, equations (18) and (19)
d = pipe inside diameter, m
e = pipe wall thickness, m
E = pipe modulus of elasticity, GPa
E^* = $E/(1-\nu^2)$
K = fluid bulk modulus, GPa
p = fluid pressure, Pa
r = radial coordinate, m
R = pipe inside radius, m
t = time, s
u = pipe wall longitudinal displacement, m
V = fluid average velocity, m/s
$\mathcal{V}$ = volume, m^3
w = pipe wall radial displacement, m
x = longitudinal coordinate, m
α = constant, (a_f/a_t)
Δ = increment
ϵ = pipe wall strain
ν = Poisson ratio
ρ = density, kg/m^3
σ = pipe wall stress, Pa
ϕ = constant, equation (20)
ψ = constant, equation (1)

Subscripts

f = fluid
0 = pipe wall
r = radial direction
t = pipe
x = longitudinal direction
θ = circumferential direction

Superscripts

$\dot{}$ = time derivative, $\partial/\partial t$
$'$ = conditions after wave action

By combining equations (9) and (11), this system under appropriate initial and boundary conditions, provides the solution for the six unknowns: p, V_x, V_r, $\dot{u}$, $\dot{w}$, σ_x.

For long pulses, which occur in a great number of waterhammer problems, the interia terms in the radial momentum relations, equations (7) and (9), are negligible [4], so that p and V_x are independent of r, and $\sigma_\theta = Rp/e$. With this assumption, and by eliminating w from equations (9) to (11), the following set of four equations results for the four unknowns: p, V_x, $\dot{u}$, σ_x:

$$\frac{1}{K}\left(1+\frac{2RK}{eE^*}\right)\frac{\partial p}{\partial t}-2\nu\frac{\partial \dot{u}}{\partial x}+\frac{\partial V_x}{\partial x}=0 \tag{12}$$

$$\frac{\partial p}{\partial x}+\rho_f\frac{\partial V_x}{\partial t}=0 \tag{13}$$

$$\frac{\partial \sigma_x}{\partial x}-\rho_t\frac{\partial \dot{u}}{\partial t}=0 \tag{14}$$

$$\frac{\partial \sigma_x}{\partial t}-\frac{\nu R}{e}\frac{\partial p}{\partial t}-E\frac{\partial \dot{u}}{\partial x}=0 \tag{15}$$

These expressions are an improvement over the classical waterhammer theory since they include a dynamic coupling between the liquid and the pipe wall for a general transient situation. The coupling exists through the Poisson ratio as seen in the second terms of equations (12) and (15). Athough much experimental work has to be done yet to test this model, the recent results of Otwell [6] indicate promising applications for piping systems.

From the eigenvalue problem associated with the system of equations (12)–(15), a set of four distinct characteristic roots are obtained, which correspond to the four velocities at which small perturbations propagate along the characteristic curves [14]. In the present case two of these represent the wavespeeds in the fluid and the other two represnt the wavespeeds in the axial direction in the pipe walls. After this analysis is performed on equations (12)–(15) the following respective liquid and solids wavespeeds are obtained:

$$a_f^* = \pm c_f\left[\frac{K/\rho_f}{1+\frac{dK}{eE}(1-\nu^2)}\right]^{1/2} \tag{16}$$

$$a_t^* = \pm c_t\left[\frac{E}{\rho_t}\right]^{1/2} \tag{17}$$

where

$$c_f^2 = 1-\frac{\nu^2}{1+\frac{eE}{dK}\left(1-\frac{K\rho_t}{E\rho_f}\right)} \tag{18}$$

$$c_t^2 = 1+\frac{\frac{dK}{eE}\nu^2}{\left(1+\frac{dK}{eE}\right)\left[\left(1+\frac{dK}{eE}\right)\frac{\rho_f E}{\rho_t K}-1\right]} \tag{19}$$

Comment on Axial Pipe Constraint. Wylie and Streeter [11] refer to three commonly assumed conditions of the pipe axial strain which are used to approximate many practical situations: 1) pipe anchored at this upstream end only; 2) pipe anchored throughout against axial motion; and 3) pipe anchored with expansion joints throughout.

Traditionally, for the first condition it is assumed that a constant stress is developed at a boundary due to the pressure rise given by equation (3), and that it travels along the pipe at the speed of a pressure pulse in the liquid. Consequently, the liquid wave speed is given by equation (1) in which $\psi = 1-\nu/2$ [11]. The second condition represents the case when the axial strain is assumed nonexistent through the pipe, and $\psi = 1-\nu^2$. The third situation implies that both axial stresses and strains are zero, with the result $\psi = 1$.

In light of the development presented herein, it is possible to examine the axial pipe-liquid interaction in a more precise fashion. The first condition represents the case in which the pipe is allowed to contract or expand freely in its radial and axial directions, with stress waves traveling in the pipe wall material in addition to the pressure waves propagating in the liquid. Either a stress or strain relationship must be imposed at a pipe boundary along with the conventional hydrodynamic condition. The appropriate mathematical model for this case is given by equations (12)–(15) and the wavepeeeds are given by equations (16) and (17).

That situation also is valid for the second and third conditions, if one assumes the axial pipe reaches to be small segments of a large pipe, and at the end of each segment a stress or strain boundary condition must be imposed. Obviously such a formulation would result in a cumbersome mathematical model, so that it is reasonable to simulate those conditions with the same limiting approximations utilized in the classical approach. For condition two the terms containing $\dot{u}$ in equations (12)–(15) must be dropped, and for condition three equations (12)–(15) reduce to equations (12) and (13). Since there is no interaction between the dynamics of the liquid and the pipe structure, the pipe wavespeeds $a_t = 0$, and the liquid wavespeeds a_f are identical with those obtained by the classical waterhammer theory.

Numerical Results

The analysis in the previous section indicates that the classical expressions for the wavespeeds in the fluid and in the pipe wall are modified when the interaction between the fluid and the pipe wall is considered. For comparison a discussion based on numerical evaluations will be presented for pipes of different materials (mild steel, cast iron, copper, aluminum and polyethylene). The physical properties used for the pipe materials considered are given in Table 1.

Wavepseeds in the Pipe Wall. The velocity of propagation of a small disturbance in the pipe wall is given by equation (17). The coefficient c_t which appears in this formula, and defined in equation (19), was evaluated for different liquids such as water, ethyl alcohol and mercury, as well as for the pipe materials given in Table 1 and pipe diameter to pipe wall thickness ratios in the range $20 < d/e < 300$. For all practical situations c_t was within 1 percent of unity. The improved model does not seem to introduce any significant change for the wavespeed in the pipe wall given by the expression $a_t = (E/\rho_t)^{1/2}$.

Wavespeeds in the Fluid. The improved waterhammer theory considered herein gives the velocity of propagation of a

Table 1 Physical properties of the pipe materials

Materials/ Properties	Steel	Cast Iron	Copper	Aluminum	Polyethylene
ρ(kg/m^3)	7600	7600	8800	2700	1000
E(GPa)	210	80	115	70	0.8
ν	0.27	0.25	0.34	0.33	0.46

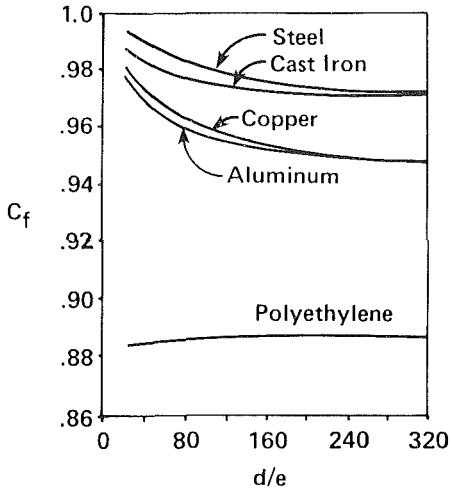

Fig. 3 Variation of the coefficients c_f with d/e for different pipe materials and water

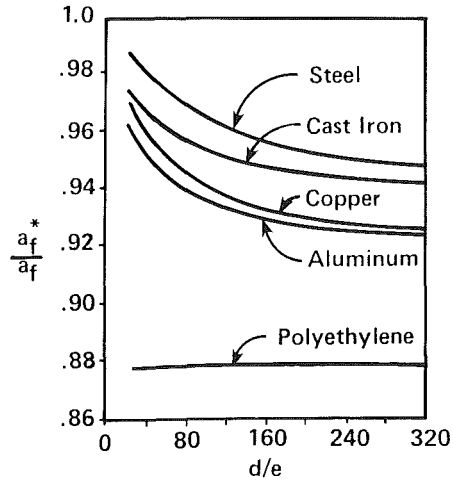

Fig. 4 Variation of the liquid wave-speed ratio (improved/classical models) with d/e for different pipe materials and water

pressure pulse in the liquid from equation (16). Consider water-filled pipes of the different materials listed in Table 1. For water, it is assumed that $\rho_f = 1000$ kg/m^3 and $K = 2.2$ GPa. Figure 3 shows the variation of the coefficient c_f with respect to d/e for those different pipe materials. It can be seen that the ratio d/e, as well as the pipe materials, have significant effects on the numerical value of this coefficient.

In order to compare the wavespeed obtained by the improved coupled model with the classical approach, one can form the ratio of the wavespeeds given by these two theories:

$$\phi = \frac{a_f^*}{a_f} = c_f \left[\frac{1 + \frac{dK}{eE}\left(1 - \frac{\nu}{2}\right)}{1 - \frac{dK}{eE}(1 - \nu^2)} \right]^{1/2} \tag{20}$$

Equation (20) is plotted in Fig. 4 where it is seen that the interaction between liquid and pipe structure causes a reduction of the wavespeed as calculated by the non-interactive formula. For metals the differences are only a few percent, although for high values of d/e, they may reach 6 or 7 percent. The most significant differences are observed for the case of non-metallic pipes, such as polyethylene, where a reduction of 12 percent is given by the improved model. It should be pointed out, however, that a viscoelastic effect may likely occur for the polyethylene pipe, a behavior which has not been included in the present study.

Summary

The review of classical waterhammer theory has shown that under the tradational assumption of neglecting any interaction between the dynamics of the liquid and the piping, the acoustic wavespeed in the liquid is not an explicit function of the longitudinal strain in the pipe, in agreement with the results of Wylie and Streeter [11]. It is also shown that the wavespeed is independent of the velocity of deformation of the pipe in the longitudinal direction.

A more complete formulation is considered which allows coupling between the liquid and pipe structure to take place; it is an adaptation of the model developed by Walker and Phillips [4], in which the inertial forces in the radial direction are neglected. Expressions are found for axial wavespeeds in the liquid and in the pipe wall material. A series of numerical evaluations shows that the wall material wavespeed maintains a value nearly equal to $(E/\rho_t)^{1/2}$. The wavespeed in the liquid is found to be lower than the value predicted from the classical waterhammer analysis: reductions in the range of 4 to 7 percent are typical for diameter-to-thickness ratios above 100.

A significant feature of the coupled model is its capability to recognize wave motion in both the liquid and in the pipe wall, thereby allowing the prediction of axial pipe vibrations generated by movement of the waterhammer waves in the liquid. There exist four compatibility relationships which can be integrated along appropriate characteristic lines to predict pressure and mean velocity in the liquid, and axial velocity and stress in the pipe wall. Whether such detail is important for practical engineering situations would depend on the particular system geometry under consideration as well as upon the particular application. In the laboratory, such coupling has been shown to be significant when unrestrained elbow fittings are present as a part of the piping system [6].

Acknowledgment

The support of the Brazilian Commission of Nuclear Energy and the National Science Foundation, through Grant No. MEA-8209049 is gratefully acknolwedged.

References

1 Joukowski, N. E., "Water Hammer" (translated by O. Simin), *Proceedings, American Water Work Association*, Vol. 24, 1904, p. 341-424.

2 Skalak, R., "An Extension of the Theory of Water Hammer," *Trans. ASME*, Vol. 78, No. 1, 1956, pp. 105-116.

3 Lin, T. C., and Morgan, G. W., "Wave Propagation Through Fluid Contained in a Cylindrical Elastic Shell," *Journal of Acoutical Society of America*, Vol. 28(6), 1956, pp. 1165-1173.

4 Walker, J. S., and Phillips, J. W., "Pulse Propagation in Fluid Filled Tubes," ASME *Journal of Applied Mechanics*, Mar. 1977, pp. 31-35.

5 Wood, D. J., "A Study of the Response of Coupled Liquid Flow-Structure Systems Subjected to Periodic Disturbances," ASME *Journal of Basic Engineering*, Vol. 90, Dec. 1968, pp. 532-540.

6 Otwell, R. S., "The Effect of Elbow Restraint on Pressure Transients in Piping Systems," Doctoral Dissertation, Michigan State University, 1984.

7 Hatfield, F. J., Wiggert, D. C., and Otwell, R. S., "Fluid-Structure Interaction in Piping by Component Synthesis," ASME JOURNAL OF FLUID ENGINEERING, Vol. 104, No. 4, Sept. 1982, pp. 318-325.

8 Parmakian, J., *Waterhammer Analysis*, Dover Publication, 1955.

9 Halliwell, A. R., "Velocity of a Water-Hammer Wave in an Elastic Pipe," *Journal of the Hydraulics Division, Proc. ASCE*, Vol. 89, No. HY4, July 1963, pp. 1-21.

10 Streeter, V. L., Discussion of the paper "Velocity of a Water-Hammer Wave in an Elastic Pipe," by Halliwell, A. R., *Journal of the Hydraulic Division, Proc. ASCE*, Vol. 89, No. HY6, Dec. 1963, pp. 295-296.

11 Wylie, B. E., and Streeter, V. L., *Fluid Transients*, FEB Press, Ann Arbor, 1982.

12 Chaudhry, M. H., *Applied Hydraulic Transients*, Van Nostrand Reinhold, 1979.

13 Hansen, A. G., *Fluid Mechanics*, John Wiley, 1967.

14 Courant, R., and Hilbert, D., *Methods of Mathematical Physics*, Vol. 2, John-Wiley, Interscience, 1962.

APPENDIX

Under the assumption that no interaction takes place between the fluid and the pipe walls, an approximate expression for the velocity of propagation of a pressure pulse in the liquid inside the pipe can be obtained by applying the conservation laws for mass and momentum for a control volume fixed, for example, to the interior walls of the pipe. In Fig. 2, let AA and BB be the acoustic wave front and the stress wave front, respectively, in the pipe wall at an instant t_0. With no loss of generality assume at that particular instant of time those waves are moving upstream with wavespeeds a_f and a_t. At time $t_0 + \Delta t$ the waves have moved to the new positions A′A′ and CC, respectively. Due to the elastic deformation of the pipe, the section AA moves to A′A′ at $t_0 + \Delta t$.

A straightforward application of the continuity equation (2) to the deformable control volume ABCCBA (fixed at the interior surface of the pipe wall) gives the following equation:

$$\rho' A' [a_f (1 + \alpha \epsilon_x) - \Delta V - \dot{u}] - \rho A \, a_f = 0 \tag{21}$$

where $\alpha = a_t / a_f$ and the primes denote variables evaluated after wave action. From the following relationships

$$\dot{u} = \epsilon_x \, a_t = \alpha \, \epsilon_x \, a_f \tag{22}$$

$$A' = A (1 + 2 \, \epsilon_\theta) \tag{23}$$

$$\rho' = \rho \left(1 + \frac{\Delta p}{K}\right) \tag{24}$$

and taking equations (22) to (24) into equation (21) one obtains:

$$\Delta V = a_f \frac{\Delta p}{K} \left[1 + \frac{K}{\Delta p} \, 2 \, \epsilon_\theta\right] \tag{25}$$

Combining equations (3) and (25) the acoustic wavespeed is obtained:

$$a_f = \left[\frac{K/\rho_f}{1 + \dfrac{K}{\Delta p} 2 \, \epsilon_\theta}\right]^{1/2} = \left[\frac{K/\rho_f}{1 + \dfrac{K}{A} \dfrac{\Delta p}{\Delta A}}\right]^{1/2} \tag{26}$$

It is interesting to observe that the longitudinal deformation of the pipe walls, ϵ_x, as well as the pipe walls stress wavespeed, a_t, do not appear in this expression.

Second-Order Accurate Explicit Finite-Difference Schemes for Waterhammer Analysis

M. H. Chaudhry
Department of Civil and Environmental Engineering, Washington State University, Pullman, Wash. 99164

M. Y. Hussaini
Institute for Computer Applications in Science and Engineering, NASA Langley Research Center, Hampton, Va.

Three second-order accurate explicit finite-difference schemes—MacCormack's method, Lambda scheme and Gabutti scheme—are introduced to solve the quasilinear, hyperbolic partial differential equations describing waterhammer phenomenon in closed conduits. The details of these schemes and the treatment of boundary conditions are presented. The results computed by using these schemes for a simple frictionless piping system are compared with the exact solution. It is shown that for the same accuracy, second-order schemes require fewer computational nodes and less computer time as compared to those required by the first-order characteristic method.

Introduction

Waterhammer phenomenon in slightly compressible liquids flowing through closed conduits having linearly elastic walls is described by a set of quasi-linear, hyperbolic, partial differential equations. The coefficients of these equations, commonly referred to as waterhammer equations, are constant. Because of the presence of the nonlinear source term representing the losses due to friction, these equations can only be numerically integrated. Steep waves or "shocks" may be generated at different boundaries due to abrupt changes in the discharge. Therefore, any numerical method used for the solution of these equations should be able to properly handle these shocks.

The method of characteristics has been widely used [1-4] for waterhammer analysis. In this method, the governing equations are transformed into ordinary differential equations which are then solved along the characteristic lines by using first- or second-order finite difference approximations [1, 2, 4]. For stability, it is necessary that $C_n < 1.0$, in which C_n = Courant number = $a\Delta t/\Delta x$; a = wave speed; Δt = computational time step and Δx = reach length. First-order methods yield satisfactory results if the friction losses are small and $C_n = 1.0$. For large friction losses such as in the flow of highly viscous liquids or for flow in small diameter tubes, computations may become unstable (1) even with $C_n < 1$. In addition, interpolations, which are necessary if $C_n \neq 1.0$, smear the shocks and the computed flow disturbances travel at a faster than the correct speed [1].

In this ppaer, three new explicit-finite difference schemes—MacCormack, Lambda, and Gabutti—are introduced for waterhammer analysis. These schemes are second-order accurate both in space and time and have been used in Computational Fluid Dynamics for the solution of hyperbolic systems. The governing equations are first presented. The details of these schemes and the treatment of the boundary conditions are then given. The results computed by using these schemes for the solution of a typical frictionless piping system are compared with the exact solution.

Governing Equations. The equations describing waterhammer in closed conduits are [1, 2]:

$$H_t + \frac{a^2}{gA} Q_x = 0 \tag{1}$$

$$Q_t + gA\, H_x + R\, Q|Q| = 0 \tag{2}$$

in which t = time; x = distance; A = cross-sectional area of the conduit; H = piezometric head above the datum; Q = discharge; $R = f/(2\,DA)$; f = Darcy-Weisbach friction factor; D = diameter of the conduit; and the subscripts x and t denote partial derivatives with respect to these variables.

Equations (1) and (2) are a set of quasilinear, hyperbolic, partial differential equations (2) having constant coefficients. Because of the non-linear source term, $R\,Q|Q|$, a closed-form solution is not possible. Therefore, numerical methods have been used to integrate these equations.

MacCormack Scheme. The MacCormack scheme [5] is second-order accurate in both space and time and is inherently dissipative. It is comprised of two steps: predictor and corrector. In each of these steps, one-sided finite-difference approximations are used. Depending upon the difference approximations for the spatial derivatives, two alternatives are possible. In the first alternative, foward finite-difference approximations are used in the predictor part and backward finite-difference approximations in the corrector part; while in the second alternative, backward finite-difference approximations are used in the predictor part and forward finite-differences in the corrector part. MacCormack recommends using these alternatives in a sequence, i.e., the first alternative at one time step, second alternative during the next time step, followed by the first alternative again.

In the following discussion, an asterisk (*) denotes the predicted values, subscript i refers to the space node and the superscript j refers to the time level (Fig. 1). A conduit having

Contributed by the Fluids Engineering Division for publication in the JOURNAL OF FLUIDS ENGINEERING. Manuscript received by the Fluids Engineering Division, April 1, 1985.

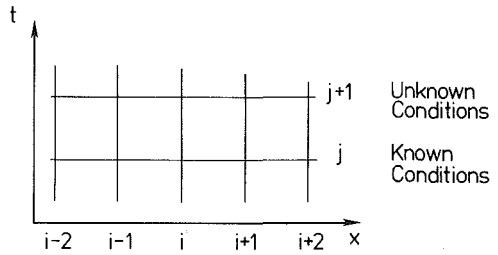

Fig. 1 Computational grid

length L is divided into n equal-length reaches. If the first node (upstream boundary) is numbered 1, then the last node (downstream boundary) will be $n + 1$. The values of H and Q are assumed to be known at the j-time level (either known initial conditions or computed during the previous time step) and their values are to be determined at the $j + 1$ time level.

Referring to Fig. 1, equations (1) and (2) for Alternative 1 may be written in the finite-difference form as follows:

Predictor Part

$$H_i^* = H_i^j - \frac{\Delta t}{\Delta x}\frac{a^2}{gA}(Q_{i+1}^j - Q_i^j)$$

$$Q_i^* = Q_i^j - \frac{\Delta t}{\Delta x} gA\,(H_{i+1}^j - H_i^j) - R\,|Q_i^j|\,Q_i^j$$

$$(i = 1, 2, \ldots, n). \tag{3}$$

Corrector Part

$$H_i^{j+1} = \frac{1}{2}\left\{H_i^j + H_i^* - \frac{\Delta t}{\Delta x}\frac{a^2}{gA}(Q_i^* - Q_{i-1}^*)\right\}$$

$$Q_i^{j+1} = \frac{1}{2}\left\{Q_i^j + Q_i^* - \frac{\Delta t}{\Delta x} gA\,(H_i^* - H_{i-1}^*) - R\,Q_i^*|Q_i^*|\right\}$$

$$(i = 2, 3, \ldots, n+1). \tag{4}$$

In Alternative 2, the predictor and corrector parts are:

Predictor

$$H_i^* = H_i^j - \frac{\Delta t}{\Delta x}\frac{a^2}{gA}(Q_i^j - Q_{i-1}^j)$$

$$Q_i^* = Q_i^j - \frac{\Delta t}{\Delta x} gA\,(H_i^j - H_{i-1}^j) - R\,Q_i^j|Q_i^j|$$

$$(i = 2, 3, \ldots, n+1) \tag{5}$$

Corrector

$$H_i^{j+1} = \frac{1}{2}\left\{H_i^j + H_i^* - \frac{\Delta t}{\Delta x}\frac{a^2}{gA}(Q_{i+1}^* - Q_i^*)\right\}$$

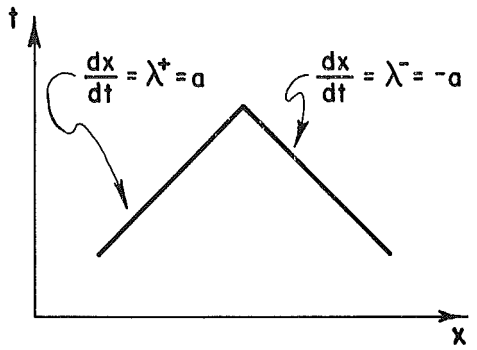

Fig. 2 Positive and negative characteristics

$$Q_i^{j+1} = \frac{1}{2}\left\{Q_i^j + Q_i^* - \frac{\Delta t}{\Delta x} gA\,(H_{i+1}^* - H_i^*) - R\,Q_i^*|Q_i^*|\right\}$$

$$(i = 1, 2, \ldots, n). \tag{6}$$

Both alternatives are stable if $a\Delta t \le \Delta x$.

Lambda Scheme. In the Moretti's Lambda Scheme [6], the governing equations are transformed into the characteristics form and then one-sided finite differences are used during the predictor and corrector parts of the computations.

Multiplying equation (2) by an unknown multipler η, adding it to equation (1), and rearranging the terms, we obtain:

$$(H_t + \eta gA\,H_x) + \eta\left(Q_t + \frac{a^2}{\eta gA}Q_x\right) + \eta\,R\,Q|Q| = 0. \tag{7}$$

Let

$$\eta gA = \frac{dx}{dt} = \frac{a^2}{\eta gA}.$$

Then

$$\eta = \pm\frac{a}{gA}. \tag{8}$$

Thus the characteristics directions, $\lambda = dx/dt$, are

$$\lambda^+ = \frac{dx}{dt} = a. \tag{9}$$

and

$$\lambda^- = \frac{dx}{dt} = -a. \tag{10}$$

in which the superscripts "+" and "−" indicate positive and negative characteristics (Fig. 2).

On the basis of equations (8) and (9), equation (7) may be written as:

$$(H_t + \lambda^+ H_x^+) + \frac{a}{gA}(Q_t + \lambda^+ Q_x^+) + \frac{aR}{gA}Q|Q| = 0 \tag{11}$$

and

Nomenclature

a = wave speed
A = cross-sectional areas of conduit
C_n = Courant number = $a\Delta t/\Delta X$
D = conduit diameter
f = Darcy-Weisbach friction factor
g = acceleration due to gravity
H = piezometric head
H_{comp} = computed piezometric head
H_{exac} = exact piezometric head

$$L_1 = \sum_{i=1}^{N} |H_{comp_i} - H_{exac_i}|/N$$

$$L_2 = \sum_{i=1}^{N} (H_{comp_i} - H_{exac_i})^2/N$$

N = number of computational nodes
Q = discharge
R = $f/(2\,DA)$
t = time
Δt = computational time step
x = distance
Δx = reach length
η = unknown multiplier
λ = characteristic direction = dx/dt

Subscripts and Superscript

i = node in x-direction
j = time level
*, ~ = predictor values

$$(H_t+\lambda^- H_x^-)-\frac{a}{gA}(Q_t+\lambda^- Q_x^-)-\frac{aR}{gA}\,Q|Q|=0. \quad (12)$$

Depending upon the characteristic direction, superscripts "+" and "−" are marked on the partial derivative with respect to x; e.g., H_x^+ refers to derivative along the positive characteristics (Fig. 2).

Subtracting equation (12) from equation (11) and multiplying the resulting equation throughout by gA/a, we obtain

$$Q_t+\frac{1}{2}\frac{gA}{a}(\lambda^+ H_x^+-\lambda^- H_x^-)$$

$$+\frac{1}{2}(\lambda^+ Q_x^+ +\lambda^- Q_x^-)+R\,Q|Q|=0. \quad (13)$$

Adding equations (11) and (12) and rearranging:

$$H_t+\frac{1}{2}(\lambda^+ H_x^+ +\lambda^- H_x^-)+\frac{1}{2}\frac{a}{gA}\cdot$$
$$(\lambda^+ Q_x^+ -\lambda^- Q_x^-)=0. \quad (14)$$

Equations (13) and (14) are referred to as equations in λ-form. From the viewpoint of partial differential equations, $H_x^+ = H_x^- = H_x$ and $Q_x^+ = Q_x^- = Q_x$. By substituting these relationships, it is clear that equations (13) and (14) are identical to equations (1) and (2). However, this will not be the case if we approximate H_x^+ and H_x^-, and Q_x^+ and Q_x^- by finite differences in different ways.

In the Moretti's Lambda Scheme the partial derivaties are replaced by the finite-difference approximations (Fig. 1) as follows:

Predictor Part

$$f_x^+=\frac{2f_i^j-3f_{i-1}^j+f_{i-2}^j}{\Delta x} \quad (15)$$

$$f_x^-=\frac{f_{i+1}^j-f_i^j}{\Delta x} \quad (16)$$

in which for brevity f is used for Q and H. By substituting these finite-difference approximations into equations (13) and (14), the following equations are obtained for the predicted values Q_i^* and H_i^*:

$$Q_i^*=Q_i^j-\Delta t\left\{\frac{1}{2}\frac{gA}{a}(\lambda^+ H_x^+-\lambda^- H_x^-)\right.$$

$$\left.+\frac{1}{2}(\lambda^+ Q_x^+ +\lambda^- Q_x^-)+R\,Q_i^j|Q_i^j|\right\} \quad (17)$$

and

$$H_i^*=H_i^j-\Delta t\left\{\frac{1}{2}(\lambda^+ H_x^+ +\lambda^- H_x^-)\right.$$

$$\left.+\frac{1}{2}\frac{a}{gA}(\lambda^+ Q_x^+ -\lambda^- Q_x^-)\right\}. \quad (18)$$

Corrector Part

$$f_x^+=\frac{f_i^*-f_{i-1}^*}{\Delta x} \quad (19)$$

$$f_x^-=\frac{-2f_i^*+3f_{i+1}^*-f_{i+2}^*}{\Delta x} \quad (20)$$

$$Q_i^{j+1}=\frac{1}{2}\left\{Q_i^j+Q_i^*-\Delta t\left[\frac{1}{2}\frac{gA}{a}(\lambda^+ H_x^+-\lambda^- H_x^-)\right.\right.$$

$$\left.\left.+\frac{1}{2}(\lambda^+ Q_x^+ +\lambda^- Q_x^-)+R\,Q_i^*|Q_i^*|\right]\right\} \quad (21)$$

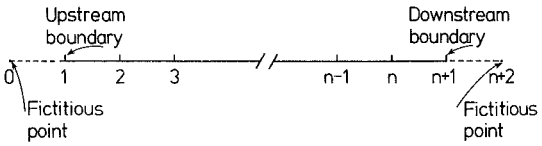

Fig. 3 Boundary and fictitious grid points

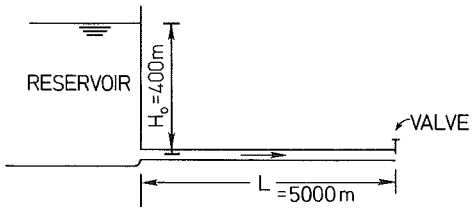

Fig. 4 Piping system

$$H_i^{j+1}=\frac{1}{2}\left\{H_i^j+H_i^*-\Delta t\left[\frac{1}{2}(\lambda^+ H_x^+ +\lambda^- H_x^-)\right.\right.$$

$$\left.\left.+\frac{1}{2}\frac{a}{gA}(\lambda^+ Q_x^+ -\lambda^- Q_x^-)\right]\right\}. \quad (22)$$

Gabutti Scheme. The Gabutti Scheme (7) is similar to the Lambda Scheme. In this scheme, the partial derivations are replaced by the finite-difference approximations as follows:

Predictor Part. The predictor part is subdivided further into two parts. Part 1:

$$f_x^+=\frac{f_i^j-f_{i-1}^j}{\Delta x} \quad (23)$$

$$f_x^-=\frac{f_{i+1}^j-f_i^j}{\Delta x} \quad (24)$$

in which f is used for brevity for Q and H.

By substituting these finite-difference approximations into equations (13) and (14), the following equations are obtained for the predicted values of $\tilde{Q}_i$ and $\tilde{H}_i$:

$$\tilde{Q}_i=Q_i^j-\Delta t\left\{\frac{1}{2}\frac{gA}{a}(\lambda^+ H_x^+-\lambda^- H_x^-)\right.$$

$$\left.+\frac{1}{2}(\lambda^+ Q_x^+ +\lambda^- Q_x^-)+R\,Q_i^j|Q_i^j|\right\} \quad (25)$$

and

$$\tilde{H}_i=H_i^j-\Delta t\left[\frac{1}{2}(\lambda^+ H_x^+ +\lambda^- H_x^-)\right.$$

$$\left.+\frac{1}{2}\frac{a}{gA}(\lambda^+ Q_x^+ -\lambda^- Q_x^-)\right]. \quad (26)$$

Part 2:

$$f_x^+=\frac{2f_i^j-3f_{i-1}^j+f_{i-2}^j}{\Delta x} \quad (27)$$

$$f_x^-=\frac{-2f_i^j+3f_{i+1}^j-f_{i+2}^j}{\Delta x} \quad (28)$$

By using these finite-difference approximations, the predicted values of time derivations Q_t^* and H_t^* are determined from equations (13) and (14).

Corrector Part

$$\tilde{f}_x^+=\frac{\tilde{f}_i-\tilde{f}_{i-1}}{\Delta x} \quad (29)$$

$$\tilde{f}_x^-=\frac{\tilde{f}_{i+1}-\tilde{f}_i}{\Delta x} \quad (30)$$

By using these finite-difference approximations and using $\tilde{Q}$ for Q in equations (13) and (14), $\tilde{H}_t$ and $\tilde{Q}_t$ are computed. Then,

$$Q_i^{j+1} = Q_i^j + \frac{1}{2}\Delta t(Q_t^* + \tilde{Q}_t) \tag{31}$$

$$H_i^{j+1} = H_i^j + \frac{1}{2}\Delta t(H_t^* + \tilde{H}_t) \tag{32}$$

Boundary Conditions. The above equations are for the interior nodes only. They cannot be used at the boundaries since the grid points are on only one side of the boundary (Fig. 3). In addition, specified conditions imposed by the boundary have to be taken into consideration. Thus, proper care has to be taken so that the boundary conditions are neither under-specified nor over-specified.

MacCormack has shown by heuristic argument that even if the accuracy of the boundary condition is an order less than that of the scheme used at the interior nodes, the overall accuracy of the solution is not adversely affected. Hyman [8] recommends that the boundary conditions be handled with utmost care since errors introduced at the boundaries will be carried unabated throughout the system independent of the accuracy of the scheme used at the interior grid points and of the size of the computational mesh.

Boundary conditions may be included in the analysis by using the characteristic equations or by extrapolating fluxes beyond the boundaries and then using the extrapolated values in the difference scheme being used at the interior points. Both of these procedures are discussed in the following paragraphs.

Characteristics Equations. The characteristic equations, equations (11) and (12), may be used at the boundaries in conjunction with the conditions imposed by the boundary. Let us illustrate the procedure by discussing the boundary condition for a constant-level reservoir at the upstream end, i.e., at $x = 0$ or $i = 1$.

Since H_1 = constant, $H_t = 0$ at Section 1. Hence, it follows from equation (12) that:

$$Q_t = \frac{gA}{a}\lambda^- H_x^- - \lambda^- Q_x^- - R\,Q|Q|. \tag{33}$$

The partial derivatives H_x^- and Q_x^- may be determined using the same finite-difference aproximations as for the interior points. Now, Q_1^{j+1} may be determined from this equation by using a forward finite-difference approximation.

Similarly, if the variation of flows were specified at the lower end, then the downstream boundary conditions may be written using equation (11).

Extrapolation Procedures. Let us illustrate the extrapolation procedure by considering the following scaler equation.

$$U_t + f_x = 0. \tag{34}$$

In alternative 1 of the MacCormack method, we cannot write forward finite-difference at the downstream boundary ($i = n + 1$) during the predictor part since there is no computational node downstream of the boundary. Similarly, we cannot write the backward finite-difference approximation at the upstream boundary ($i = 1$) during the corrector part.

However, we may assume fictitious grid points (Fig. 3) beyond the boundaries, i.e., $i = n + 2$ downstream of the downstream boundary and $i = 0$ upstream of the upstream boundary. The flux f at these fictitious points ($i = 0$ and $i = n + 2$) may be extrapolated by using the following equations:

$$f_{n+2}^j = 2f_{n+1}^j - f_n^j \tag{35}$$

$$f_0^j = 2f_1^j - f_2^j. \tag{36}$$

Now we may use forward differences at $n + 1$ during the predictor part and the backward finite difference at $i = 1$ during the corrector part of the calculations.

General Remarks. For each time step, higher-order methods require more computational effort than that required for a first-order method. However, the same accuracy is obtained by a higher-order method using fewer computational nodes than that required by a first-order method. This advantage becomes especially attractive in the analysis of multi-dimensional flows due to reduced computer time as well as storage requirements.

The derivatives of the flux function f, in a hyperbolic system determines the phase velocities. Phase or dispersion errors, and damping or dissipative erros are introduced due to errors in approximating f and its derivatives. Hyman [8] has shown that when the initial conditions consist of a single frequency, then the phase error introduced by the finite-difference approximation will be the same using second, fourth and sixth-order differences if the number of computational nodes, N, satisfy

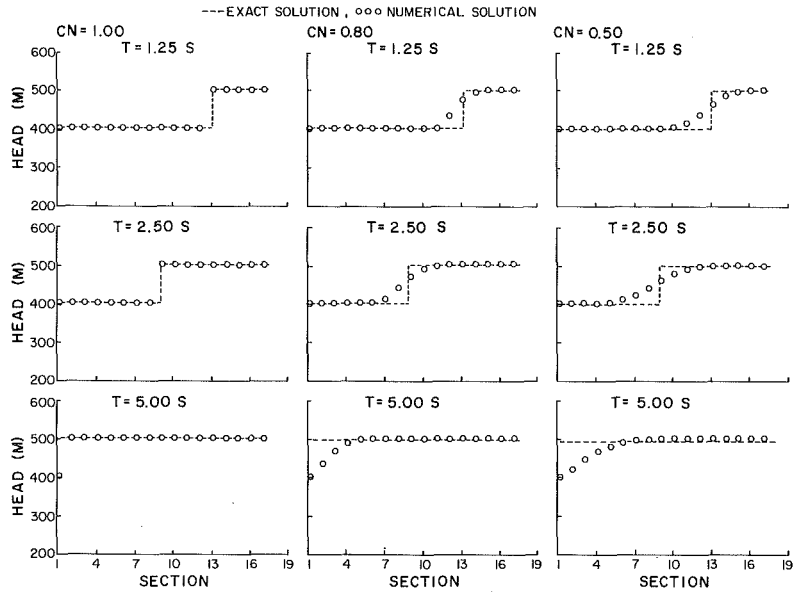

Fig. 5 Characteristic method: comparison of exact and numerical solution

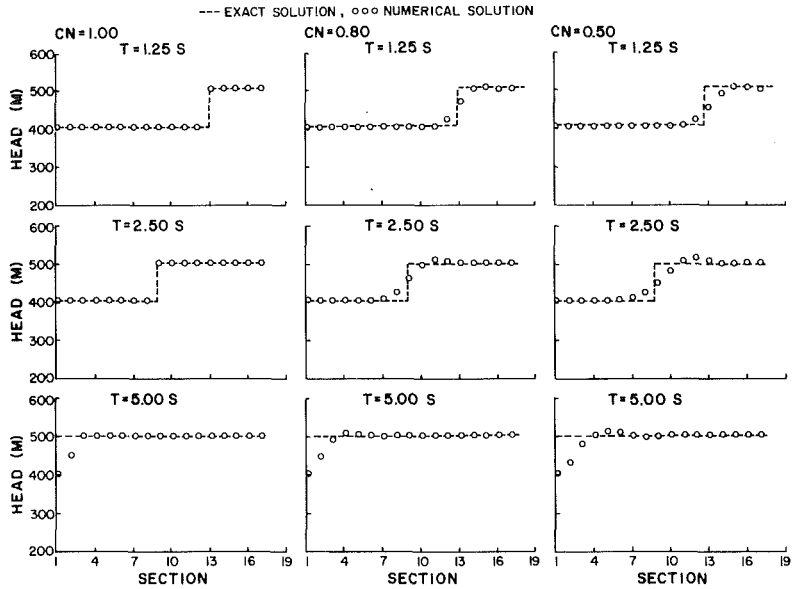

Fig. 6 MacCormack method: comparison of exact and numerical solution

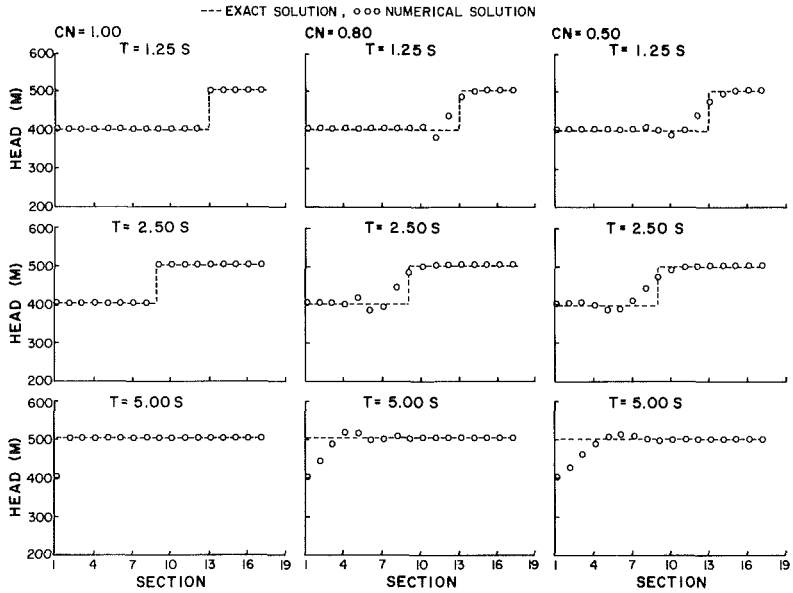

Fig. 7 Gabutti scheme: comparison of exact and numerical solution

$$N_2 = 0.36\, N_4^2 \simeq 0.12\, N_6^3 \tag{37}$$

in which the subscripts refer to the order of the method. For example, if a second-order method gives an accuracy with $N = 32$, then the same accuracy could be obtained by having $N = 10$ in a fourth-order method and $N = 7$ in a sixth-order method. Another advantage of the higher-order methods is that they reproduce better and sharper discontinuities in the solution.

Results

The piping system shown in Fig. 4 was analyzed using the above numerical schemes. In this system, pipe length, $L = 5000$ m, wave speed, $a = 1000$ m/s, pipe cross-sectional area, $A = 1$ m^2, initial steady-state flow = 0.981 m^3/s and $H_0 = 400$ m. The transient conditions were produced by instantaneously closing the downstream valve at $t = 0$. This instantaneous closure produces a 100-m high wave which travels in the upstream direction. If the system is assumed frictionless (i.e., $f = 0$), then this wave propagates to the reservoir, is reflected as a 100-m high negative wave and travels to the valve where it is reflected again.

In order to compare the computed results with the exact solution, the system was assumed frictionless. Computations were done using Courant number equal to 0.5, 0.8 and 1.0. Boundary conditions, developed by solving the characteristic equations simultaneously with the conditions imposed by the boundary and using first-order finite-difference approximations were used. At the nodes adjacent to the boundary, first-order, one-sided finite differences were used whenever three points were not available in the Lambda and Gabutti schemes.

Figures 5–8 show the computed results using each of the above schemes and the first-order characteristic method. With $C_n = 1.0$ the Lambda scheme produced unacceptable post-shock oscillations and became unstable; while the Gabutti, MacCormack, and first-order characteristic methods produced exact results. There was some smearing of the shock in the MacCormack Method after the shock was reflected at

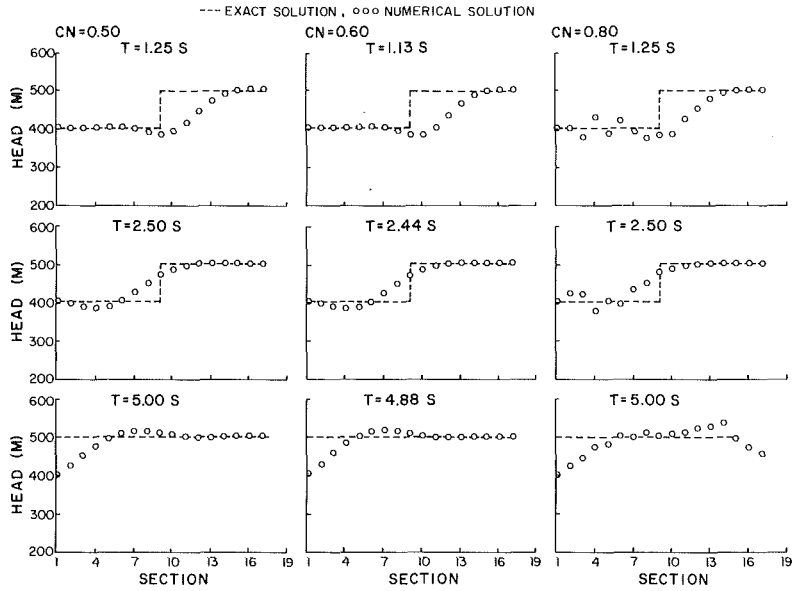

Fig. 8 Lambda scheme: comparison of exact and numerical solution

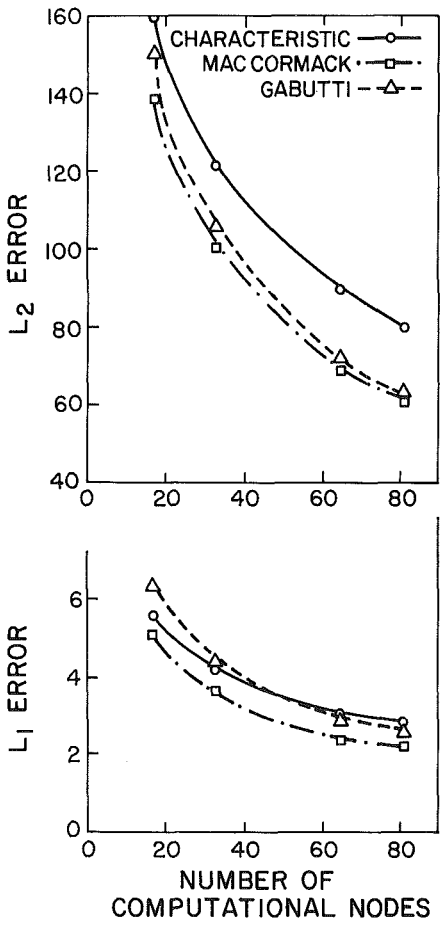

Fig. 9 L_1 and L_2 errors

the reservior. However, for $C_n < 1.0$, the shock is smeared and it propagates at a faster speed for the first-order method. With the second-order methods, the smearing of the shock is reduced although there are post-shock oscillations in the solution.

To compare the accuracy of the above schemes, L_1 and L_2 errors at time $t = 2.5$ and 5 seconds were computed using $C_n = 1.0$, 0.8 and 0.5 and using several values of N. The expression for L_1 and L_2 are:

$$L_1 = \frac{1}{N}\sum_{i=1}^{N}\left|H_{\text{comp}_i} - H_{\text{exac}_i}\right|$$

$$L_2 = \frac{1}{N}\sum_{i=1}^{N}\left\{H_{\text{comp}_i} - H_{\text{exac}_i}\right\}^2$$

where N = number of computational nodes, H_{comp_i} = computed piezometric head at node i and H_{exac_i} = exact piezometric head at node i. To conserve space only the results at $t = 2.5$ seconds for $C_n = 0.8$ are presented in Fig. 9. With $C_n = 1.0$, L_1 and L_2 were both zero for the first-order method as well as for the MacCormack and Gabutti schemes presented above. However, for $C_n < 1.0$, L_2 error in the second-order methods in much smaller than that in the first-order method. In other words, the number of computational nodes required to achieve a specified accuracy is considerably reduced for the second-order methods. For example, in order to keep L_2 error < 100 and using $C_n = 0.8$, the number of computational nodes will have to be at least 52 in the first-order characteristic method, 39 in the Gabutti scheme and 35 in the MacCormack method (see Fig. 9). However, if $C_n = 0.5$, then the minimum number of nodes required for the same L_2 error will be 136 in the characteristic method, 60 in the Gabutti scheme, and 95 in the MacCormack method.

To compare the computer time required by the above numerical methods, the piping system of Fig. 4 was analyzed from $t = 0$ to time $t = 5$ s using $C_n = 0.8$. The number of computational nodes (selected to give L_2 error = 100) were as follows: characteristic method = 52; Gabutti scheme = 39; and MacCormack method = 35. The computer time required on a DEC-10 computer was the lowest for the MacCormack method. The characteristic method, and Gabutti scheme took 180 and 168 percent of the time required by the MacCormack method.

Summary and Conclusions

With Courant number equal to unity, there is little advantage in using the second-order accurate methods over the first-order methods for waterhammer analysis. For $C_n < 1.0$,

however, the number of computational nodes required to achieve a given accuracy is reduced with the second-order accurate methods as compared to the first-order methods. This results in savings in the computer time and computer storage for the analysis of large piping systems. In addition, the second-order methods are superior for the resolution of shocks.

Acknowledgments

The studies reported herein were supported partially by the National Science Foundation Grant No. CEE-8119614 and partially by NASA under Contract Nos. NAS1-15810 and NAS1-17070 while the authors were in residence at the Institute for Computer Application in Science and Engineering, NASA Langley Research Center, Hampton, Virginia, M. Salas provided details of the Gabutti scheme.

References

1 Wylie, E. B., and Streeter, V. L., *Fluid Transients*, McGraw-Hill, New York, 1978.

2 Chaudhry, M. H., *Applied Hydraulic Transients*, Van Nostrand, New York, 1979.

3 Chaudhry, M. H., and Yevjevich, V. (ed.), *Closed-Conduit Flow*, Water Resources Publications, Littleton, Colo., 1981, pp. 167–191.

4 Chaudhry, M. H., "Numerical Methods for Solution of Transient Flow Equations," *Proc.*, Specialty Conf. Hydraulics Div., Amer. Society of Civil Engineers, Jackson, MS, Aug. 1982, pp. 633–656.

5 MacCormack, R., "Numerical Solution of the Interaction of a Shock Wave with a Laminar Boundary Layer," *Lecture Notes in Physics*, M. Holt (ed.), Vol. 8, Springler-Verlag, New York, 1971, pp. 151–163.

6 Moretti, G., "The Lambda Scheme," *Computers and Fluids*, Vol. 7, pp. 191–205.

7 Gabutti, B., "On Two Upwind Finite-Difference Schemes for Hyperbolic Equations in Non-Conservation Form," *Computer and Fluids*, Vol. 11, No. 3, 1983, pp. 207–230.

8 Hyman, J. M., "A Method of Lines Approach to the Numerical Solution of Conservation Laws," Third IMACS Symposium on Computer Methods for Partial Differential Equations, Lehigh University, Bethlehem, PA, June 1979.

Peter Dransfield
Associate Professor,
Department of Mechanical Engineering,
Monash University,
Melbourne, Australia

D. C. Davis
Superintendant Railroad Technical,
Mt. Newman Mines, Australia

Stable Floating Drops of Liquid

There are few reported situations in which a drop of liquid will remain intact in ambient conditions for an indefinite period of time. The paper describes a situation where this happens. The phenomenon was noticed during experiments concerned with the development of a novel rotational speed sensor. It proved to be a substantial rather than a passing occurrence.

Introduction

It is rare that a drop of liquid will remain intact and in equilibrium in ambient conditions for an indefinite period of time, especially if it is dropped onto a surface of the same liquid. In this latter circumstance, it is reasonable to assume that the drop would rapidly disperse in the host liquid, even if the surface of that liquid was moving.

While developing a novel rotational speed sensor using an annulus of mineral oil rotating about a horizontal axis, the formation on the free inner surface of the oil of what appeared to be a stationary drop of oil of considerable size was noticed.

Figure 1 illustrates the physical circumstances. One end of the 185-mm diameter horizontal drum is solid and the other open except for a 10 mm-deep rim. The oil is shown lying in the bottom of the drum. When the drum is rotated (500–2000 rpm were used) the oil forms an annulus rotating with the drum. If a drop of the same oil is forced out of a syringe to fall onto the rotating liquid surface it will, for a wide range of speed of rotation of the drum, remain intact and proceed to a particular position on the surface of the host liquid.

It was thought at first that the drop rolled on the surface of the rotating liquid in the manner of a single ball rolling on the rotating outer race of a ball bearing. Further experiments with various speeds of rotation of the drum, various heights of the syringe, visuality-enhancing inclusions in the drop, and various liquids, led to a more complete appreciation of the phenomenon.

Characteristics

Figure 2 shows a photograph of a stable drop of diameter approximately 2.5 mm on the surface of the moving host liquid. Typically, the drops were around this size. The dark background is the host liquid. The dark image is a reflection. Figure 3 shows one drop at four different drum speeds. The higher the speed of rotation of the drum, the higher the drop's equilibrium position on the rotating surface of liquid. It can be seen that the drop is not spherical. It is elongated, more in the shape of a jelly bean. Figure 4 shows a stable drop when the drum speed is high. Its shape is more like one popular conception of a flying saucer, with a flattened and concave bottom.

Observations over a period of experimentation include:

- The drops could be released from the syringe from a range of heights above the surface of the host fluid, and from a variety of positions around the periphery of the liquid annulus. After falling onto the moving surface the drop moves toward an equilibrium position. If the drum speed is such that a drop would remain intact, the drop's equilibrium position on the rotating surface is unique and repeatable.
- The floating drop is not spherical. The larger the drop the more the distortion. The higher the drum speed the more the distortion.
- The stable positions lie in one quadrant in the lower half of the rotating drum and oil annulus. Viewing Fig. 1 from the left and for clockwise rotation of the drum, it is the third clockwise quadrant.
- If the drum speed is high enough, the drop will move towards the horizontal diameter and will jump off the host liquid's surface and fall back on the host liquid at a lower point. If the fall is violent enough the drop will break into several smaller drops, or will disperse in the host liquid.
- A stable drop will maintain itself and its position indefinitely while the drum speed is maintained.
- A stable drop does not necessarily rotate on the moving surface of the host liquid. In fact it may have positive, negative, or zero rotation depending on the specific circumstances. If it has rotation, the magnitude of rotation is small relative to the surface speed of the host liquid.
- For a particular drum speed, a large drop assumes a lower equilibrium position than does a small drop.
- A very large drop is likely to become so elongated that it spontaneously breaks into two droplets which float apart but in unison.
- The basic experiments were conducted with Shell Tellus 46 hydraulic fluid. Stable drops were also formed with heavy oil, kerosene, and water. Floating drops of one liquid were formed on a different host liquid. Floating drops were formed on a dry rotating drum, i.e., when no host liquid was present.
- It is not necessary to initiate drops from a syringe. A pencil inserted in the rotating host liquid is effective.
- A number of drops can float on the rotating annulus at one time, and remain indefinitely.
- There is a lower threshold speed of rotation below which drops falling onto the moving liquid surface will simply disperse in the host liquid. There is a higher threshold speed beyond which the drop becomes unstable and jumps off the surface, as mentioned previously.

Contributed by the Fluids Engineering Division for publication in the JOURNAL OF FLUIDS ENGINEERING. Manuscript received by the Fluids Engineering Division, September 10, 1984.

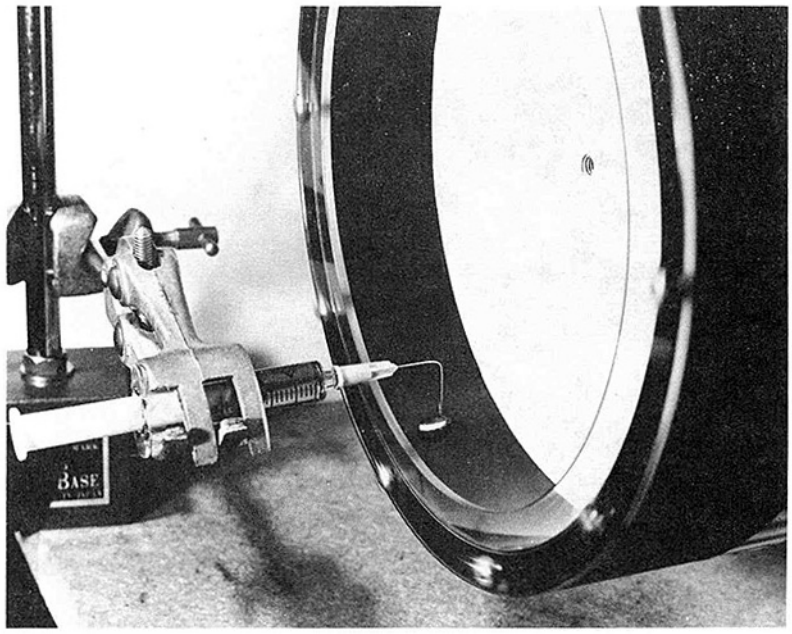

Fig. 1 The experimental rig

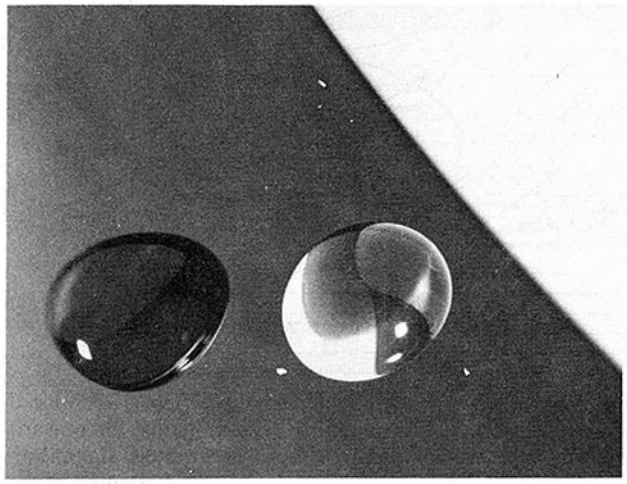

Fig. 2 A stable floating drop

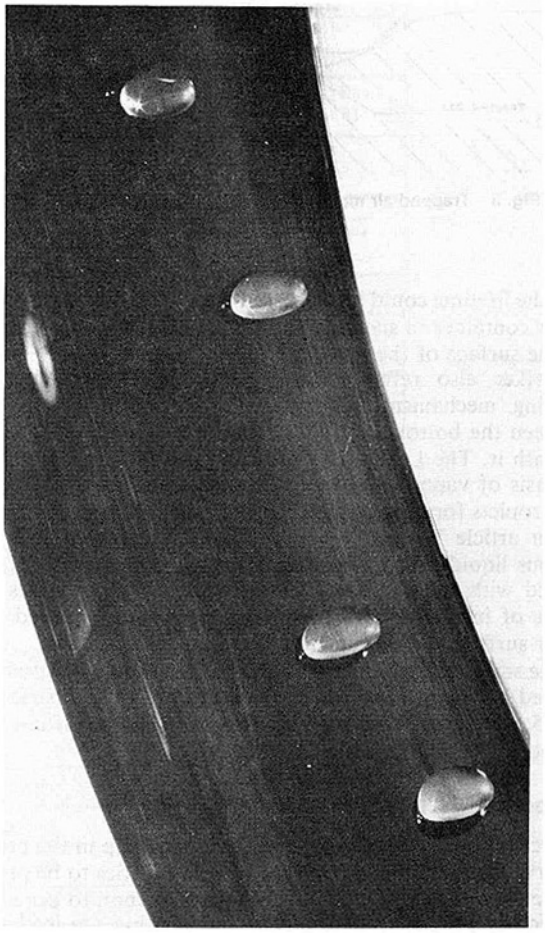

Fig. 3 The effect of drum speed on a drop's equilibrium position

• In circumstances in which a drop will go to a stable position there is no mass transfer between the drop and the host liquid.

Literature

A search of the literature showed interest in the possibility that long-lasting drops of liquids could develop. Writing in the *Scientific American* in 1978, Walker [1] traces a brief history of the observance and study of water drops which float temporarily on water surfaces under certain conditions. Osborne Reynolds is noted as having written in 1881 "On the Floating of Drops on the Surface of Water Depending Only on the Purity of the Surface," in which he concluded that floating drops are rare because impurities on water surfaces somehow destroy the floating mechanism. It seems that Reynolds considered surface tension to be the main mechanism of floating.

Walker considers that though it has been discussed for nearly a century, the final word on the mechanism of transient floating has not been reached. It has been shown that the addition of detergent to the water can cause the lifetime of a floating drop to increase from about one second to "several seconds, perhaps tens of seconds." It had been observed also

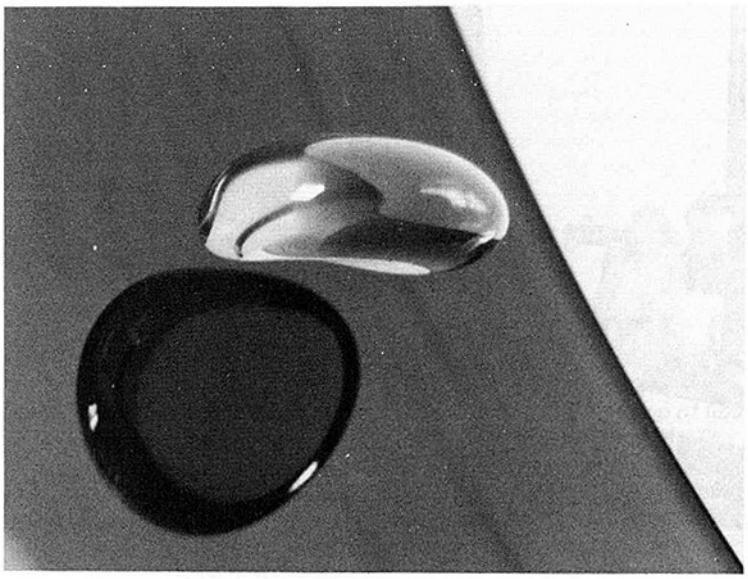

Fig. 4 Distortion of the stable drop at higher drum speeds

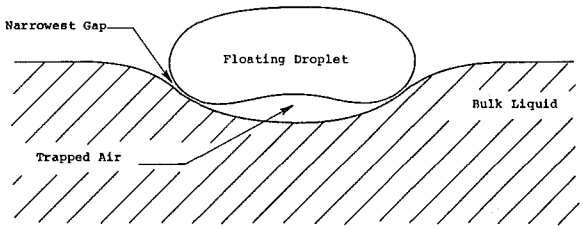

Fig. 5 Trapped-air mechanism for temporarily floating drop

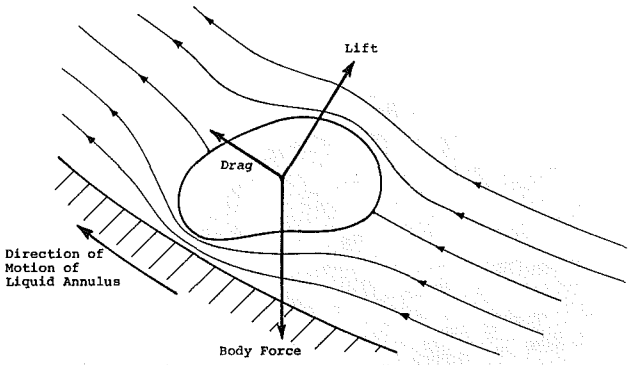

Fig. 6 Equilibrium force system for stable floating drop

that the lifetime could be increased to minutes by vibrating the water container in such a way that standing waves are set up on the surface of the host water.

Walker also refers to suggestions that the temporary floating mechanism might be due to electrical repulsion between the bottom of the floating drop and the host liquid beneath it. The Leidenfrost effect is also mentioned, though its basis of vapour layer support of droplets is rational only for droplets forming on superheated host liquid surfaces. In a recent article Walker [5] describes the placing of drops of various liquids onto a surface of water. The work was concerned with the chemistry of solubility. Walker states that drops of insoluble liquids, such as parafin oil, placed on a water surface remain intact.

The support mechanism usually proposed for the situations studied by Walker and his predecessors [2–4] is illustrated in Fig. 5. Air trapped between the drop and the host fluid gives temporary support of the drop.

Proposed Mechanism

Because of the long-term stability of the drop in the present observations and the lack of need for impurities to be present in the drop or host liquids for the phenomenon to occur, the previously proposed mechanisms for floating are irrelevant. Figure 6 shows the mechanism believed to govern the present case.

It is considered that when dropped onto the moving surface of the host fluid, the drop does not penetrate the air boundary layer associated with the moving surface. The air boundary layer drags the drop with it to a point where the forces acting on the drop are in equilibrium, with a flow pattern something like that illustrated in Fig. 6. The gravitational force on the drop is balanced by a combination of upward drag force and aerodynamic lift force due to quasi stagnation of air below the drop (this induces the bottom flattening of the drop). The drop has moved away from the host liquid surface sufficiently that any lateral forces on it due to air flows around it sum to zero. Whether or not the drop rotates clockwise, anti-clockwise, or is stationary depends on the net effect of the drag forces due to the boundary layer air flowing around it.

The importance of the air boundary layer on the stability of the phenomenon can be demonstrated by deliberately introducing a disturbance to the boundary layer flow. If an object such as a pencil is placed upstream of a stable drop so that it disturbs the air immediately in front of the drop without disturbing the surface of the annulus, the drop moves downwards and either adheres to the object or disperses into the host liquid. Similarly, an object introduced alongside a drop deflects the drop axially away from the object.

Conclusions

It is possible that the floating drop phenomenon plays a part or is present in some common situations. For example, in the break down of oil films in some high-speed bearings could there be local and temporary development of drops rather than the required continuous film? The formation and transportation of droplets during spraying is another possible area of interest.

The work could be further developed to seek a more detailed general theory allowing prediction of whether or not drops might form in particular circumstances, and if so their size, shape, location, speed of rotation, and the thickness of the air film separating drop from host fluid.

Acknowledgments

The contribution of J. S. Stecki in the discovery and early investigation of the phenomenon is acknowledged. So too is the subsequent contribution of A. Tan.

References

1 Walker, J., "Drops of Liquid Can be Made to Float . . .," *Scientific American*, Vol. 238, No. 6, June 1978.

2 Mackay, G., and Mason, S., "The Gravity Approach and Coalescence of Fluid Drops at Liquid Interfaces," *Can. J. Chem. Eng.*, Oct. 1963.

3 Bikerman, J., "Movements in a Liquid Surface," Section 59 of *Phys. Chem. of Liquid Surfaces*, Phys. Chem. Series, Vol. 20, Academic Press, 1970.

4 Strong, C. L., "Water Droplets that Float on Water . . ., *Scientific American*, Vol. 229, No. 2, Aug. 1973.

5 Walker, J., "Funny Things Happen When Drops of Oil or Other Substances are Placed on Water," *Scientific American*, Vol. 249, No. 6, Dec. 1983.

Journal of Fluids Engineering

Technical Briefs

Unsteady Flow in a Porous Medium Between Two Infinite Parallel Plates in Relative Motion

V. M. Soundalgekar[1], H. S. Takhar,[2] and M. Singh[3]

An approximate solution to the unsteady flow of a viscous incompressible fluid through a porous medium bounded by two infinite parallel plates, the lower one stationary and the upper one oscillating in its own plane, is presented here. Expressions for the transient velocity, the amplitude, the phase angle α and the skin-friction are derived and numerically calculated. It is observed that the amplitude increases with increasing σ, the permeability parameter, and ω, the frequency. Also, there is always a phase lead, and the phase angle α decreases with increasing σ.

1 Introduction

Unsteady flows are of importance from the practical point of view. The effects of free-stream oscillations on the flow of an incompressible viscous fluid were studied by Lighthill [1], Stuart [2], Soundalgekar [3] for the horizontal flat plate. By assuming the unsteady flow to be superimposed on the mean steady flow, the equations were linearized and approximate solutions were derived. In all these problems, the external flow was assumed to be oscillating about a nonzero constant mean. This is the generalization of the Stokes' second problem where the flow is due to a plate oscillating in its own plane and without any mean steady flow. Stokes' second problem is discussed in Schlichting [4]. When the plate is moving and also oscillating in its own plane, the problem becomes interesting from the point of view of industrial applications. Ishigaki [5] studied the flow of a viscous fluid between two infinite parallel plates, one of which was stationary and the other was moving and oscillating in its own plane. Approximate solutions were derived for the vleocity field.

Now, if the medium between two such parallel plates is a porous medium and the flow of viscous fluid exists through this porous medium, what is the effect of the oscillation of the plate on the motion of the fluid? Such a phenomenon has not been studied in the literature. It is now proposed to study this physical phenomenon here. In Section 2, the mathematical analysis is presented and in Section 3, the conclusions are set out.

2 Mathematical Analysis

Consider the porous medium bounded by two infinite parallel plates, the lower one is stationary and the upper one is moving steadily and oscillating in its own plane. Then neglecting the compressibility effects of the fluid, the flow in a porous medium is governed by the following equations:

$$\text{div } \bar{V}=0 \tag{1}$$

$$\rho \frac{\partial \bar{V}}{\partial t} = -\text{grad}p + \mu \nabla^2 \bar{V} - \frac{\mu}{\kappa}\bar{V} \tag{2}$$

Here p denotes the pressure, ρ the density of the fluid, μ the viscosity of the fluid, κ the permeability of the porous medium, $\bar{V}$ the velocity vector and all the quantities have their usual meaning. In equation (2), the terms representing the inertia effects are neglected because of very slow motion in the porous medium. We can show that equations (1) and (2) reduce to the following:

$$\rho \frac{\partial u'}{\partial t'} = \rho \frac{\partial U'(t')}{\partial t'} + \mu \frac{\partial^2 u'}{\partial y'^2} + \frac{\mu}{\kappa}(U'(t') - u') \tag{3}$$

where $\bar{V}(u', 0, 0)$ is the velocity vector, t' the time and y' is the normal coordinate. Also the origin is chosen on the lower plate and x'-axis taken along the lower plate in the direction of the flow. The motion of the upper plate is assumed to be $U'(t') = U_0(1+\epsilon e^{i\omega' t'})$ where U_0 is the mean of the unsteady velocity, ω' the frequency of the oscillation and $\epsilon \leq 1$ is the amplitude assumed to be very small. If the upper plate is assumed to be situated at a distance L from the lower stationary plate, then the boundary conditions are

$$u'=0 \text{ at } y'=0,\ u'=U'(t')=U_0(1+\epsilon e^{i\omega' t'}) \text{ at } y'=h. \tag{4}$$

Introducing the following nondimensional quantities

$$\begin{aligned} u &= u'/U_0,\ y=y'/h,\ U=U'/U_0,\ t=t'\nu/h^2 \\ \sigma^2 &= h^2/\alpha,\ \omega=\omega' h^2/\nu \end{aligned} \tag{5}$$

in equations (3) and (4), we have

$$\frac{\partial u}{\partial t} = \frac{\partial U}{\partial t} + \frac{\partial^2 u}{\partial y^2} + \sigma^2(U-u) \tag{6}$$

and the boundary conditions are

$$u(0)=0,\ u(1)=1+\epsilon e^{i\omega t}. \tag{7}$$

We now assume that the unsteady flow is superimposed on the mean steady flow. Then we can represent the plate and the fluid velocity as

$$U(t) = 1+\frac{\epsilon}{2}(e^{i\omega t}+e^{-i\omega t}) \tag{8}$$

$$u(t) = f_0(y)+\frac{\epsilon}{2}\{f_1(y)e^{i\omega t}+\bar{f}_1(y)e^{-i\omega t}\}. \tag{9}$$

Here the bar denotes a complex conjugate. In equation (9), we neglect the coefficients of ϵ^2 as these terms are very small in magnitude because $\epsilon \leq 1$. Substituting equations (8) and (9) in

[1]Gulf Polytechnic, Bahrain, Middle East.
[2]Department of Engineering, Manchester University, Manchester, M13 9PL U.K.
[3]Department of Mathematics, Simon Fraser University, Burnaby, (B.C.) Canada. V5A 1S6.

Contributed by the Fluids Engineering Division of The American Society of Mechanical Engineers. Manuscript received by the Fluids Engineering Division, August 14, 1984.

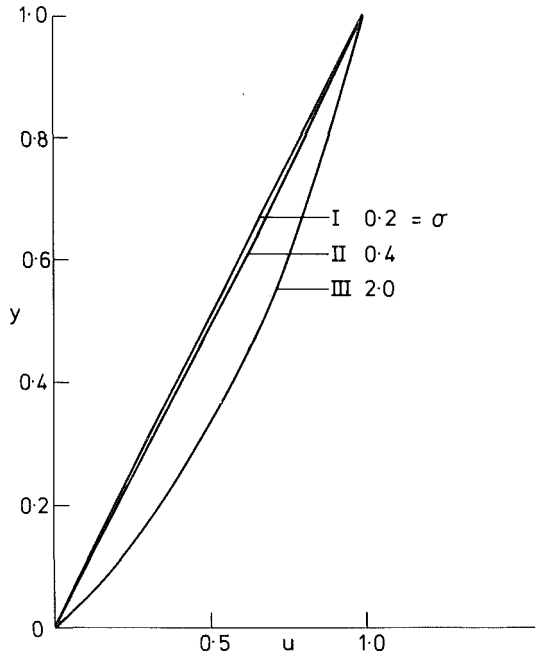

Fig. 1 Transient velocity profiles $\epsilon = 0.2$, $\omega = 5$

equations (6) and (7), equating the harmonic and the non-harmonic terms, we have

$$f_0'' - \sigma^2 f_0 = -\sigma^2 \qquad (10)$$
$$f_0(0) = 0,\ f_0(1) = 1$$

$$f_1'' - (\sigma^2 + i\omega) f_1 = -(\sigma^2 + i\omega) \qquad (11)$$
$$f_1(0) = 0,\ f_1(1) = 1.$$

The solutions of the systems of equations (10) and (11) are as follows:

$$f_0(y) = 1 - \cosh\sigma y + \coth\sigma \sinh\sigma y \qquad (12)$$

$$f_1(y) = 1 - \cosh\sigma_1 y + \coth\sigma_1 \sinh\sigma_1 y \qquad (13)$$

where

$$\sigma_1^2 = \sigma^2 + i\omega.$$

The velocity field is now represented by

$$u = 1 - \cosh\sigma y + \coth\sigma \sinh\sigma y + \epsilon e^{i\omega t}\{1 - \cosh\sigma_1 y + \coth\sigma_1 \sinh\sigma_1 y\}. \qquad (14)$$

In terms of the fluctuating parts, we can express equation (14) as

$$u = 1 - \cosh\sigma y + \coth\sigma \cdot \sinh\sigma y + \epsilon e^{i\omega t}(M_r + iM_i) \qquad (15)$$

where $M_r + iM_i$ = coefficient of $\epsilon e^{i\omega t}$ in equation (14). The real part of (15) now gives the transient velocity as

$$u = 1 - \cosh\sigma y + \coth\sigma \sinh\sigma y - \epsilon M_i. \qquad (16)$$

The numerical values of u are calculated from equation (16) and these are plotted in Fig. 1 for different values of permeability parameter σ. We observe from this figure that an increase in σ leads to an increase in the transient velocity. But σ increases when the permeability κ decreases. It is also physically possible because when the permeability of the porous medium decreases the resistance to the motion of the fluid in the porous medium decreases and this causes the transient velocity to increase. However, the transient velocity is not affected appreciably by the frequency ω because the influence of the frequency on the transient velocity is resisted by the porous medium. Hence the effects of ω are not shown on the figure.

Table 1 Values of the amplitude $|B|$ and $\tan\alpha$

ω:	10	15	20
σ		$\lvert B\rvert$	
0.2	3.1792	3.8509	4.4563
0.4	3.1808	3.8520	4.4566
2.0	3.3064	3.9387	4.5091
σ		$\tan\alpha$	
0.2	0.9960	0.9973	0.9980
0.4	0.9841	0.9894	0.9920
0.2	0.6770	0.7683	0.8198

From the velocity field, we now study the skin-friction. It is given in nondimensional form as

$$\tau = \frac{1}{R}\left.\frac{\partial u}{\partial y}\right|_{y=0} \qquad (17)$$

where $\tau = \tau'/\rho U_0^2$ and $R = \rho U_0 h/\mu$.

Here R is the Reynolds number. From (14 and (17)), we get

$$\tau = \frac{1}{R}(\sigma \tanh\sigma + \epsilon e^{i\omega t}\sigma_1 \tanh\sigma_1)$$

and in terms of the amplitude and phase, we can write (18) as

$$\tau = \frac{1}{R}[\sigma \tanh\sigma + \epsilon |B| \cos(\omega t + \alpha)] \qquad (19)$$

where

$$B = B_r + iB_i = \sigma_1 \tanh\sigma_1$$

and $\tan\alpha = B_i/B_r$.

We have calculated the numerical values of the amplitude $|B|$ and the phase angle α and their values are entered in Table 1. We observe from this table that the amplitude $|B|$ increases with increasing ω and σ. Physically, this is possible because when the permeability of the porous medium decreases, the resistance by the porous medium also decreases and hence there is a rise in the value of $|B|$. But the phase angle α decreases with increasing σ. However, there is always a phase-lead for all values of σ and ω.

3 Conclusions

1. An increase in the permeability parameter σ leads to an increase in the transient velocity
2. An increase in σ or ω leads to an increase in the amplitude of the skin-friction.
3. There is always a phase-lead, the phase angle α being found to decrease with increasing σ.

References

1 Lighthill, M. J., "The Response of Laminar Skin-Friction and Heat Transfer to Fluctuations in the Stream Velocity," *Proc. Roy. Soc.* (London), Vol. A224, 1954, pp. 1-23.

2 Stuart, J. T., "A Solution of the Navier-Stokes and Energy Equations Illustrating the Response of Skin-Friction and Temperature of an Infinite Plate Thermometer to Fluctuations in the Stream Velocity," *Proc. Roy. Soc.* (London), Vol. A231, 1955, pp. 116-130.

3 Soundalgekar, V. M., "The Effects of Suction on the Flow of an Incompressible Fluid Past an Infinite Porous Plate with Fluctuations in the Stream Velocity," *Regional Journal of Energy*, Heat Mass Transfer, Vol. 3, 1981, pp. 271-278.

4 Schlichting, H., *Boundary Layer Theory*, McGraw-Hill, New York, 1968.

5 Ishgaki, H., "An Exact Periodic Solution of the Energy Equation," *J. Fluid Mechanics*, Vol. 50, 1971, pp. 657-668.